Damping and Fretting of Frictional Contacts in the Steady-State



Nils Cwiekala

St Peter's College

University of Oxford

A thesis submitted for the degree of

Doctor of Philosophy

Trinity 2022

Abstract

Contacts in mechanical assemblies are often subject to a constant load together with an oscillatory component. The latter might originate from vibration such that the component experiences a high number of load cycles. Different dissipative processes affect the steady-state behaviour of the assembly. In terms of contacts the most apparent is friction along the interface, which might lead to surface damage. Locally, the contact might act as a stress raiser, such that the material in the neighbourhood experiences plastic deformation. Cracks nucleating from the damaged surface and propagated in each load cycle are another limiting factor for the component's life. All these effects can be studied individually, but in reality they will affect each other to a certain degree. After a review of analytical and asymptotic contact descriptions, this thesis aims to describe the interaction between interfacial slip and other dissipative or life-limiting effects. A graphical method is presented to determine if a given loading causes the material in the contact region to reach the onset of plasticity. The limits of the elastic regime are explored and evaluated with this method.

Strong analogies exist between plasticity and slip. Shakedown, a process in which the generation of residual stresses in the first load cycles counteracts further dissipation, is one example. In the context of plasticity the residual stresses are generated due to plastic deformation, while it is due to relative slip displacements in the context of friction. However, it is shown that principles, established in the context of plasticity, are not generally transferable to friction. Repeated frictional slip may lead to surface degradation with a reduction of the contact extent. Simple calibrations are derived between the external contact loading and multipliers characterising the stress field around the edge of the resulting contact. Following the same basic idea makes it possible to identify crack tip stress intensity factors of cracks nucleating from the contact region. These intensity factors characterise the stress field around the crack tip, but also are used to assess the crack propagation per load cycle.

Preface

This thesis contains a collection of research performed by the author in the Department of Engineering Science at the University of Oxford under the supervision of Professor David A. Hills. This work is original and no part of it has been submitted for a degree at this university or elsewhere. Some of the work described in this thesis has been published or is under consideration for publication in the following papers:

- N. Cwiekala and D. A. Hills (2021b). "Half-plane contacts subject to remote tension". In: *The Journal of Strain Analysis for Engineering Design* 56 (8), pp. 539–547
- N. Cwiekala and D. A. Hills (2021c). "Stress intensity factor calibration for short cracks at the edge of semi-infinite contacts". In: *Engineering Fracture Mechanics* 247, p. 107692
- N. Cwiekala and D. A. Hills (2021a). "Asymptotic description of fretting wear and fretting fatigue for incomplete contacts". In: *Engineering Fracture Mechanics* 256, p. 107986
- N. Cwiekala, J. R. Barber, and D. A. Hills (2022b). "Memory-free loading paths for a coupled continuous contact problem with friction". In: *Mechanics Research Communications* 124, p. 103958
- N. Cwiekala, J. R. Barber, and D. A. Hills (2022a). "Frictional Shakedown of a Coupled Continuous Contact". In: *International Journal of Solids and Structures*. in preparation

Some of the work described in this thesis has been presented at the following conferences:

- N. Cwiekala and D. A. Hills (2019). "Frictional Shakedown for Continuous Coupled Contacts". *ASME 2019 International Mechanical Engineering Congress & Exposition*, Salt Lake City, USA.
- N. Cwiekala and D. A. Hills (2022). "Elastic Limit Calculation for Flat and Rounded Contacts". *18th European Mechanics of Materials Conference*, Oxford, United Kingdom.

Acknowledgements

I would like to use this opportunity to thank my supervisor Professor David Hills, to whom I am deeply grateful. His ability to support in difficult moments, to challenge where necessary, but to give freedom where possible created an atmosphere with the opportunity to thrive not only academically, but also personally. I also would like to thank Professor James Barber from the University of Michigan for his invaluable feedback and challenging my ideas when my perspective was too narrow.

I sincerely thank Rolls-Royce plc and the Engineering and Physical Sciences Research Council (EPRSC) for their financial support under the Prosperity Partnership Grant 'Cornerstone: Mechanical Engineering Science to Enable Aero Propulsion Futures' [EP/R004951/1].

I am very grateful to have met and worked with many different colleagues at the Department of Engineering Science, of which I would like to mention Ms. Amanda Bradbury and Mr. Hisham Elamin for support of all kinds, Dr. Robert Paynter for his support with academical problems, and especially Mr. Daniel Riddoch, Dr. Hendrik Andresen and Dr. Jhonatan Da Ponte Lopes for their support, interesting conversations over lunch and becoming good friends.

Last but not least, I would like to thank my family especially my parents and my brothers Jan, Tim and Tobias for their unconditional support, and my friends here and back at home for their companionship. My deepest gratitude goes to my partner Alessa whom I cannot thank enough for facing unimagined challenges to be with me and support me.

Contents

1 Introduction **1**

1.1 Fretting 1

1.1.1 Fretting Fatigue 2

1.1.2 Fretting Wear 2

1.2 Damping 2

1.3 Summary 4

2 Contact Fundamentals **6**

2.1 Half-Plane Approximation and Plane Elasticity 6

2.2 Contact Classification 8

2.3 Frictionless Indentation 11

2.3.1 Definition of Contact 11

2.3.2 Application of a Line Load - The Flamant Solution 13

2.3.3 Distributed Normal Traction 15

2.3.4 Contact of Deformable Bodies 15

2.3.5 Contact Examples 17

2.4 Tangential Loading 22

2.4.1 Material Coupling 23

2.4.2 Fully Stuck Contacts 24

2.4.3 Friction and Gross Sliding 25

2.5 Partial Slip 27

2.5.1 Origins of Partial Slip 27

2.5.2 Jäger-Ciavarella Theorem 29
2.6 Subsurface Contact Stress 32
2.6.1 Muskhelishvili Complex Potential 32
2.6.2 Explicit Stress Field 34
2.7 Shakedown 35
2.7.1 Melan's Theorem 36
2.7.2 Shakedown of Uncoupled Contacts 36
2.7.3 Shakedown of Coupled Contacts 36
2.7.4 The System Memory 40

3 Asymptotic Contact Description 42
3.1 Asymptotic Contact Tractions 43
3.1.1 Asymptotic Normal Traction for Incomplete Contacts 43
3.1.2 Asymptotic Shear Traction for Fully Adhered Contacts 45
3.1.3 Asymptotic Shear Traction for Partial Slip Contacts 47
3.2 Williams' Solution 49
3.2.1 Eigenvalues 50
3.2.2 Stress Field 52

4 Distributed Dislocation Technique 56
4.1 Dislocations 57
4.2 Formulation 58
4.3 Gauss-Chebyshev Quadrature 60
4.4 Crack Tip Stress Intensity Factor 62
4.5 Krenk's Interpolation 63

5 Stress Field at the Edge of Incomplete Contacts 65
5.1 Elastic Limit Calculation 66
5.1.1 Normal Loading 67
5.1.2 Shear Loading 69
5.1.3 Differential Bulk Tension 73

5.1.4 Conclusion 75
5.2 Comparison between Muskhelishvili Potential and Williams' Solution for Contacts 76
5.2.1 Series Expansion of the Muskhelishvili Potential 77
5.2.2 Williams' Solution for Arbitrary Terms 81
5.2.3 Comparison and Conclusion 84
5.3 Half-plane contacts subject to remote tension 85

6 Short Cracks at the Edge of Incomplete Contacts 99
6.1 Stress intensity factor calibration for short cracks at the edge of semi-infinite contacts 99
6.2 Threshold Analysis for Short Cracks 118
6.2.1 Introduction 118
6.2.2 Application to Fretting Fatigue Experiments 120
6.2.3 Results and Conclusion 124
6.3 Asymptotic description of fretting wear and fretting fatigue for incomplete contacts 126

7 Shakedown of a Continuous Coupled Contact 142
7.1 Memory-free loading paths for a coupled continuous contact problem with friction 142
7.2 Frictional Shakedown of a Coupled Continuous Contact 154

8 Conclusion 171

Bibliography 175

Appendices 185
A Subsurface Stress for Flat and Rounded Contacts 185
A.1 Normal Loading 185
A.2 Shear Loading 188
A.3 Differential Bulk Tension 191

A.4 Abbreviations for Complex Split 196
B Experimental Data 197
B.1 Experimental Results by Nowell 197
B.2 Experimental Results by Dini 199
B.3 Experimental Results by Szolwinski and Farris 200
B.4 Experimental Results by Hojjati-Talemi et al. 202

Chapter 1

Introduction

Common engineering problems often involve the study of the response of a structure subject to external loads. Aside from body forces, such as gravity or magnetic attraction, contacts are the only way to apply these forces. Consequently, almost all mechanical assemblies involve the contact of different components to transfer forces from one to another. The characteristics of such contacts in terms of the contact geometry or the specific loading typically differs for different components or mechanical assemblies. In order to improve the understanding of contacts, the field of *contact mechanics* is concerned with the classification of different types of contacts as well as the study and description of those idealised contact scenarios. Before giving a recap of fundamental contact mechanics in the next chapter, the practical relevance of the field of contact mechanics will be discussed.

1.1 Fretting

Contacts are often subject to a constant component of load (such as bolt tightening) or slowly varying load (such as the centrifugal forces developed in a gas turbine) together with a high frequency oscillatory component, normally originating in vibration. A constant component of load may serve to establish and keep the two bodies in contact. Even though the contact loading might be such that there is, macroscopically, no relative rigid body movement between the two contacting bodies, depending on their geometry, tangential loading might cause local regions of relative slip displacement,

referred to as *partial slip*. We will look at the phenomenon and possible origins of partial slip in more detail as part of the next chapter, but note for now, that it may cause a change in the contact tractions. If the tangential loading is oscillatory in nature, we might find local regions of forward and backward relative displacements. We refer to these regions of repeated forward and backward partial slip, as *fretting*.

1.1.1 Fretting Fatigue

The life of mechanical structures subject to an oscillating load might be limited by fatigue, even though the stress throughout the structure is nominally well below the yield limit at every instant (Barber, 2011b). Fatigue refers to the nucleation and propagation of cracks over a certain number of load cycles. Such fatigue cracks often nucleate in a region of a stress concentration such as the region adjacent to a notch. A contact may also act as such a local stress raiser. We find this, together with the varying contact stress due to fretting, to encourage the nucleation of fatigue cracks, and we refer to this phenomenon as *fretting fatigue*. We will look at the nucleation and propagation of fretting cracks in Section 6.1.

1.1.2 Fretting Wear

Wear describes the surface damage due to relative movement and friction between contacting bodies. It is commonly experienced in macroscopic slip and the corresponding large slip displacements. The comparatively small slip displacements that we find in partial slip are in principle not sufficient to cause wear. However, localised and oscillatory slip displacements in terms of fretting may cause surface damage, referred to as *fretting wear*. In Section 6.3 the effect of fretting wear will be examined in more detail.

1.2 Damping

We addressed, briefly, the damaging effects of partial slip in terms of fretting wear and fretting fatigue. Furthermore, friction in terms of cyclic slip dissipates energy

and therefore causes damping, limiting the severity of fretting fatigue. The damping properties of a contact experiencing oscillatory loading may change over time. Fretting wear causes a change in surface shape and hence a change in damping properties. The surface damage due to fretting wear will cause a profile reduction within the slip region, until eventually all slip has eased. The final worn contact will be fully stuck and consequently no energy will be dissipated so that the contact will not contribute to the system damping any more.

By *frictional shakedown* we refer to a different process causing a change to the system's damping properties, not related to a change in profile of the contacting bodies. If the contact starts off in partial slip, but, owing to the development of interfacial slip displacements with attendant tractions, becomes stuck, it is said to 'shake down', a term borrowed from plasticity theory where it implies the evolution of an initial region of plasticity to an elastic state. This happens because of the self-generation of a beneficial residual state of stress which is introduced by slip displacements and is described in more detail in Section 2.7. Contacts which are fully stuck may actually have a slightly higher stress concentration at their edges but do not suffer from surface degradation, and they also, evidently, do not damp energy. One ambition of the gas turbine industry is to produce a 'whole engine model' in which, at some level of fidelity, all joints or contacts are included, and it would be valuable to know if, in the steady state, they are adhered or suffering cyclic slip.

One possible method of analysis is simply to form a model of the contact and track out the evolution of the interfacial behaviour as a function of time, but this does not seem a very realistic proposition in the case of the engine where there are hundreds of contacts and their responses will, to some extent interact. So, it would be valuable to be able to predict the steady state response without tracking out the transient response, if this is possible. Theorems, enabling such a prediction, are well known in terms of plastic shakedown, so that the transferability of concepts from plasticity to frictional shakedown is subject to ongoing research. We will investigate the shakedown properties of contacts in Section 7.2.

1.3 Summary

In Chapter 2, we start with an overview of the assumed simplifications regarding geometry and material behaviour. A taxonomy of the different classes of contacts is given before we look at a formal definition of contacts. This serves as a starting point for the discussion of known analytical contact descriptions, which look at the deformation and stress resulting from different contact loadings. The chapter ends by reviewing the analogies between plastic and frictional processes, focusing on the steady-state behaviour. Chapter 3 continues with the review of the literature by looking at an asymptotic description of contacts. Here, the focus on the region close to one contact edge, where cracks are most likely to nucleate, allows a generalisation of contact problems as well as a description of loading scenarios where, for the finite contact, no analytical solution can be found. Chapter 4 prepares a semi-analytical approach for the solution of singular integral equations which is used throughout the thesis.

Chapter 5 focuses on the stress field surrounding incomplete contacts. We start in Section 5.1 with a finite contact description leading the equivalent stress for the entire subsurface field. Based on this we identify the loads corresponding to the first material point reaching the onset of plasticity. This allows us to assess, for given loads, if the assumption of linear elasticity is justified. In Section 5.2 we then focus at the edge of the contact and the corresponding asymptotic description of the subsurface stress field. A comparison between the stress components derived via the Muskhelishvili complex potential and those obtained from the Williams' solution, prepares an investigation of tangentially loaded contacts and their asymptotic representation. Specifically, in Section 5.3, we try to show how the origin of the shear traction affects the subsurface stress field, even though the resulting contact shear traction is the same.

In Chapter 6 we introduce a crack in one of the contacting bodies. The crack now sees the stress field derived in the previous chapter. Simple calibrations are found, in Section 6.1, between the asymptotic contact multipliers, characterising the contact tractions, and the resulting crack tip stress intensity factors. The crack tip stress intensity is an

important quantity when trying to describe the crack propagation per load cycle, and the derived calibrations allow us to identify it without the need of solving a singular integral equation. We apply these calibrations, in Section 6.2, to experimental results and identify an asymptotic approximation of the conditions necessary for crack arrest. The same ideas are then applied in Section 6.3, to derive an asymptotic description of long term wear.

The last research chapter (Chap. 7) looks at frictional shakedown of coupled contacts. Section 7.1 prepares the following analysis by introducing the contact of a shrink-fitted disc in an infinite plane. A semi-analytical description of the problem, based on the methodology introduced in Chapter 4, is derived. This description provides the resulting contact tractions for a state of partial slip and allows us to identify the conditions for the derived state to be memory-free. Based on the introduced contact geometry, we look in Section 7.2 at the shakedown behaviour of coupled contacts when being subject to varying loads. The main results of the thesis are summarised in Chapter 8.

Chapter 2

Contact Fundamentals

The subject of contact mechanics dates back approximately 140 years to when Hertz described the contact of glass lenses to study its effect on optical interference (Hertz, 1881). Hertz's publication "Über die Berührung fester elastischer Körper" describes the contact of elastic spheres loaded normal to the contact interface. It provides results for the size of the contact area and the pressure distribution. Hertz's description assumes the contact to be frictionless, and the contacting bodies were required to have a quadratic profile. Since then, progress in the subject of contact mechanics aimed to remove those restrictions (Johnson, 1985). Results of this include the generalisation of contact geometries as well as consideration of frictional contact interfaces.

Here we introduce the approximations and assumptions made throughout this work, before we give a classification of different types of contacts. Various potential ways in which they might be loaded are discussed, as well as the resulting contact tractions. Relative displacements between the contacting bodies will be described for problems in partial slip.

2.1 Half-Plane Approximation and Plane Elasticity

Throughout this work we assume the contacting bodies to be linear elastic. The extent of the contact is assumed to be small compared to the size of the contacting bodies. Consequently, the exact geometry of the bodies, far away from the contact, is not important. This allows us to assume that the bodies extend to infinity, away from the

contact region (Barber, 2018). Furthermore, those bodies which do not have sharp corners, and whose curvature is small near the contact area, can be treated as half-spaces.

Additionally, we will restrict ourselves to a two-dimensional description of contacts, and consequently the aforementioned treatment by half-spaces simplifies to half-planes. The two-dimensional, or plane, description assumes that none of the stress or strain components shows a gradient with respect to the out-of-plane, or z, direction. This assumption holds if the extent of the contact in the out-of-plane direction is infinitely long, and remains an appropriate assumption if it is long compared to contact width. For such a case the components of strain in the out-of-plane direction, ε_{xz}, ε_{yz} and ε_{zz}, vanish, and consequently it is known as *plane strain*.

Another case in which a two-dimensional description seems appropriate is the in-plane contact of 'thin' plates. The contacting bodies would then have free surfaces in the z-direction and consequently the stress components σ_{xz}, σ_{yz} and σ_{zz} approximately vanish throughout the entire thickness. We refer to such conditions as *plane stress*. However, compared to the contact width, most contacts actually have a significant extent in the out-of-plane direction such that the conditions for plane stress are not met. We will therefore focus on a plane strain description, but note that solutions for plane stress can always be derived by a corresponding substitution of the elastic constants (Barber, 2018). Additionally, where appropriate, we will make use of Kolosov's constant, κ, defined as

$$\kappa = \begin{cases} 3 - 4\nu & \text{for plane strain,} \\ \frac{3-\nu}{1+\nu} & \text{for plane stress,} \end{cases} \tag{2.1}$$

where ν is Poisson's ratio. This allows us to express the linear stress-strain relationship,

referred to as *Hooke's law*, by

$$\begin{aligned}\varepsilon_{xx} &= \frac{\kappa+1}{8\mu}\sigma_{xx} + \frac{\kappa-3}{8\mu}\sigma_{yy} \ , \\ \varepsilon_{yy} &= \frac{\kappa-3}{8\mu}\sigma_{xx} + \frac{\kappa+1}{8\mu}\sigma_{yy} \ , \\ \varepsilon_{xy} &= \frac{1}{2\mu}\sigma_{xy} \ ,\end{aligned} \tag{2.2}$$

where μ is the modulus of rigidity and both the plane strain or plane stress solution can then be obtained by choosing the corresponding case of (2.1).

Generally, we assume the problems considered to be static such that we may neglect inertia effects. The equilibrium conditions for every material point of the considered bodies (and in the absence of body forces like gravity), can then be expressed as $\mathrm{div}(\boldsymbol{\sigma}) = \mathbf{0}$. For plane problems this reduces to the two equations

$$\frac{\partial \sigma_{xx}}{\partial x} + \frac{\partial \sigma_{xy}}{\partial y} = 0 \ , \qquad \frac{\partial \sigma_{yy}}{\partial y} + \frac{\partial \sigma_{xy}}{\partial x} = 0 \ . \tag{2.3}$$

We will later address, and prohibit, interpenetration of the contacting bodies, but we also want to restrict each individual body to deformations not leading to self-interpenetration or the formation of voids. In terms of the strains (2.2) this is expressed by the so called *compatibility conditions*. For plane problems these reduce to a single equation

$$\frac{\partial^2 \varepsilon_{xx}}{\partial y^2} + \frac{\partial^2 \varepsilon_{yy}}{\partial x^2} = 2\frac{\partial^2 \varepsilon_{xy}}{\partial x \partial y} \ . \tag{2.4}$$

2.2 Contact Classification

In mechanical assemblies contacts arise in numerous different contact geometries which may experience different types of loading. The simplifications introduced allow the classification of general contacts to those shown in Figure 2.1. All the contacts are established by a load P normal to the contact interface. The load is then transferred from one body to the other via the contact interface where we find a normal traction

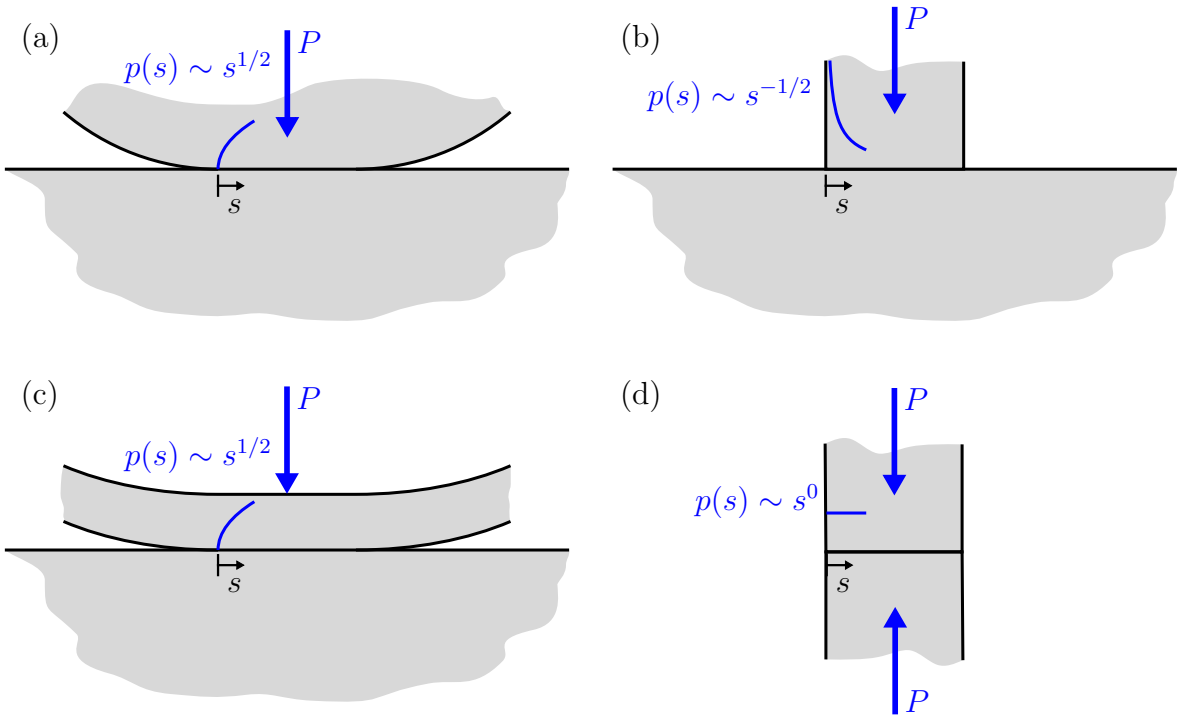


Figure 2.1: Classification of contacts (each contact established by normal force P) (a) incomplete contact formed by a cylinder pressed into a half-plane, (b) square block pressed into a half-plane forming a complete contact (c) receding contact formed by a layer of material pressed into a half-plane (d) common-edge contact of two square blocks pressed into contact (Hills and Andresen, 2021).

p. It is one of the main concerns of the study of contacts to find the exact distribution of this normal traction along the contact interface, and we follow the convention that a positive contact traction, p, corresponds to a compressive (negative) stress.

Figure 2.1(a) shows an *incomplete* contact formed by a cylinder pressed into a half-plane. The term 'incomplete' refers to the extent of the contact which depends on the applied load, P. If the load is increased the contact area extends or 'advances' at both sides while it will shrink to an infinitesimal size if the load is reduced to almost zero. For this type of contact we find the profile of the contacting bodies to have a common tangent at the edge of the contact, and the contact pressure, $p(s)$, to fall continuously to zero (Hills and Nowell, 1994). Both of the contacting bodies in Figure 2.1(a) are free of sharp corners and the curvature of the cylinder is small compared to the size of the contact. This allows us to approximate both of the contacting bodies by half-planes, and the results correspond to what we find for two cylinders pressed into contact. Consequently, Figure 2.1(a) represents the two dimensional case of a *Hertzian*

contact.

The contact shown in Figure 2.1(b), on the other hand, is said to be *complete*, i.e. the size of the contact (once established) is independent of the loading. Here, the contact size is defined by the width of the block which is pressed into the half-plane. The block has sharp corners and therefore cannot be approximated by a half-plane. At the edges of the contact the profile of the deformed bodies do not have a common tangent and we find the contact pressure to show a singularity when approaching the edge of the contact (Hills and Nowell, 1994).

The contact shown in Figure 2.1(c) differs from the two aforementioned classes of contacts in terms of the relationship between the applied normal load and the extent of the contact. Initially, an infinite flat elastic strip rests on an elastic half-plane, and both bodies are in contact along the entire length of the strip. Once we load the strip with a centred line load, P, the contact area *recedes* as shown in Figure 2.1(c). It snaps to its final size, even if the load is infinitesimal. A further increase of the normal load will change the contact pressure as well as the displacements but the separation points remain unchanged. In terms of the asymptotic contact pressure, $p(s)$, at the edge of the contact, this type of contact shows similarities to an incomplete contact. With the contacting bodies having a common tangent at the edge of the contact, we find the normal traction to be square root bounded, as for the incomplete contact shown in Figure 2.1(a). This type of contact arises in engineering assemblies, for example in the form of bolted joints or 'high strength friction grip' connections and early contributions to studies of this type of contact were made by Keer et al. (1972).

Figure 2.1(d), finally, shows a contact, which, in terms of the contact extent, is similar to a complete contact, i.e. the contact size is independent of the load P. It differs from the contacts shown before in terms of the contact traction at the edge of the contact. At the *common edge* of the contacting bodies shown we find the contact pressure neither falls to zero nor shows a singular behaviour when approaching the edge. Instead it tends to a finite value.

In Figure 2.1 and the description above we focus on the contact traction at the edge

of the contact. This is a reasonable approach when, for example, looking at fretting fatigue as cracks are found to nucleate from the contact edge. If we 'zoom in' on the edge of the contact, the tractions may be accurately represented by a single term and all other geometric features, including the other edge of the finite contact, are considered to be far away from the region of interest. The contact edge is then represented by a semi-infinite contact and we refer to this approach as an *asymptotic* analysis of the contact problem which in detail will be discussed in Chapter 3.

2.3 Frictionless Indentation

Above, we have introduced different contact examples and addressed the relationship between contact geometry and resulting normal traction, $p(x)$. Here, a formal description of the profile of two non-conformal bodies allows a general definition of contacts.

2.3.1 Definition of Contact

We follow the notation introduced by (Barber, 2018) and describe the profiles of two arbitrarily shaped and undeformed bodies by the functions $g_1(x)$ and $g_2(x)$. Each function represents the gap we would find if we place the corresponding body in contact with a plane surface, such that the two touch at precisely one point or along a line in plane problems. If we want to describe the contact between the two bodies, we may define the reference frame as the configuration in which both the bodies make contact at one point, O (Fig. 2.2(a)). At this point, and if the profiles are smooth surfaces, their tangent and normal vectors align. We define the composite initial gap function

$$g_0(x) = g_1(x) + g_2(x), \tag{2.5}$$

representing the gap between the contacting bodies, measured parallel to the aligned normal. While (2.5) gives the initial gap, this may be modified by the application of a normal load, P, pressing the bodies against each other, while we assume that interpenetration is not possible. The contact will now cause the bodies to deform, and

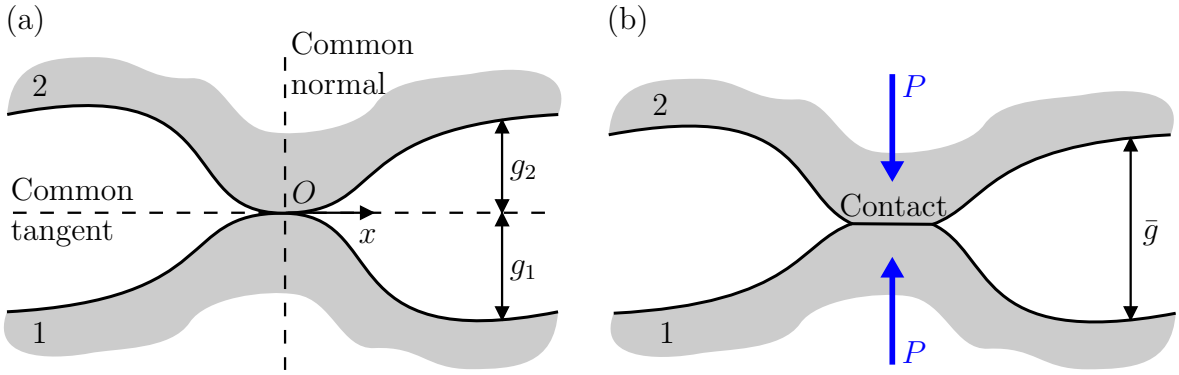


Figure 2.2: Contact of (a) undeformed bodies with initial gap (Barber, 2018) and (b) deformed bodies under the application of a normal load, P, with resulting gap.

we may describe the resulting gap by a superposition of different terms. The normal load, P, may cause a rigid body relative displacement, here defined for the upper body and denoted by Δ, as well as a small rigid-body rotation, Ω, around the initial point of contact, O, and which we define as positive if clockwise. Furthermore, the deformation of the bodies causes a surface displacement $v(x)$ in normal (and $u(x)$ in tangential) direction. The resulting gap is given by

$$\bar{g}(x) = g_0(x) - \Delta - \Omega\, x + g(x)\ . \tag{2.6}$$

where $g(x) = v_2(x) - v_1(x)$ is the relative surface normal displacement. Initially established at a discrete point, O, the contact may now range over a finite region where necessarily the gap (2.6) has vanished (Fig. 2.2(b)) such that (Barber, 2010)

$$v_1(x) - v_2(x) = g_0(x) - \Delta - \Omega\, x \qquad \text{for} \quad x \in \text{Contact}\ . \tag{2.7}$$

In the remaining region, where the bodies are not in contact, we find $\bar{g}(x) > 0$. We assume, for now, that the contact is frictionless such that the only traction transmitted via the contact interface is a normal traction, $p(x)$. As previously mentioned, we follow the convention that a positive normal traction corresponds to a compressive stress normal to the interface, i.e. $p(x) = -\sigma_{yy}(x, 0)$. Furthermore, we neglect cohesive effects such that the contact normal traction can never be negative, i.e. no tensile stress can be transmitted via the contact interface. Where the bodies are not in contact,

$x \notin$ Contact, the surfaces are traction free with $p(x) = 0$. The contact problem can then be expressed in terms of a linear complementary (LCP) condition (Barber, 2018)

$$p(x)\,\bar{g}(x) = 0\ . \tag{2.8}$$

Our main interest, here, is to find the extent of the contact as well as the present distribution of contact normal traction, $p(x)$.

2.3.2 Application of a Line Load - The Flamant Solution

The first step in finding the normal contact traction, for a given geometry of the contacting bodies, is the derivation of the stress field caused by a concentrated normal load, P, applied to a half-plane as shown in Figure 2.3(a). The state of stress was found by Flamant (1892) as a special case of Boussinesq's (1885) three-dimensional solution for the application of a point load on a half-space. Flamant showed that the resulting stress field is a direct stress, acting everywhere towards the point of the load application. For the polar coordinate system shown in Figure 2.3(a) this can be expressed as

$$\sigma_{rr}(r,\theta) = \frac{2P}{\pi r}\sin(\theta)\ , \quad \sigma_{\theta\theta} = \sigma_{r\theta} = 0\ . \tag{2.9}$$

Timoshenko and Goodier (1951) found the corresponding Airy stress function

$$\phi(r,\theta) = -\frac{P}{\pi} r\theta\cos(\theta)\ , \tag{2.10}$$

and showed that the resulting displacement field fulfils the necessary compatibility conditions. The state of stress can be expressed in Cartesian coordinates (Johnson,

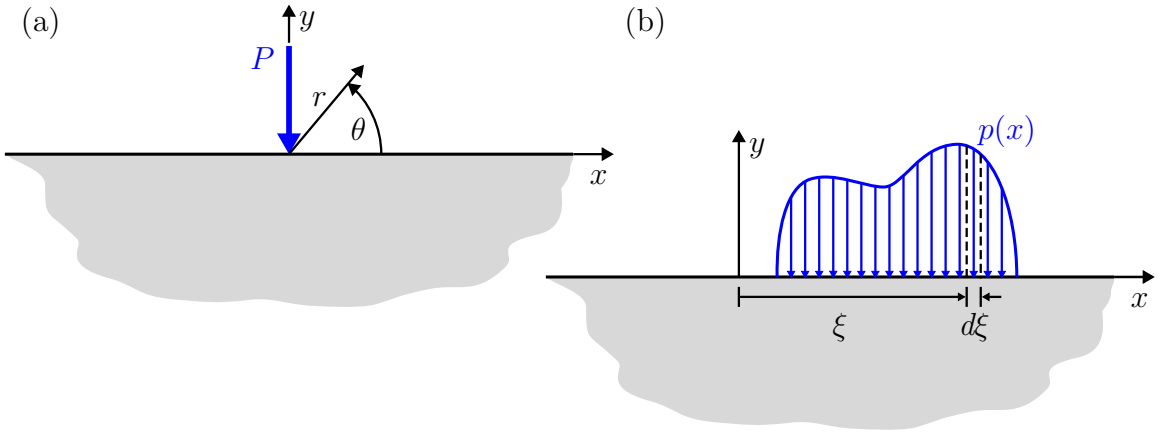


Figure 2.3: Half-plane loaded with (a) a line load, P, applied at the origin and (b) an arbitrary pressure distribution $p(x)$.

1985) by

$$\begin{aligned}\sigma_{xx}(x,y) &= \frac{2P}{\pi}\frac{x^2 y}{(x^2+y^2)^2}\,,\\ \sigma_{yy}(x,y) &= \frac{2P}{\pi}\frac{y^3}{(x^2+y^2)^2}\,,\\ \sigma_{xy}(x,y) &= \frac{2P}{\pi}\frac{xy^2}{(x^2+y^2)^2}\,.\end{aligned} \tag{2.11}$$

From the stress field (2.11) we may find the corresponding strains by invoking Hooke's law. The resulting surface displacements of the half-plane, $u(x)$ and $v(x)$, may then be found by integration and are available in standard literature (Barber, 2010) as part of the displacements resulting from the Michell solution (Michell, 1899). After imposing symmetry around the origin by superposing a rigid body displacement we find (Barber, 2010)

$$u(x) = -\frac{P}{4}\frac{\kappa-1}{2\mu}\mathrm{sgn}(x)\,, \tag{2.12}$$

$$v(x) = \frac{P}{2\pi}\frac{\kappa+1}{2\mu}\ln|x|\,, \tag{2.13}$$

where the $\mathrm{sgn}(x)$ function is defined as -1 for $x<0$ and 1 for $x>0$.

2.3.3 Distributed Normal Traction

We may now use the Flamant solution, (2.12) and (2.13), to represent a distributed normal traction, $p(x)$, by the superposition of a set of point loads, each of magnitude $p(\xi)\mathrm{d}\xi$, as shown in Figure 2.3(b). However, this only allows us to determine the surface displacements up to a rigid body displacement. Contact problems are therefore often formulated in terms of the displacement gradient. The gradient of the surface displacements of the half-plane are then given by

$$\frac{\partial u(x)}{\partial x} = -\frac{\kappa - 1}{4\mu} p(x) \ , \tag{2.14}$$

$$\frac{\partial v(x)}{\partial x} = \frac{\kappa + 1}{4\pi\mu} \int_{\text{Contact}} \frac{p(\xi)}{x - \xi} \mathrm{d}\xi \ , \tag{2.15}$$

and we note that the gradient of the surface strain $\partial u(x)/\partial x = \varepsilon_{xx}(x, 0)$. The first of equations (2.2) and equations (2.14) then give us two expressions for the surface strains. Equating both expressions, and keeping in mind that $p(x) = -\sigma_{yy}(x, 0)$, leads to

$$\sigma_{yy}(x, 0) = \sigma_{xx}(x, 0) \ , \tag{2.16}$$

stating that under any distribution of surface normal pressure the direct components of stress, in tangential and normal direction to the surface, are equal and compressive (Johnson, 1985).

The integrand in equation (2.15) shows a singularity for a point x within the integration range. Therefore, equation (2.15) forms a singular integral equation which needs to be evaluated in a Cauchy Principal Value sense. We will briefly discuss solution strategies in the next section, and for a detailed discussion refer to the corresponding literature.

2.3.4 Contact of Deformable Bodies

For the contact between two bodies we consider the relative surface displacements resulting from the corresponding deformation $g(x) = v_2(x) - v_1(x)$ and $h(x) = u_2(x) -$

$u_1(x)$. Their gradients are related to the normal traction, present at the contact interface, via

$$\frac{1}{A}\frac{\partial h(x)}{\partial x} = \beta p(x) \ , \tag{2.17}$$

$$\frac{1}{A}\frac{\partial g(x)}{\partial x} = -\frac{1}{\pi}\int_{\text{Contact}} \frac{p(\xi)}{x-\xi}\mathrm{d}\xi \ , \tag{2.18}$$

where it should be noted that there is a change of sign in equation (2.15) if we consider body 2, i.e. the body in the upper half-plane, as the y-axis is directed into the body now, and not outwards as for the definition in Section 2.3.3 (Hills et al., 1993). The composite compliance, A, and Dundurs' constant (Dundurs, 1967), β, depend solely on the elastic properties of the contacting bodies and are given by

$$A = \frac{\kappa_1 + 1}{4\mu_1} + \frac{\kappa_2 + 1}{4\mu_2} \tag{2.19}$$

and (Hills and Nowell, 1994)

$$\beta = \frac{\mu_2(\kappa_1 - 1) - \mu_1(\kappa_2 - 1)}{\mu_2(\kappa_1 + 1) + \mu_1(\kappa_2 + 1)}. \tag{2.20}$$

The subscripts refer to the corresponding body as shown in Figure 2.2. The solution to the singular integral equation (2.18) provides the relative surface displacement and normal traction sufficient to ensure that there is no overlap between the contacting bodies. We note from equation (2.17) that the tangential surface displacements resulting from the contact pressure may differ for both bodies, depending on their elastic properties. For the frictionless case considered here, this relative tangential displacement has no consequences for the state of stress. However, we note that it vanishes if $\beta = 0$, as, for example, it will be the case for elastically similar bodies.

Equilibrium with external forces is ensured by the condition

$$P = \int_{\text{Contact}} p(\xi)\mathrm{d}\xi \ , \tag{2.21}$$

where P is the normal load pressing the two bodies together and p is the resulting normal traction transmitted via the contact interface shown in Figure 2.2(b).
Equation (2.18) allows us to tackle a wide range of contact problems. The solution or inversion of a singular integral equation of this kind is given by (Hills et al., 1993)

$$p(x) = -\frac{w(x)}{\pi A} \int_{\text{Contact}} \frac{g'(\xi)}{w(\xi)(\xi - x)} \mathrm{d}\xi + Cw(x) \ , \tag{2.22}$$

where the constant C and the fundamental function $w(x)$ are characteristic for the desired end-point behaviour and are given by Hills et al. (1993) for different cases.

2.3.5 Contact Examples

We will demonstrate, here, the solution procedure for a few examples where an analytical solution is known.

The Hertzian Contact

First, let us consider the two dimensional version of a Hertzian contact. This can be thought of as two infinitely long cylinders with radii R_1 and R_2 pressed into contact along their longitudinal axis. We note that if we let R_1 tend to infinity, we recover the contact of a cylinder and a half-plane shown in Figure 2.1(a). If the contact area is small compared to the curvature of the cylinders, we may approximate the surface profiles by parabolic functions, i.e. $g_1(x) = x^2/2R_1$ and $g_2(x) = x^2/2R_2$. For such a symmetric contact configuration we assume the contact to range over the interval $[-a \quad a]$ along which necessarily the gap (2.6) has vanished, and that the deformation will not give rise to a rigid body rotation, i.e. $\Omega = 0$. From equation (2.7) we find $g(x) = \Delta - g_0(x) = \Delta - g_1(x) - g_2(x)$ such that we may make the following replacement in equation (2.22)

$$g'(x) = -\frac{x}{R} \ , \tag{2.23}$$

where

$$\frac{1}{R} = \frac{1}{R_1} + \frac{1}{R_2} \,. \tag{2.24}$$

We assume bounded-bounded end-point behaviour as the pressure at the contact edges, $x = \pm a$, vanishes. The corresponding fundamental function $w(x)$ is then given by (Hills et al., 1993)

$$w(x) = \sqrt{a^2 - x^2} \,, \tag{2.25}$$

and the constant $C = 0$. For this case the inversion (2.22) yields

$$\begin{aligned} p(x) &= \frac{\sqrt{a^2 - x^2}}{\pi A R} \int_{-a}^{a} \frac{\xi}{\sqrt{a^2 - \xi^2}(\xi - x)} \mathrm{d}\xi \\ &= \frac{1}{AR}\sqrt{a^2 - x^2} \,. \end{aligned} \tag{2.26}$$

The contact half-width, a, may be found from the equilibrium condition (2.21) which leads

$$P = \int_{-a}^{a} p(\xi)\mathrm{d}\xi = \frac{\pi a^2}{2AR} \,. \tag{2.27}$$

Equation (2.27) connects the applied normal load to the extent of the contact and is frequently referred to as the contact law. We use equation (2.27) to rewrite expression (2.26) as

$$p(x) = \frac{2P}{\pi a}\sqrt{1 - \left(\frac{x}{a}\right)^2} \,, \tag{2.28}$$

where we note that $p_0 = 2P/\pi a$ is the peak pressure at the centre of the contact. The resulting elliptical pressure distribution is shown in Figure 2.4(b).

The Flat-Ended Punch

For the complete contact of a flat-ended punch and a half-plane, shown in Figure 2.1(b), the elastic deformation of the indenter, due to the sharp corners, cannot be described under the assumption of it being a half-plane. However, we are able to find a solution for the assumption of the punch being rigid, i.e. $\mu_2 \to \infty$.

The vertical displacement of the half-plane surface now has a constant value along the contact interface, namely the rigid body displacement, Δ, of the punch. Correspondingly, we find $g'(x) = 0$, and the integral term on the right hand side of equation (2.22) vanishes. For the expected singular end-point behaviour at both edges of the contact we choose the fundamental function (Hills et al., 1993)

$$w(x) = \frac{1}{\sqrt{a^2 - x^2}} \,, \tag{2.29}$$

in equation (2.22) such that the contact traction is given by

$$p(x) = \frac{C}{\sqrt{a^2 - x^2}} \,. \tag{2.30}$$

The constant, C, is found by imposing equilibrium with external forces (eq. (2.21)), which gives $C = P/\pi$, such that the final contact traction can be written as

$$p(x) = \frac{P}{\pi a} \frac{1}{\sqrt{1 - \left(\frac{x}{a}\right)^2}} \,. \tag{2.31}$$

The corresponding contact traction is shown in Figure 2.4(b).

The Flat but Rounded Punch

Figure 2.4(a) shows another example of an incomplete contact which might be regarded as an intermediate configuration between the Hertzian and the flat-ended punch. The profile of the punch shows a central flat region of half-width b, and rounded edges of radius R. Initially, for an infinitesimally small normal load the punch and the half-plane will make contact over the central flat portion, i.e. $a = b$. Once the normal load

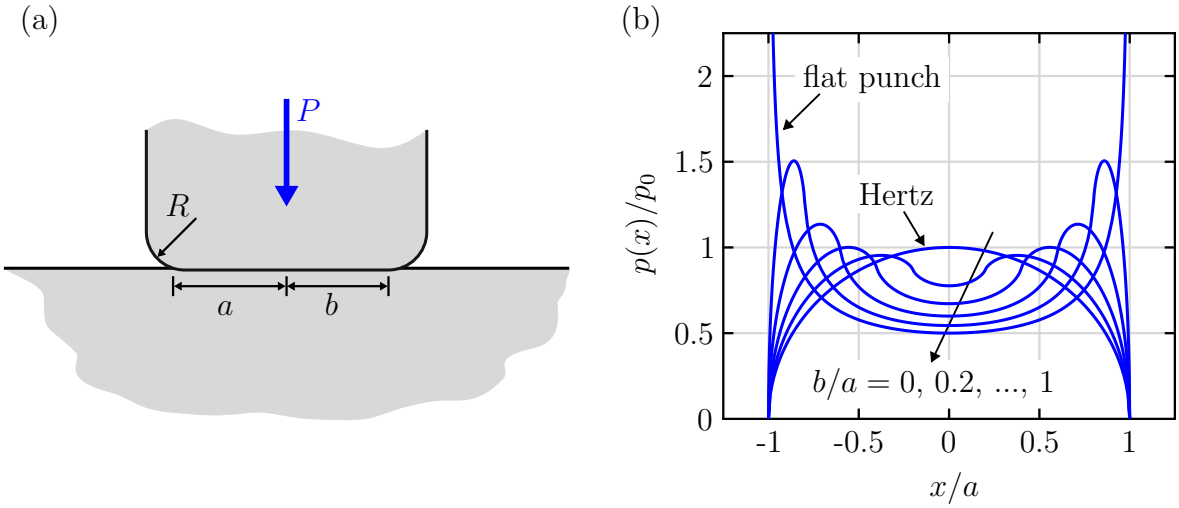


Figure 2.4: (a) Contact between half-plane and flat and rounded punch under a normal load, P, and (b) resulting normal traction, $p(x)$, for different ratios b/a as well as the extreme cases of a Hertzian contact and a punch with sharp corners.

is increased, the contact will extend into the rounded region of the indenter such that $b/a < 1$. We note that we may recover the Hertzian contact geometry for $b \to 0$. The indenter may be treated as a half-plane as it does not have sharp corners, but this approximation becomes less accurate the smaller R or the closer the ratio b/a gets to 1.

The resulting normal traction was found by Ciavarella et al. (1998). The profile of the indenter is given by

$$g_2(x) = \begin{cases} (x+b)^2/2R & -a < x \leq -b \\ 0 & -b < x < b \\ (x-b)^2/2R & b \leq x < a \end{cases}, \tag{2.32}$$

such that we may make the following substitution in equation (2.22)

$$g'(x) = \begin{cases} -(x+b)/R & -a < x \leq -b \\ 0 & -b < x < b \\ -(x+b)/R & b \leq x < a \end{cases}. \tag{2.33}$$

As for the Hertzian contact we expect bounded-bounded end-point behaviour such that

the fundamental function is given by (2.25) and $C = 0$. It can then be shown (Vázquez et al., 2010) that the normal traction results to

$$p(x) = \frac{a}{\pi AR}\left(2\arccos\left(\frac{b}{a}\right)\sqrt{1-\left(\frac{x}{a}\right)^2} + \frac{b-x}{a}F(x,a,b) + \frac{b+x}{a}F(x,a,-b)\right) , \tag{2.34}$$

where

$$F(x,a,b) = \log\left(\left|\frac{\sqrt{\frac{1-x/a}{1+x/a}} - \sqrt{\frac{1-b/a}{1+b/a}}}{\sqrt{\frac{1-x/a}{1+x/a}} + \sqrt{\frac{1-b/a}{1+b/a}}}\right|\right) . \tag{2.35}$$

Again, the extent of the contact is determined by imposing vertical equilibrium (2.21) and is given in an implicit form by (Vázquez et al., 2010)

$$P = \frac{a^2}{AR}\left(\arccos\left(\frac{b}{a}\right) - \frac{b}{a}\sqrt{1-\left(\frac{b}{a}\right)^2}\right) . \tag{2.36}$$

We note that we can recover the Hertzian normal traction (2.28) and contact law (2.27) for $b \to 0$ in equations (2.34) and (2.36). However, it is not possible to recover directly the pressure distribution for a flat punch with sharp corners from the expressions introduced above.

The results obtained from equation (2.34) are visualised for different ratios $b/a = 0, 0.2, 0.4, 0.6, 0.8$, together with the results obtained for a flat punch with sharp corners, in Figure 2.4(b). It is easily verified from equations (2.34) and (2.36) that the form of the normal traction along the normalised contact interface, x/a, depends solely on the ratio b/a, while it is simply scaled by the factor $p_0 = 2P/\pi a$. Consequently, we used p_0 to normalise the contact tractions in Figure 2.4(b). We note, however, that this factor is the maximum pressure only for the Hertzian case.

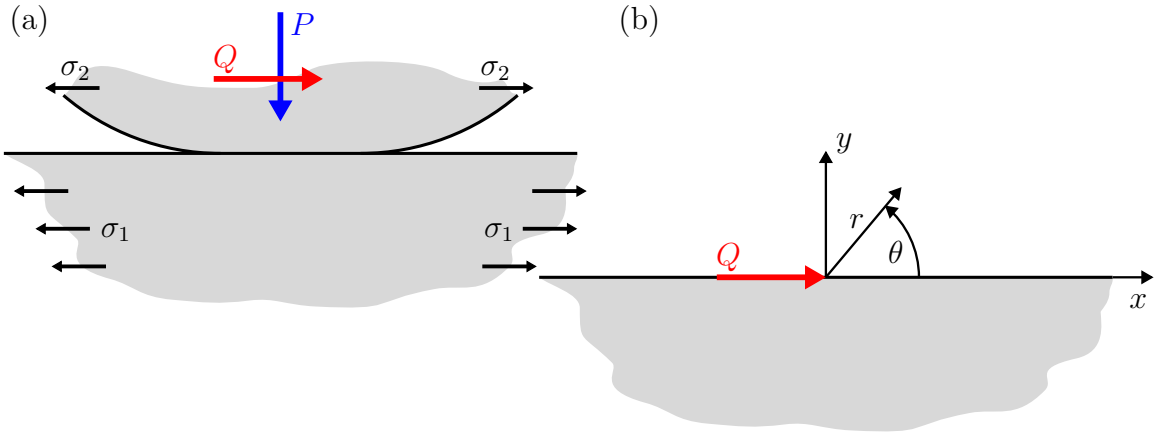


Figure 2.5: Half-plane contact subject to normal and tangential loading.

2.4 Tangential Loading

Additionally to the normal load, P, the contact might experience loading tangential to the contact interface, for example by a shear force, Q, or a differential bulk tension, $\sigma_0 = \sigma_1 - \sigma_2$, as shown in Figure 2.5(a). These loads will generally cause an interfacial shear traction, $q(x)$, along the contact interface.

In order to find this shear traction we follow similar steps as for the determination of the normal traction. We start by identifying the stress field and resulting surface displacements caused by a single force, Q, applied tangentially to the surface of a half-plane as shown in Figure 2.5(b). The corresponding Airy stress function (analogous to eq. (2.10)) is

$$\phi(r,\theta) = -\frac{Q}{\pi} r\theta \sin(\theta) \,, \tag{2.37}$$

and the resulting surface displacements are

$$u(x) = -\frac{Q}{2\pi}\frac{\kappa+1}{2\mu}\ln|x| \,, \tag{2.38}$$

$$v(x) = -\frac{Q}{4}\frac{\kappa-1}{2\mu}\mathrm{sgn}(x) \,, \tag{2.39}$$

where we note the similarities between equations (2.12, 2.13) and (2.38, 2.39), for the normal and tangential loading, respectively. As for the normal problem, we may

use the displacements identified for a single load as a Green's function to represent a distributed shear traction. The gradient of the surface displacements, equivalent to equations (2.14) and (2.15), is given by

$$\frac{\partial u(x)}{\partial x} = -\frac{\kappa+1}{4\pi\mu}\int_{\text{Contact}} \frac{q(\xi)}{x-\xi}\mathrm{d}\xi \ , \tag{2.40}$$

$$\frac{\partial v(x)}{\partial x} = -\frac{\kappa-1}{4\mu} q(x) \ . \tag{2.41}$$

The relative normal and tangential surface displacement, $g(x) = v_2(x) - v_1(x)$ and $h(x) = u_2(x) - u_1(x)$, caused by a distributed shear traction acting at the contact interface between two bodies yields

$$\frac{1}{A}\frac{\partial h(x)}{\partial x} = \frac{1}{\pi}\int_{\text{Contact}} \frac{q(\xi)}{x-\xi}\mathrm{d}\xi \ , \tag{2.42}$$

$$\frac{1}{A}\frac{\partial g(x)}{\partial x} = \beta q(x) \ , \tag{2.43}$$

where A and β are still defined by equations (2.19) and (2.20). We note that a shear traction causes a relative normal displacement, similarly to the relative tangential displacement caused by a normal traction, specified by equation (2.17).

2.4.1 Material Coupling

We refer to the effect of a shear traction causing a relative normal displacement as well as a normal traction causing a relative tangential displacement as *coupling*.

For a combined loading, i.e. when there is a shear as well as a normal traction transferred from one of the contacting bodies to the other, the gradient of the relative displacements can be found by superposition. From equations (2.17, 2.18) and (2.42, 2.43) we find

$$\frac{1}{A}\frac{\partial h(x)}{\partial x} = \frac{1}{\pi}\int_{\text{Contact}} \frac{q(\xi)}{x-\xi}\mathrm{d}\xi + \beta p(x) \ , \tag{2.44}$$

$$\frac{1}{A}\frac{\partial g(x)}{\partial x} = -\frac{1}{\pi}\int_{\text{Contact}} \frac{p(\xi)}{x-\xi}\mathrm{d}\xi + \beta q(x) \ , \tag{2.45}$$

and note that the coupling terms are multiplied by the coefficient β. Consequently, the system uncouples not only if the contact is frictionless, as in Section 2.3, but also if $\beta = 0$. One common example of $\beta = 0$ is if both of the contacting bodies have similar elastic properties, but also other special cases may be found.

2.4.2 Fully Stuck Contacts

If the contacting bodies are made of the same material then the system is said to be uncoupled and the normal traction can be found as above (Sect. 2.3). For the application of a shear force, Q, the shear traction may then be found from equation (2.42). The resulting singular integral equation is of the same kind as equation (2.18), and consequently the inversion is still given by equation (2.22), where $p(x)$ and $g'(x)$ are replaced by $q(x)$ and $h'(x)$. If the two bodies are stuck together such that there is no relative tangential displacement in the contact region, i.e. $h'(x) = 0$, then the solution may be found by following the same steps as for the flat-ended punch where $g'(x)$ vanished. We obtain

$$q(x) = \frac{C}{\sqrt{a^2 - x^2}} \, , \tag{2.46}$$

where now the constant, C, is found by imposing equilibrium with external forces in tangential direction

$$Q = \int_{\text{Contact}} q(\xi) \mathrm{d}\xi \, , \tag{2.47}$$

which gives $C = Q/\pi$. The resulting contact shear traction is then given by

$$q(x) = \frac{Q}{\pi a} \frac{1}{\sqrt{1 - \left(\frac{x}{a}\right)^2}} \, , \tag{2.48}$$

and we note that this result is independent of the contact geometry.

For a fully stuck contact subject to a differential bulk tension, σ_0, the governing singular integral equation requires some changes compared to equation (2.42) (Barber, 2018),

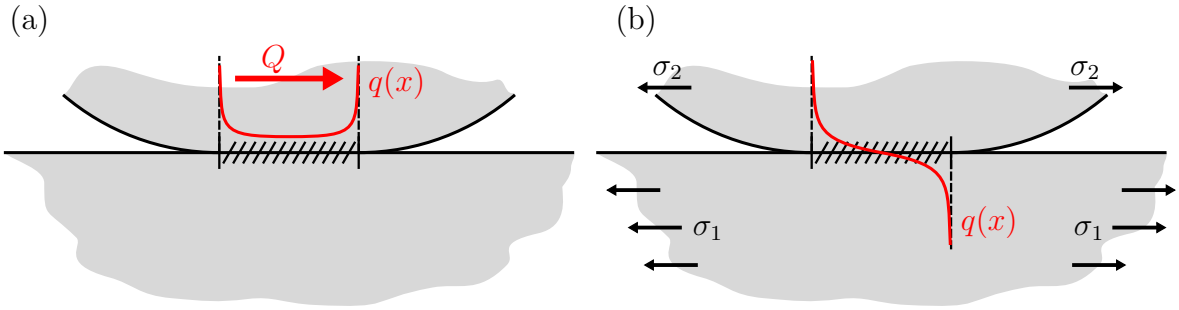


Figure 2.6: Interfacial shear traction, $q(x)$, for a fully stuck half-plane contact subject to (a) a shear force, Q, and (b) a differential bulk tension, $\sigma_0 = \sigma_1 - \sigma_2 > 0$.

and takes the form

$$\frac{1}{\pi}\int_{\text{Contact}} \frac{q(\xi)}{x-\xi}\mathrm{d}\xi = \frac{\sigma_0}{4}\,. \tag{2.49}$$

Barber (2018) shows that the solution to equation (2.49) is given by

$$q(x) = -\frac{\sigma_0}{4}\frac{x/a}{\sqrt{1-\left(\frac{x}{a}\right)^2}}\,, \tag{2.50}$$

The resulting shear traction for both the application of a shear force, Q, as well as a differential bulk tension, σ_0, are schematically shown in Figure 2.6. For combined loading the shear traction may be found from superposition. We note that the effect of a shear force is intensified by a differential bulk tension at one of the contact edges while it is reduced at the other.

2.4.3 Friction and Gross Sliding

If the contact is neither frictionless nor fully stuck, we need to specify the tangential contact behaviour, as for the normal problem we have prohibited interpenetration of the two bodies.

For the description of tangential contact behaviour of metals, it is commonly accepted to use Coulomb's friction law, formulated by Amontons (1699) and Coulomb (1785). Their observations were based on rigid body motions, and the friction law states that during gross sliding the friction force, Q, is proportional to the normal load, P, and

opposes the direction of motion. Furthermore, they found that the force is independent of the velocity of the relative motion and the size of the contact area. This implies that the tangential load contacts can sustain is limited by

$$|Q| \leq fP, \tag{2.51}$$

where f denotes the proportionality factor, referred to as the coefficient of friction. The case $|Q| = fP$ now corresponds to gross sliding, i.e. a continuously increasing relative tangential displacement along the entire contact interface. On the other hand, the contacting bodies are macroscopically stuck together, i.e. there is no rigid body displacement if $|Q| < fP$, but this does not mean that the whole interface is stuck. While equation (2.51) considers the externally applied forces, we can make a point-wise or local statement with respect to the contact tractions which reads

$$|q(x)| \leq fp(x). \tag{2.52}$$

This equation states, that at every point, the shear traction, $q(x)$, is limited by the normal traction, $p(x)$, multiplied with the coefficient of friction, f. If equation (2.52) is equally fulfilled, relative tangential (slip) displacements $h(x) = u_2(x) - u_1(x)$ may develop. Every surface particle of the contacting bodies will then take one of the following states

$$\dot{h} = 0 \qquad \bar{g} = 0 \qquad p > 0 \qquad |q| \leq fp \qquad \text{stick} \tag{2.53}$$

$$\dot{h} > 0 \qquad \bar{g} = 0 \qquad p > 0 \qquad q = fp \qquad \text{forward slip} \tag{2.54}$$

$$\dot{h} < 0 \qquad \bar{g} = 0 \qquad p > 0 \qquad q = -fp \qquad \text{backward slip} \tag{2.55}$$

$$\bar{g} > 0 \qquad p = 0 \qquad q = 0 \qquad \text{separation .} \tag{2.56}$$

Alternatively, the tangential contact problem may be expressed in terms of the LCP

(c.f. eq. (2.8)) condition

$$\dot{h}(x)\left(|q(x)| - fp(x)\right) = 0 \quad \forall\, x\ . \tag{2.57}$$

For gross sliding we require every point in the contact region to slip simultaneously with either (2.54) or (2.55) being satisfied everywhere. Consequently, for the uncoupled case, $\beta = 0$, the shear tractions are known once the normal tractions have been found. Coupled contact problems lead a singular integral equation of the second kind and details of the solution procedure are given by Hills et al. (1993) and Barber (2018).

2.5 Partial Slip

While equation (2.51) represents a condition for gross sliding, equation (2.52) provides a similar condition for each material point along the contact interface. Accordingly, we can find regions of relative tangential displacement between the contacting surfaces, while macroscopically the contacting bodies are stuck together, i.e. not every point along the contact interface is in the same state (2.53 - 2.55). We refer to these regions as regions of partial slip.

2.5.1 Origins of Partial Slip

From equation (2.52), we see that generally partial slip is favoured by a small contact pressure. For the contact configurations shown in Figures 2.1(a) and (c), with the contact pressure falling to zero at the edges, it is therefore almost inevitable to find regions of partial slip in the presence of a shear traction. The following examples are a selection of various origins of partial slip, described in more detail by Hills and Urriolagoitia Sosa (1999).

A shear traction might be caused by the application of tangential loading, Q, as shown in Figure 2.7(a) for a Hertzian contact. We see the formation of two regions of partial slip at the edges of the contact, surrounding a central stick region (for $|Q| < fP$). The partial slip solution for this type of contact, subject to a monotonically increasing or

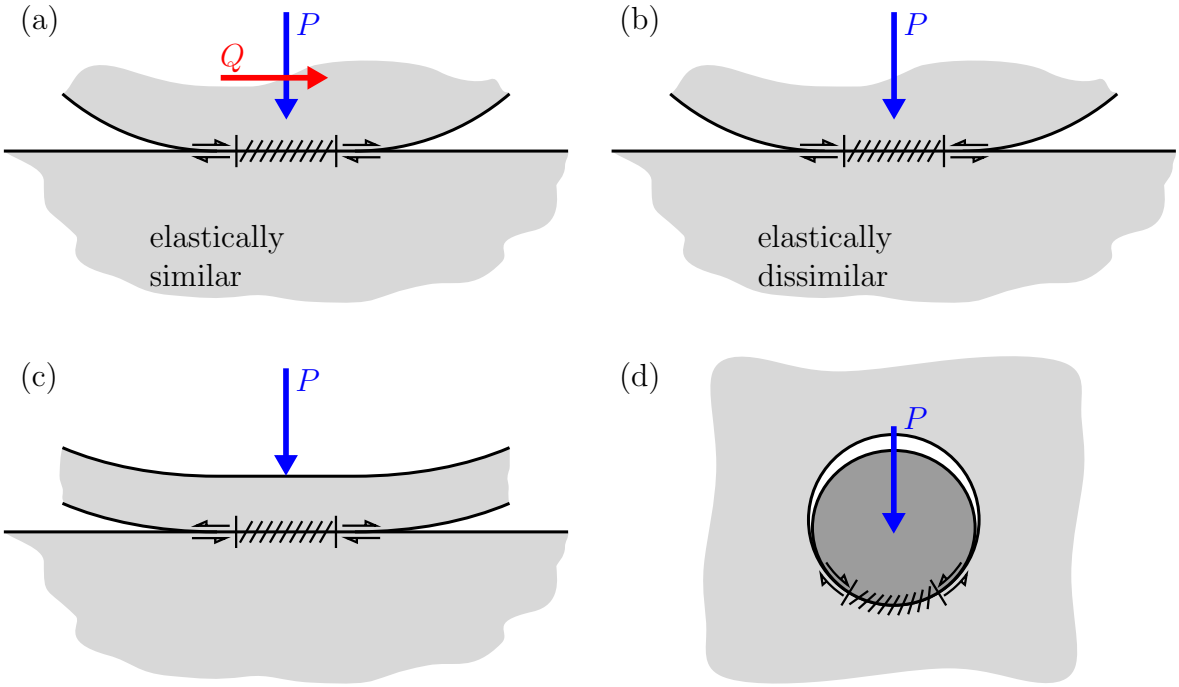


Figure 2.7: Different contacts in a state of partial slip (a) elastically similar half-planes subject to normal and shear force (b) elastically dissimilar half planes (c) receding contact (d) conformal contact.

cyclically varying shear force was independently found by Cattaneo (1938) and Mindlin (1949).

If the two contacting bodies are made from different materials, the application of a normal load P, alone, might be sufficient to cause a violation of the slip condition at the edges (Fig. 2.7(b)). The elastic mismatch here is a source of coupling, meaning that the relative tangential displacements are affected by the normal traction distribution, as it has been shown in equation (2.17). The partial slip solution for the case shown was studied by Spence (1968) while the problem with a subsequently applied shear force was described by Nowell (1988).

With the receding and conformal contacts shown in Figures 2.7(c) and (d), respectively, we find further examples of contacts where the application of a single load causes partial slip. For the receding contact a stick zone remains centred below the point where the normal load is applied. At the depth of the interface between strip and substrate this load causes an antisymmetric shear traction, which together with the bounded normal traction violates the slip condition (2.52) at remote points. The study of the partial slip problems for receding contacts include recent publications like Chaise et al. (2014)

and Lopes and Hills (2019).

Conforming contacts, like that shown in Figure 2.7(d), arise in many engineering applications, for example fasteners in the form of pin loaded attachment lugs. They cannot generally be described using half plane theory since the contact size is significant compared to the intrinsic dimensions, namely the radius of the curvature. Depending on the initial clearance between pin and hole the contact is either advancing, for a positive clearance, or receding. It snaps to its final size in case of a *neat-fit* condition with the pin and the hole having the same diameter or it smoothly recedes to its final size for a negative clearance, meaning the pin is shrink-fitted into the hole. In all aforementioned cases the surface of pin and hole will share a common tangent at the edge of the contact with the contact pressure being bounded (similar to what we find for incomplete contacts as shown in Figure 2.1(a)). In contrast to Figure 2.7(b), where the coupling was caused by the different elastic properties, here the curvature of the contact interface provides a source of coupling, and the shear tractions caused by the normal load will give rise to zones of partial slip at the edges of the contact. We may refer to the different sources of coupling as material and geometrical coupling. A first solution for a conformal contact, assuming that there is no friction between disc and plate, is given by Persson (1964) for elastic similarity. This formulation was extended to dissimilar materials by Ciavarella and Decuzzi (2001b). A partial slip solution restricted to the advancing contact case was found by Sundaram and Farris (2010b). For cases where the clearance is small, the contact may be modelled as a crack between a circular inclusion and a matrix (Kelly et al., 1994), and this was done for the frictionless case by Hou and Hills (2001).

2.5.2 Jäger-Ciavarella Theorem

A very powerful result in the solution procedure of uncoupled partial slip problems is the so-called Jäger-Ciavarella theorem (Jäger, 1997; Ciavarella, 1998). It allows us, for a wide range of contact geometries and loading cases, to represent the shear tractions along the contact interface as a simple superposition of the full sliding shear traction,

$f\,p(x)$, and a scaled version of the full sliding shear traction acting over the stick-region of the contact.

We consider the incomplete symmetric contact of two elastically similar bodies, which can be represented as half-planes, and where the contact is established over an interval $[-a \quad a]$ by the application a normal load, P. Subsequently a shear load, $Q < fP$ will be applied to the contact. We recollect that, for an incomplete contact, the contact pressure falls to zero at both ends, $|x| = a$. Furthermore, we know that if the two bodies were stuck together, the shear traction would be given by (2.48) and show singularities at the edges of the contact (c.f. Fig. 2.6(a)). It is clear that for every finite coefficient of friction, f, the tractions at the edges of the contact will tend to cause partial slip in a yet unknown region $c < |x| \leq a$, where the contact will be in a state described by (2.54), i.e. $\dot{h} > 0$ and $q = f\,p(x)$. Within a central region, $|x| \leq c$, the contact will be stuck with $\dot{h} = 0$ and $q < f\,p(x)$ (c.f. eq. (2.53)), such that we can express the shear traction as a superposition of the full sliding shear traction, $fp(x)$, and a yet unknown term, $q^*(x)$, which, as we will see, has the tendency to reduce the shear traction inside the stick-zone. The integral equation (2.42) then reads

$$\frac{1}{A}\frac{\partial h(x)}{\partial x} = \frac{1}{\pi}\left(\int_{-a}^{a}\frac{fp(\xi)}{x-\xi}\mathrm{d}\xi + \int_{-c}^{c}\frac{q^*(\xi)}{x-\xi}\mathrm{d}\xi\right) \qquad |x| \leq a\,. \tag{2.58}$$

As in the case of a fully stuck contact (Sect. 2.4.2), once the contact is established, there will be no relative tangential displacement inside the stick zone, i.e. $h'(x) = 0$ for $|x| \leq c$. Furthermore, by comparison with equation (2.18) we note that the first term inside the brackets of equation (2.58) equals $-f\,g'(x)/A$, such that the singular integral equation may be rewritten to

$$\frac{f}{A}\frac{\partial g(x)}{\partial x} = \frac{1}{\pi}\int_{-c}^{c}\frac{q^*(\xi)}{x-\xi}\mathrm{d}\xi \qquad |x| \leq c\,. \tag{2.59}$$

By comparison with equation (2.53), expression (2.59) shows that the corrective traction simply is a scaled full sliding traction, $-fp(x)$. In particular the sliding traction corresponding to the same contact geometry, but subject to a lower normal load,

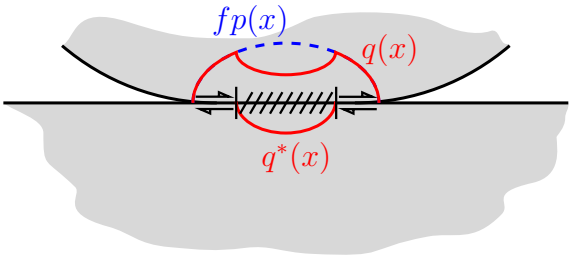


Figure 2.8: Partial slip shear traction, $q(x)$, as superposition of full-sliding term, $fp(x)$, and corrective term, $q^*(x)$, following the Jäger-Ciavarella theorem (Jäger, 1997; Ciavarella, 1998).

$P^* < P$, such that the contact half-width equals c. The stick-zone half-width, c, is found by imposing tangential equilibrium which reads

$$Q = \int_{-a}^{a} fp(\xi)\mathrm{d}\xi - \int_{-c}^{c} q^*(\xi)\mathrm{d}\xi = f(P - P^*) \,, \tag{2.60}$$

such that $P^* = P - Q/f$, and c is found by evaluating the contact law (2.27) for P^*.

Application to a Hertzian Contact

Following the Jäger-Ciavarella theorem, the shear traction for a Hertzian contact loaded by a normal force and a subsequently applied shear force can be found by using the contact law (2.27) together with equation (2.60) to identify the extent of the slip zone

$$c = \sqrt{\frac{2AR}{\pi}\left(P - \frac{Q}{f}\right)} = a\sqrt{1 - \frac{Q}{fP}} \,. \tag{2.61}$$

As described above, and shown by equation (2.59), the resulting shear traction will be a superposition of the full sliding traction $f\,p(x)$, where we use equation (2.28), and a scaled version acting along the stick region $-c < x < c$, such that it reads

$$q(x) = fp_0 \left(\sqrt{1 - \left(\frac{x}{a}\right)^2} - \frac{c}{a}\sqrt{1 - \left(\frac{x}{c}\right)^2} \right) \,, \tag{2.62}$$

and needs to be interpreted in terms of its real parts. The different terms as well as the resulting shear traction are shown in Figure 2.8.

It can be shown that the Jäger-Ciavarella theorem does not only apply to every contact

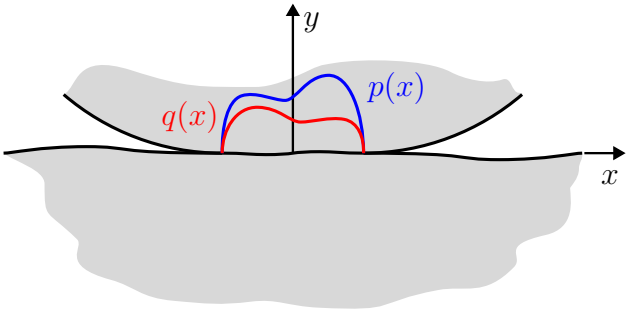


Figure 2.9: Contact with both bodies being capable of an idealisation as a half-plane and arbitrary contact tractions $p(x)$ and $q(x)$.

capable of an idealisation by half-planes (Barber, 2018), but also for more complex loading scenarios such as the combined application of a shear force and a differential bulk tension. However, the effect of the bulk tension has to be moderate in the sense that the shear traction and corresponding slip displacements are of similar sign at both edges of the contact.

2.6 Subsurface Contact Stress

Section 1.1.1 describes the environment of a contact which favours the nucleation and propagation of fatigue cracks. Crucial, here, are not necessarily the actual contact tractions, but rather the corresponding subsurface stress field, and in particular the stress parallel to the contact interface. For contacting bodies capable of an idealisation as a half-plane, we can derive the subsurface stress field from the Muskhelishvili complex potential (Muskhelishvili, 1964).

2.6.1 Muskhelishvili Complex Potential

Figure 2.9 shows a general contact with arbitrary contact tractions $p(x)$ and $q(x)$. Once the tractions along the contact interface are known, Muskhelishvili's potential, $\phi(z)$, is

given by

$$\phi^n(z) = \frac{1}{2\pi i}\int_{\text{Contact}} \frac{\sigma_{yy}(x,0)}{x-z}dx \tag{2.63}$$

$$\phi^t(z) = \frac{1}{2\pi}\int_{\text{Contact}} \frac{\sigma_{xy}(x,0)}{x-z}dx, \tag{2.64}$$

where $z = x + iy \in \mathbb{C}$. $\phi^n(z)$ and $\phi^t(z)$ refer to the stress field induced by the normal traction, $p(x) = -\sigma_{yy}(x,0)$, and the shear traction, $q(x) = \sigma_{xy}(x,0)$, respectively. The total interior stress field, of those bodies which can be idealised as half-planes, can be found by simple superposition in an implicit form viz

$$\sigma_{xx}(x,y) + \sigma_{yy}(x,y) = 2\left[\phi(z) + \overline{\phi(z)}\right], \tag{2.65}$$

$$\sigma_{yy}(x,y) - \sigma_{xx}(x,y) + 2i\sigma_{xy}(x,y) = 2\left[(\overline{z}-z)\frac{d}{dz}\phi(z) - \phi(z) - \overline{\phi(\overline{z})}\right]. \tag{2.66}$$

Here, if the complex potential can be expressed by $\phi(z) = u(x,y) + iv(x,y)$, then $\overline{\phi(z)} = u(x,y) - iv(x,y)$ and $\overline{\phi(\overline{z})} = u(x,-y) - iv(x,-y)$ (Vázquez et al., 2012).
For the contact of a half-plane and an indenter, where both bodies have identical elastic properties, Vázquez et al. (2012) present a new method to obtain the Muskhelishvili potential without the need for surface integration. The part of the potential, $\phi^n(z)$, corresponding to the normal traction, has been found to be

$$\phi^n(z) = \frac{i}{2A}g_2'(z) + \frac{1}{2}p(z), \tag{2.67}$$

where A is the contact compliance, still given by equation (2.19), and x is replaced by z in the derivative of the of the indenter profile, $g_2'(x)$, as well as the contact normal traction, $p(x)$. The part of the potential corresponding to the shear traction, $\phi^t(z)$, is given by

$$\phi^t(z) = -\frac{\Lambda}{2} - \frac{i}{2}q^{\text{ad}}(z). \tag{2.68}$$

Here, $q^{\mathrm{ad}}(x)$ is the shear stress along the adhered or stick region of the contact interface, where again, x was replaced by z. Λ is a problem-specific parameter given by the integral

$$-\frac{1}{\pi}\int_{\mathrm{Contact}}\frac{q(t)}{t-x}dt=\Lambda, \tag{2.69}$$

for all $x \in$ stick zone, and where the integral must be taken in the Cauchy principal value sense (Vázquez et al., 2012).

2.6.2 Explicit Stress Field

Based on the above, Vázquez et al. (2013) introduced equations to obtain explicitly the stress field from the Muskhelishvili complex potential, bypassing the implicit form (2.65, 2.66). The interior contact stress field of the half-plane $y < 0$, then, is given by

$$\begin{aligned}
\sigma^n_{xx}(x,y) &= -\phi^n(z)+\phi^n(\bar{z})-iy\left(\frac{\partial}{\partial z}\phi^n(z)+\frac{\partial}{\partial \bar{z}}\phi^n(\bar{z})\right)\\
\sigma^n_{yy}(x,y) &= -\phi^n(z)+\phi^n(\bar{z})+iy\left(\frac{\partial}{\partial z}\phi^n(z)+\frac{\partial}{\partial \bar{z}}\phi^n(\bar{z})\right)\\
\sigma^n_{xy}(x,y) &= y\left(\frac{\partial}{\partial z}\phi^n(z)-\frac{\partial}{\partial \bar{z}}\phi^n(\bar{z})\right),
\end{aligned} \tag{2.70}$$

for the application of a normal traction and correspondingly

$$\begin{aligned}
\sigma^t_{xx}(x,y) &= 2\left(\phi^t(z)+\phi^t(\bar{z})\right)+iy\left(\frac{\partial}{\partial z}\phi^t(z)-\frac{\partial}{\partial \bar{z}}\phi^t(\bar{z})\right)\\
\sigma^t_{yy}(x,y) &= -iy\left(\frac{\partial}{\partial z}\phi^t(z)-\frac{\partial}{\partial \bar{z}}\phi^t(\bar{z})\right)\\
\sigma^t_{xy}(x,y) &= i\left(\phi^t(z)-\phi^t(\bar{z})\right)-y\left(\frac{\partial}{\partial z}\phi^t(z)+\frac{\partial}{\partial \bar{z}}\phi^t(\bar{z})\right),
\end{aligned} \tag{2.71}$$

for the application of a shear traction. An important characteristic of the stress field derived from the Muskhelishvili complex potential, is that any function $\phi(z)$ fulfils the equilibrium conditions while the corresponding strains meet the compatibility requirements. This might simply be checked by substituting expressions (2.70) or (2.71) into equations (2.3) and (2.4).

2.7 Shakedown

The concept of *shakedown* is well known and studied in elasto-plasticity. Shakedown is one possible response of a structure subject to cyclic loading, other than an elastic response throughout the whole loading history, or steady state plasticity. The last may appear in two different forms. The structure can experience either a fully reversing plastic deformation in the steady state, known as cyclic plasticity, or the plastic strains may accumulate with every load cycle, referred to as ratchetting and normally resulting in plastic collapse (Churchman et al., 2006).

The analogy between frictional slip and plastic slip is quite strong insofar as there is an elastic limit beyond which the structure will respond with a plastic deformation, being a dissipative process. For frictional slip the structure can suffer a limit loading (eq. (2.52)) before energy dissipation will start at the contact interface, in the form of partial slip. Furthermore, frictional slip is an orthogonal process *within the slip plane*, but not in an overall sense. Both plastic and frictional slip processes are history dependent and frictional equivalents of elasto-plastic steady state responses may be found. While cyclic plasticity corresponds to fully reversing frictional slip displacements for each cycle, the equivalent to ratchetting may be described as an accumulation of partial slip displacements resulting in a gradual rigid body motion. The contact is said to be shaken down if residual stresses resulting from partial slip, in the first load cycles, prevent the contact from experiencing any slip in subsequent cycles. It is worth mentioning that incomplete contacts, as shown in Figure 2.1(a), can never achieve a shaken down state because the contact pressure always falls smoothly to zero in a square root bounded manner near the edge, so that it is impossible to inhibit slip.

The frictional steady state behaviour, if the contact retains some slip in cyclic loading, is of great practical interest, since contacting bodies not only suffer surface damage at the contact interfaces, but also the system damping of mechanical assemblies is strongly affected. The question arises if some or all elasto-plastic principles apply to frictional contacts as well.

2.7.1 Melan's Theorem

Melan's elastic-plastic shakedown theorem states that *'if a residual stress state may be found which, together with the applied stress, lies always within the yield (or frictional slip) boundary, shake down to an elastic (or fully stuck) condition* ***will*** *occur'* (Melan, 1936) where the terms in brackets have been added to the original quote to make it applicable to contact problems. In other words, *'the system will shake down if it can'*, as Barber (2016) stated it in a more concise way.

2.7.2 Shakedown of Uncoupled Contacts

The question if this theorem applies to frictional contacts was probed analytically from basic principles by Klarbring et al. (2007) for discrete contact formulations as well as Barber et al. (2008) for the continuum. It was concluded that the Melan's theorem *would* apply to frictional contacts only when the contact area does not change during oscillatory loading and there is 'no coupling', that is, where the change in interfacial shearing tractions produces no relative change in the shape of the contacting bodies, and therefore no change in the contact pressure distribution. Therefore, the steady state response for uncoupled contacts is independent of any initial conditions. Consequently the cyclic behaviour of mechanical assemblies, with frictional contacts falling in the above described category, does not depend on any assembly sequence.
Uncoupled contacts strictly arise only when the bodies pressed together are geometrically the same and made from the same material, but this statement is almost true for any incomplete contact which is capable of idealisation within the framework of a half-plane (space). Other contacts will show at least some degree of coupling.

2.7.3 Shakedown of Coupled Contacts

As counter examples show, Melan's theorem does not apply to coupled contacts, and we expect a region where initial conditions control whether the system shakes down or not. An idealised problem was tackled by Ahn et al. (2008) who, for a discrete two

node contact, showed how the coupling affects the shakedown behaviour. The shear and normal force, q_i and p_i, at each node i are connected to the relative tangential and normal displacements h_i and g_i, via

$$\begin{bmatrix} q_i \\ p_i \end{bmatrix} = \begin{bmatrix} \tilde{q}_i \\ \tilde{p}_i \end{bmatrix} + \begin{bmatrix} A_{ji} & B_{ij} \\ B_{ji} & C_{ji} \end{bmatrix} \begin{bmatrix} h_i \\ g_i \end{bmatrix}, \tag{2.72}$$

with $\tilde{q}_i$ and $\tilde{p}_i$ representing the bilateral reactions due to external loads at each node and $\boldsymbol{A}, \boldsymbol{B}$ and $\boldsymbol{C}$ are the sub-matrices of the contact stiffness matrix (note that for the uncoupled case the matrix $\boldsymbol{B}$ is null). For the assumption of no separation, $g_i = 0$, the sliding condition $|q_i| \leq f p_i$ for both nodes yields four constraints

$$\begin{aligned} &\text{I} && (A_{11} - fB_{11})\, h_1 + (A_{12} - fB_{12})\, h_2 \leq f\tilde{p}_1 - \tilde{q}_1 \\ &\text{II} && (A_{11} - fB_{11})\, h_1 + (A_{12} - fB_{12})\, h_2 \geq -f\tilde{p}_1 - \tilde{q}_1 \\ &\text{III} && (A_{21} - fB_{21})\, h_1 + (A_{22} - fB_{22})\, h_2 \leq f\tilde{p}_2 - \tilde{q}_2 \\ &\text{IV} && (A_{21} - fB_{21})\, h_1 + (A_{22} - fB_{22})\, h_2 \geq -f\tilde{p}_2 - \tilde{q}_2 \end{aligned} \tag{2.73}$$

which will, in the h_1-h_2-space spanned by the tangential relative displacements of both contact nodes, exclude the grey area (Fig. 2.10), to define an admissible region. The normal and shear force, p_i and q_i, corresponding to tangential displacements, h_i, outside the admissible region, would violate at least one of the four constraints (2.73), and consequently tangential relative displacements, h_i, outside the admissible region can never be reached as long as the sliding condition $|q_i| \leq f p_i$ holds. The location of the four visualised constraints depends on the bilateral loads, $\tilde{q}_i$ and $\tilde{p}_i$, due to external loading only, while the slope is defined by the sub-matrices $\boldsymbol{A}, \boldsymbol{B}$ and $\boldsymbol{C}$.

Depending on the slope and location of the constraints in h_1-h_2-space, the admissible region can take different shapes which are explained in more detail by Ahn et al. (2008) and Barber (2016). The application of external oscillating loads at node 1 can be visualised in h_1-h_2-space by a movement of constraints I and II along the h_1-axis (approaching each other when the absolute value of the ratio of $\tilde{q}_1$ and $\tilde{p}_1$ is increased)

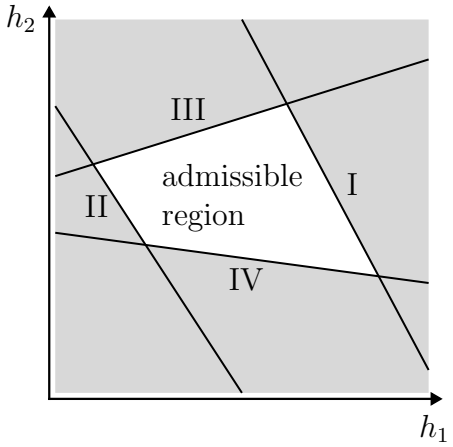


Figure 2.10: Slip condition constraining admissible region in h_1-h_2-space.

and similarly a movement of constraints III and IV along the h_2-axis for oscillating external loads at node 2. By means of the movement of constraints, the shakedown behaviour can be predicted. If the magnitude of cyclic loading is such that, even for the most critical loading, the admissible region is still a quadrilateral, the system will certainly shake down. If, on the other hand the most critical loading is such that three constraints meet in one point or one constraint even becomes inactive, so that the admissible region forms a triangle, shakedown *is* conditional on initial conditions. The system will *never* shake down if the admissible region becomes a null-space at some point during the load cycle.

We note that we described the slope of the constraints to be dependent on sub-matrices of the contact stiffness matrix, and that the pair of constraints corresponding to a node become parallel if the system is uncoupled with $\boldsymbol{B} = \boldsymbol{0}$. These observations illustrate why for uncoupled contacts there will be no conditional shakedown: The admissible region, forming a parallelogram, will change its shape from being a quadrilateral to a null space without ever becoming a triangle, and hence shakedown will never depend on initial conditions.

Jang and Barber (2011a) investigated the phenomenon of 'conditional shakedown' using the model of an elastic block in compression, and incorporating an array of arbitrarily oriented short cracks which might be 'closed and stuck' or 'closed and slipping' due to the block being subject to a cyclic shear load. They describe the steady state loading with a hydrostatic compression of magnitude p_0 and a cyclic shear stress of

magnitude λp_0. They were able, from this, to speculate the existence, generally, of a set of load factors for a coupled contact problem, viz, (1) λ_1 the load factor below which, no matter what the path of entry into the cyclic load, shakedown to a fully stuck interface will occur, (2) λ_2 the load factor such that, if $\lambda_1 < \lambda < \lambda_2$, shakedown would conditionally occur, depending on the initial path of entry, (3) λ_3 the load factor such that, if $\lambda_2 < \lambda < \lambda_3$ there would be steady state slip but the amplitude of steady-state slip would depend on the initial path, and finally if $\lambda > \lambda_3$ there would be steady state slip and the magnitude of slip, and hence the energy dissipated, would be unique. Barber's speculation was formed from an analysis in which each contact was treated as a point, that is the individual contacts (cracks) could not be in partial slip, and in an effort to examine these ideas in the context of a distributed contact Flicek et al. (2015) considered, by the finite element method, a complete contact, as shown in Figure 2.1(a), with potential areas of slip, and evaluated the load factors corresponding to those defined by Jang and Barber (2011a). They considered a measure of the degree of coupling, and looked at the conditional shakedown range and the spread of steady state energy dissipation.

Barber (2016) extended the set of different load factors for coupled contacts, to a definition dividing the region of a unique dissipation depending on the existence of a point in the load cycle when all nodes slip simultaneously, i.e. where rigid body motion was a possibility. So, to summarise, the possible responses are:

$\lambda < \lambda_1$	Shakedown for all initial conditions
$\lambda_1 < \lambda < \lambda_2$	Shakedown or cyclic slip depending on initial conditions.
$\lambda_2 < \lambda < \lambda_3$	Cyclic slip, but the steady state depends on initial conditions. At least some nodes must be permanently stuck.
$\lambda_3 < \lambda < \lambda_4$	Unique cyclic slip (or one of a few such states) approached asymptotically. The permanent stick zone $\mathcal{T} = \emptyset$.
$\lambda > \lambda_4$	Unique cyclic slip reached after one or two cycles. There is some time during each cycle when all nodes slip.

2.7.4 The System Memory

The dependence of coupled contacts on initial conditions or the loading history implies that the contact possesses some form of 'memory' (Barber, 2011a). We consider a discretised contact with N contact nodes. The system (2.72) then consists of $2N$ equations for the $4N$ unknowns p_i, q_i, g_i and h_i.

We consider a specific loading such that at a specific instant all N contact nodes experience either slip or separation. For those nodes experiencing slip we find, from equations (2.54 - 2.55), that we may replace q_i by $\pm f p_i$ while the relative normal displacement, g_i, vanishes. For those nodes experiencing separation we know from equation (2.56) that both p_i and q_i vanish. This reduces the system (2.72) to $2N$ equations for the $2N$ unknowns, such that the instantaneous displacements are completely defined by the instantaneous external loads, and hence are independent of the loading history. In other words the system memory is erased.

On the other hand, if a node i is permanently stuck during a periodic loading, we know from equation (2.53) that the relative normal displacement g_i is zero, and that the relative tangential displacement h_i is constant, i.e. $\dot{h}_i = 0$. The node therefore 'remembers' the displacement at the entry of the periodic loading, such that the system memory resides in the slip displacements h_i of those nodes which are permanently stuck (Barber, 2016).

For load cases with $\lambda_3 < \lambda < \lambda_4$ all nodes experience slip at one instant during the load cycle even though at no instant all nodes slip simultaneously. Barber (2016) describes this as causing an exchange of memory between different nodes. For each load cycle this may lead to a gradual loss of memory, and hence the asymptotic approach of a unique state.

This process is illustrated by Barber (2011a) for a two node discrete contact, as considered by Ahn et al. (2008). For a loading with $\lambda_3 < \lambda < \lambda_4$, the admissible region shown in Figure 2.10 vanished to a null space, i.e. both nodes will experience slip at some point during the load cycle. The now 'overlapping' extreme positions of all four constraints (2.73) are shown in Figure 2.11. The constraints advance in the direction

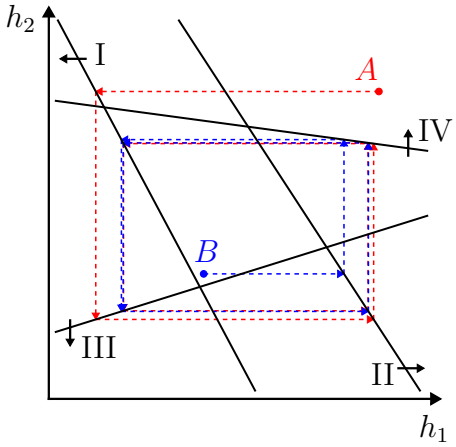


Figure 2.11: Convergence of slip displacements, for a coupled contact subject to external loading with $\lambda_3 < \lambda < \lambda_4$ and different initial conditions, to a unique steady-state.

indicated by small arrows until they reach the extreme position, and the external loads are defined such that each constraint recedes before the next advances to its extreme position. In doing so they follow a sequence ...I→III→II→IV→I... . Figure 2.11 shows how for different initial slip displacements, A and B, the same steady-state variation of h_1 and h_2 is approached after a small number of load cycles (Barber, 2011a).

Chapter 3

Asymptotic Contact Description

In the previous chapter we have looked at finite contact descriptions and presented analytical results for specific load cases. However, there are certain loading scenarios, such as a simultaneous application of shear force and bulk tension, where the bulk tension is large enough to cause slip displacements in opposite directions at the contact edges, or a simultaneous variation of shear force and bulk tension, for which closed-form solutions cannot be found. For those cases, where we cannot find a solution for the finite contact, we might still be interested in the state of stress in the neighbourhood of one contact edge, where cracks are most likely to nucleate. A semi-infinite, or asymptotic, consideration of the contact allows us to describe the stress field by means of the leading or dominating term resulting from a series expansion around the contact edge. Compared to the mathematically exact description of the finite contact, the quality of the asymptotic solution strongly depends on the distance from the contact edge, so we require the distance to the observation point to be small compared to every finite dimension characterising the contact. By consideration of the dominating term only, the asymptotic representation of contacts reduces the number of independent parameters, and increases the comparability between different loading scenarios or contact geometries. In the following, an asymptotic description will be derived for some simple contact geometries in order to demonstrate its range of application.

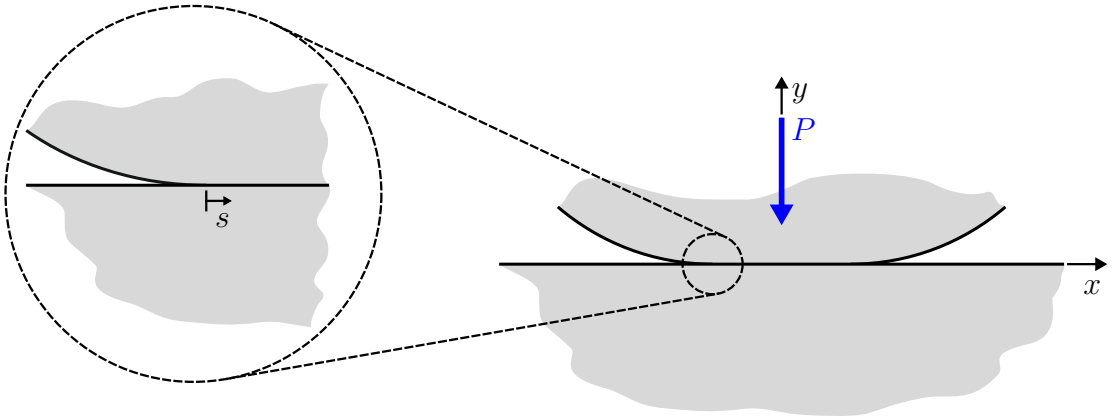


Figure 3.1: Asymptotic representation of an incomplete contact as a zoom-in on the contact edge.

3.1 Asymptotic Contact Tractions

Figure 3.1 shows an incomplete contact, where both bodies can be represented by half-planes. The contact is established by the normal load P, and ranges along the interval $[-a \quad a]$. We may think of the asymptotic description of a contact as a 'zoom-in' on the contact edge, as shown in Figure 3.1, and note that it looks like the tip of a semi-infinite crack. We may shift the origin from the centre of the contact interface to the edge, via

$$s = x + a \; . \tag{3.1}$$

Close to the edge, $s \ll a$, we may use the leading term of a series expansion for a sufficiently accurate representation of the contact tractions. We refer to such a single-term representation of the contact tractions as an *asymptotic contact traction*.

3.1.1 Asymptotic Normal Traction for Incomplete Contacts

For incomplete contacts the contact pressure falls, in a square-root bounded manner, smoothly to zero when approaching the edge of the contact. This suggests that an asymptotic representation of the contact normal traction takes the form

$$p(s) \simeq L_I \sqrt{s} \qquad 0 \leq \frac{s}{a} \ll 1 \; , \tag{3.2}$$

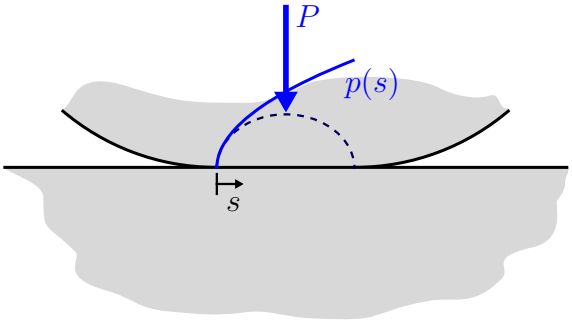


Figure 3.2: Asymptotic (solid) and finite (dashed) contact normal traction for an incomplete Hertzian contact.

where L_I is a geometry and load dependent multiplier defined as

$$L_I = \lim_{s \to 0} \frac{p(s)}{\sqrt{s}} \, . \tag{3.3}$$

For the special case of a Hertzian contact, the normal traction is given by equation (2.28). A shift of the contact edge via equation (3.1) and taking the first term of a binomial expansion leads to

$$p(s) \simeq \frac{2P}{\pi a} \sqrt{\frac{2}{a}} \sqrt{s} \qquad 0 \leq \frac{s}{a} \ll 1 \, , \tag{3.4}$$

such that for a Hertzian contact the asymptotic normal multiplier is given by

$$L_I = \frac{2P}{\pi a} \sqrt{\frac{2}{a}} \, . \tag{3.5}$$

The corresponding normal traction is shown in Figure 3.2. A comparison to the finite contact traction shows the dependence of the asymptotic approximation on s. Although it has, here, only been shown for a Hertzian contact, we note that the form of equation (3.2), i.e. that the normal traction is square-root bounded, results for all incomplete contacts. For symmetric incomplete contacts it can be shown that (Dini et al., 2004)

$$L_I = \frac{1}{\pi} \sqrt{\frac{2}{a}} \frac{\mathrm{d}P}{\mathrm{d}a} \, , \tag{3.6}$$

where $\mathrm{d}P/\mathrm{d}a$ is the derivative of the contact law (for the Hertzian case given by eq. (2.27)). For the flat and rounded contact shown in Figure 2.4(a), the contact law is given by equation (2.36) and evaluation of (3.6) leads to

$$L_I = \frac{2}{\pi AR}\sqrt{2a}\arccos\left(\frac{b}{a}\right) \ . \tag{3.7}$$

It should be noted that the validity of the asymptotic expression is strongly dependent on the contact geometry. For a Hertzian contact under normal load the smallest finite length characterising the contact is the contact half-width, a, while it might only be the part of the radiused edge in contact, $a - b$, for the flat and rounded geometry.

3.1.2 Asymptotic Shear Traction for Fully Adhered Contacts

The contact, initially established by a normal load P and ranging over an interval $[-a \quad a]$, may subsequently be loaded tangentially by a shear force, Q, or differential bulk tension, σ_0, or a combination of both. In a first step we assume the interface to be fully adhered such that no relative tangential displacements occur along the contact interface. The finite problem of a tangentially loaded contact with a stuck interface has been addressed in Section 2.4.2. We have shown the resulting square-root singular shear traction in Figure 2.6, and deduce that an asymptotic representation takes the form

$$q(s) \simeq K_{II}\frac{1}{\sqrt{s}} \qquad 0 \leq \frac{s}{a} \ll 1 \ , \tag{3.8}$$

where the asymptotic contact multiplier K_{II} is defined as

$$K_{II} = \lim_{s\to 0} q(s)\sqrt{s} \ . \tag{3.9}$$

For the finite contact the shear traction resulting from the application of a shear force, Q, is given by equation (2.48). A shift of the coordinate system followed by a binomial

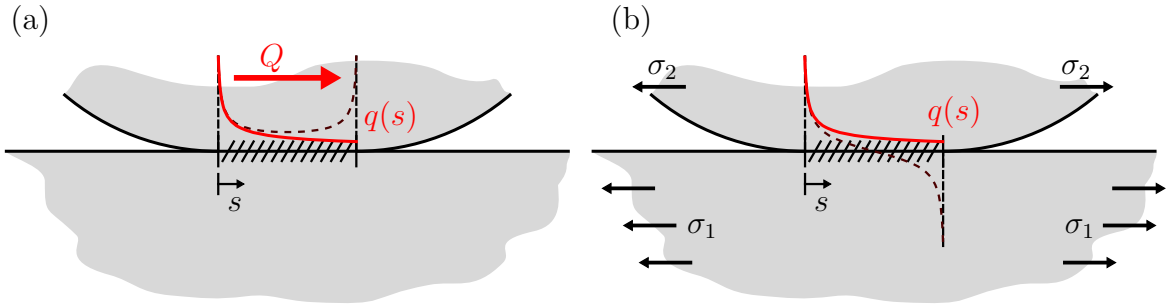


Figure 3.3: Asymptotic (solid) and finite (dashed) contact shear traction for a fully adhered contact subject to (a) a shear traction, Q, and (b) a differential bulk tension, $\sigma_0 = \sigma_1 - \sigma_2$.

expansion (where all but the first term are dropped), leads to

$$q(s) \simeq \frac{Q}{\pi a}\sqrt{\frac{a}{2}}\frac{1}{\sqrt{s}} \qquad 0 \leq \frac{s}{a} \ll 1 \,, \tag{3.10}$$

such that we find

$$K_{II} = \frac{Q}{\pi\sqrt{2a}} \,. \tag{3.11}$$

The asymptotic form of the fully stuck shear traction (3.10) is shown in Figure 3.3(a), and compared to the shear traction derived for a finite contact subject to a shear force. For the contacting bodies being subject to a differential bulk tension, while the interface remains adhered, the resulting shear traction is given by (2.50). Here a shift of the origin to the contact edge as well as the series expansion leads to

$$q(s) \simeq \frac{\sigma_0}{4}\sqrt{\frac{a}{2}}\frac{1}{\sqrt{s}} \qquad 0 \leq \frac{s}{a} \ll 1 \,, \tag{3.12}$$

where again all but the leading term were neglected. The shear traction is then of the same form as for the application of a shear force, such that for a combined loading the shear traction may be given by (3.8), while the asymptotic multiplier is (Hills et al., 2016)

$$K_{II} = \frac{Q}{\pi\sqrt{2a}} + \frac{\sigma_0}{4}\sqrt{\frac{a}{2}} \,. \tag{3.13}$$

We note that this result is geometry independent and hence the singularity at the contact edge depends on the tangential loading and the contact half-width only.
A comparison to the shear traction for a finite fully adhered contact subject to a differential bulk tension is shown in Figure 3.3(b). We note by comparison of Figures 3.3(a) and (b) that the asymptotic shear traction lies in between the finite traction for the application of a shear force and for a differential bulk tension. Consequently, the quality of the asymptotic approximation will increase for a mixed loading of shear force and bulk tension.

3.1.3 Asymptotic Shear Traction for Partial Slip Contacts

Here, we want to derive an asymptotic representation of the shear traction for an incomplete contact in a state of partial slip. We start from the shear traction for a finite Hertzian contact subject to a shear force, Q, which is given by equation (2.62). Dini and Hills (2004) show that shifting the origin to the edge of the contact with $s = x + a$, and making the contact semi-infinite by taking the limit $a \to \infty$ leads to

$$q(x) \simeq f L_I(\sqrt{s} - \sqrt{s-d}) \,, \tag{3.14}$$

where again equation (3.14) has to be interpreted in terms of its real parts. L_I is the asymptotic normal multiplier for a Hertzian contact given by (3.5), and $d = a - c$ is the size of the slip zone. Further, it may be noted that expression (3.14) follows the Jäger-Ciavarella theorem (Sect. 2.5.2) in the sense that the shear traction for an incomplete contact in a state of partial slip is represented as the superposition of a full sliding shear traction and a scaled version of the same. The scaling factor for the asymptotic representation, equation (3.14), is 1, and this is a result of taking the limit $a \to \infty$ (Dini and Hills, 2004).
Dini and Hills (2004) obtain an asymptotic expression of the slip-zone size, d, by considering the slip-zone to be small compared to the overall size of the contact, i.e. $s \to$

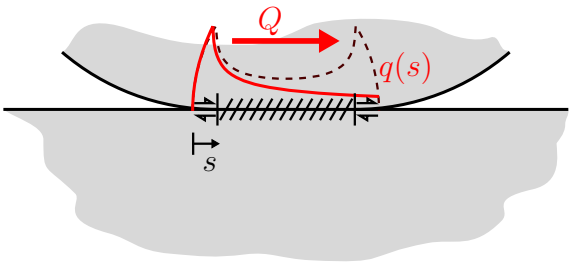


Figure 3.4: Asymptotic (solid) and finite (dashed) contact shear traction for a partial slip Hertzian contact subject a shear traction, Q.

∞ in equation (3.14), leading to

$$q(x) \simeq fL_I \frac{d}{2\sqrt{s}} \qquad s \gg d \,. \tag{3.15}$$

We further note that for $s \gg d$ the effect of the slip zone on the shear traction inside the stick region becomes negligible such that the shear traction can be represented by equation (3.8). Equating (3.8) and (3.15) leads to

$$d = \frac{2K_{II}}{fL_I} \,, \tag{3.16}$$

where K_{II}, for the application of a shear force, is given by equation (3.11). The resulting asymptotic shear traction is shown in Figure 3.4.

Although derived from the solution for a Hertzian contact subject to a normal and subsequently applied shear force, it can be shown that equation (3.14) is suitable for the description of general partial slip incomplete contacts subject to tangential loading in form of a shear force as well as a differential bulk tension (Dini et al., 2005). We may then use equations (3.6) and (3.13) for the asymptotic normal and shear multiplier (Dini et al., 2005).

An asymptotic representation of the subsurface stress field can be obtained following the steps described in Section 2.6. We may either directly use the derived asymptotic contact tractions in equations (2.67) and (2.68) to obtain the asymptotic complex potentials, or start from the finite contact tractions derived in Sections 2.3-2.5 to obtain the finite complex potentials from equations (2.63) and (2.64). The latter requires a horizontal shift of the origin by $w = z + a$, where a is the contact half-width and

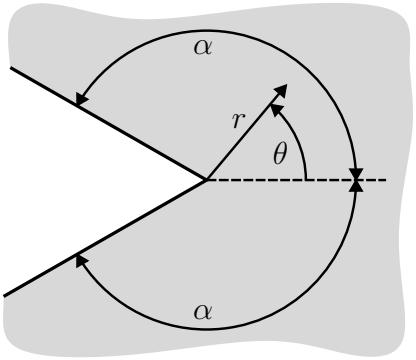


Figure 3.5: Notch of internal half-angle α.

$z = x+iy$ is a complex coordinate, followed by an binomial expansion. Consideration of the leading term only yields the same asymptotic expression for the complex potentials as the direct derivation via equations (2.67) and (2.68).

An alternative approach to describe semi-infinite contacts is the representation by a semi-infinite notch, described in the following.

3.2 Williams' Solution

Originally derived by Williams (1952) for the asymptotic description of the stress field around a notch, in terms of contact mechanics the Williams' solution is particularly helpful to find the stress field at the corner of a semi-infinite contact. Figure 3.5 shows a notch as treated by the Williams' solution and we note that an internal wedge half-angle $\alpha = 3\pi/4$ may be used to represent the edge of a complete contact as shown in Figures 2.1(b) and 3.1, where the contacting bodies are fully stuck. In contrast to all the previous considerations of a complete contact of a half-plane and a flat-ended punch, here, we do not have to treat the punch as being rigid, but instead it has to be made from the same material as the half-plane, such that both bodies can be modelled as a monolith. An angle of $\alpha = \pi$ may be used to represent the edge of an incomplete contact (Fig. 2.1(a)), which after zooming in sufficiently, looks like a semi-infinite crack.

3.2.1 Eigenvalues

For the general notch shown in Figure 3.5, remote in-plane loading may either cause the faces of the notch to be drawn apart or sheared in-plane (or any combination of the two), and we will refer to these by mode I and II loading, respectively. The stress field around the notch apex may then be represented by a series expansion in r. For the stresses to vary with r^n around the notch apex, we can find the corresponding terms for a stress potential, the *Airy stress function*, ψ, from the Michell solution

$$\begin{aligned}\psi = r^{n+2} &\left(A_1 \cos\left((n+2)\,\theta\right) + A_2 \sin\left((n+2)\,\theta\right)\right.\\ &\left. + A_3 \cos\left(n\theta\right) + A_4 \sin\left(n\theta\right)\right). \end{aligned} \tag{3.17}$$

These are the only terms for which the stresses vary with r^n while fulfilling the bi-harmonic equation, $\nabla^4\psi = 0$, i.e. ensuring compatibility of strains. For a consistent notation, following Williams (1952), we replace n by $\lambda - 1$ to find

$$\begin{aligned}\psi = r^{\lambda+1} &\left(A_1 \cos\left((\lambda+1)\,\theta\right) + A_2 \sin\left((\lambda+1)\,\theta\right)\right.\\ &\left. + A_3 \cos\left((\lambda-1)\,\theta\right) + A_4 \sin\left((\lambda-1)\,\theta\right)\right). \end{aligned} \tag{3.18}$$

The stresses are then found to be

$$\sigma_{rr} = \frac{1}{r}\frac{\partial\psi}{\partial r} + \frac{1}{r^2}\frac{\partial^2\psi}{\partial\theta^2} \qquad \sigma_{\theta\theta} = \frac{\partial^2\psi}{\partial r^2} \qquad \sigma_{r\theta} = -\frac{\partial}{\partial r}\left(\frac{1}{r}\frac{\partial\psi}{\partial\theta}\right)$$

leading to

$$\begin{aligned}
\sigma_{rr} &= \lambda r^{\lambda-1} \begin{bmatrix} -A_1\,(\lambda+1)\cos\left((\lambda+1)\,\theta\right) - A_2\,(\lambda+1)\sin\left((\lambda+1)\,\theta\right) \\ -A_3\,(\lambda-3)\cos\left((\lambda-1)\,\theta\right) - A_4\,(\lambda-3)\sin\left((\lambda-1)\,\theta\right) \end{bmatrix} \\
\sigma_{\theta\theta} &= \lambda r^{\lambda-1} \begin{bmatrix} A_1\,(\lambda+1)\cos\left((\lambda+1)\,\theta\right) + A_2\,(\lambda+1)\sin\left((\lambda+1)\,\theta\right) \\ +A_3\,(\lambda+1)\cos\left((\lambda-1)\,\theta\right) + A_4\,(\lambda+1)\sin\left((\lambda-1)\,\theta\right) \end{bmatrix} \\
\sigma_{r\theta} &= \lambda r^{\lambda-1} \begin{bmatrix} A_1\,(\lambda+1)\sin\left((\lambda+1)\,\theta\right) - A_2\,(\lambda+1)\cos\left((\lambda+1)\,\theta\right) \\ +A_3\,(\lambda-1)\sin\left((\lambda-1)\,\theta\right) - A_4\,(\lambda-1)\cos\left((\lambda-1)\,\theta\right) \end{bmatrix}.
\end{aligned} \tag{3.19}$$

For mode I loading we expect the direct stresses to vary symmetrically and the shear stress to vary anti-symmetrically with θ. As may be seen from equation (3.19), the corresponding terms in the stress function (3.18) are those involving A_1 and A_3. For mode II loading the opposite is true and consequently the associated terms of the stress function are those involving A_2 and A_4. In any case of loading, the free notch faces are required to be traction free with $\sigma_{\theta\theta} = \sigma_{r\theta} = 0$ for $\theta = \pm\alpha$, leading a set of four homogeneous equations for the four constants A_i. After some manipulation and neglecting trivial solutions we find the two systems (Barber, 2010)

$$\begin{bmatrix} (\lambda+1)\sin\left((\lambda+1)\,\alpha\right) & (\lambda-1)\sin\left((\lambda-1)\,\alpha\right) \\ (\lambda+1)\cos\left((\lambda+1)\,\alpha\right) & (\lambda+1)\cos\left((\lambda-1)\,\alpha\right) \end{bmatrix} \begin{Bmatrix} A_1 \\ A_3 \end{Bmatrix} = \mathbf{0} \tag{3.20}$$

and

$$\begin{bmatrix} (\lambda+1)\cos\left((\lambda+1)\,\alpha\right) & (\lambda-1)\cos\left((\lambda-1)\,\alpha\right) \\ (\lambda+1)\sin\left((\lambda+1)\,\alpha\right) & (\lambda+1)\sin\left((\lambda-1)\,\alpha\right) \end{bmatrix} \begin{Bmatrix} A_2 \\ A_4 \end{Bmatrix} = \mathbf{0} \tag{3.21}$$

for mode I and II loading, respectively. Systems (3.20) and (3.21) have a solution if and only if the determinant of the corresponding coefficient matrix vanishes. This

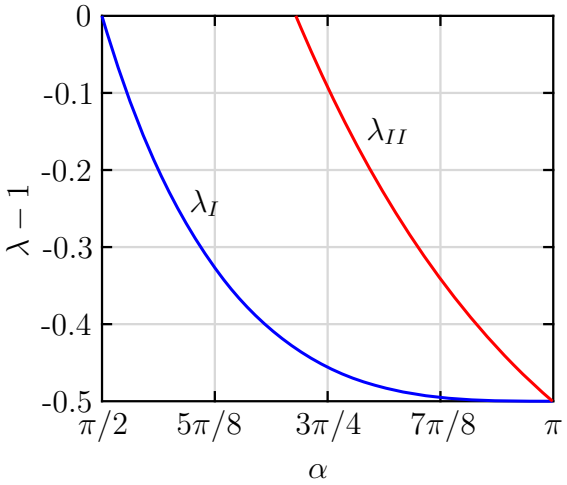


Figure 3.6: Leading mode I and mode II eigenvalue for a varying notch angle α.

leads to the characteristic equations

$$\lambda \sin(2\alpha) + \sin(2\lambda\alpha) = 0, \tag{3.22}$$

$$\lambda \sin(2\alpha) - \sin(2\lambda\alpha) = 0 \tag{3.23}$$

where λ_I will be an eigenvalue of (3.22) and λ_{II} of (3.23) for the case of mode I and II loading, respectively. From energy considerations, and noting that the stresses (3.19) are proportional to $r^{\lambda-1}$, it can be shown, that λ_I and λ_{II} are restricted to positive solutions of equations (3.22) and (3.23) (Barber, 2010). The smallest positive solution of (3.22) and (3.23) are shown in Figure 3.6 for a varying notch angle, α.

3.2.2 Stress Field

To determine the stress field corresponding to each solution, λ_I, we need to find the constants A_1 and A_3. The two equations (3.20), however, will not be linearly independent, and consequently we can identify the stress field only up to one unknown, say A_I. Both equations (3.21) are then satisfied for (Barber, 2010)

$$A_1 = A_I (\lambda_I - 1) \sin((\lambda_I - 1)\alpha) \tag{3.24}$$

$$A_3 = -A_I (\lambda_I + 1) \sin((\lambda_I + 1)\alpha). \tag{3.25}$$

Inserting λ_I, as a solution of equation (3.22), and expressions (3.24 - 3.25) in the symmetric part of equations (3.19), yields expressions for the stress field associated with mode I loading

$$\begin{aligned}
\sigma_{rr} &= A_I \lambda_I r^{\lambda_I - 1} \begin{bmatrix} -(\lambda_I - 1)\sin((\lambda_I - 1)\alpha)(\lambda_I + 1)\cos((\lambda_I + 1)\theta) \\ +(\lambda_I + 1)\sin((\lambda_I + 1)\alpha)(\lambda_I - 3)\cos((\lambda_I - 1)\theta) \end{bmatrix} \\
\sigma_{\theta\theta} &= A_I \lambda_I r^{\lambda_I - 1} \begin{bmatrix} (\lambda_I - 1)\sin((\lambda_I - 1)\alpha)(\lambda_I + 1)\cos((\lambda_I + 1)\theta) \\ -(\lambda_I + 1)\sin((\lambda_I + 1)\alpha)(\lambda_I + 1)\cos((\lambda_I - 1)\theta) \end{bmatrix} \\
\sigma_{r\theta} &= A_I \lambda_I r^{\lambda_I - 1} \begin{bmatrix} (\lambda_I - 1)\sin((\lambda_I - 1)\alpha)(\lambda_I + 1)\sin((\lambda_I + 1)\theta) \\ -(\lambda_I + 1)\sin((\lambda_I + 1)\alpha)(\lambda_I - 1)\sin((\lambda_I - 1)\theta) \end{bmatrix}.
\end{aligned} \tag{3.26}$$

Following similar steps for mode II loading leads to

$$\begin{aligned}
\sigma_{rr} &= A_{II} \lambda_{II} r^{\lambda_{II} - 1} \begin{bmatrix} -(\lambda_{II} + 1)\sin((\lambda_{II} - 1)\alpha)(\lambda_{II} + 1)\sin((\lambda_{II} + 1)\theta) \\ (\lambda_{II} + 1)\sin((\lambda_{II} + 1)\alpha)(\lambda_{II} - 3)\sin((\lambda_{II} - 1)\theta) \end{bmatrix} \\
\sigma_{\theta\theta} &= A_{II} \lambda_{II} r^{\lambda_{II} - 1} \begin{bmatrix} (\lambda_{II} + 1)\sin((\lambda_{II} - 1)\alpha)(\lambda_{II} + 1)\sin((\lambda_{II} + 1)\theta) \\ -(\lambda_{II} + 1)\sin((\lambda_{II} + 1)\alpha)(\lambda_{II} + 1)\sin((\lambda_{II} - 1)\theta) \end{bmatrix} \\
\sigma_{r\theta} &= A_{II} \lambda_{II} r^{\lambda_{II} - 1} \begin{bmatrix} -(\lambda_{II} + 1)\sin((\lambda_{II} - 1)\alpha)(\lambda_{II} + 1)\cos((\lambda_{II} + 1)\theta) \\ (\lambda_{II} + 1)\sin((\lambda_{II} + 1)\alpha)(\lambda_{II} - 1)\cos((\lambda_{II} - 1)\theta) \end{bmatrix},
\end{aligned} \tag{3.27}$$

and by a superposition of (3.26) and (3.27) we can describe the stress field for arbitrary in plane loading.

Looking at a notch, the stress field close to the apex might be sufficiently described by the smallest value of λ satisfying equation (3.22) or (3.23), i.e. the leading or dominating term of the series representation of the stress field. In contact mechanics, however, when considering the contacting bodies as a monolith we might also be interested in further terms. For θ chosen to align with the contact interface, the coordinate r will coincide with s in Figure 3.1. From all the different solutions, λ_I, to equation (3.22), we might then choose one, appropriate to represent a specific form of the different asymptotic

contact tractions shown in Figure 2.1 and discussed in Section 3.1. After calibrating the unknown value of A_I via the known contact traction, equations (3.26) provide the contact stress field around the edge of the contact in an asymptotic form.

We may show this for the example of an incomplete contact. Here, the edge of the contact, sufficiently zoomed-in as shown in Figure 3.1, will look like a semi-infinite crack. We choose $\alpha = \pi$ for the local contact geometry, and $\theta = 0$ for the line of observation to align with the contact interface. The stress component $\sigma_{\theta\theta}$ will then correspond to the contact normal traction. Equations (3.26) reduce to

$$\begin{aligned} \sigma_{rr} &= 2A_I\lambda_I\left(\lambda_I+1\right)r^{\lambda_I-1}\sin\left(\lambda_I\pi\right)\ , \\ \sigma_{\theta\theta} &= 2A_I\lambda_I\left(\lambda_I+1\right)r^{\lambda_I-1}\sin\left(\lambda_I\pi\right)\ , \\ \sigma_{r\theta} &= 0\ . \end{aligned} \tag{3.28}$$

We may now wish to describe the stress field caused by a normal load, P, pressing the two bodies into contact, and we know from equation (3.2) the the normal traction is square-root bounded. It is easily verified that in equation (3.28), a choice of $\lambda_I = 3/2$ will lead the desired variation of the stress with the distance to the contact edge. The stress components will then be given by

$$\begin{aligned} \sigma_{rr} &= -\frac{15}{2}A_I\sqrt{r}\ , \\ \sigma_{\theta\theta} &= -\frac{15}{2}A_I\sqrt{r}\ , \\ \sigma_{r\theta} &= 0\ , \end{aligned} \tag{3.29}$$

and we note by comparison of the component $\sigma_{\theta\theta}$ to equation (3.2), that the desired calibration is given by $A_I = -\frac{2}{15}L_I$.

Substituting $\alpha = \pi$, $\lambda_I = 3/2$ and $A_I = -\frac{2}{15}L_I$ into equations (3.26) will then yield the entire stress field caused by an asymptotic contact normal traction of the form (3.2). A choice of $\lambda_I = 1/2$ in equation (3.28) may be used to describe adhesion of the contacting bodies. We may follow a similar procedure for mode II loading where the

choice of $\lambda_{II} = 1/2$ and a subsequent calibration between K_{II} and A_{II} may be used to derive the stress field caused by an asymptotic fully stuck shear traction of the form (3.8), and a choice of $\lambda_{II} = 3/2$ if we look at an asymptotic description of contacts in a state of partial slip or full sliding.

Chapter 4

Distributed Dislocation Technique

The distributed dislocation technique is frequently used for the solution of crack problems as described in Hills et al. (1996). Including the description of contacts in the form of closed cracks, it may equivalently be used for the description of partial slip in contacts.

Here, we give a short review of basic concepts as they were explained in Hills et al. (1996). We follow Bueckner's theorem, in describing a crack in a remote stress field (Fig. 4.1(a)) by a superposition of the stresses arising in the uncracked body (Fig. 4.1(b)) and the stresses resulting from equal and opposite tractions to those induced by the far stress field, along the crack surface as shown in Figure 4.1(c) (Bueckner, 1958).

The separation (or slip displacement) of material forming a crack can mathematically

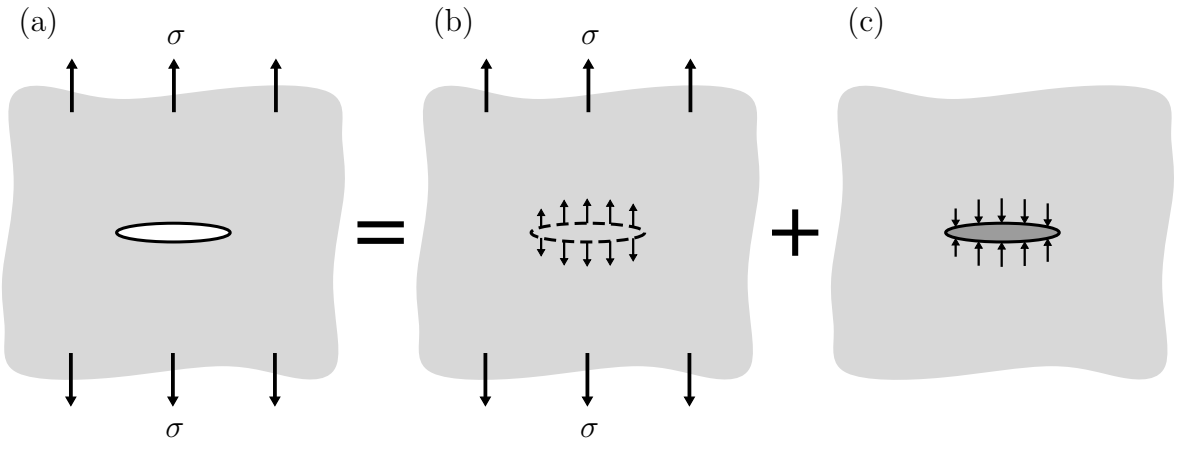


Figure 4.1: Bueckner's principle for a crack in remote stress σ: a) Crack in remote stress b) tractions in uncracked body c) tractions caused by separation.

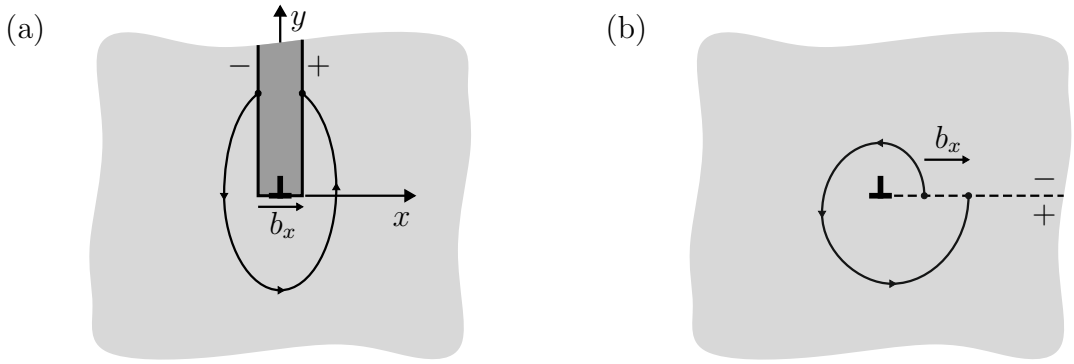


Figure 4.2: Dislocation discontinuity resulting from a) climb edge dislocation with cut perpendicular to b_x and b) glide edge dislocation with cut tangential to b_x.

be described by dislocations.

4.1 Dislocations

As the last paragraph indicates, a dislocation in two dimensions can be visualised by making a cut from the dislocation core to any infinitely remote point and displacing the two sides of the cut relative to each other. The constant relative displacement along the path-cut is known as the Burgers vector. This procedure can be visualised by at least two means. Figure 4.2(a) shows a slit from the dislocation core along the y-axis and inserted material with the thickness b_x, forming a climb edge dislocation. Alternatively, we may form a glide edge dislocation as shown in Figure 4.2(b). Here the cut is made from the dislocation core along the y-axis and one side is displaced by b_x before the two sides are rejoined.

The stresses, resulting from a solitary dislocation, in an infinite plane, with Burgers vector components in x- and y-direction, b_x and b_y, respectively, and with $r^2 = x^2 + y^2$, are given by

$$\begin{aligned}
\sigma_{xx}(x,y) &= \frac{2\mu}{\pi(\kappa+1)}\left[b_x\left(-\frac{y}{r^4}\left(3x^2+y^2\right)\right)+b_y\left(\frac{x}{r^4}\left(x^2-y^2\right)\right)\right] \\
\sigma_{yy}(x,y) &= \frac{2\mu}{\pi(\kappa+1)}\left[b_x\left(\frac{y}{r^4}\left(x^2-y^2\right)\right)+b_y\left(\frac{x}{r^4}\left(x^2+3y^2\right)\right)\right] \\
\sigma_{xy}(x,y) &= \frac{2\mu}{\pi(\kappa+1)}\left[b_x\left(\frac{x}{r^4}\left(x^2-y^2\right)\right)+b_y\left(\frac{y}{r^4}\left(x^2-y^2\right)\right)\right],
\end{aligned} \tag{4.1}$$

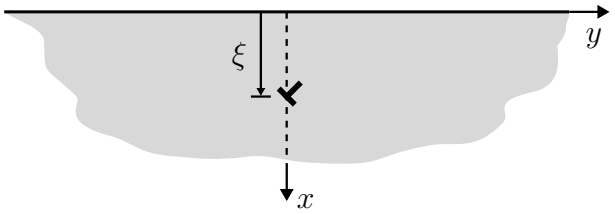


Figure 4.3: Dislocation in a half-plane.

where μ is the modulus of rigidity and κ Kolosov's constant. With corresponding abbreviations for the *kernel* functions K, equation (4.1) can be expressed as

$$\begin{bmatrix} \sigma_{xx}(x,y) \\ \sigma_{yy}(x,y) \\ \sigma_{xy}(x,y) \end{bmatrix} = \frac{2\mu}{\pi(\kappa+1)} \begin{bmatrix} K_{xxx}(x,y) & K_{yxx}(x,y) \\ K_{xyy}(x,y) & K_{yyy}(x,y) \\ K_{xxy}(x,y) & K_{yxy}(x,y) \end{bmatrix} \begin{bmatrix} b_x \\ b_y \end{bmatrix} . \tag{4.2}$$

The functions K are the kernel functions for a dislocation in an infinite plane and different formulations are required for dislocations close to any geometric feature. For example the kernel functions for a dislocation in a half-plane are given in Hills et al. (1996), and if the dislocation as well as the observation point are located on the x-axis, as shown in Figure 4.3, then the kernels reduce to

$$\begin{aligned} K_{xxx} &= K_{xyy} = K_{yxy} = 0 \, , \\ K_{xxy} &= K_{yyy} = \frac{1}{x-\xi} - \frac{1}{x+\xi} - \frac{2\xi}{(x+\xi)^2} + \frac{4\xi^2}{(x+\xi)^3} \, , \\ K_{yxx} &= \frac{1}{x-\xi} + \frac{1}{x+\xi} + \frac{2x}{(x+\xi)^2} - \frac{4x^2}{(x+\xi)^3} \, . \end{aligned} \tag{4.3}$$

4.2 Formulation

To derive a formulation for the analysis of crack opening or slip displacement, for the interface lying on the axis $y = 0$ it is convenient to consider a single infinitesimal dislocation located at point $x = \xi \, (y = 0)$, with an infinitesimal Burgers vector $\delta b_x \equiv B_x(\xi)\delta\xi$ and $\delta b_y \equiv B_y(\xi)\delta\xi$, where $B_i(\xi)$ are the densities of dislocations. The components of stress $\bar{\sigma}_{ij}$, resulting from a distributed density of dislocations, along the

axis $y = 0$ on the interval $[a, b]$, therefore can be expressed as

$$\begin{aligned}
\bar{\sigma}_{xx}(x,0) &= \frac{2\mu}{\pi(\kappa+1)} \int_a^b \left[B_x(\xi)K_{xxx}(x,\xi) + B_y(\xi)K_{yxx}(x,\xi)\right] d\xi \\
\bar{\sigma}_{yy}(x,0) &= \frac{2\mu}{\pi(\kappa+1)} \int_a^b \left[B_x(\xi)K_{xyy}(x,\xi) + B_y(\xi)K_{yyy}(x,\xi)\right] d\xi \\
\bar{\sigma}_{xy}(x,0) &= \frac{2\mu}{\pi(\kappa+1)} \int_a^b \left[B_x(\xi)K_{xxy}(x,\xi) + B_y(\xi)K_{yxy}(x,\xi)\right] d\xi
\end{aligned} \tag{4.4}$$

where $B_i(\xi)$, the dislocation density, is

$$B_i(\xi) = \frac{db_i(\xi)}{d\xi}. \tag{4.5}$$

Following Bueckner's theorem (Fig. 4.1) the final stresses are derived from superposition of these corrective stresses $\bar{\sigma}_{ij}(x, y)$ and the bilateral stresses $\tilde{\sigma}_{ij}(x, y)$ induced by the remote stresses only, in the absence of the crack, i.e.

$$\sigma_{ij}(x,y) = \tilde{\sigma}_{ij}(x,y) + \bar{\sigma}_{ij}(x,y). \tag{4.6}$$

The dislocation densities, B_x and B_y, are usually unknown and may be derived from boundary conditions. For example the normal and shear traction, $p(x)$ and $q(x)$, respectively, have to vanish along the crack faces if the crack is open or they have to fulfil the slip condition (2.52) for the modelling of partial slip. The typically occurring singularity in the kernel functions K (c.f. eqs. (4.1) and (4.3)) leads a singular integral equation.

The relative normal displacement may be found from the dislocation density via

$$g(x) = \int_a^x B_y(\xi) d\xi \ , \tag{4.7}$$

and the requirement that a crack is closed at both ends

$$\int_a^b B_y(\xi) d\xi = 0 \ , \tag{4.8}$$

forms a side condition for the solution of the singular integral equation to determine the dislocation density B_y. The relative tangential displacement is given by

$$h(x) = \int_a^x B_x(\xi) d\xi \ , \tag{4.9}$$

and analogous to equation (4.8) we express the requirement that there is no relative tangential displacement between the ends of the crack or the slip zone as

$$\int_a^b B_y(\xi) d\xi = 0 \ . \tag{4.10}$$

As a first step of the solution process the integral range may be normalised. A general normalisation is given by

$$\begin{aligned} 2\xi &= (b-a)s + (b+a), \\ 2x &= (b-a)t + (b+a), \end{aligned} \tag{4.11}$$

so that (s,t) span $[-1 \quad 1]$.

For simple problems, when the crack lies in an infinite plane, the solution of the singular integral equation, arising in the determination of the dislocation densities, can be found by an exact inversion as shown in Section 2.3.4. For more complicated cases, when the kernel includes bounded terms to account for the presence of free boundaries, a numerical solution will be needed using, for example the *Gauss-Chebyshev Quadrature*.

4.3 Gauss-Chebyshev Quadrature

The description of the numerical quadrature merits a whole subsection in Hills et al. (1996), which gives detailed guidance and comparison to other numerical schemes.

The solution technique depends on the end-point behaviour of the dislocation density, which might either be bounded or singular, and Table 4.1 and 4.2 connect the four possible combinations with the corresponding formulae.

	Singular	Bounded
Singular	I	II
Bounded	III	IV

Table 4.1: The four cases of end-point behaviour

Case	$\omega(s)$	s_i	t_k	n	W_i
I	$(1-s^2)^{-1/2}$	$\cos\left(\pi\frac{2i-1}{2N}\right)$	$\cos\left(\pi\frac{k}{N}\right)$	1	$\frac{1}{N}$
II	$(1-s)^{1/2}(1+s)^{-1/2}$	$\cos\left(\pi\frac{2i}{2N+1}\right)$	$\cos\left(\pi\frac{2k-1}{2N+1}\right)$	0	$\frac{2(1-s_i)}{2N+1}$
III	$(1-s)^{-1/2}(1+s)^{1/2}$	$\cos\left(\pi\frac{2i-1}{2N+1}\right)$	$\cos\left(\pi\frac{2k}{2N+1}\right)$	0	$\frac{2(1+s_i)}{2N+1}$
IV	$(1-s^2)^{1/2}$	$\cos\left(\pi\frac{i}{N+1}\right)$	$\cos\left(\pi\frac{2k-1}{2(N+1)}\right)$	-1	$\frac{1-s_i^2}{N+1}$

Table 4.2: Gauss-Chebyshev quadrature formulae

For each of the four given cases the dislocation density may be expressed by a bounded function $\phi(s)$ and a corresponding fundamental function $\omega(s)$

$$B(s) = \omega(s)\phi(s) \tag{4.12}$$

and therefore an integral equation, normalised by equation (4.11), and containing the dislocation density $B(s)$ and the corresponding kernel function $K(s,t)$, can, for N quadrature points, be expressed as

$$\int_{-1}^{1} B(s)K(s,t)ds = \pi\sum_{i=1}^{N} W_i\phi(s_i)K(s_i,t_k) \qquad k = 1...N-n. \tag{4.13}$$

Here, W_i are the weight functions, t_k are the $N-n$ collocation points and s_i are the N integration points corresponding to the problem specific end-point behaviour, as stated in Table 4.1 and 4.2. This yields a set of $N-n$ algebraic equations, which can be solved for the bounded function $\phi(s)$ at the integration points s_i. The side conditions (4.8) and (4.10), which may be required for the numerical solution, are given in discretised form by

$$\pi\sum_{i=1}^{N} W_i\phi_y(s_i) = 0\ , \tag{4.14}$$

and

$$\pi \sum_{i=1}^{N} W_i \phi_x(s_i) = 0 \ . \tag{4.15}$$

The corresponding stresses, for example the xx-component, resulting from a particular dislocation density, for example $B_y(s)$, can be expressed as

$$\bar{\sigma}_{xx}(t, y) = \frac{2\mu}{\kappa + 1} \sum_{i=1}^{N} W_i \phi_y(s_i) K_{yxx}(s_i, t_k, y) \ . \tag{4.16}$$

Note that this equation is valid only at the collocation points t_k, inside the crack or slip region ($y = 0, |t| < 1$), or outside the slip region it may be evaluated at any point (Hills et al., 1996).

4.4 Crack Tip Stress Intensity Factor

We have already looked at the singularity arising at the tip of a crack in Section 3.2 (there specified by an internal wedge angle $\alpha = \pi$), and found the surrounding stress field to be square root singular. The intensity of the singularity at the crack tip corresponds the multipliers $A_{I,II}$ in equations (3.26) and (3.27) and is related to the gradient of the opening displacement at the crack ends. This allows us to find the multipliers as

$$K_I^c(\pm 1) = \pm\sqrt{\pi l}\frac{2\mu}{\kappa + 1}\phi_y(\pm 1), \tag{4.17}$$

$$K_{II}^c(\pm 1) = \pm\sqrt{\pi l}\frac{2\mu}{\kappa + 1}\phi_x(\pm 1), \tag{4.18}$$

where $K_{I,II}^c = \sqrt{2\pi} A_{I,II}$ are the mode I and II crack tip stress intensity factors at the ends of a buried crack (closed at both ends) of half-length l. For a surface breaking crack (open at one end) of length l the crack tip stress intensity factors differ by a

Case	$M_E(+1)$	$\Phi_E(+1)$	$M_E(-1)$	$\Phi_E(-1)$
I	$\frac{1}{N}$	$\frac{\sin\left(\pi\frac{2i-1}{4N}(2N-1)\right)}{\sin\left(\pi\frac{2i-1}{4N}\right)}$	$\frac{1}{N}$	$\frac{\sin\left(\pi\frac{i}{2N+1}(2N-1)\right)}{\sin\left(\pi\frac{i}{2N+1}\right)}$
II	1	$\frac{\sin\left(\pi\frac{i(2N-1)}{2N+1}\right)}{\sin\left(\pi\frac{i}{2N+1}\right)}$	$\frac{2}{2N+1}$	$\cot\left(\frac{\pi}{2}\frac{2i-1}{2N+1}\right)\sin\left(\pi\frac{N(2i-1)}{2N+1}\right)$
III	$\frac{2}{2N+1}$	$\cot\left(\frac{\pi}{2}\frac{2i-1}{2N+1}\right)\sin\left(\pi\frac{N(2i-1)}{2N+1}\right)$	1	$\frac{\sin\left(\pi\frac{i(2N-1)}{2N+1}\right)}{\sin\left(\pi\frac{i}{2N+1}\right)}$
IV	1	$\cot\left(\frac{\pi}{2}\frac{i}{N+1}\right)\sin\left(\pi\frac{iN}{N+1}\right)$	1	$\cot\left(\frac{\pi}{2}\frac{i}{N+1}\right)\sin\left(\pi\frac{iN}{N+1}\right)$

Table 4.3: Krenk's interpolation formulae for end-points (Hills et al., 1996).

factor of $\sqrt{2}$, such that at the closed end they are given by (Hills et al., 1996)

$$K^c_{I,II}(\pm 1) = \sqrt{2\pi}\sqrt{l}\frac{2\mu}{\kappa+1}\phi_{y,x}(+1). \tag{4.19}$$

4.5 Krenk's Interpolation

We may note that none of the integration points s_i coincides with the end of the integration range and hence, the numerical quadrature does not provide the value of the bounded function at the end points of the integral range, $\phi(\pm 1)$. Consequently, a numerical integration scheme is needed to find the crack tip stress intensity factors. The values $\phi(\pm 1)$ were found by Krenk (1975) in terms of an interpolation and are given in a general form by

$$\phi(+1) = M_E(+1)\sum_{i=1}^{N}\Phi_E(+1)\phi(s_i), \tag{4.20}$$

$$\phi(-1) = M_E(-1)\sum_{i=1}^{N}\Phi_E(-1)\phi(s_{N+1-i}), \tag{4.21}$$

where the quantities $M_E(\pm 1)$ and $\Phi_E(\pm 1)$ differ depending on the end-point behaviour (specified by Table 4.1), and are given in Table 4.3.

For intermediate points, s, other than the quadrature specific integration points, s_i, Krenk (1975) obtains the values of the bounded function ϕ by interpolation. The

Case	M_I	$\Phi_I(s)$	γ
I	$\frac{2}{N}$	$\cos\left(\pi\frac{j(2i-1)}{2N}\right)\cos\left(j\gamma\right)$	$\arccos(s)$
II	$\frac{4}{2N+1}$	$\sin\left(\pi\frac{i}{2N+1}\right)\sin\left(\pi\frac{i(2j+1)}{2N+1}\right)\frac{\sin(2(j+1)\gamma)}{\sin(\gamma)}$	$\arccos\left(\sqrt{\frac{s+1}{2}}\right)$
III	$\frac{4}{2N+1}$	$\cos\left(\frac{\pi}{2}\frac{2i-1}{2N+1}\right)\cos\left(\frac{\pi}{2}\frac{(2i-1)(2j+1)}{2N+1}\right)\sqrt{\frac{2}{s+1}}\cos(2(j+1)\gamma)$	$\arccos\left(\sqrt{\frac{s+1}{2}}\right)$
IV	$\frac{2}{N+1}$	$\sin\left(\pi\frac{i}{N+1}\right)\sin\left(\pi\frac{i(j+1)}{N+1}\right)\frac{\sin((j+1)\gamma)}{\sin(\gamma)}$	$\arccos(s)$

Table 4.4: Krenk's interpolation formulae for intermediate points (Hills et al., 1996).

intermediate values of ϕ are given by (Hills et al., 1996)

$$\phi(s) = M_I \sum_{i=1}^{N} \left(\frac{1}{2} + \sum_{j=1}^{N-1} \Phi_I(s) \right) \phi(s_i) \qquad \text{case } I \ , \tag{4.22}$$

$$\phi(s) = M_I \sum_{i=1}^{N} \left(\sum_{j=0}^{N-1} \Phi_I(s) \right) \phi(s_i) \qquad \text{cases } II,\ III,\ IV \ , \tag{4.23}$$

where the constants M_I and functions $\Phi_I(s)$ are given in Table 4.4 for the different cases of end-point behaviour.

Chapter 5

Stress Field at the Edge of Incomplete Contacts

In Chapter 6 we will address the problem of fretting fatigue and fretting wear with cracks nucleating in the neighbourhood of the edge of incomplete contacts. Before doing so it is worth, here, looking in detail at the subsurface stress field. Generally, we assume linear elastic material behaviour, and it is necessary to establish some means of checking the validity of this assumption. In the first section of this chapter we will therefore present a simple graphical method to find the limit load before the onset of plasticity is reached. For tangential loading we show how the coefficient of friction affects the strength of the contact.

In the second section we look at the edge of incomplete contacts in more detail, specifically the asymptotic representation of the contact stress field. For the finite consideration of contacts in the first section of this chapter we derive the stress field via the Muskhelishvili complex potential (Sec. 2.6). As indicated in Section 3.2, the Williams' solution provides an additional way to identify the subsurface stress field in an asymptotic single-term representation. The second section of this chapter presents a formal comparison of the two, establishing the relationship between mode I and II loading, as defined for the Williams' solution, and normal and tangential potential function, ϕ^n and ϕ^t, as introduced in Section 2.6.

The stress field associated with a contact shear traction is addressed in the third section.

Such a shear traction may be excited by either a shear force, Q, or a differential bulk tension, σ_0. It is known that under full stick conditions the asymptotic form of the shear traction is characterised by the contact multiplier, K_{II}, as discussed in Section 3.1. In the case of a differential bulk tension the shear traction is independent of the exact combination of bulk tension present in the two bodies, but depends on the difference only. For the subsurface stress field of a body, this certainly does not hold. The stress field in the neighbourhood of a contact will depend on both the contact shear traction and the remote tension applied to the body. This section aims to investigate the asymptotic subsurface stress field in the neighbourhood of the contact edge, and how it is affected by the exact combination of loads, all leading the same asymptotic shear traction.

5.1 Elastic Limit Calculation

Among others, Johnson (1963) as well as Hills and Sackfield (1984) described the elastic limit for rolling and sliding Hertzian contacts, before Ciavarella et al. (1998) looked at sequential loading of flat but rounded contacts subject to a normal and shear force in the presence of friction. Here, we will extend previous results by the consideration of a differential bulk tension, and present a simple graphical method to determine if the given loading exceeds the elastic limit.

The effect of the coefficient of friction is of practical interest as real components may experience a high number of load cycles resulting from vibrations, and the presence and magnitude of slip displacements may be affected by different surface treatments or coatings. We investigate, how for the same contact and external loading, the presence of slip displacements affect the severity of the state of stress. This is of particular interest as plastic dissipation in each load cycle may be crucial for the component's life span. In the following we will consider the example of a flat and rounded contact treated in Section 2.3.5 and shown in Figure 2.4(a). This geometry covers a range of contact problems as it includes a Hertzian contact for the choice $b \to 0$, and may be used to approximate the results for an almost complete contact by choosing $b/a \to 1$.

5.1.1 Normal Loading

For a flat and rounded contact, loaded by a normal load, P, we may rearrange the contact law (2.36) to give

$$\frac{PAR}{b^2} = \left(\frac{a}{b}\right)^2 \left(\arccos\left(\frac{b}{a}\right) - \frac{b}{a}\sqrt{1-\left(\frac{b}{a}\right)^2}\right) \ , \tag{5.1}$$

and note that the right hand side depends solely on the yet unknown ratio a/b, while the left hand side is formed by typically known quantities like the external loading, elastic properties, A (eq. (2.19)), and the geometry parameters R and b. The visualisation of equation (5.1) is shown in Figure 5.1(a), and we note that the horizontal axis is reversed to allow for a better combined readability of Figure 5.1(a) and (b).

The resulting normal traction is given by equation (2.34). Substituting the normal traction as well as the punch profile (2.32), into equation (2.67) we can obtain the Muskhelishvili complex potential (Vázquez et al., 2014). Explicit equations for the subsurface stress field may then be derived via equations (2.70), where a split of the potential into its real and imaginary part leads to a representation in real algebra. Details of the procedure are given by Vázquez et al. (2014). For brevity we will limit ourselves, here, to the final representation of the subsurface stress field, but a detailed derivation is given in Appendix A.1. Following the steps described above, the stress caused by a normal load pressing the bodies into contact, can be expressed as

$$\begin{aligned}
\sigma^n_{xx}(x,y) &= \frac{1}{\pi AR}\left[-2\pi y \pm 2(v_1 + y\,u_6)\arccos\left(\frac{b}{a}\right)\right. \\
&\qquad \left. +(x-b)u_2 - (x+b)u_3 - 2y(v_2 - v_3)\right] \ , \\
\sigma^n_{yy}(x,y) &= \frac{1}{\pi AR}\left[\pm 2(v_1 - y\,u_6)\arccos\left(\frac{b}{a}\right) + (x-b)u_2 - (x+b)u_3\right] \ , \\
\sigma^n_{xy}(x,y) &= \frac{1}{\pi AR}\left[\mp 2\,y\,v_6\arccos\left(\frac{b}{a}\right) - y(u_2 - u_3)\right] \ ,
\end{aligned} \tag{5.2}$$

where the upper sign corresponds to the case $x \leq 0$, and the lower sign to $x > 0$. The functions $u_1(x,y,a)$, $v_1(x,y,a)$, $u_2(x,y,a,b)$, $v_2(x,y,a,b)$, $u_3(x,y,a,b)$, $v_3(x,y,a,b)$,

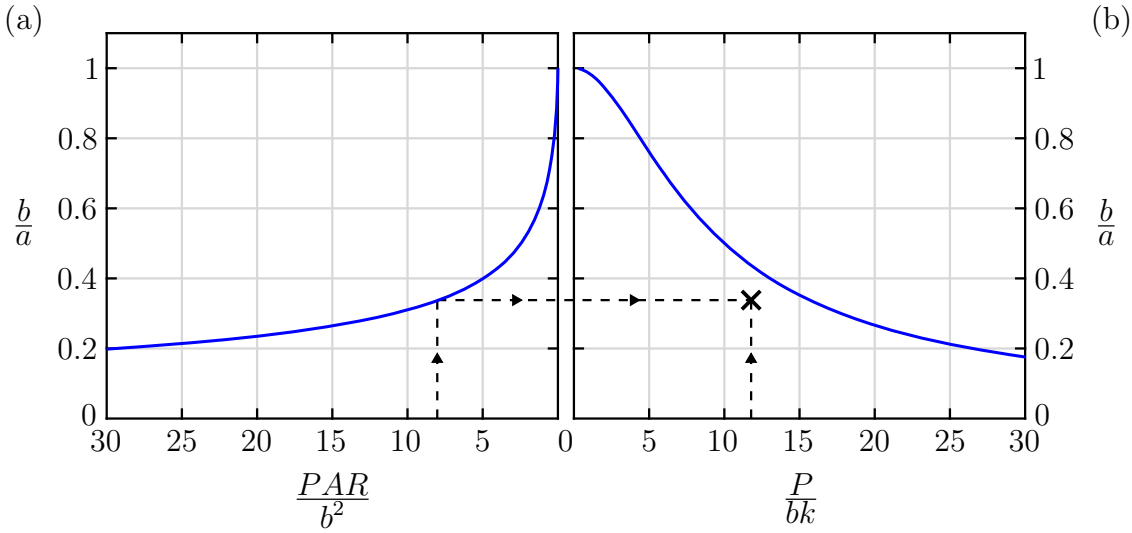


Figure 5.1: (a) Contact law and (b) elastic limit for a flat and rounded contact subject to a normal load, P (plane strain with $\nu = 0.3$).

$u_6(x, y, a)$ and $v_6(x, y, a)$ are given in Appendix A.4, and the arguments have been omitted in equation (5.2) for brevity.

We may now use the stress components (5.2) to calculate the *von Mises* yield parameter, $\sqrt{J}$, which for plane problems is defined as

$$\sqrt{J} = \sqrt{\frac{1}{6}\left[(\sigma_{xx} - \sigma_{yy})^2 + (\sigma_{xx} - \sigma_{zz})^2 + (\sigma_{yy} - \sigma_{zz})^2\right] + \sigma_{xy}^2}\,. \tag{5.3}$$

For plane stress conditions we have $\sigma_{zz} = 0$ in equation (5.3), while under plane strain we find $\sigma_{zz} = \nu\,(\sigma_{xx} + \sigma_{yy})$. We have seen in Section 2.3.5 that the form of the contact normal traction depends only on the ratio b/a, while it is simply scaled by the factor $p_0 = 2P/(\pi a)$. Certainly, the same will then apply to the subsurface stress field such that the location of the maximum $\sqrt{J}$ (relative to the contact half-width) as well as the ratio $\sqrt{J_{\max}}/p_0$ simply depend on the ratio b/a. The most severely stressed material point will then reach the yield stress in pure shear, k (a material property), if $k = \sqrt{J_{\max}} = 2P\sqrt{J_{\max}}/(p_0\pi a)$, and we may rearrange this expression to yield

$$\frac{P}{b\,k} = \frac{\pi}{2}\frac{a}{b}\frac{p_0}{\sqrt{J_{\max}}}\,. \tag{5.4}$$

Following the arguments above, we note that the right hand side of equation (5.4) depends solely on the ratio b/a, such that for each ratio b/a we may find the normalised

normal load $P/(b\,k)$ sufficient to cause the onset of yield. The corresponding results are shown in Figure 5.1(b). The axes are arranged such that we have the typically known quantities on the horizontal axis, and we note that Figure 5.1(a) and (b) share the vertical axis.

Figure 5.1 may then be read the following way: From the geometry of the contact, the material and the normal load, we find directly the horizontal position in Figure 5.1(a). When the normal load, P, is increased we move from the top right (where P is 0) of Figure 5.1(a) along the curve to the bottom left. From this we directly obtain the current ratio b/a, which will give us the vertical position in Figure 5.1(b). The horizontal position in Figure 5.1(b) is again determined by the contact load, P, the flat half-width b, and the yield strength of the material in pure shear, k. If the determined point lies underneath the curve, none of the points in the neighbourhood of the contact has reached the elastic limit.

5.1.2 Shear Loading

Additionally to the normal load the contact may experience a shear force, Q. The resulting shear traction, $q(x)$, or rather the corresponding subsurface stress field, will affect the maximum load the contact can sustain before the elastic limit is reached.

Sliding

For a frictional contact, the maximum sustainable shear force, $Q = fP$, will cause gross sliding between the contacting bodies, as discussed in Section 2.4.3. From equation (2.54) we know that the shear traction, $q(x)$, will correspond to the normal traction scaled by the coefficient of friction, $q(x) = fp(x)$, where the normal traction for the here considered flat and rounded contact is given by equation (2.34). For the full sliding case the normal and tangential Muskhelishvili complex potentials are related via $\phi^t(z) = if\phi^n(z)$ (Vázquez et al., 2014). However, we see by comparison of equations (2.70) and (2.71) that the form of the stress field will differ. Vázquez et al. (2014) derive

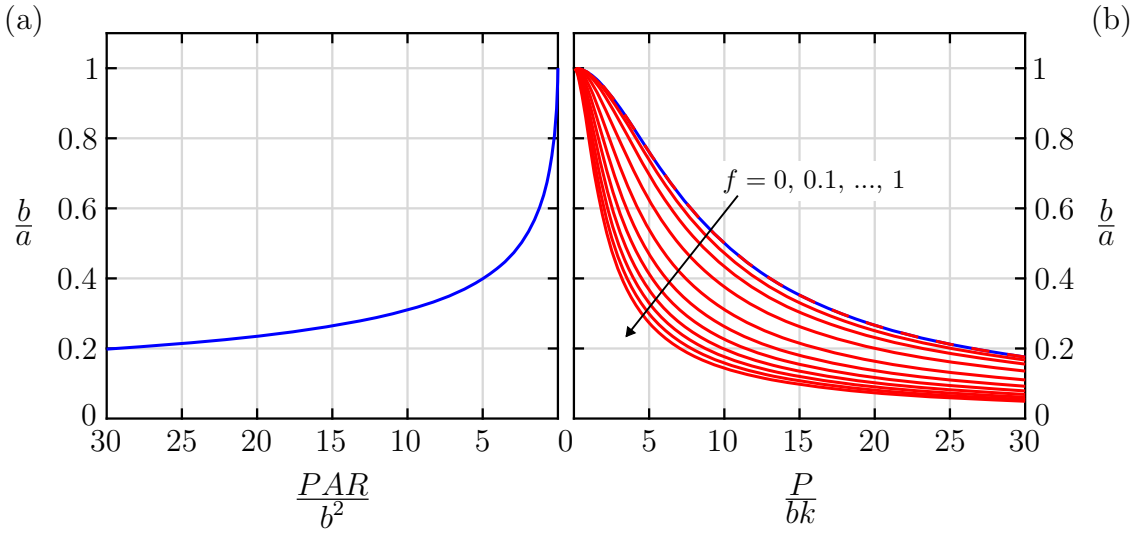


Figure 5.2: (a) Contact law and (b) elastic limit for a flat and rounded contact subject to a normal load, P, and a shear force $Q = fP$, causing full sliding (plane strain with $\nu = 0.3$).

explicit equations for the interior stress field which are given by

$$\begin{aligned}
\sigma^t_{xx}(x,y) &= \frac{f}{\pi AR}\left[\mp 2(2u_1 - y\,v_6)\arccos\left(\frac{b}{a}\right)\right. \\
&\qquad \left. +2(x-b)v_2 - 2(x+b)(v_3+\pi) + 3y(u_2-u_3)\right] , \\
\sigma^t_{yy}(x,y) &= \frac{y\,f}{\pi AR}\left[\mp 2\,v_6\arccos\left(\frac{b}{a}\right) - u_2 + u_3\right] , \\
\sigma^t_{xy}(x,y) &= \frac{f}{\pi AR}\left[\pm 2(v_1 + y\,u_6)\arccos\left(\frac{b}{a}\right)\right. \\
&\qquad \left. +(x-b)u_2 - (x+b)u_3 - 2y(v_2 - v_3 - \pi)\right] ,
\end{aligned} \tag{5.5}$$

where, again, the upper sign corresponds to the case $x \leq 0$, and the lower sign to $x > 0$. The functions u_i and v_i are also given in Appendix A.4, and have the same arguments as in Section 5.1.1. The different steps in the derivation of equations (5.5) are shown in Appendix A.2.

The elastic limit for a flat and rounded contact subject to a normal load, P, and a shear force, $Q = fP$, sufficient to cause gross slip, may then be derived by superposition of equations (5.2) and (5.5). We follow the same steps as for the normal problem, but note that the part of the interior stress field associated with the shear traction scales with the coefficient of friction while the normal part does not. Consequently, the elastic

limit curve will now depend on the coefficient of friction. The maximum normal load, such that a fully sliding contact does not cause plastic deformation, is shown in Figure 5.2(b) for a varying ratio b/a and different coefficients of friction.

For the special case of a frictionless contact $f = 0$, there will be no shear traction along the contact interface, and the solution corresponds to the elastic limit for the normal load only. Generally, we find the stress field caused by the tangential loading, and superimposed on the stress field resulting from the normal loading, to reduce the maximum load the contact can sustain before reaching the onset of plasticity. This effect appears to be magnified by an increasing coefficient of friction. However, for a fully sliding contact an increase of the coefficient of friction also means a higher tangential load. It appears more sensible to investigate how a varying coefficient of friction affects the severity of the subsurface stress field for a fixed external loading. We will address this problem in the next section.

Partial Slip

A stationary flat and rounded contact subject to a monotonically increasing shear force, $Q < fP$, has a central stick zone whose decreasing half-width, c, is given implicitly by the expression (Vázquez et al., 2014)

$$\frac{Q}{fP} = 1 - \frac{c^2 \arccos\left(\frac{b}{c}\right) - b\sqrt{c^2 - b^2}}{a^2 \arccos\left(\frac{b}{a}\right) - b\sqrt{a^2 - b^2}} \,. \tag{5.6}$$

We note that generally $b \leq c \leq a$, and that for $b \to 0$ this equation reduces to the corresponding expression for the Hertzian contact (2.62), as expected. Following the Jäger-Ciavarella theorem (Sec. 2.5.2), the resulting shear traction, $q(x)$, can be found from superposition of a full sliding shear traction $q(x) = f\,p(x)$ and a scaled version acting over the stick zone and with the tendency to reduce the shear tractions. This

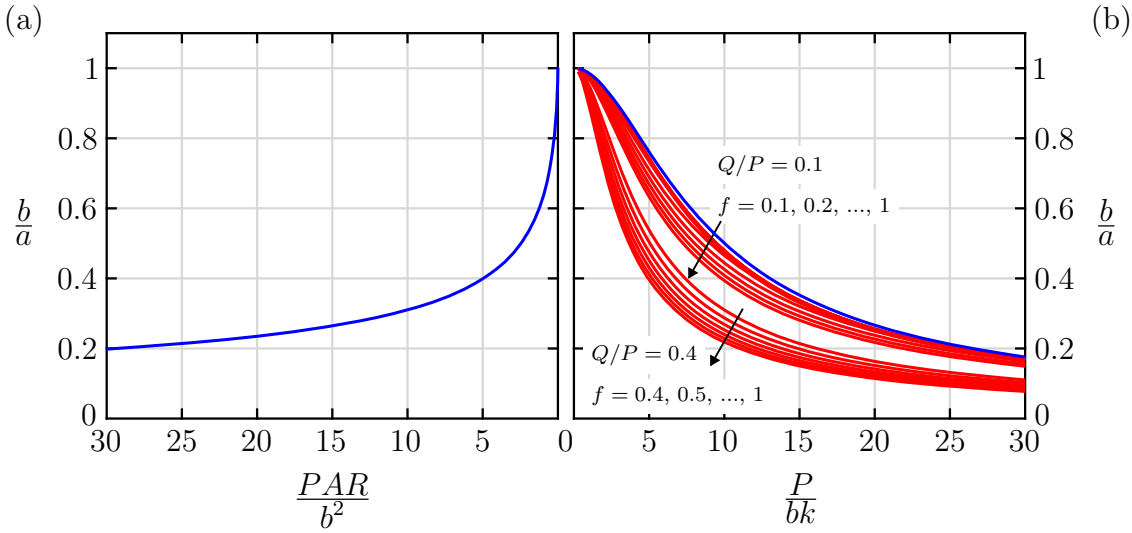


Figure 5.3: (a) Contact law and (b) elastic limit for a flat and rounded contact subject to a combination of normal and shear force causing a state of partial slip with $Q/P = 0.1$ and 0.4, and a varying coefficient of friction, f (plane strain with $\nu = 0.3$).

corrective shear traction, $q^*(x)$, is given by

$$q^*(x) = \frac{-c\,f}{\pi AR}\left(2\arccos\left(\frac{b}{c}\right)\sqrt{1-\left(\frac{x}{c}\right)^2} + \frac{b-x}{c}F(x,c,b) + \frac{b+x}{c}F(x,c,-b)\right), \tag{5.7}$$

where the function $F(x,c,b)$ is given by equation (2.35). Similarly to the contact tractions the interior stress field may be found by a superposition. We have already found the stress field for the full sliding shear traction (5.5), and the stress caused by the corrective shear traction, $q^*(x)$, can be expressed as the negative of equations (5.5), after replacing the contact half-width, a, with the half-width of the stick zone, c. This includes the arguments of all the functions occurring, u_i and v_i. For example the arguments of the function $u_2(x,y,a,b)$, used to describe the stress field caused by the full sliding shear traction, will be replaced, such that it reads $u_2(x,y,c,b)$, for the stress field caused by the corrective shear traction.

When looking at fully sliding contacts we have already addressed the additional parameter introduced into our elastic limit considerations due to the fact that, in contrast to the stress caused by the normal load, the stress due to the tangential loading scales with the coefficient of friction, f. Here, we now have a third term which does not

only scale with f, but also with the extent of the stick zone c. Thus, the maximum normal load which can be sustained before the first material point reaches the onset of plasticity, will now depend not only on f, but also the ratio Q/P. Figure 5.3 shows the limit load identified for two different ratios of tangential to normal loading, $Q/P = 0.1$ and 0.4, where for each we vary the coefficient of friction between the lowest possible value (for which the given load causes full sliding) and $f = 1$. Figure 5.3 shows that for a given external loading, the material in the neighbourhood of the contact will be less likely to reach the onset of plasticity if there is less friction along the contact interface.

5.1.3 Differential Bulk Tension

In addition to the shear load, the contacting bodies may be subject to a differential bulk tension $\sigma_0 = \sigma_1 - \sigma_2$, as shown in Figure 2.5(a). We have seen in Figure 2.6(a) that the application of a shear force causes shear tractions of similar sign at both contact edges. Consequently, the slip displacements will also be of the same sign at both edges. If, simultaneously, the contacting bodies are subject to a differential bulk tension this will increase the shear traction at one edge and decrease it at the other, as described in Section 2.4.2. The bulk tension is said to be moderate if the sign of the shear traction, at both edges, is still determined by the shear force, and consequently we find slip displacements in the same direction at both edges. The bulk tension will then cause the slip zone to increase at one edge and decrease at the other, changing not only its position by a shift, e, but also its extent c. The stick zone half-width is then no longer given by equation (5.6). Instead we have to solve for the extent as well as the shift of the stick zone simultaneously. The two coupled equations are given by (Vázquez et al., 2010)

$$\frac{Q}{fP} = 1 - \frac{c^2\left(\arccos\left(\frac{b-e}{c}\right) + \arccos\left(\frac{b+e}{c}\right)\right) - b\sqrt{c^2-(b-e)^2} - b\sqrt{c^2-(b+e)^2}}{2\left(a^2\arccos\left(\frac{b}{a}\right) - b\sqrt{a^2-b^2}\right)}\,, \tag{5.8}$$

and

$$\frac{\pi AR\sigma_0}{4f} = \sqrt{c^2-(b-e)^2} - \sqrt{c^2-(b+e)^2} \\ - (b-e)\arccos\left(\frac{b-e}{c}\right) + (b+e)\arccos\left(\frac{b+e}{c}\right) . \tag{5.9}$$

We see from equation (5.9) that a central stick zone, i.e. $e = 0$, requires $\sigma_0 = 0$, and that for this case equation (5.8) reduces to equation (5.6), as expected. The shift due to a moderate differential bulk tension is limited by $e < a - c$, at which the slip zone at one end has vanished. We may also note from equations (5.8) and (5.9) that a real solution requires $e < c - b$, such that the slip zone at either edge can never penetrate into the flat region (unless we reach full sliding).

The resulting shear traction may be represented by superposition of a full sliding term and a corrective term, i.e. the Jäger-Ciavarella theorem still applies. However, the corrective shear traction will now act over the asymmetric interval $[-c+e \quad c+e]$. It is given by (Vázquez et al., 2010)

$$q^*(x) = \frac{-c\,f}{\pi AR}\left(\sqrt{1-\left(\frac{x-e}{c}\right)^2}\left(\arccos\left(\frac{b-e}{c}\right)+\arccos\left(\frac{b+e}{c}\right)\right)\right. \\ \left. + \frac{b-x}{c}F(x-e,c,b-e) + \frac{b+x}{c}F(x-e,c,-b-e)\right) , \tag{5.10}$$

which naturally reduces to equation (5.7) for $e \to 0$. Explicit expressions for the interior stress field in real algebra are then given by

$$\sigma^t_{xx}(x,y) = \frac{f}{\pi AR}\left[\pm(2u_1 - y\,v_6)\left(\arccos\left(\frac{b-e}{c}\right)+\arccos\left(\frac{b+e}{c}\right)\right)\right. \\ - 2(x-b)v_2 + 2(x+b)(v_3+\pi) - 3y(u_2-u_3) \\ \left. -y\,v_7\left(\sqrt{c^2-(b-e)^2}-\sqrt{c^2-(b+e)^2}\right)\right] , \\ \sigma^t_{yy}(x,y) = \frac{y\,f}{\pi AR}\left[\pm v_6\left(\arccos\left(\frac{b-e}{c}\right)+\arccos\left(\frac{b+e}{c}\right)\right)+u_2-u_3\right. \\ \left. +v_7\left(\sqrt{c^2-(b-e)^2}-\sqrt{c^2-(b+e)^2}\right)\right] , \tag{5.11}$$

$$\sigma_{xy}^{t}(x,y) = \frac{f}{\pi AR}\left[\mp 2(v_1 + y\,u_6)\left(\arccos\left(\frac{b-e}{c}\right) + \arccos\left(\frac{b+e}{c}\right)\right)\right.$$
$$-(x-b)u_2 + (x+b)u_3 + 2y(v_2 - v_3 - \pi)$$
$$\left.-y\,v_7\left(\sqrt{c^2-(b-e)^2} - \sqrt{c^2-(b+e)^2}\right)\right]\,,$$

where the functions $u_1(x-e,y,c)$, $v_1(x-e,y,c)$, $u_2(x-e,y,c,b-e)$, $v_2(x-e,y,c,b-e)$, $u_3(x-e,y,c,b+e)$, $v_3(x-e,y,c,b+e)$, $u_6(x-e,y,c)$, $v_6(x-e,y,c)$, $u_7(x-e,y,c)$ and $v_7(x-e,y,c)$ are given in Appendix A.4, and for brevity their arguments have been dropped in equations (5.11). The upper sign in equations (5.11) corresponds to the case $x \leq 0$, and the lower sign to $x > 0$. The necessary steps in the derivation of equations (5.11) are given in Appendix A.3. For a half-plane which is in contact with a flat and rounded punch and loaded with normal load, P, shear load, Q, and where there is a bulk tension applied to the half-plane such that $\sigma_0 = \sigma_1$, we find the total stress field in the half-plane by superposition of equations (5.2), (5.5) and (5.11) as well as a stress $\sigma_{xx}(x,y) = \sigma_0/2$, resulting from the $\Lambda = \sigma_0/4$ in equation (2.68) (Vázquez et al., 2012) and the bulk stress σ_1 applied to the half plane.

The additional load will now introduce an additional factor into our consideration of the elastic limit load. Equivalent results to those shown in Figure 5.1(b) will now depend not only on the coefficient of friction, f, and the shear load, Q, but also the differential bulk tension, σ_0. Figure 5.4 shows elastic limit curves for a specific combination of $Q/P = \sigma_0/p_0 = 0.3$ and different coefficients of friction. As for the partial slip case, a reduction of the coefficient of friction tends to reduce the severity of the subsurface stress field.

5.1.4 Conclusion

In this section we have looked in detail at the subsurface stress field in the neighbourhood of a contact. With the determination of the elastic limit load we have established a measure to check the justification of a linear elastic material description, which is generally assumed throughout this work. As part of this we have shown that, for a

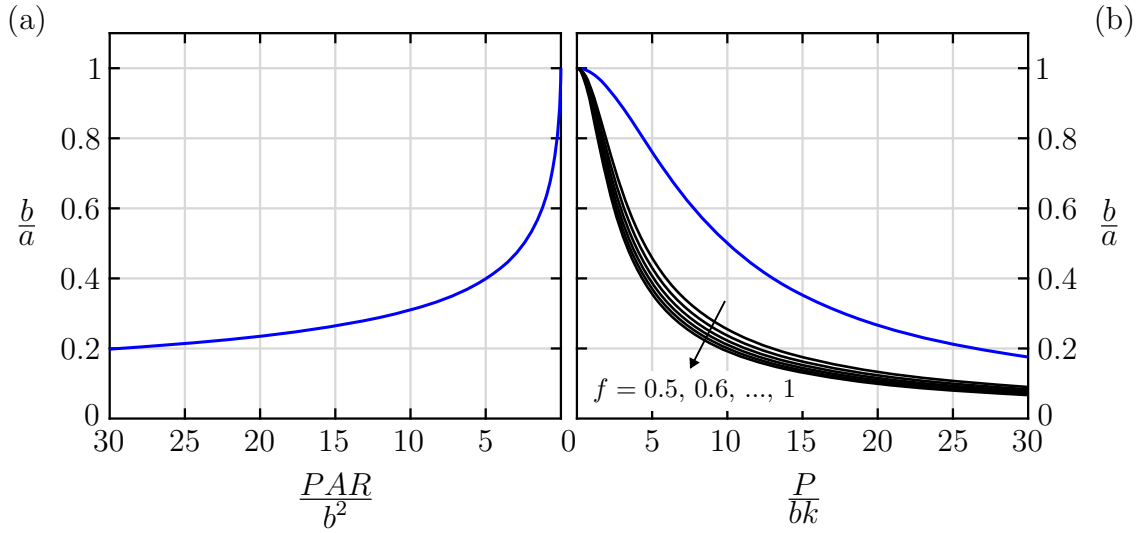


Figure 5.4: (a) Contact law and (b) elastic limit for a flat and rounded contact subject to a combination of normal and shear force as well as a differential bulk tension with $Q/P = \sigma_0/p_0 = 0.3$ and a varying coefficient of friction, f (plane strain with $\nu = 0.3$).

given loading, a reduction of the contact surface friction will reduce the severity of the stress field, i.e. ensuring that the material is further away from reaching the onset of plasticity.

It should be noted that in this section the phrase 'severity of the subsurface stress field' simply refers to the maximum von Mises yield parameter $\sqrt{J}$. However, the limiting dissipative or damage mechanism might not be plasticity but for example the nucleation of contact cracks. For the consideration of those cracks it might not be the maximum von Mises yield parameter characterising the severity of the subsurface stress field, but for example the maximum tensile stress parallel to the contact interface.

5.2 Comparison between Muskhelishvili Potential and Williams' Solution for Contacts

In Section 2.6 we introduced the derivation of the subsurface stress field, caused by a distribution of surface tractions, via the Muskhelishvili complex potential. An asymptotic representation of the interior stress field in the neighbourhood of the contact edge can be derived via a series expansion of the finite expression of the Muskhelishvili potential as described in Chapter 3. The stress field around the tip of a semi-infinite

crack may be derived via the Williams' solution as described in Section 3.2. We note that the tip of a semi-infinite crack looks like the edge of an incomplete contact if sufficiently 'zoomed-in'. This provides us with two methods to derive the stress field in the neighbourhood of an incomplete contact edge. Here, we want to compare the two methods (with respect to their applicability) in terms of an asymptotic contact analysis.

5.2.1 Series Expansion of the Muskhelishvili Potential

As a starting point we use the two-dimensional equivalent of a Hertzian contact, specifically the contact between a half-plane and a cylinder shown in Figure 2.1(a). The normal pressure, $p(x)$ resulting from a normal load, P, pressing the bodies into contact, is given by equation (2.28). The Muskhelishvili potential is obtained by inserting expression (2.28) into equation (2.63) and for the lower half-plane ($y < 0$) it leads (Hills et al., 1993)

$$\phi^n(z) = \frac{ip_0}{2\pi a}\int_{-a}^{a}\frac{\sqrt{a^2-x^2}}{x-z}\mathrm{d}x = \begin{cases} \frac{ip_0}{2a}\left(z+\sqrt{z^2-a^2}\right) & x<0 \\ \frac{iP}{\pi a^2}\left(z-\sqrt{z^2-a^2}\right) & x\geq 0 \end{cases}. \tag{5.12}$$

A shift of the origin to the edge of the contact, with $w = z + a$, in the negative branch of the potential function (5.12) yields

$$\begin{aligned} \phi^n(w) &= i\frac{p_0}{2a}\left(w-a+\sqrt{w^2-2wa}\right) \\ &= i\frac{p_0}{2a}\left(w-a+\sqrt{2a}\sqrt{-w}\sqrt{1-w/2a}\right) \\ &\simeq i\frac{p_0}{2a}\left(w-a+\sqrt{2a}\sqrt{-w}\left(1-\frac{w}{4a}+\frac{w^2}{32a^2}-...\right)\right), \end{aligned} \tag{5.13}$$

where we used a binomial expansion for one of the square-root terms. An asymptotic description of the subsurface stress field is then derived by dropping all but the dominant terms. Care must be taken as specific terms may affect specific stress components only. The leading term of the series expansion of the potential function (5.13) is the

constant term $-ip_0/2$. However, it is easily verified by inserting this term into equations (2.70), that it leads a null stress field. Taking into account only the following square-root bounded term $ip_0/\sqrt{2a}\sqrt{-w} = iL_I/2\sqrt{-w}$ leads to the desired square-root bounded normal traction along the contact interface.

We may generally assume that every potential function, derived for a finite description of an arbitrary contact problem, may be represented by a series expansion around the contact edge such that

$$\phi^n(w) = \frac{i}{2}\sum_k A_k(-w)^k. \tag{5.14}$$

Analogously, a series representation of a general potential function associated with a surface shear traction may take the form

$$\phi^t(w) = \frac{1}{2}\sum_k A_k(-w)^k. \tag{5.15}$$

As discussed in Section 2.6, each individual of the terms in (5.14) and (5.15) will lead to a stress field fulfilling the equilibrium conditions (2.3), and the corresponding strain field fulfils the compatibility conditions (2.4).

We may separate the factor $(-w)^k$, occurring in equations (5.14) and (5.15), into its real and imaginary parts, leading to

$$(-w)^k = r^k\left[\cos\left(k(\theta+\pi)\right) + i\sin\left(k(\theta+\pi)\right)\right] \ , \tag{5.16}$$

where $r = \sqrt{s^2+y^2}$ is the distance to the contact edge and θ is the angle to the contact interface as defined in Figure 5.5. It is easily verified that for $\partial(-w)^k/\partial z$, we simply have to replace k by $k-1$ in equation (5.16), and multiply the resulting expression by $-k$. Substituting a single term of equations (5.14) and (5.15), in its separated form (5.16), into equations (2.70) or (2.71) leads to explicit expressions for the subsurface stress field in real algebra. The polar components of the stress field resulting from a

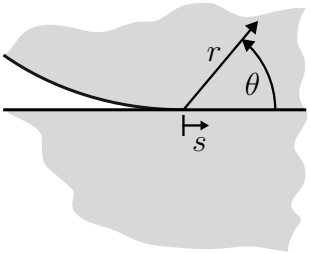


Figure 5.5: Asymptotic or semi-infinite representation of incomplete contact.

single-term normal traction are given by

$$\begin{aligned}
\sigma^n_{rr}(r,\theta) &= \frac{1}{2}A_k r^k \left[-(k-2)\sin\left(k(\theta+\pi)\right) + k\sin\left((k+2)(\theta+\pi)\right)\right] \\
\sigma^n_{\theta\theta}(r,\theta) &= \frac{1}{2}A_k r^k \left[(k+2)\sin\left(k(\theta+\pi)\right) - k\sin\left((k+2)(\theta+\pi)\right)\right] \\
\sigma^n_{r\theta}(r,\theta) &= A_k r^k k\sin(\theta)\sin\left((k+1)(\theta+\pi)\right) \ ,
\end{aligned} \tag{5.17}$$

and for the tangential problem we obtain

$$\begin{aligned}
\sigma^t_{rr}(r,\theta) &= \frac{1}{2}A_k r^k \left[-(k-2)\cos\left(k(\theta+\pi)\right) + (k+2)\cos\left((k+2)(\theta+\pi)\right)\right] \\
\sigma^t_{\theta\theta}(r,\theta) &= -A_k r^k (k+2)\sin(\theta)\sin\left((k+1)(\theta+\pi)\right) \\
\sigma^t_{r\theta}(r,\theta) &= \frac{1}{2}A_k r^k \left[k\sin\left(k(\theta+\pi)\right) - (k+2)\sin\left((k+2)(\theta+\pi)\right)\right] \ .
\end{aligned} \tag{5.18}$$

Along the surface of the lower half-plane, with $\theta = -\pi$, 0, as well as perpendicular to the surface ($\theta = -\pi/2$) the stress reduces to

$$\begin{aligned}
\frac{1}{Ar^k}\begin{bmatrix}\sigma^n_{rr}(r,\theta)\\ \sigma^n_{\theta\theta}(r,\theta)\\ \sigma^n_{r\theta}(r,\theta)\end{bmatrix} &= \begin{bmatrix}0\\0\\0\end{bmatrix}_{\theta=-\pi} = \begin{bmatrix}-(k-1)\sin\left(\frac{k\pi}{2}\right)\\ (k+1)\sin\left(\frac{k\pi}{2}\right)\\ -k\cos\left(\frac{k\pi}{2}\right)\end{bmatrix}_{\theta=-\frac{\pi}{2}} \\
&= \begin{bmatrix}\sin(k\pi)\\ \sin(k\pi)\\ 0\end{bmatrix}_{\theta=0} \left(= \begin{bmatrix}\sin(2k\pi)\\ \sin(2k\pi)\\ 0\end{bmatrix}_{\theta=\pi} \right) \ ,
\end{aligned} \tag{5.19}$$

for the normal problem and

$$\frac{1}{Ar^k}\begin{bmatrix}\sigma^t_{rr}(r,\theta)\\ \sigma^t_{\theta\theta}(r,\theta)\\ \sigma^t_{r\theta}(r,\theta)\end{bmatrix} = \begin{bmatrix}2\\0\\0\end{bmatrix}_{\theta=-\pi} = \begin{bmatrix}-k\cos\left(\frac{k\pi}{2}\right)\\ (k+2)\cos\left(\frac{k\pi}{2}\right)\\ -(k+1)\sin\left(\frac{k\pi}{2}\right)\end{bmatrix}_{\theta=-\frac{\pi}{2}}$$
$$= \begin{bmatrix}2\cos(k\pi)\\0\\-\sin(k\pi)\end{bmatrix}_{\theta=0} \left(= \begin{bmatrix}2\cos(2k\pi)\\0\\-\sin(2k\pi)\end{bmatrix}_{\theta=\pi}\right), \tag{5.20}$$

for the stresses caused by the application of a surface shear traction. We immediately see that, for both the normal as well as the shear problem, the free surface at $\theta = -\pi$ is traction-free, independent of the value k. Along the line $\theta = 0$ we find the shear traction to vanish for the normal problem while the normal traction vanishes for the tangential problem, as expected. We have obtained the stress field (5.17) and (5.18) via equations (2.70) and (2.71), which strictly are only valid in the lower half-plane. However, evaluation of (5.17) and (5.18) along the line $\theta = \pi$, shows that only solutions characterised by $k = ..., -\frac{1}{2}, 0, \frac{1}{2}, 1, \frac{3}{2}, 2, \frac{5}{2}, ...$ lead to vanishing tractions. If we restrict ourselves to these solutions and consider the direct stresses caused by a normal traction (eq. (5.17)), we find the 'half-integer' values ($k = ..., -\frac{1}{2}, \frac{1}{2}, \frac{3}{2}, \frac{5}{2}, ...$) lead to a stress field symmetric in θ, while the integer solutions ($k = ..., -1, 0, 1, 2, ...$) lead to an anti-symmetric stress field. For the direct stresses caused by a shear traction (eq. (5.18)) the opposite is true.

Expressions (5.19) show that the stress field (5.17) fulfils condition (2.16), i.e. the direct stress components caused by a surface normal traction, and oriented normal and tangential to the surface ($\theta = -\pi, 0$) are compressive and equal. Additionally, we note that not only a constant term, as derived in equation (5.13), leads a vanishing surface traction, but indeed every term associated with an integer value of k shares this property. This not only applies to the normal but also the tangential problem as we may see from equations (5.20).

5.2.2 Williams' Solution for Arbitrary Terms

We start our consideration of the Williams' solution from equations (3.26) and (3.27), giving the symmetric and anti-symmetric stress field for arbitrary eigenvalues $\lambda_{I,II}$. For the derivation of these equations we used the substitutions (3.24, 3.25) for the symmetric, and equivalent expressions for the anti-symmetric solution. These expressions form one set of possible solutions for the requirement that the free surfaces at $\theta = \pm\alpha$ are traction free, and the determination of the constants A_1 and A_3 (or A_2 and A_4 for the anti-symmetric case). However, they are trivial in the sense that for $\alpha = \pi$, the integer eigenvalues, solving (3.22) and (3.23), give rise to a null stress field, i.e. $A_1 = A_3 = 0$. Here, for the specific geometry of an incomplete contact ($\alpha = \pi$), it seems a more meaningful choice to replace equations (3.24) and (3.25) by

$$A_1 = A_I \left[(\lambda_I - 1)\sin\left((\lambda_I - 1)\,\alpha\right) + (\lambda_I + 1)\cos\left((\lambda_I - 1)\,\alpha\right)\right] \tag{5.21}$$

$$A_3 = -A_I \left[(\lambda_I + 1)\sin\left((\lambda_I + 1)\,\alpha\right) + (\lambda_I + 1)\cos\left((\lambda_I + 1)\,\alpha\right)\right] \ , \tag{5.22}$$

which still satisfy both conditions (3.20) for all λ_I (where λ_I is a solution of equation (3.22)). These expressions lead to $A_1 \neq 0$ and $A_3 \neq 0$ also for the integer values of λ_I. Corresponding replacements for the anti-symmetric case are given by

$$A_2 = A_{II} \left[(\lambda_{II} - 1)\cos\left((\lambda_{II} - 1)\,\alpha\right) + (\lambda_{II} + 1)\sin\left((\lambda_{II} - 1)\,\alpha\right)\right] \tag{5.23}$$

$$A_4 = -A_{II} \left[(\lambda_{II} + 1)\cos\left((\lambda_{II} + 1)\,\alpha\right) + (\lambda_{II} + 1)\sin\left((\lambda_{II} + 1)\,\alpha\right)\right] \ , \tag{5.24}$$

and for every λ_{II} which is a solution to (3.23), it can be shown that these expressions fulfil both conditions (3.21).

We make substitutions (5.21, 5.22) together with $A_2 = A_4 = 0$ and $\alpha = \pi$, in equations

(3.19), to derive the symmetric stress field given by

$$\begin{aligned}
\sigma_{rr}^{I} &= A_I \lambda_I (\lambda_I + 1) r^{\lambda-1} \begin{bmatrix} [(\lambda_I - 1)\sin(\lambda_I \pi) + (\lambda_I + 1)\cos(\lambda_I \pi)]\cos((\lambda_I + 1)\theta) \\ -[(\lambda_I - 3)\sin(\lambda_I \pi) + (\lambda_I - 3)\cos(\lambda_I \pi)]\cos((\lambda_I - 1)\theta) \end{bmatrix} \\
\sigma_{\theta\theta}^{I} &= A_I \lambda_I (\lambda_I + 1) r^{\lambda-1} \begin{bmatrix} -[(\lambda_I - 1)\sin(\lambda_I \pi) + (\lambda_I + 1)\cos(\lambda_I \pi)]\cos((\lambda_I + 1)\theta) \\ +[(\lambda_I + 1)\sin(\lambda_I \pi) + (\lambda_I + 1)\cos(\lambda_I \pi)]\cos((\lambda_I - 1)\theta) \end{bmatrix} \\
\sigma_{r\theta}^{I} &= A_I \lambda_I (\lambda_I + 1) r^{\lambda-1} \begin{bmatrix} -[(\lambda_I - 1)\sin(\lambda_I \pi) + (\lambda_I + 1)\cos(\lambda_I \pi)]\sin((\lambda_I + 1)\theta) \\ +[(\lambda_I - 1)\sin(\lambda_I \pi) + (\lambda_I - 1)\cos(\lambda_I \pi)]\sin((\lambda_I - 1)\theta) \end{bmatrix}
\end{aligned} \tag{5.25}$$

For the anti-symmetric stress field we use $\alpha = \pi$ and $A_1 = A_3 = 0$ together with substitutions (5.23, 5.24) in equations (3.19) to obtain

$$\begin{aligned}
\sigma_{rr}^{II} &= A_{II} \lambda_{II} (\lambda_{II} + 1) r^{\lambda-1} \begin{bmatrix} [(\lambda_{II} - 1)\cos(\lambda_{II} \pi) + (\lambda_{II} + 1)\sin(\lambda_{II} \pi)]\sin((\lambda_{II} + 1)\theta) \\ -[(\lambda_{II} - 3)\cos(\lambda_{II} \pi) + (\lambda_{II} - 3)\sin(\lambda_{II} \pi)]\sin((\lambda_{II} - 1)\theta) \end{bmatrix} \\
\sigma_{\theta\theta}^{II} &= A_{II} \lambda_{II} (\lambda_{II} + 1) r^{\lambda-1} \begin{bmatrix} -[(\lambda_{II} - 1)\cos(\lambda_{II} \pi) + (\lambda_{II} + 1)\sin(\lambda_{II} \pi)]\sin((\lambda_{II} + 1)\theta) \\ +[(\lambda_{II} + 1)\cos(\lambda_{II} \pi) + (\lambda_{II} + 1)\sin(\lambda_{II} \pi)]\sin((\lambda_{II} - 1)\theta) \end{bmatrix} \\
\sigma_{r\theta}^{II} &= A_{II} \lambda_{II} (\lambda_{II} + 1) r^{\lambda-1} \begin{bmatrix} [(\lambda_{II} - 1)\cos(\lambda_{II} \pi) + (\lambda_{II} + 1)\sin(\lambda_{II} \pi)]\cos((\lambda_{II} + 1)\theta) \\ -[(\lambda_{II} - 1)\cos(\lambda_{II} \pi) + (\lambda_{II} - 1)\sin(\lambda_{II} \pi)]\cos((\lambda_{II} - 1)\theta) \end{bmatrix}
\end{aligned} \tag{5.26}$$

For the symmetric stress field (eqs. (5.25)), evaluation at the angles $\theta = -\pi$ and $\theta = 0$

leads to

$$\frac{1}{A_I\lambda_I\left(\lambda_I+1\right)r^{\lambda_I-1}}\begin{bmatrix}\sigma^I_{rr}(r,\theta)\\ \sigma^I_{\theta\theta}(r,\theta)\\ \sigma^I_{r\theta}(r,\theta)\end{bmatrix} = -\begin{bmatrix}\sin\left(2\pi\lambda_I\right)+2\cos\left(2\pi\lambda_I\right)+2\\ \sin\left(2\pi\lambda_I\right)\\ \sin\left(2\pi\lambda_I\right)\end{bmatrix}_{\theta=-\pi}$$
$$= \begin{bmatrix}2\sin\left(\lambda_I\pi\right)+4\cos\left(\lambda_I\pi\right)\\ 2\sin\left(\lambda_I\pi\right)\\ 0\end{bmatrix}_{\theta=0}. \tag{5.27}$$

Evaluation of equations (5.26) at the same angles leads to

$$\frac{1}{A_{II}\lambda_{II}\left(\lambda_{II}+1\right)r^{\lambda_{II}-1}}\begin{bmatrix}\sigma^{II}_{rr}(r,\theta)\\ \sigma^{II}_{\theta\theta}(r,\theta)\\ \sigma^{II}_{r\theta}(r,\theta)\end{bmatrix} = \begin{bmatrix}2\sin\left(\pi\lambda_{II}\right)\left(2\sin\left(\pi\lambda_{II}\right)+\cos\left(\pi\lambda_{II}\right)\right)\\ \sin\left(2\pi\lambda_I\right)\\ \sin\left(2\pi\lambda_I\right)\end{bmatrix}_{\theta=-\pi}$$
$$= \begin{bmatrix}0\\ 0\\ 2\sin\left(\lambda_I\pi\right)\end{bmatrix}_{\theta=0}. \tag{5.28}$$

Equations (5.27) and (5.28) show that the symmetric stress field never includes a shear traction along $\theta = 0$, while the anti-symmetric stress field does not come with a normal traction along the same line. It seems natural, then, to associate the symmetric stress field with mode I or normal loading and the anti-symmetric stress field with mode II or tangential loading. However, the integer values of $\lambda_{I,II}$ do not cause any contact tractions along $\theta = 0$. This is similar to what we have found for integer values k in the consideration of single-term Muskhelishvili potentials, but for integer values of $\lambda_{I,II}$ it also makes it less obvious then to make the connection between the symmetric stress field and normal loading or the anti-symmetric stress field and tangential loading.

Condition (2.16), required for normal loading, may be expressed here as $\sigma_{rr}(r,\theta) = \sigma_{\theta\theta}(r,\theta)$ for $\theta = -\pi$ and $\theta = 0$. Indeed, we note from equation (5.27) that the symmetric stress field only fulfils condition (2.16) for half-integer values of λ_I, i.e. $\lambda_I =$

..., $\frac{1}{2}$, $\frac{3}{2}$, $\frac{5}{2}$, $\frac{7}{2}$, ... , while the anti-symmetric stress field fulfils condition (2.16) for $\lambda_{II} \in \mathbb{Z}$.

5.2.3 Comparison and Conclusion

Generally, for half-integer values of $\lambda_{I,II}$, and by comparison of equations (5.17, 5.18) for the stress field derived from the Muskhelishvili complex potential and (5.25, 5.26) for those stresses derived from the Williams' solution, we find

$$\begin{bmatrix} \sigma^n_{rr}(r,\theta) \\ \sigma^n_{\theta\theta}(r,\theta) \\ \sigma^n_{r\theta}(r,\theta) \end{bmatrix} = \begin{bmatrix} \sigma^I_{rr}(r,\theta) \\ \sigma^I_{\theta\theta}(r,\theta) \\ \sigma^I_{r\theta}(r,\theta) \end{bmatrix} \quad \text{and} \quad \begin{bmatrix} \sigma^t_{rr}(r,\theta) \\ \sigma^t_{\theta\theta}(r,\theta) \\ \sigma^t_{r\theta}(r,\theta) \end{bmatrix} = \begin{bmatrix} \sigma^{II}_{rr}(r,\theta) \\ \sigma^{II}_{\theta\theta}(r,\theta) \\ \sigma^{II}_{r\theta}(r,\theta) \end{bmatrix} \qquad \forall \lambda_{I,II} + \frac{1}{2} \in \mathbb{Z} \,, \tag{5.29}$$

where we have made the substitutions $k = \lambda_I - 1$ and $A_k = -2A_I\lambda_I(\lambda_I + 1)$ in equation (5.17) as well as $k = \lambda_{II} - 1$ and $A_k = 2A_{II}\lambda_{II}(\lambda_{II} + 1)$ in equation (5.18).
For integer values $\lambda_{I,II}$ equation (5.29) does not hold and we recall from Section 5.2.1, that normal loading leads to an anti-symmetric stress field around the contact edge for integer values of k. Indeed, it is easily verified that for $\lambda_{I,II} \in \mathbb{Z}$

$$\begin{bmatrix} \sigma^n_{rr}(r,\theta) \\ \sigma^n_{\theta\theta}(r,\theta) \\ \sigma^n_{r\theta}(r,\theta) \end{bmatrix} = \begin{bmatrix} \sigma^{II}_{rr}(r,\theta) \\ \sigma^{II}_{\theta\theta}(r,\theta) \\ \sigma^{II}_{r\theta}(r,\theta) \end{bmatrix} \quad \text{and} \quad \begin{bmatrix} \sigma^t_{rr}(r,\theta) \\ \sigma^t_{\theta\theta}(r,\theta) \\ \sigma^t_{r\theta}(r,\theta) \end{bmatrix} = \begin{bmatrix} \sigma^{I}_{rr}(r,\theta) \\ \sigma^{I}_{\theta\theta}(r,\theta) \\ \sigma^{I}_{r\theta}(r,\theta) \end{bmatrix} \qquad \forall \lambda_{I,II} \in \mathbb{Z} \,, \tag{5.30}$$

where we made the substitutions $k = \lambda_{II} - 1$ and $A_k = -2A_{II}\lambda_{II}(\lambda_{II} + 1)$ in equation (5.17) as well as $k = \lambda_I - 1$ and $A_k = -2A_I\lambda_I(\lambda_I + 1)$ in equation (5.18).
We compared the stress fields derived via the Muskhelishvili complex potential and those derived from the Williams' solution. It has been shown that the Williams' solution, with $\alpha = \pi$, may be used to derive the asymptotic stress field for incomplete contact problems. As expected, the symmetric stress field may be associated with the

contacting bodies loaded normal to the interface. However, this only holds for solutions characterised by half-integer eigenvalues, i.e. $\lambda_I = ..., \frac{1}{2}, \frac{3}{2}, \frac{5}{2}, \frac{7}{2}, ...$. For integer values, $\lambda_{I,II} \in \mathbb{Z}$, it is the anti-symmetric stress field which may be associated with normal contact loading. For tangential loading of incomplete contact problems the opposite relation, between symmetric and anti-symmetric stress fields derived via the Williams' solution and the contact problem, holds.

The objection may be raised that it is meaningless, for integer values of $\lambda_{I,II}$ or k, to make such a connection between symmetric or anti-symmetric stress fields and normal or tangential loading, as the integer values do not give rise to any contact *tractions* at all, but as we have seen in equation (5.13) they do arise as part of a contact problem.

5.3 Half-plane contacts subject to remote tension

In the current chapter, we have looked in detail at the subsurface stress field and, based on a finite contact description, derived a graphical approach to determine if the assumption of linear elasticity is justified. Based on an asymptotic consideration of the contact edge, we have identified the terms which need to be considered for the asymptotic description of the subsurface stress field. The stress field, here, may be derived from the Muskhelishvili complex potential or the Williams' solution.

The following paper compares the subsurface stress field for an asymptotic description of incomplete contacts loaded with a tangential force, Q, or a differential bulk tension σ_0. It is shown that, even though the asymptotic form of the contact shear traction may be similar for both cases, the subsurface stress field in the neighbourhood of the contact edge differs in the component parallel to the contact edge, which is critical for the propagation of fretting fatigue cracks.

Half-plane contacts subject to remote tension

N. Cwiekala[a,1], D. A. Hills[a]

[a]*Department of Engineering Science, University of Oxford, Parks Road, OX1 3PJ Oxford, United Kingdom*

Abstract

The state of stress present in an elastic half-plane contact problem, where one or both bodies is subject to remote tension has been investigated, both for conditions of full stick and partial slip. The state of stress present near the contact edges is studied for different loading scenarios in an asymptotic form. This is of practical relevance to the study of contacts experiencing fretting fatigue, and enables the environment in which cracks nucleate to be specified.

Keywords:
bulk tension, half-plane contact, partial slip, fretting fatigue, asymptotes

1 Introduction

Fretting and fretting fatigue are important problems arising in gas turbines and a wide range of mechanical assemblies - in fact wherever there are components in notionally stationary contact but where the applied loads or vibration cause very small amounts of differential motion between the contacting surfaces and which consequently may cause damage promoting cracks to nucleate. Of course it is the presence of shear tractions, $q(x)$, which induces slip and, for elastically similar bodies, this may have two origins - the application of a shear force Q (Fig. 5.6(a)) or the presence of a differential tension $\sigma_0 = \sigma_1 - \sigma_2$ acting parallel with the surface, Figure 5.6(b). Unless the tensions parallel with the surface are equal in each body shear tractions will certainly develop, and which may add to or subtract from the effect of shear force, depending on which edge of the contact is being studied.

In some problems, such as the standard laboratory test for fretting fatigue strength, Figure 5.6(d), it is very easy to identify the bulk tension present in each component (here, none in the pad and simply the tension in the dogbone specimen) but in many cases it is very much harder to isolate the effect of tension, such as in the fanblade dovetail arrangement in Figure 5.6(e), with the blade being subject to a centrifugal and vibrational load, F_{c} and F_{v}, respectively. Andresen et al. (2020) have recently looked at means of identifying the effective bulk

[1]Corresponding author
Email address: nils.cwiekala@eng.ox.ac.uk (N. Cwiekala)

tension present, and there is little doubt that it has a first order effect on both the magnitude of slip and also on the state of stress present in each body. Here we concentrate on the latter, and look at contacts represented by half-planes being a typical approximation for incomplete contacts (Andresen et al., 2020). These contacts typically arise when bodies with convex surfaces are pressed against each other by a normal load, and show the characteristic that the contact area increases in size with an increasing normal load. In the standard laboratory test (Fig. 5.6(d)) as well as the fanblade dovetail arrangement (Fig. 5.6(e)) we find this type of contact. We study the differences for the application of a differential tension compared to the application of a shear load, and how the combination of σ_1 and σ_2 affects the state of stress around the edge of the contact.

We start from the assumption that the coefficient of friction, f, is sufficiently high to prevent all slip at the interface. If all slip is inhibited, the problem is equivalent to an infinite plane with two semi-infinite cracks indented into it from $\pm\infty$ to $\pm a$, Figure 5.6(b), and we start from the case where the upper half-plane ($y > 0$) is free of remote loads while the lower is subjected to remote tension $\sigma_1 = \sigma_0$. It has been shown (Hills et al., 2011), using the Mossakovskii-Barber approach, that the traction arising along the interface, $y = 0$ and $|x| < a$, is given by

$$\sigma_{xy}(x,0) = q(x) = -\frac{\sigma_0}{4}\frac{x}{\sqrt{a^2 - x^2}} \tag{5.31}$$

and the state of stress in the body is therefore the sum of the state of stress induced in a half-plane by tractions (5.31) applied along the surface together with, for the lower body only, uniform remote tension σ_0.

2 State of stress present

If we consider only the half-plane $y < 0$ and exert tractions (5.31) over the surface the Muskhelishvili complex potential is given by (Muskhelishvili, 1964),

$$\begin{aligned}\phi(z) &= \frac{1}{2\pi}\int_{\text{Contact}} \frac{\sigma_{xy}(x,0)}{x-z}dx \\ &= -\frac{\sigma_0}{8\pi}\int_{-a}^{a} \frac{x\left(a^2-x^2\right)^{-\frac{1}{2}}}{x-z}dx \\ &= \begin{cases} -\frac{\sigma_0}{8}\left(1+\frac{z}{\sqrt{z^2-a^2}}\right) & x<0 \\ -\frac{\sigma_0}{8}\left(1-\frac{z}{\sqrt{z^2-a^2}}\right) & x\geq 0 \end{cases},\end{aligned} \tag{5.32}$$

where $z = x + iy$, $i = \sqrt{-1}$.
The same result is obtained without the need for any integration by making use of the relationship (Vázquez et al., 2012)

$$\phi(z) = -\frac{\Lambda}{2} - \frac{1}{2}i\sigma_{xy}^{ad}(z) \tag{5.33}$$

where σ_{xy}^{ad} is the shear stress inside the stick zone. The quantity Λ is a load case dependent parameter defined by the singular integral equation

$$\frac{1}{\pi}\int_{\text{Contact}} \frac{\sigma_{xy}(\xi,0)}{x-\xi}d\xi = \Lambda \tag{5.34}$$

$\forall\, x \in$ stick zone, and where the Cauchy

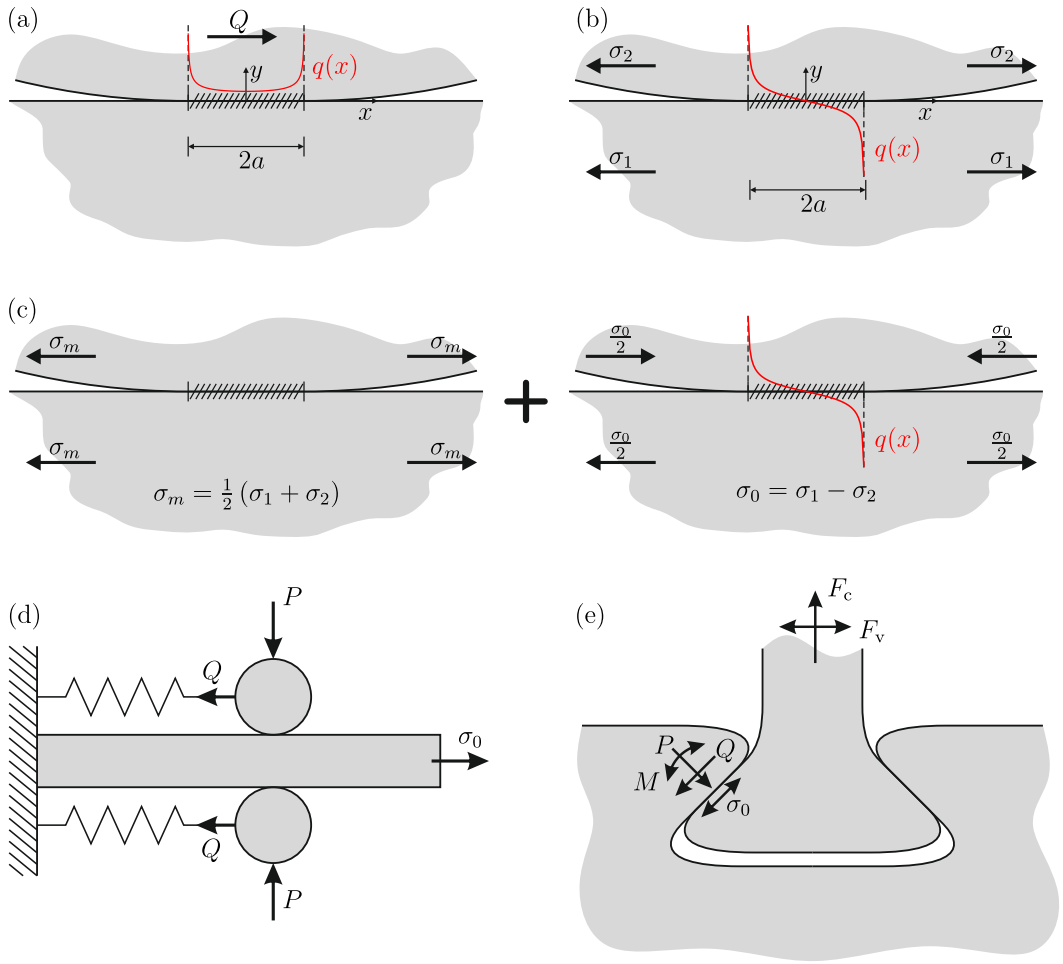


Figure 5.6: Shear traction in different contact settings; (a) shear traction $q(x)$ resulting from tangential load Q, (b) shear traction resulting from differential bulk tension σ_0, both for incomplete, fully stuck contacts, (c) representation of arbitrary combinations of σ_1 and σ_2 by superposition of equal tension (magnitude and sign) in both bodies and equal (magnitude) but opposite tension, (d) Schematic representation of standard fretting fatigue test (Nowell et al., 1988), (e) Schematic representation of dovetail arrangement subject to external loads (Andresen et al., 2019).

principal value must be considered. For a differential bulk tension σ_0, $\Lambda = \sigma_0/4$, independent of the individual components σ_1 and σ_2. Here, relation (5.33) simply provides a different route to the same result obtained in equation (5.32), but later on when looking at contacts in partial slip with a comparatively complicated form of the resulting shear traction it provides a much simpler way of obtaining the complex potential compared to the evaluation of the integral over the contact interface. Independent of how the complex potential $\phi(z)$ is obtained, the corresponding state of stress is given by (Vázquez et al., 2013)

$$\begin{aligned}\sigma_{xx}(x,y) &= 2\left(\phi(z)+\phi(\bar{z})\right) \\ &\quad + iy\left(\frac{\partial}{\partial z}\phi(z) - \frac{\partial}{\partial \bar{z}}\phi(\bar{z})\right), \\ \sigma_{yy}(x,y) &= -iy\left(\frac{\partial}{\partial z}\phi(z) - \frac{\partial}{\partial \bar{z}}\phi(\bar{z})\right),\end{aligned} \tag{5.35}$$

$$\sigma_{xy}(x,y) = i\left(\phi(z) - \phi(\bar{z})\right) - y\left(\frac{\partial}{\partial z}\phi(z) + \frac{\partial}{\partial \bar{z}}\phi(\bar{z})\right).$$

Explicit expressions in real algebra can be found by separation of real and imaginary part of the potential function to $\phi(z) = u(x,y) + i\,v(x,y)$ (Vázquez et al., 2013). The components of stress are then obtained from the complex potential (5.32) and in the half-plane $y < 0$ are

$$\begin{aligned}
\sigma_{xx}(x,y) &= -\frac{\sigma_0}{2} \mp \frac{\sigma_0}{8}\frac{4c_1x^2\left(x^2+y^2+\sqrt{c_1}\right)}{c_1x\sqrt{2c_1\left(\sqrt{c_1}+c_2\right)}} \\
&\mp \frac{\sigma_0}{8}\frac{a^2\left(-c_1c_2+c_2^3-4x^2\left(c_1+y^2\left(\sqrt{c_1}+c_2\right)\right)\right)}{c_1x\sqrt{2c_1\left(\sqrt{c_1}+c_2\right)}}, \\
\sigma_{yy}(x,y) &= \pm\frac{\sigma_0}{16}\frac{a^2}{c_1^2}\frac{1}{x}\sqrt{2c_1\left(\sqrt{c_1}+c_2\right)} \\
&\quad\times\left(c_2\left(c_2-\sqrt{c_1}\right)-4x^2y^2\right), \quad (5.36) \\
\sigma_{xy}(x,y) &= \mp\frac{\sigma_0}{4}\frac{yc_1\left(x^2+y^2-\sqrt{c_1}\right)}{c_1\sqrt{2c_1\left(\sqrt{c_1}+c_2\right)}} \\
&\quad\mp\frac{\sigma_0}{4}\frac{ya^2c_2\left(\sqrt{c_1}+2c_2\right)}{c_1\sqrt{2c_1\left(\sqrt{c_1}+c_2\right)}},
\end{aligned}$$

with $c_1 = ((a+x)^2+y^2)((a-x)^2+y^2)$ and $c_2 = x^2-y^2-a^2$. The main steps of the derivation are given in Appendix A. With the upper signs corresponding to $x < 0$ and the lower signs to $x \geq 0$, expressions (5.36) describe the state of stress induced by tractions (5.31). We will refer to this solution as the *contact* stress field in what follows. For the full stress field in the lower body ($y < 0$) we need to superimpose the remote bulk tension σ_1. We note that if we want to express the remotely applied stresses σ_1 and σ_2 by their difference σ_0 and their mean $\sigma_m = \frac{1}{2}(\sigma_1+\sigma_2)$, then the *contact* stress field depends on the difference only, while the full stress field depends on the mean as well.

The full subsurface stress field for the load case represented by Figure 5.6(b) with $\sigma_1 = \sigma_0$ and $\sigma_2 = 0$ is shown in Figure 5.7. As expected σ_{yy} and σ_{xy} vanish if we move sufficiently far away from the contact. The stress parallel to the surface σ_{xx} tends to σ_0 remote from the contact and to $\sigma_0/2 = \sigma_m$ within the contact.

If the tension in each body is the same in magnitude and sign the presence of the interface has no effect and there is a uniform σ_{xx} stress everywhere. Note that, generally if a tension σ_1 is present in one body and σ_2 in the other body (Fig. 5.6(b)) the solution may be found by superposition of these two solutions viz. a mean stress of $\frac{1}{2}(\sigma_1+\sigma_2)$, everywhere, together with stresses of $\pm\frac{1}{2}(\sigma_1-\sigma_2)$ applied to the two bonded half-planes (Fig. 5.6(c)).

The special case of tension applied to one body and an equal compression in the other, both of magnitude $\sigma_0/2$ ($\sigma_m = 0$), may also be treated by the relations found and the non-vanishing components of the full stress field along the surface ($y \to 0$) are shown in Figure 5.8. We see that for the case of equal and opposite loading, as $\sigma_m = 0$, the stress parallel to the surface vanishes along the interface, i.e. on $y = 0$, $|x| < a$. At points remote to the contact it tends to $\sigma_1 = \sigma_0/2$.

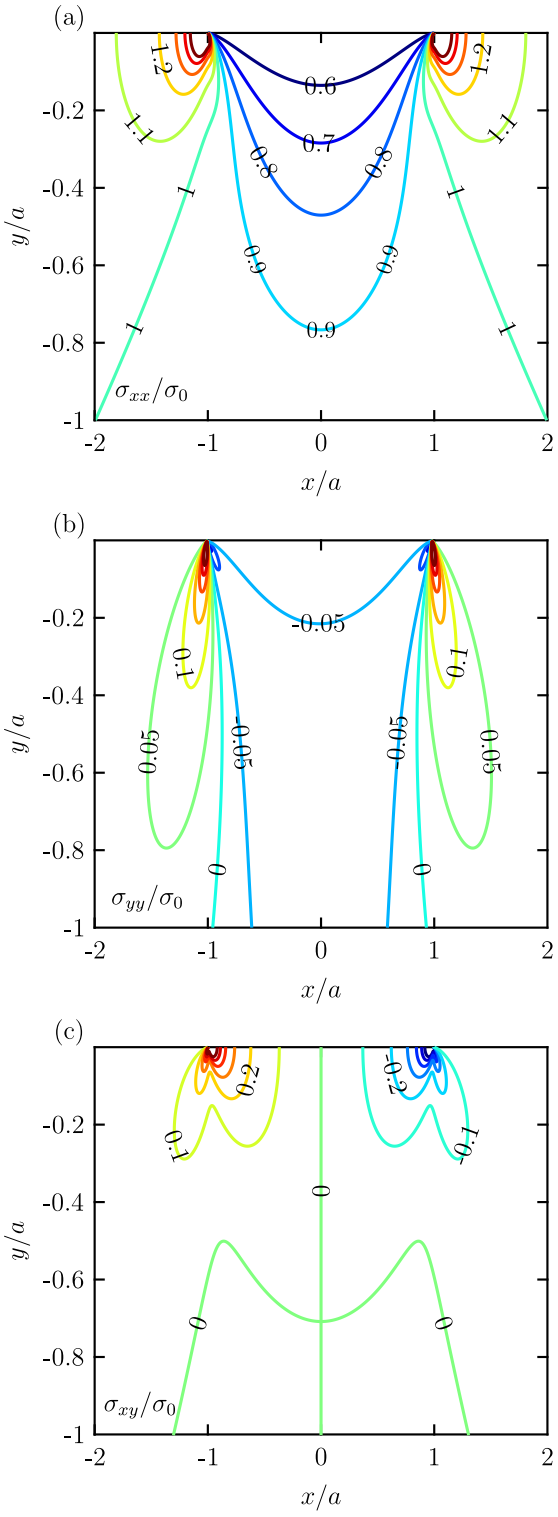


Figure 5.7: Subsurface stress field for fully stuck contact with differential bulk tension, σ_0, applied to the lower body only; (a) normalised stress σ_{xx}/σ_0, (b) normalised stress σ_{yy}/σ_0, (c) normalised stress σ_{xy}/σ_0

Furthermore, we use Figure 5.8 to compare the stress along the contact interface, $y = 0$, to the stress present for the application of a shear load as shown in Figure 5.6(a). We used different normalisations for both load cases to ensure that the shear stress shows the same severity in the singularity when approaching the edge of the contact (Fig. 5.8(b)). We note from Figure 5.8(a) that even though the stress parallel to the surface does vanish for both load cases inside the contact, $|x| < a$, and the resulting singularity in the stress parallel to the interface is similar for both load cases, the stress will differ remote from the contact.

2.1 Asymptotic solutions

In the previous section we examined the state of stress in adhered half-plane contacts subject to remote tension, in detail, and compared some results with the stress state induced by the application of a shear force. One reason for doing this was as a prelude to understanding how the different forms of load affect the behaviour of contact edges, under adhered conditions and in the presence of slip. So far we considered the stress inside the contact region, $|x| < a$ and remote from the contact, $|x| \gg a$, but not the singularity at the edge of the contact.

We have had some success in representing the state of stress near an incomplete contact edge in asymptotic form. The contact pressure is locally square root bounded but, if the contact is adhered the shear tractions induced are, as we have just seen, square root singular in form. One important aspect of the asymptotic representation which has

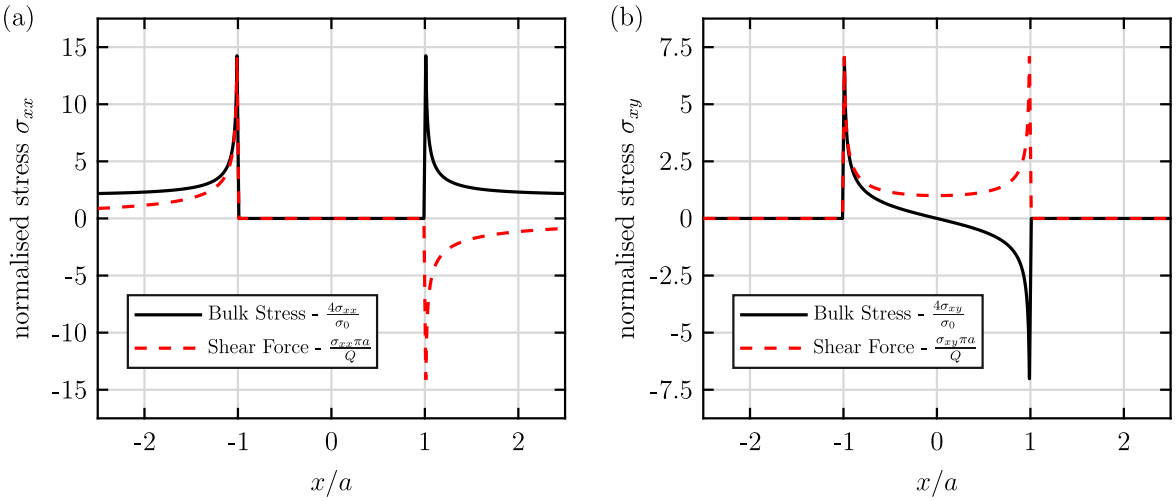


Figure 5.8: Non-vanishing components of stress along the contact interface for the application of equal and opposite remote stress $\sigma_0/2$ (solid) and the application of a shear load (dashed) corresponding to Figure 5.6(a); (a) normalised stress σ_{xx}, (b) normalised stress σ_{xy}.

been missing is an understanding of the asymptotic field when the shear tractions are excited by bulk tension; information is lost when only the surface tractions induced are considered, and here we derive the local solution when tension induced, first under conditions of full stick. If we move the origin to the left hand edge by the transformation $s = x + a$ equation (5.31) becomes

$$\begin{aligned}\sigma_{xy}(s) &= -\frac{\sigma_0}{4}\frac{s-a}{\sqrt{2as-s^2}} \\ &\approx K_{II}\frac{1}{\sqrt{s}} \quad \text{for } s \ll a\end{aligned} \tag{5.37}$$

where $K_{II} = \sigma_0\sqrt{a}/4\sqrt{2}$ (Hills et al., 2016). To find the stress parallel to the surface or the subsurface stress field in an asymptotic description we can proceed in one of two ways. Either we start from the negative branch of the finite potential function (5.32) and again apply a shift of the origin with $w = z + a$ followed by a binomial expansion as well as the corresponding simplifications to the derivation of the asymptotic contact shear traction which yields

$$\begin{aligned}\phi(w) &= -\frac{\sigma_0}{8}\left(1 + \frac{w-a}{\sqrt{w^2-2aw}}\right) \\ &\approx \frac{K_{II}}{2}\frac{1}{\sqrt{-w}} - \frac{\sigma_0}{8} \quad \text{for abs}(w) \ll a.\end{aligned} \tag{5.38}$$

The different steps with corresponding assumptions for the derivation of equation (5.37) and (5.38) are given in Appendix B. For the potential function the same result can be obtained by using the asymptotic expression of the shear traction (5.37) in equation (5.33) and choosing the appropriate branch of the function $\pm\sqrt{w}$

$$\begin{aligned}\phi(w) &= -\frac{\Lambda}{2} - \frac{1}{2}i\sigma_{xy}^{ad}(w) \\ &= -\frac{\sigma_0}{8} + \frac{1}{2}iK_{II}\frac{1}{\sqrt{w}} \\ &= \frac{K_{II}}{2}\frac{1}{\sqrt{-w}} - \frac{\sigma_0}{8}.\end{aligned} \tag{5.39}$$

The resulting potential function differs from the potential function for the application of a shear load by the constant term $-\sigma_0/8$ only. From equation (5.35) we can immediately see that a constant real term in the potential function will contribute to the stress parallel to the surface only and we find $\sigma_{xx} = -\sigma_0/2$. The complete stress field includes the superposition of the remotely applied tension σ_1 (for the lower body). In the neighbourhood of the contact edge the stress parallel to the surface then differs by $-\sigma_0/2 + \sigma_1 = \sigma_m$ for the two load cases. All other components of stress are unchanged, i.e. the shear force induced K_{II} solution and the bulk stress induced K_{II} solution are the same. We note that for the special case of an equal tension and compression in the two bodies, i.e. $\sigma_m = 0$ as considered before, the whole stress field in the neighbourhood of the contact edge will be the same as when the stress is excited by a shear force.

3 Effect of slip

We now want to investigate the effect of a differential bulk stress on the subsurface stress field by allowing for local slip at the contact interface of an incomplete contact. We consider, here, a finite Hertzian contact with the known contact pressure

$$\begin{aligned}\sigma_{yy}(x,0) &= p(x) \\ &= -\frac{p_0}{a}\sqrt{a^2-x^2} \quad \text{for } |x| \le a,\end{aligned} \tag{5.40}$$

where p_0 is the peak contact pressure. After the application of the normal load we apply a bulk tension σ_0 to the lower body. Symmetric zones of slip will establish themselves at the edges of the contact. The resulting shear traction was found by Nowell and Hills (1987), Ciavarella and Macina (2003) and Moore et al. (2018). Moore et al. (2018) use distributed dislocations along the contact interface to account for relative displacements of the two bodies and found the side condition for the determination of the stick-zone half-width, c, generally, as

$$-\int_c^a \frac{p(s)ds}{\sqrt{s^2-c^2}} = \frac{\pi\sigma_0}{8f}, \tag{5.41}$$

where f is the coefficient of friction, as before. If the Hertzian pressure distribution (5.40) is substituted into (5.41), Ciavarella and Macina's (2003) implicit expression

$$K(k) - E(k) = \frac{\pi\sigma_0}{8fp_0} \tag{5.42}$$

is recovered, where $K(k)$ and $E(k)$ represent the complete elliptic integral of the first and second kind respectively with k being the *elliptic modulus*[2]. In equation (5.42) and the following

$$k = \sqrt{1-\left(\frac{c}{a}\right)^2}. \tag{5.43}$$

The shear traction inside the stick zone is then given by (Ciavarella and Macina,

[2]Note that there are different conventions for the notation of elliptic integrals in terms of the elliptic modulus k or the parameter $m = k^2$.

2003),

$$\sigma_{xy}(x,0) = \frac{2}{\pi}\frac{fp_0 x}{a^2}\sqrt{c^2-x^2}\left[\Pi\left(n,k\right) - K\left(k\right)\right] \quad \text{for} \quad |x| < c \qquad (5.44)$$

where $\Pi\left(n,k\right)$ represents the complete elliptic integral of the third kind, k is again given by equation (5.43) and

$$n = \sqrt{\frac{a^2-c^2}{a^2-x^2}} \qquad (5.45)$$

is the so called *characteristic* of Π. The complex potential is then simply derived by substitution of equation (5.44) in expression (5.33), where $\Lambda = \sigma/4$ as for the fully stuck case, giving

$$\phi(z) = -\frac{\sigma_0}{8} \pm \frac{2}{\pi}\frac{fp_0 z}{a^2}\sqrt{z^2-c^2}\left[\Pi\left(n,k\right) - K\left(k\right)\right]. \qquad (5.46)$$

Again, the upper sign in equation (5.46) corresponds to $x < 0$ and the lower sign to $x > 0$. For the case of an equal tension and compression of magnitude $\sigma_0/2$ in the two bodies, the non-vanishing stresses along the contact interface are shown in Figure 5.9. As for the fully stuck case the stress parallel to the surface vanishes inside the stick region and has its maximum at the edge of and exterior to the contact.

We compare the results for the case of an equal tension and compression in the two bodies to the stresses resulting from two different load cases, one where we apply a shear load to the upper body and a second where we have a mix of differential bulk tension and shear load such that one edge of the contact (the right hand end) remains stuck. In each case the slip zone, $d = a - c$, at the left hand edge is of the same size and the slip displacement is in the same direction. Figure 5.9(b) shows the resulting shear stress which is similar for all three cases within the slip zone at the left hand edge. We are now able to compare the maximum stress parallel to the surface for the three load cases under consideration, as this is most important in terms of fretting damage. For the assumed slip zone size of $d/a = 0.25$ we see that the stress will be higher if the relative displacement is caused by a bulk tension compared to a shear force (Fig. 5.9(a)). Figure 5.10 shows the stress parallel to the interface at the edge of the contact not only for the slip-zone size of $d/a = 0.25$, considered before, but for a continuous slip zone size.

For a slip zone size of $d/a \to 1$ and the application of a shear load we recover the result of $\sigma_{xx}/fp_0 = 2$ for a sliding contact (Hills and Nowell, 1994) while the consideration of the contact stress field alone with the application of a differential bulk tension leads to $\sigma_{xx}/fp_0 = 4/\pi$ as shown by Ciavarella and Macina (2003). Of course the results for the full stress field are somewhat arbitrary, in the case of differential bulk tension and mixed loading, since the same slip zone size could originate from different combinations of applied bulk tension and compression in the two bodies, but the stress inside the stick zone will vanish only, for the special case of equal remote tension and compression.

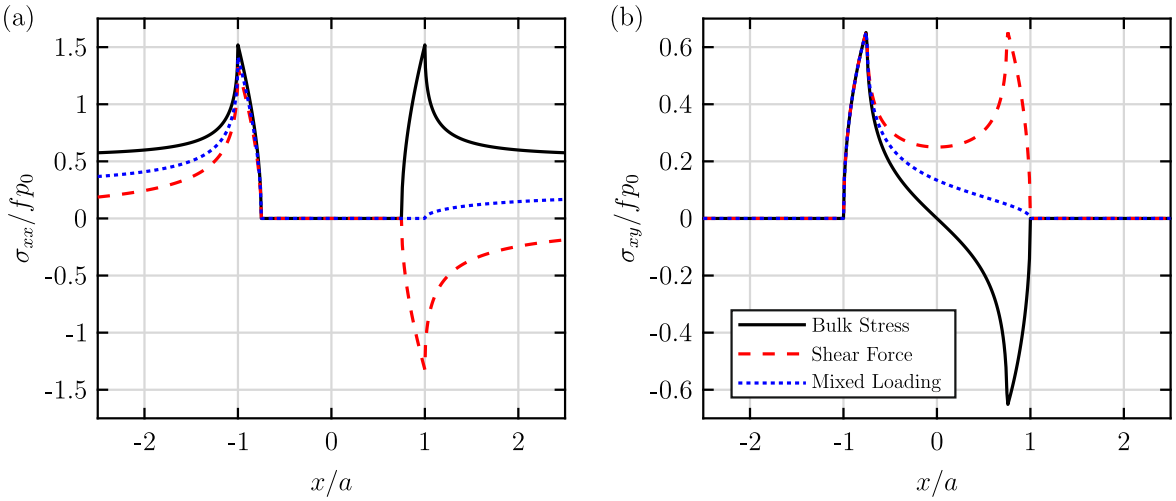


Figure 5.9: Non-vanishing components of stress along the contact interface for the application of equal and opposite remote stress σ_0 (solid), the application of a shear load (dashed) and mixed loading such that the contact is fully stuck at the leading edge (dotted) and a slip zone side of $d/a = 0.25$ at the trailing edge; (a) normalised stress σ_{xx}, (b) normalised stress σ_{xy}.

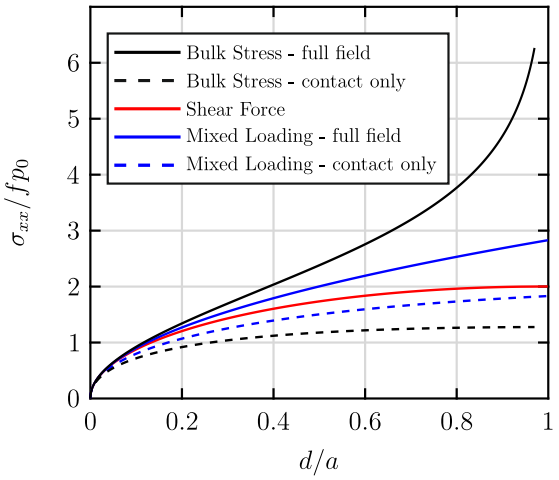


Figure 5.10: Maximum stress parallel to the surface plotted over the slip zone size at the left hand edge of the contact.

We find from Figure 5.10 that the difference in the maximum stress parallel to the surface vanishes for $d \ll a$ and we will look at this in more detail by considering the asymptotic description.

3.1 Asymptotic solutions

Again, the subsurface stress-field might be described in an asymptotic formulation. It is worth noting that by representing each of the elliptical integrals in equation (5.42) by the first two terms of the corresponding series expansion around the edge of the contact, i.e. $c/a = 1$, we recover the known asymptotic expression (Dini and Hills, 2004)

$$\begin{aligned} \frac{\pi\sigma_0}{8fp_0} &= K(k) - E(k) = \frac{\pi}{2}\left(1 - \frac{c}{a}\right) \\ \Leftrightarrow \frac{\sigma_0 a}{4fp_0} &= a - c \\ \Leftrightarrow \frac{2K_{II}}{fL_I} &= d \end{aligned} \tag{5.47}$$

for the slip zone d where the shear traction results from a tangential force and the asymptotic multiplier L_I is defined as

$$L_I = \lim_{s\to 0} \frac{p(s)}{\sqrt{s}}. \tag{5.48}$$

Furthermore, for an asymptotic representation of the bilateral contact tractions with $q(s) = K_{II}/\sqrt{s}$ (cf. equation (5.37)) and $p(s) = L_I\sqrt{s}$, Moore et al. (2018)

derive the dislocation density to[3]

$$B_x(s) = -\frac{\kappa+1}{2\mu} f L_I \sqrt{d-s}, \quad (5.49)$$

where μ is the shear modulus of the contacting bodies and $\kappa = 3-4\nu$ is Kolosov's constant for plane strain with ν being Poisson's ratio. The resulting shear traction inside the stick zone is then given by

$$\begin{aligned}\sigma_{xy}(x,0) &= \frac{2\mu}{\pi(\kappa+1)} \frac{1}{\sqrt{s}} \int_0^d \frac{\sqrt{\xi} B_x(\xi)}{\xi - s} d\xi \\ &= f L_I \left(\sqrt{s} - \sqrt{s-d} \right) \end{aligned} \quad (5.50)$$

for $d \leq s$, and is therefore similar to the case where the shear traction originates from a tangential force Q (Dini and Hills, 2004). The *contact* stress field in the neighbourhood of the contact edge in terms of the complex potential is obtained by substitution of equation (5.50) into equation (5.33) leading to

$$\begin{aligned}\phi(w) &= -\frac{\Lambda}{2} - \frac{1}{2} i \sigma_{xy}^{ad}(w) \\ &= -\frac{\sigma_0}{8} - \frac{1}{2} i f L_I \left(\sqrt{w} - \sqrt{w-d} \right) \\ &= -\frac{f L_I}{2} \left(\sqrt{-w} - \sqrt{-w+d} \right) - \frac{\sigma_0}{8}. \end{aligned} \quad (5.51)$$

This complex potential for the asymptotic representation of the *contact* stress field is basically recovering the results obtained by Dini et al. (2005) but in a much more straightforward manner. We see that it differs from the stress field, associated with the application of a shear load, by a constant stress $\sigma_{xx} = -\sigma_0/2$ parallel to the surface, as it does for the fully stuck case (provided that the slip zones d are of equal size).

The full stress field for the lower body is then obtained by superposition of the remotely applied stress σ_1 and following the same arguments as for the fully stuck case we see that the full stress field in the asymptotic representation differs by the constant term $\sigma_{xx} = \sigma_m$ to the stress field associated with the application of a shear load and consequently they match for the special case of equal tension and compression in the two bodies (with $\sigma_m = 0$). Figure 5.11 shows the normalised xx-component, σ_{xx}/fp_0, of the finite full stress field around the left slip zone in the lower body for the application of an equal tension, $\sigma_1 = \sigma_0/2$, and compression, $\sigma_2 = -\sigma_0/2$ (solid lines) obtained from the finite potential (5.46). The shown stress field is characteristic for a relative slip zone size $d/a = 0.1$ ($\sigma_0/fp_0 = 0.41$ from equation (5.42)). The dashed lines represent the percentage mismatch $100\left(\sigma_{xx}^{\text{finite}} - \sigma_{xx}^{\text{asympt.}}\right)/\sigma_{xx}^{\text{finite}}$ between the finite and the asymptotic description of the stress field. It is shown that the agreement is within 10 % for a depth down to $0.8\,d$ and generally the error decreases when approaching the slip region at the contact interface.

4 Conclusion

The state of stress in an incomplete contact pair induced by differential remote tensions has been explored for the cases of infinite friction (no slip) and finite friction, and for the cases of contacts

[3] Note that equation (29) in the original publication (Moore et al., 2018) is a factor of -2 wrong.

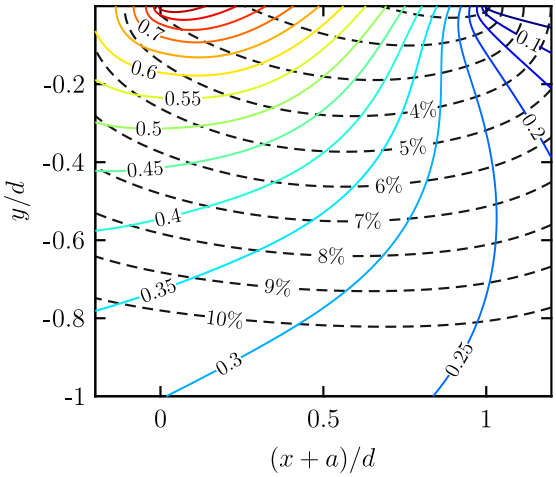


Figure 5.11: Normalised xx-component, σ_{xx}/fp_0, of the finite full stress field (solid lines) and percentage mismatch to the asymptotic stress field (dashed lines) for $d/a = 0.1$.

of finite size, such as shown in Figure 5.6(a) and (b), as well as an asymptotic description of the contact edge. The differences between the state of stress induced, generally, and with particular attention to the near edge, have been investigated. It is found that, to within the accuracy of a first order description of the contact edge there is no difference in the local components σ_{yy} and σ_{xy}. The stress acting parallel with the free surface, and which is responsible for the early propagation of any crack which may form, differs by the mean value of applied bulk tensions $\sigma_m = \frac{1}{2}(\sigma_1 + \sigma_2)$. The only scenario where the local stress parallel to the surface is similar regardless whether the local shear tractions originate from a shear force or a differential bulk tension, is the special case of an equal tension and compression of the two bodies, i.e. $\sigma_m = 0$. Furthermore, the state of stress close to the contact edge depends on the mean value of applied bulk tensions, σ_m, so that a comparison of the stress field in which cracks nucleate in the fanblade dovetail arrangement (Fig. 5.6(e)) and in the standard laboratory test (Fig. 5.6(d)) depends not only on σ_0 but also σ_m.

Declaration of conflicting interests

The authors declare that there is no conflict of interest.

Funding

The authors disclosed receipt of the following financial support for the research, authorship, and/or publication of this article: This work was supported by Rolls-Royce plc and the Engineering and Physical Sciences Research Council under the Prosperity Partnership Grant 'Cornerstone: Mechanical Engineering Science to Enable Aero Propulsion Futures' [EP/R004951/1].

Appendix A

Vázquez et al. (2013) describe how to derive the stress in terms of the real variables (x,y). In the case considered here the complex potential, $\phi(z)$, is defined by means of the complex function $f(z) = z/\sqrt{z^2 - a^2}$ and we need to find a split into a real and an imaginary part $f(z) = u(x, y) + iv(x, y)$ so that

$$\begin{aligned}\phi(z) &= -\frac{\sigma_0}{8}\left(1 + \frac{z}{\sqrt{z^2 - a^2}}\right) \\ &= -\frac{\sigma_0}{8}\left(1 + f(z)\right) \\ &= -\frac{\sigma_0}{8} - \frac{\sigma_0}{8}u(x, y) - i\frac{\sigma_0}{8}v(x, y).\end{aligned} \tag{5.52}$$

For $f(z) = z/\sqrt{z^2 - a^2}$ we find the corresponding split to (Vázquez et al., 2014)

$$u(x,y) = \frac{x\left(x^2 + y^2 - a^2 + \sqrt{c_1}\right)}{\sqrt{2c_1\sqrt{c_1} + 2c_1c_2}} \tag{5.53}$$

and

$$v(x,y) = -\frac{y\left(x^2 + y^2 + a^2 - \sqrt{c_1}\right)}{\sqrt{2c_1\sqrt{c_1} + 2c_1c_2}}, \tag{5.54}$$

where $c_1 = ((a+x)^2 + y^2)((a-x)^2 + y^2)$ and $c_2 = x^2 - y^2 - a^2$. The derivatives of ϕ are then given to (Vázquez et al., 2013)

$$\frac{\partial}{\partial z}\phi(z) = -\frac{\sigma_0}{8}\left(\frac{\partial}{\partial x}u(x,y) - i\frac{\partial}{\partial y}u(x,y)\right) \tag{5.55}$$

and

$$\frac{\partial}{\partial \bar{z}}\phi(\bar{z}) = -\frac{\sigma_0}{8}\left(\frac{\partial}{\partial x}u(x,y) + i\frac{\partial}{\partial y}u(x,y)\right). \tag{5.56}$$

The derivatives of the real part, $u(x,y)$, with respect to x and y are then given by

$$\frac{\partial}{\partial x}u(x,y) = \frac{a^2}{\sqrt{2}c_1^2}\sqrt{c_1\left(\sqrt{c_1} + c_2\right)} \left(\sqrt{c_1} - 2c_2\right) \tag{5.57}$$

and

$$\frac{\partial}{\partial y}u(x,y) = \frac{1}{2\sqrt{2}}\frac{a^2}{c_1^2 xy}\sqrt{c_1\left(\sqrt{c_1} + c_2\right)} \left(c_2\left(c_2 - \sqrt{c_1}\right) - 4x^2y^2\right). \tag{5.58}$$

Substitution of these relations back into equations (5.35) leads the expressions given by (5.36).

Appendix B

Shifting the origin in equation (5.31) to the left contact edge with $s = x + a$ yields

$$\begin{aligned}\sigma_{xy}(s) &= -\frac{2\sigma_0}{4}\frac{s-a}{\sqrt{2as - s^2}} \\ &= -\frac{\sigma_0}{2}\frac{s-a}{\sqrt{2a}\sqrt{s}}\frac{1}{\sqrt{1 - s/2a}},\end{aligned} \tag{5.59}$$

and after a binomial expansion of the last square root term

$$\begin{aligned}\sigma_{xy}(s) &= -\frac{\sigma_0}{2}\frac{s-a}{\sqrt{2a}\sqrt{s}}\frac{1}{(1 - s/4a + ...)} \\ &\approx \frac{\sigma_0}{2}\sqrt{\frac{a}{2}}\frac{1}{\sqrt{s}} - \frac{\sigma_0}{2\sqrt{2a}}\sqrt{s} \\ &\text{for } \frac{s}{4a} \ll 1.\end{aligned} \tag{5.60}$$

Close to the contact edge, $s \to 0$, the first term, being square root singular, will dominate and we drop the second (square root bounded) term for the asymptotic description to find the result stated in equation (5.37)

$$\sigma_{xy}(s) = \frac{\sigma_0}{2}\sqrt{\frac{a}{2}}\frac{1}{\sqrt{s}} = K_{II}\frac{1}{\sqrt{s}}. \tag{5.61}$$

For the asymptotic description of the subsurface stress field we start from the negative branch of the complex potential function (5.32), again with a shift of the origin via $w = z + a$ to the left contact edge

$$\begin{aligned}\phi(w) &= -\frac{\sigma_0}{8}\left(1 + \frac{w-a}{\sqrt{w^2 - 2aw}}\right) \\ &= -\frac{\sigma_0}{8}\left(1 + \frac{1}{\sqrt{2a}}\frac{1}{\sqrt{-w}}\frac{w-a}{\sqrt{1 - w/2a}}\right).\end{aligned} \tag{5.62}$$

Again we perform a binomial expansion of the last square root term and find

$$\begin{aligned}\phi(w) &= -\frac{\sigma_0}{8}\left(1+\frac{1}{\sqrt{2a}}\frac{1}{\sqrt{-w}}\frac{w-a}{(1-w/4a+...)}\right)\\ &\approx -\frac{\sigma_0}{8}\left(1+\frac{1}{\sqrt{2a}}\frac{1}{\sqrt{-w}}(w-a)\right)\\ &\qquad\text{for}\quad w \ll 4a\\ &= \frac{1}{2}\frac{\sigma_0}{4}\sqrt{\frac{a}{2}}\frac{1}{\sqrt{-w}} - \frac{\sigma_0}{8} + \frac{\sigma_0}{8}\frac{1}{\sqrt{2a}}\sqrt{-w}.\end{aligned} \tag{5.63}$$

Again, dropping the square root bounded term for asymptotic description leads to equation (5.38)

$$\begin{aligned}\phi(w) &= \frac{1}{2}\frac{\sigma_0}{4}\sqrt{\frac{a}{2}}\frac{1}{\sqrt{-w}} - \frac{\sigma_0}{8}\\ &= \frac{K_{II}}{2}\frac{1}{\sqrt{-w}} - \frac{\sigma_0}{8}.\end{aligned} \tag{5.64}$$

Chapter 6

Short Cracks at the Edge of Incomplete Contacts

In this chapter, we examine cracks nucleating in the neighbourhood of incomplete contacts, experiencing the subsurface stress field investigated in the previous chapter. The cracks are required to be short compared to any other length characterising the contact, such as the contact half-width, a, or the size of the slip-zone, d, so that they may experience only the asymptotic subsurface stress field. This chapter's main objective is to derive simple equations or calibrations connecting the asymptotic contact multipliers to the resulting crack tip stress intensity factors.

6.1 Stress intensity factor calibration for short cracks at the edge of semi-infinite contacts

We start with a publication considering cracks in the subsurface stress field of incomplete contacts in a state of partial slip and deriving calibrations between the asymptotic contact multipliers and crack tip stress intensity factors. In the second section, these calibrations will be used to predict a component's life, and the results will be compared with experiments from the literature.

Stress intensity factor calibration for short cracks at the edge of semi-infinite contacts

N. Cwiekala[a,1], D. A. Hills[a]

[a]*Department of Engineering Science, University of Oxford, Parks Road, OX1 3PJ Oxford, United Kingdom*

Abstract

An asymptotic representation of the sub surface stress field allows us to find crack tip stress intensity factors for cracks nucleating from the edge of incomplete contacts. For the asymptotic representation to be valid we require the cracks to be short compared to any other dimension characterising the contact. The general asymptotic formulation allows us to incorporate the results in different contact problems as long as the contact is incomplete. We show that, for the load cases considered, crack closure is not an issue as long as the mode I stress intensity factor is positive.

Keywords:
Short cracks, Fretting fatigue, Asymptotic analyses, Stress intensity factor

1 Introduction

Cracks originating at contacts invariably nucleate at, or very close to, the contact edge. It follows that the environment, in terms of stress, which they experience is governed by the adjacent local surface tractions together with remote tension applied parallel with the free surface. When the contact is either fully stuck, or undergoing frictional sliding, series representations of the tractions may also be used. When the contact is in partial slip the discontinuity in the gradient of the shear traction at the stick-slip interface makes it difficult to use a single series representation but, following the Jäger-Ciavarella theorem (Jäger, 1997; Ciavarella, 1998), we may use a series representation of the sliding traction, at the edge of the contact, and superimpose a series representation of the corrective traction at the stick-slip interface.

If the contacting bodies are made from the same material and we consider, for the time being, the effects of normal loading only, near the edges of the contact the problem domain is itself equivalent to that of a semi-infinite crack under mode I loading. Obviously in a crack the remote loading will be tensile in character whereas here it is compressive, and we assume that small amounts of material are removed from the surfaces of the half-planes exterior to the contact to pre-

[1]Corresponding author
Email address: nils.cwiekala@eng.ox.ac.uk (N. Cwiekala)

vent interpenetration (Fig. 6.1(a)). The permissible forms of solution which may arise may be found by looking at the Williams solution (Williams, 1952) for a wedge of included angle 2π radians. The eigenvalues for this problem are, in the usual notation, $\lambda = 1/2, 1, 3/2, 2...$ and it is useful to think of a general term as being $n/2$, and to separate out the cases when n is odd and when n is even, so that the state of stress may be written in the form

$$\begin{aligned}\sigma_{ij}(r,\theta) = {} & K_I r^{-1/2} k_{ij}^I(\theta) + L_I r^{1/2} l_{ij}^I(\theta) \\ & + M_I r^{3/2} m_{ij}^I(\theta) + ... \\ & + A_I a_{ij}^I(\theta) + B_I r b_{ij}^I(\theta) \\ & + C_I r^2 c_{ij}^I(\theta) + ... \end{aligned} \tag{6.1}$$

where the indices ij may be rr, $\theta\theta$ or $r\theta$, and the coordinate system is shown in Figure 6.1(a). As the terms in the first and second line all have non zero values of tractions on $\theta = 0$, i.e. $k_{\theta\theta}^I(0)$, $l_{\theta\theta}^I(0)$, $m_{\theta\theta}^I(0)$ are all non zero, and hence may be matched to the contact pressure of the bodies along the line of the interface, whereas the terms in the third and fourth line do not give rise to tractions, ie. $a_{\theta\theta}(0) = b_{\theta\theta}(0) = c_{\theta\theta}(0) = 0$.

The first (singular) term, associated with multiplier K_I and eigenvector $k_{ij}^I(\theta)$ in equation (6.1), corresponds to a constant displacement over the contact patch, and this will not arise in problems in which the contact is sufficiently large for adhesive stresses not to be relevant, so that the dominant term in the series is simply square root bounded in form, and we define the scaling on the multiplier, L_I, such that

$$L_I = \lim_{r\to 0} \frac{p(r)}{\sqrt{r}}, \tag{6.2}$$

where $p(r)$ is the contact pressure as shown in Figure 6.1(a).

Turning to the effects of shear, if the bodies are in *sliding* contact then a formulation for two wedges, each of included angle π radians and where there is frictional sliding along the interface would be needed, following the Comninou (1976) method. On the other hand, if the bodies are *adhered*, again we may think of the edge of the contact as the tip of a semi-infinite crack subject to mode II loading. Now, the anti-symmetric form of the Williams solution, specialised to 2π radians, applies. The stress field is then given by an equation similar to (6.1), only this time all subscripts and superscripts, I, are replaced by II, to account for the mode II loading.

$$\begin{aligned}\sigma_{ij}(r,\theta) = {} & K_{II} r^{-1/2} k_{ij}^{II}(\theta) + L_{II} r^{1/2} l_{ij}^{II}(\theta) \\ & + M_{II} r^{3/2} m_{ij}^{II}(\theta) + ... \\ & + A_{II} a_{ij}^{II}(\theta) + B_{II} r b_{ij}^{II}(\theta) \\ & + C_{II} r^2 c_{ij}^{II}(\theta) + ... \end{aligned} \tag{6.3}$$

If the normal load is applied first and then shearing tractions are excited, we expect a square root singular response in the shear traction, $q(r)$, as shown in Figure 6.1(a). Close to the edge of the contact the dominant term of this shear traction is the leading term in equation (6.3), so that we might define a shear

traction stress intensity factor at the contact edge, K_{II}, by

$$K_{II} = \lim_{r \to 0} q(r) \sqrt{r}. \tag{6.4}$$

We wish also to study the case when there is partial slip, and where there is a slip zone at the contact edge of length d. If this arises, for example, as a result of applying the normal load first, holding that constant, and then applying a shear force and/or bulk tension, the slip zone size is related to the multipliers already defined by

$$fd = \frac{2K_{II}}{L_I}, \tag{6.5}$$

where f is the coefficient of friction. If the shear loading is oscillatory and of range ΔK_{II}, then this should replace the numerator on the RHS of this equation, for the steady state response. In this case the dominant term we consider in the series (6.3), is the square root bounded term associated with the multiplier L_{II}. Inside the slip zone, the shear traction is limited by friction with

$$q_s(r) = fL_I\sqrt{r}, \tag{6.6}$$

and following the Jäger-Ciavarella theorem (Jäger, 1997; Ciavarella, 1998), outside the slip zone it may be represented as the superposition of equation (6.6) and a second corrective distribution, $q_c(r)$, of equal magnitude but opposite sign positioned at point $r = d$ (Fig. 6.1(b)).

We wish to find the crack tip stress intensity factors for a crack, short with respect to any finite dimension into which the above solutions might be collocated, and which is located precisely at the contact edge and developing perpendicular to the contact surface, as shown in Figure 6.1(c). It is recognised that, in reality, cracks might initially develop at an angle (in the 'stage 1' sense of Forsyth, 1961), and that they may also nucleate from a point within the slip region but, for now, and to reduce the number of independent variables within the formulation, we will use this simplification. The crack tip stress intensity factors will be defined in the customary way which includes a factor of $\sqrt{2\pi}$ compared with those used for the contact edge quantification, eg.

$$K_I^c = \lim_{s \to 0} \sigma_{yy}(s) \sqrt{2\pi s}, \tag{6.7}$$

where s is the distance measured from the crack tip, and the component of stress is defined in the Cartesian coordinate system shown in Figure 6.1(c).

2 Contact Stress Field

To find the crack tip stress intensity factors, we need to know the state of stress associated with each of the basic traction distributions shown in Figure 6.1(a) and (b). Together with the crack, we introduce an additional (this time Cartesian) coordinate system, having the x-axis aligned with the crack line and the y-axis aligned with the contact interface (Fig. 6.1(c)). The origin of this Cartesian coordinate system will be located at the origin of the contact traction under consideration. For all tractions shown in Figure 6.1(a) and (b), but the corrective

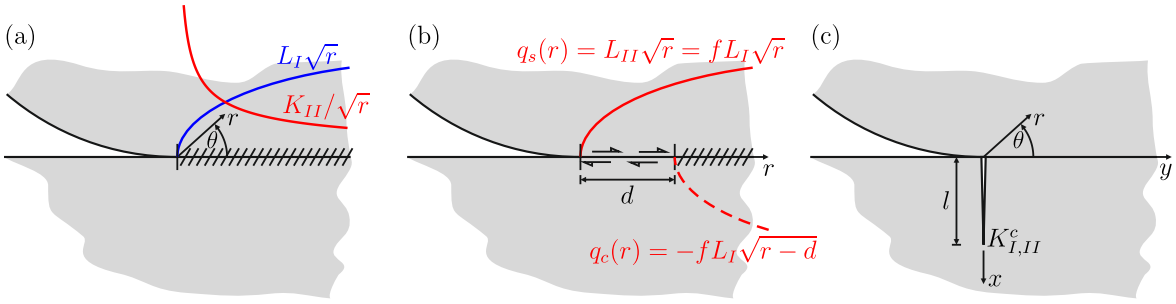


Figure 6.1: Edge of incomplete contact with (a) normal and fully stuck shear traction, (b) partial slip traction as superposition of two square root bounded shear tractions and (c) a crack nucleating from the contact edge.

shear, $q_c(r)$, this will coincide with the origin of the crack, so that the crack is positioned along $y = 0$. When considering the corrective shear traction, on the other hand, the crack will be located at $y = -d$. Consequently, we are particularly interested in what the tractions are along these lines (still in the absence of the crack).

2.1 *Normal traction - square root bounded*

The square root bounded term of the symmetric part of the Williams solution, $L_I r^{1/2} l^I_{ij}(\theta)$, representing the stress field near the contact edge, resulting from normal loading, is associated with the eigenvalue $\lambda = 3/2$. The corresponding eigenvector is

$$l^I_{ij}(\theta) = \frac{1}{4}\begin{bmatrix} -3\cos\left(\frac{\theta}{2}\right) - \cos\left(\frac{5\theta}{2}\right) \\ -5\cos\left(\frac{\theta}{2}\right) + \cos\left(\frac{5\theta}{2}\right) \\ -\sin\left(\frac{\theta}{2}\right) + \sin\left(\frac{5\theta}{2}\right) \end{bmatrix}. \tag{6.8}$$

The stress along a line $y = 0$ is then found from $l^I_{ij}(-\pi/2)$ to be

$$\sigma_{ij}(r, -\pi/2) = \begin{bmatrix} \sigma_{rr} \\ \sigma_{\theta\theta} \\ \sigma_{r\theta} \end{bmatrix} = \frac{L_I}{2\sqrt{2}} r^{1/2} \begin{bmatrix} -1 \\ -3 \\ 1 \end{bmatrix}. \tag{6.9}$$

2.2 *Shear traction - square root bounded*

The stress field induced by a square root bounded shear traction is associated with the eigenvalue $\lambda = 3/2$ and the corresponding eigenvector of the anti-symmetric part of the Williams solution. The stress field and, in particular, the stress along $y = 0$ are given by

$$\begin{aligned}\sigma_{ij}(r, \theta) &= \frac{L_{II}}{4} r^{1/2} \begin{bmatrix} 3\sin\left(\frac{\theta}{2}\right) + 5\sin\left(\frac{5\theta}{2}\right) \\ 5\sin\left(\frac{\theta}{2}\right) - 5\sin\left(\frac{5\theta}{2}\right) \\ -\cos\left(\frac{\theta}{2}\right) + 5\cos\left(\frac{5\theta}{2}\right) \end{bmatrix} \\ &= \frac{L_{II}}{2\sqrt{2}} r^{1/2} \begin{bmatrix} 1 \\ -5 \\ -3 \end{bmatrix}_{\theta=-\frac{\pi}{2}}. \end{aligned} \tag{6.10}$$

For the partial slip case, as shown in Figure 6.1(b), we need, in preparation, to find the tractions along a perpendicular line, located at a distance d from the shear traction distribution. The

substitutions $r = \sqrt{x^2+d^2}$ and $\theta = \arctan(x/d) - \pi$ together with a rotation of the state of stress by an angle $\varphi = -(\pi/2+\theta)$ to align with the x-y-system, yield expressions for the tractions given by

$$\sigma_{yy}(x,-d) = -\frac{L_{II}}{2\sqrt{2}}\sqrt{\sqrt{x^2+d^2}+d} \times \left(5 - \frac{d}{\sqrt{x^2+d^2}}\right) \quad (6.11)$$

and

$$\sigma_{xy}(x,-d) = -\frac{L_{II}}{2\sqrt{2}}\sqrt{\sqrt{x^2+d^2}-d} \times \left(3 + \frac{d}{\sqrt{x^2+d^2}}\right). \quad (6.12)$$

2.3 Shear traction - square root singular

For a square root singular shear traction the corresponding eigenvalue is $\lambda = 1/2$. Again the complete stress field as well as the stress along $y = 0$, are obtained by finding the eigenvector from the anti-symmetric part of the Williams solution as

$$\sigma_{ij}(r,\theta) = \frac{K_{II}}{4\sqrt{r}} \begin{bmatrix} -5\sin\left(\frac{\theta}{2}\right) + 3\sin\left(\frac{3\theta}{2}\right) \\ -3\sin\left(\frac{\theta}{2}\right) - 3\sin\left(\frac{3\theta}{2}\right) \\ \cos\left(\frac{\theta}{2}\right) + 3\cos\left(\frac{3\theta}{2}\right) \end{bmatrix} = \frac{K_{II}}{2\sqrt{2}} r^{-1/2} \begin{bmatrix} 1 \\ 3 \\ -1 \end{bmatrix}_{\theta=-\frac{\pi}{2}}. \quad (6.13)$$

The reader's attention is drawn to the counter-intuitive result, that a square root bounded shear traction, acting away from the origin, causes a state of compression, $\sigma_{\theta\theta} < 0$, along the line $\theta = -\pi/2$ (equation (6.10)). As counter-intuitive as this results is, we can show that it is exactly this result which causes the direct stress to be positive when looking at a partial slip contact. For the partial slip contact the stress, σ_{yy}, caused by the sliding shear traction, $q_s(r)$, along the line $\theta = -\pi/2$, can be found from equation (6.10), and for this specific angle we find $\sigma_{yy} = \sigma_{\theta\theta}$ as well as $r = x$. The stress caused by the corrective shear traction, $q_c(r)$, along the same line is given by equation (6.11), although, as the shear traction itself, it will be opposite in sign. For the partial slip case with $L_{II} = fL_I$, the superposition of both contributions yields

$$\sigma_{yy}(x) = \frac{fL_I}{2\sqrt{2}}\left(\sqrt{\sqrt{x^2+d^2}+d} \times \left(5 - \frac{d}{\sqrt{x^2+d^2}}\right) - 5\sqrt{x}\right), \quad (6.14)$$

which will be positive for every combination of $x, d \geq 0$. Furthermore, we may consider the partial slip shear traction outside the slip zone with

$$q(r) = q_s(r) + q_c(r) = fL_I\left(\sqrt{r} - \sqrt{r-d}\right). \quad (6.15)$$

After substituting $fL_I = 2K_{II}/d$, by making use of equation (6.5), and taking the limit $d \to 0$, we find

$$q(r) = \lim_{d\to 0} 2K_{II}\frac{\sqrt{r}-\sqrt{r-d}}{d} = K_{II}\frac{1}{\sqrt{r}}, \quad (6.16)$$

which is, precisely, the fully stuck shear traction as defined by equation (6.4). Consequently, the superposition of direct stresses (6.14) has to correspond to what we find from the fully stuck solution (equation (6.13)) as well. After similar substitutions with $fL_I = 2K_{II}/d$, we find the stress for the limit $d \to 0$ in equation (6.14) to

$$\begin{aligned}\sigma_{yy}(x) = \lim_{d\to 0} \frac{K_{II}}{\sqrt{2}}\frac{\sqrt{x}}{d}\left(\sqrt{\sqrt{1+\left(\frac{d}{x}\right)^2}+\frac{d}{x}}\right.\\ \left.\times\left(5-\frac{d}{\sqrt{x^2+d^2}}\right)-5\right)\\ = \frac{3}{2\sqrt{2}}K_{II}\frac{1}{\sqrt{x}}. \qquad (6.17)\end{aligned}$$

which is the same result we get from the fully stuck solution (6.13).

3 Formulation

The crack tip stress intensity factors are found by starting with the solution for a dislocation within an elastic half-plane, and then distributing them along the line of the crack so that, when added to the stress already there, they give rise to traction-free crack faces. The stress in the absence of the crack (or the dislocations) is the stress arising from the surface contact loading, found in the previous section, and referred to as $\widetilde{\sigma}_{iy}$ in the following. Note that the dislocations give rise to 'uncoupled' tractions along a line perpendicular to the surface of the interface. In the coordinate set shown in Figure 6.1(c), a climb dislocation of Burgers vector $b_y(\xi, 0)$ induces a traction $\bar{\sigma}_{yy}(x, 0)$ given by

$$\bar{\sigma}_{yy}(x,0) = \frac{2\mu b_y(\xi,0)}{\pi(\kappa+1)}F(x,\xi)$$

with

$$\begin{aligned}F(x,\xi) = \Bigg[&\frac{1}{x-\xi}-\frac{1}{x+\xi}\\ &-\frac{2\xi}{(x+\xi)^2}+\frac{4\xi^2}{(x+\xi)^3}\Bigg],\end{aligned}$$

where μ is the shear modulus of the lower body and $\kappa = 3-4\nu$ is Kolosov's constant for plane strain with ν being Poisson's ratio. A glide dislocation with Burgers vector $b_x(\xi, 0)$ induces a stress

$$\bar{\sigma}_{xy}(x,0) = \frac{2\mu b_x(\xi,0)}{\pi(\kappa+1)}F(x,\xi). \qquad (6.18)$$

We therefore have that the direct traction, $N(x)$ present along the line $y = 0$ is given by the superposition of the stress induced by the surface contact loading, $\widetilde{\sigma}_{yy}(x, 0)$, and the stress associated with the distributed dislocations, $\bar{\sigma}_{yy}(x, 0)$, to

$$\begin{aligned}N(x) = \widetilde{\sigma}_{yy}(x,0)\\ +\frac{2\mu}{\pi(\kappa+1)}\int_0^l F(x,\xi)B_y(\xi)\,d\xi.\end{aligned} \qquad (6.19)$$

Dislocations have been distributed over the interval $[0 \quad l]$, where l is the length of the crack, and the dislocation density $B_y(x) = db_y/dx$. Similarly, the shear traction, $S(x)$, is given by

$$\begin{aligned}S(x) = \widetilde{\sigma}_{xy}(x,0)\\ +\frac{2\mu}{\pi(\kappa+1)}\int_0^l F(x,\xi)B_x(\xi)\,d\xi\end{aligned} \qquad (6.20)$$

where $\widetilde{\sigma}_{xy}(x,0)$ is the stress induced by the surface contact loading, and the dislocation density $B_x(x) = db_x/dx$. The requirement that the crack faces be traction-free is given by

$$N(x) = S(x) = 0 \qquad 0 < x < l. \quad (6.21)$$

These are two uncoupled singular integral equations of the first kind with generalised Cauchy kernels which may be treated in the usual way using the method developed by Erdogan et al. (1973).

As an example we will show the steps needed to identify the crack tip stress intensity factor for a square root bounded normal traction. To identify the mode I stress intensity factor, K_I^c, we replace $\widetilde{\sigma}_{yy}$ in equation (6.19) by the corresponding stress component from equation (6.9) to find

$$\frac{3L_I}{2\sqrt{2}}\sqrt{x} = \frac{2\mu}{\pi(\kappa+1)}\int_0^l F(x,\xi)B_y(\xi)\,d\xi. \quad (6.22)$$

where we note that r aligns with x. In the case of the mode II crack tip stress intensity factor, K_{II}^c, we would need to make the corresponding substitution in equation (6.20), and for finding the crack tip stress intensity factors corresponding to other surface tractions, which might be a square root singular or bounded shear traction, we may use the corresponding stress from equations (6.10) to (6.13), to replace $\widetilde{\sigma}_{ij}$ in equations (6.19) and (6.20).

In equation (6.22) we normalise the integral range with

$$s = 2\frac{\xi}{l} - 1 \qquad \text{and} \quad (6.23)$$

$$t = 2\frac{x}{l} - 1, \quad (6.24)$$

to find

$$\frac{3L_I}{2\sqrt{2}}\sqrt{l}\sqrt{\frac{t+1}{2}} = \frac{2\mu}{\pi(\kappa+1)}\int_{-1}^{1} F(t+1,s+1)B_y(s)\,ds. \quad (6.25)$$

The first step in the numerical solution procedure of this singular integral equation, is then to prescribe the form of the solution, $B_y(s)$. Following the standard assumptions for surface breaking cracks, specified in Hills et al. (1996), we assume the dislocation density to be square root singular at the tip of the crack and square root bounded at its mouth. This allows us to express the dislocation density as

$$B_y(s) = \phi(s)\omega(s), \quad (6.26)$$

where $\phi(s)$ is an unknown but regular function, and $\omega(s)$ is a fundamental function with

$$\omega(s) = \sqrt{\frac{1+s}{1-s}} \quad (6.27)$$

for the prescribed bounded-singular endpoint behaviour. Following the numerical quadrature introduced by Erdogan et al. (1973) we are now able to express the integral equation (6.25) by

$$\frac{3}{2\sqrt{2}}\sqrt{\frac{t_k+1}{2}} = \pi\sum_{i=1}^{N} W_i F(t_k{+}1, s_i{+}1)\hat{\phi}_y(s_i), \quad (6.28)$$

with

$$\hat{\phi}_y = \frac{2\mu}{\pi\,(\kappa+1)}\frac{\phi_y}{L_I\sqrt{l}}. \tag{6.29}$$

The N integration and collocation points, s_i and t_k, as well as the weights, W_i, are given by

$$s_i = \cos\left(\pi\frac{2i-1}{2N+1}\right) \quad i = 1, ..., N, \tag{6.30}$$

$$t_k = \cos\left(\pi\frac{2k}{2N+1}\right) \quad k = 1, ..., N \tag{6.31}$$

and

$$W_i = 2\frac{1+s_i}{2N+1}. \tag{6.32}$$

Equation (6.28), now, forms a system of N equations for the N unknowns $\hat{\phi}_y\,(s_i)$. The crack tip stress intensity factor is then found to (Hills et al., 1996)

$$K_I^c = \sqrt{2\pi}\sqrt{l}\frac{2\mu}{(\kappa+1)}\phi_y(1), \tag{6.33}$$

where the unknown, $\phi_y(1)$, at the crack tip can be found from the solution of equation (6.28), $\phi_y\,(s_i)$, via Krenk's interpolation (Krenk, 1975). Using relation (6.29) we find

$$\frac{K_I^c}{L_I l} = \pi\sqrt{2\pi}\hat{\phi}_j(1), \tag{6.34}$$

where $\hat{\phi}_j(1)$ is the primary output of the analysis, which is independent of the actual crack length, l (cf. equation (6.28)).

4 Calibrations

Using the method described in the previous section the crack tip stress intensity factors caused by a square root bounded contact pressure, a square root bounded shear traction and a square root singular shear traction were first determined for the case of the crack nucleating from the origin of the contact traction. The results are given by

$$\begin{Bmatrix} K_I^c \\ K_{II}^c \end{Bmatrix} = \begin{bmatrix} -1.565\,l & -2.608\,l & 3.628 \\ 0.522\,l & -1.565\,l & -1.209 \end{bmatrix} \begin{Bmatrix} L_I \\ L_{II} \\ K_{II} \end{Bmatrix}, \tag{6.35}$$

where for the square root bounded contact tractions we found convergence for $N = 40$ but for the square root singular shear traction the method required $N = 200$ integration points for the results to converge. Notice that, because the last term in the right hand column vector has dimensions of $[FL^{-3/2}]$, as have both the entries in the left hand column vector, of course, the entries connecting these quantities are dimensionless numbers; that is, the crack tip stress intensity factor is independent of the crack length. It can also be verified by writing down the equivalent equations to (6.22) to (6.34), only this time using the stress caused by a singular shear traction for $\widetilde{\sigma}_{yy}$.

The repertoire of solutions may be increased by finding the stress intensity factors when the crack is offset from the edge of the region where the tractions are applied by an amount d. This is relevant to the case case for the corrective shear traction, shown in figure 6.1(b), as

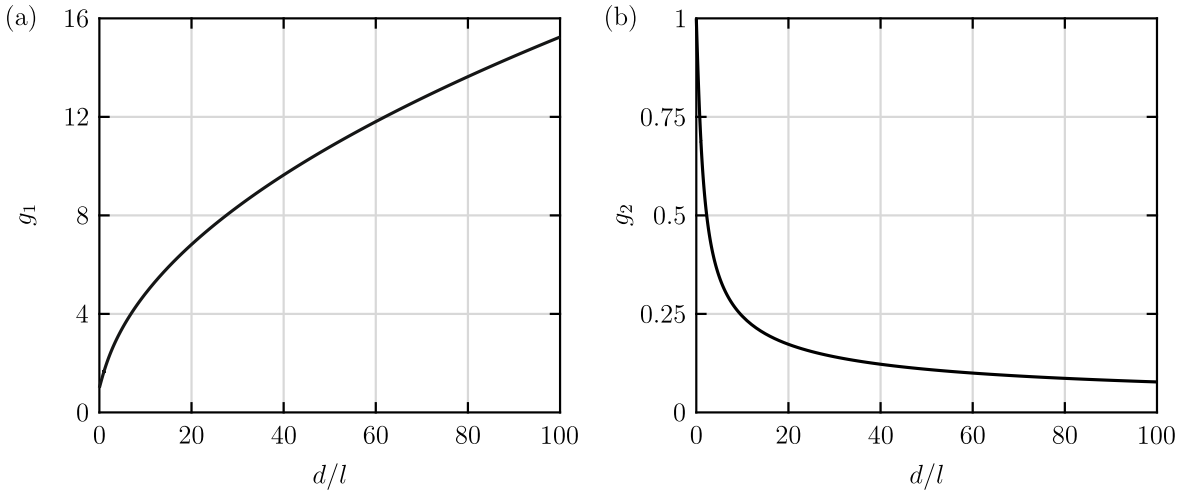


Figure 6.2: Influence of remote distance, d, on calibrations of (a) mode I and (b) mode II crack tip stress intensity factors and contact multiplier, L_{II}.

this means that we can solve the state of stress when partial slip prevails. Here, we have to use equations (6.11) and (6.12) for the bilateral stress, $\widetilde{\sigma}_{yy}$ and $\widetilde{\sigma}_{xy}$, in equations (6.19) and (6.20), respectively. As shown for the square root bounded normal traction, in the previous section, we are able to incorporate the factor $\sqrt{l}$ in the unknown $\hat{\phi}$ to get a general solution, independent of the crack length, l, but this time the solution of the singular integral equation will still depend on the ratio d/l (cf. equations (6.11) and (6.12)). The relevant dimensionless parameter describing the problem is therefore exactly this ratio, d/l, and we write

$$\left\{ \begin{array}{c} K_I^c \\ K_{II}^c \end{array} \right\} = \left[\begin{array}{c} -2.608\, g_1\left(d/l\right) \\ -1.565\, g_2\left(d/l\right) \end{array} \right] l\, L_{II}, \tag{6.36}$$

where the functions $g_i\left(d/l\right)$, are the solution of the calibration for different ratios d/l. The results for discrete ratios, $0 < d/l < 100$, are given in Figure 6.2, and of course we find $g_i\left(0\right) = 1$.

Using the formulation introduced above we can only find the calibration for discrete ratios d/l, but no closed form solution for $g_i\left(d/l\right)$. To make use of these functions in subsequent calculations we fit rational functions to the results obtained for discrete values of d/l. These rational functions are formed of polynomial ratios of the form

$$g_i\left(\frac{d}{l}\right) \approx \frac{\sum_{j=0}^{5} p_j \left(\frac{d}{l}\right)^j}{\sum_{i=0}^{5} q_j \left(\frac{d}{l}\right)^j}, \tag{6.37}$$

and the identified coefficients for the functions g_i, as well as details of the procedure used for the fit are listed in Appendix A. The approximations of g_i are included in Figure 6.2, but are indistinguishable from the numerical results. It should be noted that these analytical approximations should only be used for cracks whose length is short compared to any other dimension characterising the contact, i.e. $d/l > 1$, and we will look at this in more detail at the end of this section.

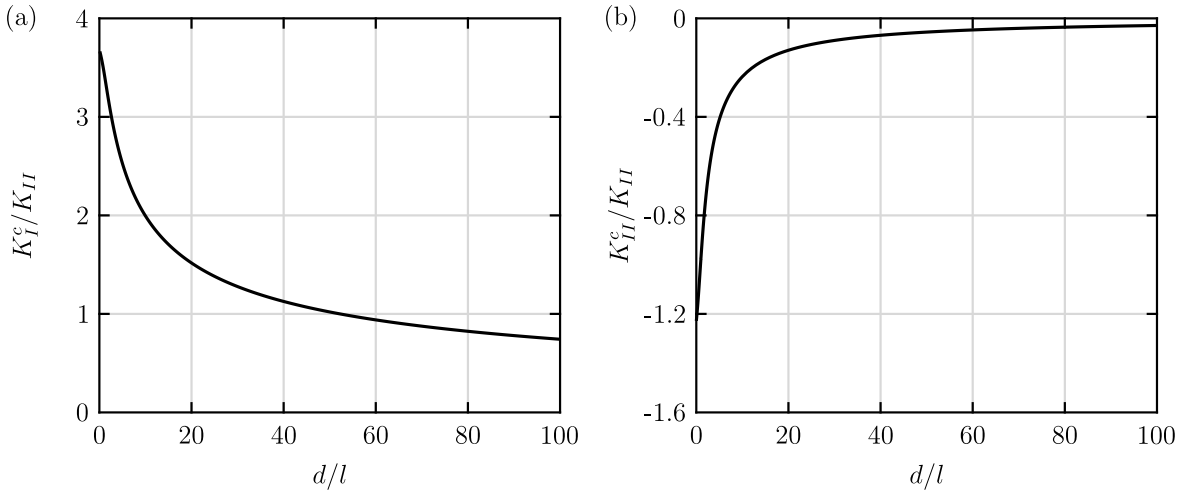


Figure 6.3: (a) mode I and (b) mode II crack tip stress intensity factors for cracks originating from the edge of a partial slip contact.

With this to hand we are able to find the crack tip stress intensity factor for a crack originating from the edge of an incomplete contact in partial slip, as shown in Figure 6.1(b). For the sliding shear traction, $q_s(r)$, we have the calibration given by equation (6.35), and we superimpose the calibration (6.36) for the remote corrective shear traction, $q_c(r)$, keeping in mind that this will be of opposite sign. For the superposition of both, we use equation (6.5) and normalise by the shear traction stress intensity factor, K_{II}, as defined by equation (6.4), which leads to

$$\frac{K_I^c}{K_{II}} = 2.608\frac{2l}{d}\left(g_1\left(\frac{d}{l}\right) - 1\right) \tag{6.38}$$

and

$$\frac{K_{II}^c}{K_{II}} = 1.565\frac{2l}{d}\left(g_2\left(\frac{d}{l}\right) - 1\right), \tag{6.39}$$

for the mode I and II crack tip stress intensity factors. For the chosen normalisation we find the results to be independent of the coefficient of friction, f. Figure 6.3 shows the solution of equations (6.38) and (6.39) for a varying ratio d/l and we find that, for $f \to \infty$ and therefore $d \to 0$, the normalised asymptotic crack tip stress intensity factors approach values of 3.628 and -1.209 for mode I and II, and therefore we recover the calibration for the fully stuck case with a square root singular shear traction as expected (cf. §2).

Looking at the form of equation (6.38) and (6.39), we notice that as $d \to 0$, and correspondingly $g_i\,(d/l) \to 1$, even small relative errors in the analytical approximation of $g_i\,(d/l)$, may lead to unacceptable inaccuracies in the term $g_i\,(d/l) - 1$. These will be magnified by multiplication of the term $1/d$, with d being close to zero. Caution should therefore be exercised when using the collocated rational functions for ratios $d/l < 1$. In the following we will restrict our considerations to cracks which are short compared to

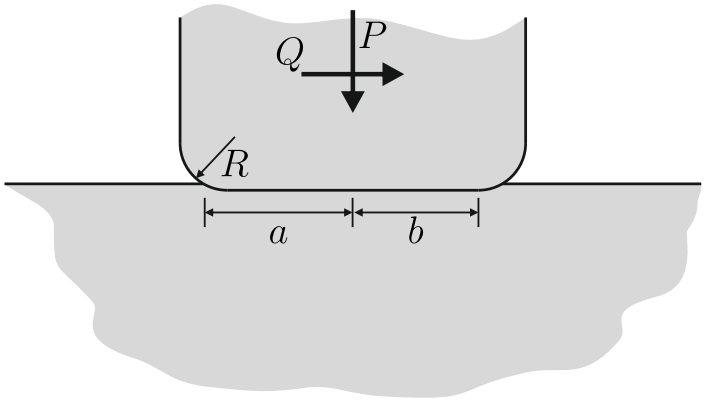


Figure 6.4: Finite contact between a flat and rounded punch and a half-plane.

any other dimension characterising the contact, $d/l > 1$, and may use equation (6.37) for $g_i\,(d/l)$ without reservations.

5 Comparison with finite Contact problems

In §2 we identified the subsurface stress field corresponding to an asymptotic description of the contact tractions characterised by the contact multiplier, L_I and L_{II} for a square root bounded normal and shear traction, or K_{II} for a square root singular shear traction (equations (6.9) - (6.13)). Using these single term representations of the bilateral stress ($\widetilde{\sigma}_{yy}$ and $\widetilde{\sigma}_{xy}$) we found a general solution of the singular integral equations (6.19) and (6.20) connecting the contact multipliers to the crack tip stress intensity factors and in the following we will refer to this solution as the asymptotic calibration which is given in §4. The disadvantage of the identified calibrations is that, following from the asymptotic description of the stress field, the quality of the solution depends upon the distance from the crack tip to the edge of the contact, i.e. the crack length needs to be small compared to any finite dimension characterising the contact.

The advantage of the asymptotic calibration becomes apparent when looking at how we find the crack tip stress intensity factor for a crack at the edge of a finite contact. We use the same procedure we used for the calibrations (§3), but when considering the finite description of the contact stress field in equations (6.19) and (6.20), its complex form (compared to the asymptotic description), does not allow us to find a general solution and consequently we have to solve the singular integral equations each time we want to find the crack tip stress intensity factors for a different crack length or contact geometry. The procedure of identifying the crack tip stress intensity factors for a finite consideration of the contact is described in some more detail by Araújo and Nowell (1999).

Here, we want to check the calibrations derived in the last paragraph against the results we get for a crack in a stress field corresponding to a finite contact. Different example finite contact problems will be treated to illustrate the universality

of the asymptotic calibration. First, look at a flat and rounded contact as shown in Figure 6.4 where the contacting bodies are elastically similar. The material compliance, A, for plain strain, is given by

$$A = \frac{2\,(1-\nu)}{\mu}, \tag{6.40}$$

with ν and μ being Poisson's ratio and shear modulus, respectively. The punch has a central flat section of width $2b$ and both corners are rounded with radius R. The geometry corresponds to the Hertzian contact when $b = 0$. The contact half-width a can be found from the contact law (Vázquez et al., 2010). The application of a tangential load $Q < fP$ will lead to slip near the edges and a central stick zone of half-width c with $b < c \leq a$. The contact tractions as well as the corresponding subsurface stress field for the finite contact, needed for $\widetilde{\sigma}_{yy}$ and $\widetilde{\sigma}_{xy}$ in equations (6.19) and (6.20), are given by Vázquez et al. (2010) and Vázquez et al. (2014).

The contact multiplier for the asymptotic solution is given by Dini et al. (2004) and is

$$\begin{aligned} L_I &= \frac{1}{\pi}\sqrt{\frac{2}{a}}\frac{dP}{da} \\ &= \frac{2}{\pi AR}\sqrt{2a}\arccos\left(\frac{b}{a}\right). \end{aligned} \tag{6.41}$$

We note that for $b = 0$, we recover the Hertzian contact multiplier $L_I = \sqrt{2a}/AR$ (Dini and Hills, 2004). Details of the evaluation of the integral equations, corresponding to equations (6.19) and (6.20) are omitted, here, for brevity, but follow the same steps as introduced in §4.

We will look at the effects of normal and shear traction, separately, before turning to the combined contact problem. Figure 6.5 shows the crack tip stress intensity factor (Fig. 6.5(a) mode I and (b) mode II) for a crack originating from the edge of the incomplete contact shown in Figure 6.4, loaded by a force, P, normal to the contact interface. We consider different ratios of the length of the flat portion to the contact half-width, b/a, where $b/a = 0$ characterises a Hertzian contact. The crack tip stress intensity factor is calculated for different crack lengths, l, ranging from $0 < l \leq a - b$, and we compare the solutions for the finite contact with the asymptotic calibration, where we get the normalised crack tip stress intensity factor from the simple relations

$$\frac{K_I}{L_I(a-b)} = -1.565\frac{l}{a-b} \tag{6.42}$$

and

$$\frac{K_{II}}{L_I(a-b)} = 0.522\frac{l}{a-b}. \tag{6.43}$$

The length of the rounded portion in contact, $a - b$, is chosen as the best salient length scale. We find good agreement close to the edge of the contact, i.e. for small crack lengths l. For longer crack lengths the linear solution we get from the asymptotic stress field is not able to capture the more complex behaviour we get for the finite contact any more.

It is recognised that the crack tip stress intensity factor cannot take negative val-

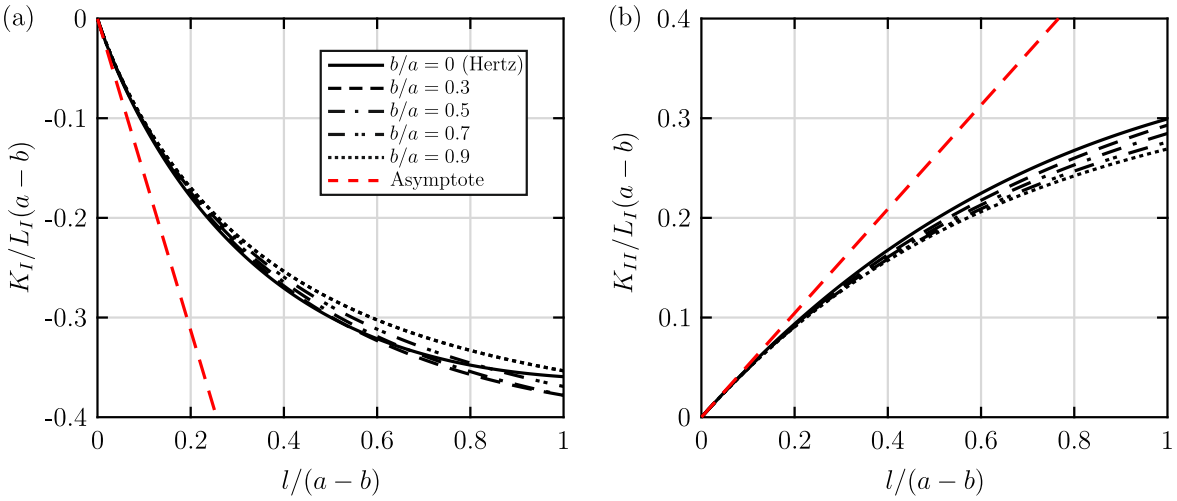


Figure 6.5: Flat and rounded contact: Comparison of asymptotic calculation of (a) mode I and (b) mode II crack tip stress intensity factor with those found from the finite contact problem corresponding to a normal load only, for different ratios of flat portion and contact half-width b/a (Legend in (a) applies to both subfigures).

ues as it vanishes for crack tip closure. Figure 6.5 here shows the influence of the normal loading on the crack tip stress intensity factor. Note that it always tends to induce closure.

Turning to the effects of the shear, similar to what we have done for the normal problem, we want to compare the asymptotic calibration, given by equations (6.38) and (6.39) for a partial slip shear traction, to the results we find for the consideration of the finite contact. Various crack lengths are considered, ranging up to the slip zone size, d, given by equation (6.5). Figure 6.5 shows the values for the crack tip stress intensity factor (Fig. 6.6(a,c,e) mode I and (b,d,f) mode II), again for different contact geometries, b/a, and crack lengths, l/d. The shear traction is excited by a tangential force, $Q/fP = 0.1, 0.4, 0.9$, as shown in Figure 6.4. Similar to the results for the normal problem we compare the results for the finite contact problem to the asymptotic calibration, and we find very good agreement for all crack lengths considered.

The results for the crack tip stress intensity factor for a crack at the edge of a finite contact, loaded by normal and tangential traction, are now compared to the superposition of the asymptotic results shown before. The combination of the calibration for a square root bounded normal traction as well as the two square root bounded shear tractions, representing the partial slip solution, are now needed, and yield the following equations

$$\frac{K_I^c}{K_{II}} = 2.608\frac{2l}{d}\left(g_1\left(\frac{d}{l}\right) - 1\right) - 1.565\frac{2}{f}\frac{l}{d} \quad \text{and} \tag{6.44}$$

$$\frac{K_{II}^c}{K_{II}} = 1.565\frac{2l}{d}\left(g_2\left(\frac{d}{l}\right) - 1\right) + 0.522\frac{2}{f}\frac{l}{d}. \tag{6.45}$$

In difference to the asymptotic results

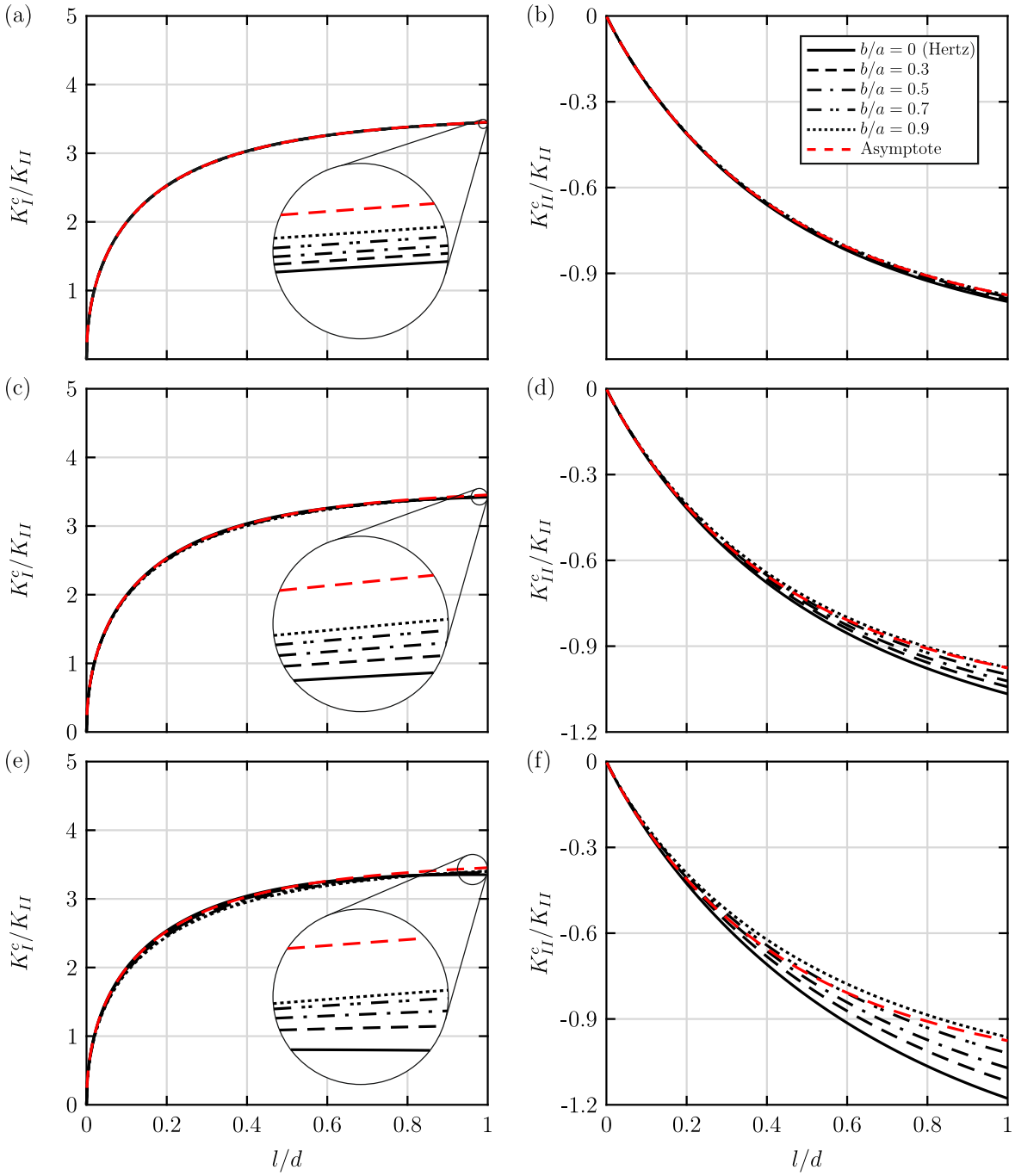


Figure 6.6: Flat and rounded contact: Comparison of asymptotic calculation of (a,c,e) mode I and (b,d,f) mode II crack tip stress intensity factor with those found from the finite contact problem corresponding to a shear load, $Q/fP = 0.1$(a,b), 0.4(c,d) and 0.9(e,f), for different ratios of flat portion and contact half-width b/a (Legend in (b) applies to all subfigures).

presented in Figure 6.5 and 6.6, being independent of the choice of material parameter or geometry, we see that the results for the combined case depend on the coefficient of friction f. Figure 6.7 shows the asymptotic results for a coefficient of friction $f = 0.75$ compared to the finite solution with different geometries, b/a, as well as different ratios of tangential loading Q/fP.

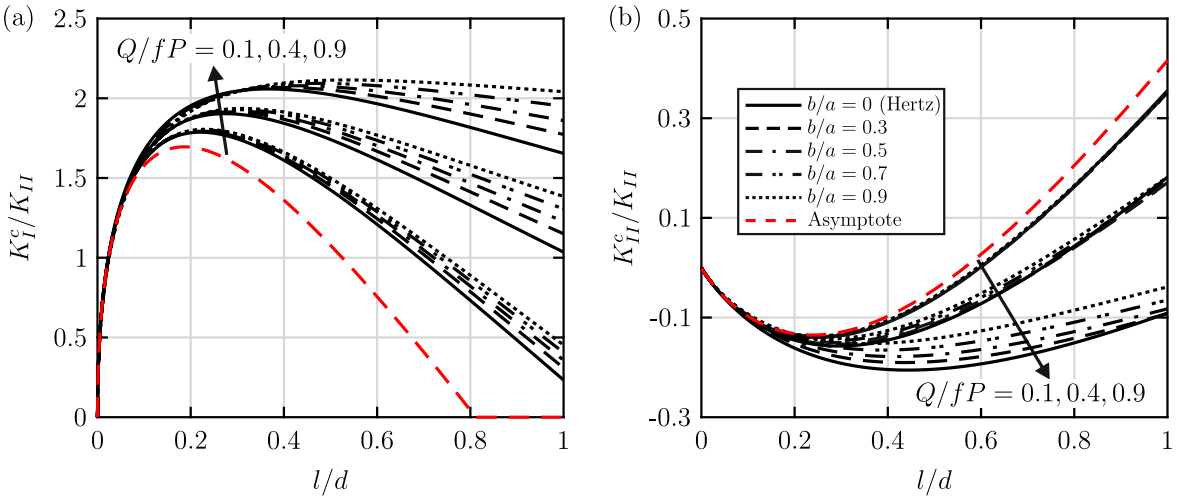


Figure 6.7: Comparison of asymptotic calculation of (a) mode I and (b) mode II crack tip stress intensity factor to calculation with consideration of the finite stress field corresponding to to a mixed loading of normal and shear force for different ratios of slip zone and contact half-width Q/fP as well as flat portion and contact half-width b/a. Crack length varies from 0 to the length of the slip zone $0 \leq l \leq d$ (Coefficient of friction $f = 0.75$; Legend in (b) applies to both subfigures).

6 Discussion

For the shown results and the formulation (§3) to be valid we require the crack to be open along its entire length. We know that this will certainly hold if the stress field, in the absence of the crack, is such that $\sigma_{yy}(x) > 0$ for $0 \leq x \leq l$. For a perpendicular crack in the stress field associated with an incomplete contact in partial slip, the asymptotic form of the direct stress along the crack length, in its absence, can be found from equations (6.9), (6.10) and (6.11) and is

$$\frac{\sigma_{yy}(x)\sqrt{d}}{K_{II}} = -\frac{1}{2\sqrt{2}}\sqrt{\frac{x}{d}}\left(5+\frac{3}{f} - \sqrt{\sqrt{1+\left(\frac{d}{x}\right)^2}+\frac{d}{x}}\left(5-\frac{d}{\sqrt{x^2+d^2}}\right)\right) \tag{6.46}$$

where, again, we substituted $L_{II} = f\,L_I$ and chose an appropriate normalisation.

The point, x/d, where the stress changes sign from tension (close to the surface) to compression is then given by the implicit equation

$$\sqrt{\sqrt{1+\left(\frac{d}{x}\right)^2}+\frac{d}{x}}\left(5-\frac{1}{\sqrt{1+\left(\frac{x}{d}\right)^2}}\right) - 5 - 3/f = 0, \tag{6.47}$$

and we find this to depend on the coefficient of friction. The numerical solution of equation (6.47) is shown for different values of $0 < f \leq 1$ in Figure 6.8(a).

Of course the crack might still be completely open, even if a part of it extends into the compressive region. Therefore we look at the opening gap of the crack, $g(x)$, which is given by

$$g(x) = -\int_x^l B_y(\xi)d\xi. \tag{6.48}$$

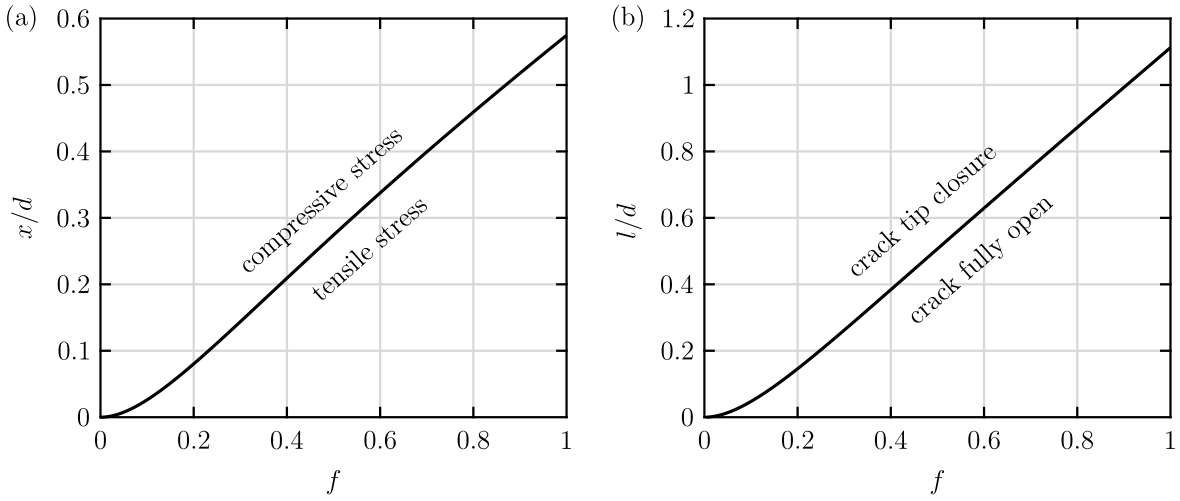


Figure 6.8: (a) normalised depth, x/d, where the stress in the absence of the crack changes from tensile (close to the surface) to compression (away from the surface), for a varying coefficient of friction, f. (b) For a varying coefficient of friction, f, the line denotes the boundary in relative crack length, l/d, with the crack being fully open for shorter cracks and showing crack tip closure for longer cracks.

If $g(x) > 0$ for $0 < x < l$, then this is both, necessary and sufficient for the crack to be open. For the square root bounded normal and shear traction, (6.9) and (6.10), respectively, as well as the remotely applied corrective shear traction (6.11), Figure 6.9 shows the different contributions to the gap opening. In Figure 6.9(a) we see the gap opening for a crack originating from the edge of an incomplete contact where the normal traction can be represented by a square root bounded asymptote. The corresponding Figure for a square root bounded shear traction is 6.9(b) while the opening corresponding to the corrective shear traction, i.e. the remote shear traction, is given in Figure 6.9(c) for different ratios of crack length to slip zone size l/d. Figure 6.9(d) is then the combined gap opening (the sum of (a), (b) and (c), where the contributions corresponding to the shear tractions are multiplied by the coefficient of friction (here $f = 0.75$)). The resulting gap opening needs to be positive for the whole crack length for the results to be valid. We find the crack opening to depend on the ratio l/d and that the crack will always start to close at the crack tip first. For closure at the crack tip we know that $K_I = 0$, and consequently for $K_I > 0$, the crack will be fully open and the introduced formulation is valid. Figure 6.9(d) shows that the crack starts to close for $l/d = 0.812$ where the crack is fully open for $l/d < 0.812$ and partly closed with $K_I = 0$ if $l/d > 0.812$. This coincides with the result we get from looking at the crack tip stress intensity factor, i.e. the point the crack tip stress intensity factor vanishes as shown in Figure 6.7 (both Figure 6.7 and 6.9 for a coefficient of friction $f = 0.75$).

Equation (6.44) enables us to find the crack length l/d where the crack starts to close, i.e. the crack tip stress intensity

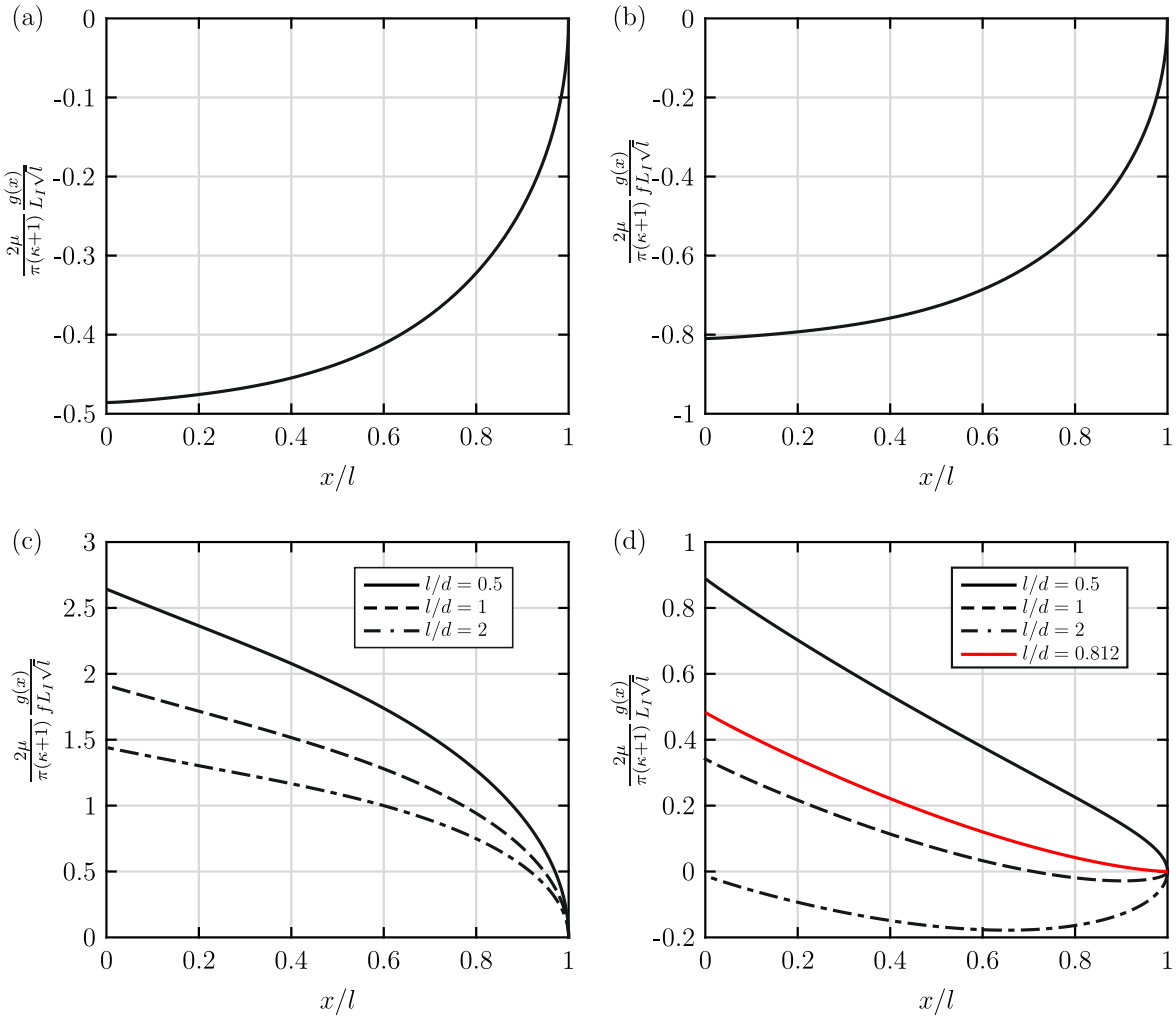


Figure 6.9: Normalised crack opening $g(x)$ for a crack in the stress field corresponding to (a) a bounded normal traction, (b) a bounded shear traction, (c) the corrective shear traction (also bounded but acting at a distance d) as well as (d) the combined opening corresponding to the stress field for an incomplete contact in partial slip.

factor vanishes, and we find the location l/d given by the implicit equation

$$2.608\left(g_1\left(\frac{d}{l}\right)-1\right)-1.565\frac{1}{f}=0, \tag{6.49}$$

and its solution for $0 < f \leq 1$ is plotted in Figure 6.8(b).

7 Conclusion

From the asymptotic representation of the contact tractions we have found the corresponding stress field, and in particular the tractions along the line of a crack originating from the contact interface at the contact edge, by the Williams solution. Making use of the distributed dislocation method the solution of singular integral equations provided us with calibrations linking the contact multipliers, which characterise the contact tractions, to the crack tip stress intensity factors for cracks originating from and perpendicular to the contact interface. With these very simple relations to hand the crack tip stress intensity factors for crack near the contact edge can be calculated

without the need for the solution of singular integral equations or even the exact knowledge of the subsurface stress field. By comparison with the results derived by the consideration of the stress field corresponding to a finite contact we showed that the asymptotic calibration allows us to find the crack tip stress intensity factor close to the contact edge. Generally we showed that cracks for the considered load cases start to close at the tip and consequently will be fully open, and the formulation valid for $K_I > 0$. The general asymptotic form of the contact stress field allows us to incorporate the results into different incomplete contact problems as long as the geometry dependent contact multiplier, L_I, is known.

Acknowledgements

N. Cwiekala and D. A. Hills thank Rolls-Royce plc and the EPSRC for the support under the Prosperity Partnership Grant 'Cornerstone: Mechanical Engineering Science to Enable Aero Propulsion Futures', Grant Ref: EP/R004951/1.

Appendix A

We used the built in *MATLAB* function `fit()` to identify the different coefficients. The highest coefficient, q_i, is generally chosen to be 1, and a coefficient p_i or $q_i = 0$, represents the choice of a lower order for the corresponding polynomial, rather than the result of the fit. The identified coefficients for the two functions g_i are listed in table 6.1. To avoid the rational function becoming unstable around where the polynomial in the denominator has a change in sign (is close to zero), we specified lower bounds as $q_i \geq 0$.

Table 6.1: Identified coefficients for the fit of rational functions to the results of the remote calibration.

Calibration	p_5	p_4	p_3	p_2	p_1	p_0
g_1	6.38e-3	131	7.98e4	1.84e6	2.03e6	2.33e5
g_2	4.72e-3	42.25	1.16e4	2.13e5	3.70e5	7.52e5
	q_5	q_4	q_3	q_2	q_1	q_0
g_1	0	1	3222	3.65e5	1.92e6	2.27e5
g_2	1	1304	8.87e4	4.55e5	6.59e5	7.53e5

6.2 Threshold Analysis for Short Cracks

In the last section we identified calibrations between crack tip stress intensity factors and the asymptotic contact traction multipliers. These are used, here, to predict crack arrest in fretting contact problems. The procedure is based on principles of linear elastic fracture mechanics and applied to fretting fatigue experiments available in the literature.

6.2.1 Introduction

Araújo and Nowell (1999) use the short crack threshold procedure first developed by Kitagawa and Takahashi (1976) to analyse cracks originating at the edge of (finite) Hertzian contacts. Assumptions beyond those made by the original authors must be made, because in their original deliberations the load was fully reversing and there was no steady component.

We summarise, briefly, the procedure needed. The crack tip stress intensity factor, K_I, under uniform mode I tension, σ_0, is given by

$$K_I = Y\sigma_0\sqrt{\pi l}\ , \tag{6.50}$$

where l is the crack length and Y is a calibration factor being, e.g. $Y = 1$ for a crack in an infinite plane or $Y = 1.1215$ for an edge crack. Further we take, as material properties, the long crack (plain) fatigue threshold stress intensity, ΔK_0, and the (plain) fatigue limit for the material, $\sigma_{\rm fl}$, and define the threshold for transition between long and short crack behaviour, b_0, by an equality between the fracture mechanics and classical views of the threshold condition, i.e. set

$$\Delta K_0 = \sigma_{\rm fl}\sqrt{\pi b_0}\ . \tag{6.51}$$

Now think of there as being a short crack threshold, $\Delta K_{\rm th}$ (still a material property because it may be defined wholly by material properties), expressed in terms of the

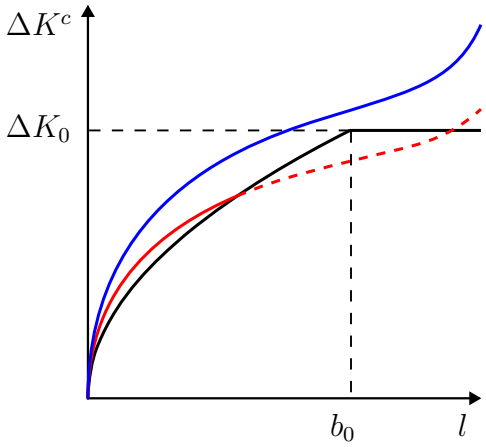


Figure 6.10: Schematic of crack tip stress intensity factor, K^c, over crack length, with short crack threshold, ΔK_{th}, for fretting fatigue (Araújo and Nowell, 1999).

crack length l ($< b_0$), defined by

$$\Delta K_{\text{th}} = \Delta K_0 \sqrt{\frac{l}{b_0}} \qquad \text{for} \quad \frac{l}{b_0} < 1, \tag{6.52}$$

and the long crack threshold remains at ΔK_0, while the transition crack length is given by

$$b_0 = \frac{1}{\pi} \left(\frac{\Delta K_0}{\sigma_{\text{fl}}} \right)^2 . \tag{6.53}$$

Figure 6.10 shows in black the crack tip stress intensity factor below which the crack will arrest and above which it will propagate. For cracks of length l shorter than the transition crack length, b_0, this is given by the short crack threshold, ΔK_{th} (eq. (6.52)). For longer cracks it is the constant long crack fatigue threshold stress intensity, ΔK_0. The blue and red curve show the variation of the crack tip stress intensity factor with the crack length as it might be found for fretting fatigue cracks, nucleating from the edge of incomplete contacts. The blue curve corresponds to a loading scenario for which the crack tip stress intensity factor is always above the threshold, and consequently the crack will propagate. The red curve corresponds to a different loading for which, at some length $l < b_0$, the crack tip stress intensity factor 'falls' below the threshold. At this length the crack tip stress intensity factor is too low to propagate the crack and it will arrest. This is indicated by the red line continuing as a dashed line into crack

lengths it cannot reach.

El Haddad et al. (1979) modified equation (6.52) to derive a smoother transition from short to long crack growth with the short crack threshold now defined by

$$\Delta K_{\text{th}} = \Delta K_0 \sqrt{\frac{l}{l + b_0}} \,, \tag{6.54}$$

such that we find a more conservative prediction of the short crack threshold.

6.2.2 Application to Fretting Fatigue Experiments

To show the application of the methods introduced before, combined with the crack tip stress intensity factor calibration found in the previous section, we will look at different experimental series of fretting fatigue tests. These experiments usually look at the number of load cycles a contact can bear when being subject to a varying loads and before one of the contacting bodies fails due to fracture. A schematic of such an experimental fretting fatigue test is shown in Figure 5.6(d). The contact is established by a normal load, P, and held constant. The bulk tension has a range $\Delta\sigma_0$ and, for experimental set-ups as schematically shown in Figure 5.6(d), it gives rise to a varying shear load (in phase) of range ΔQ, induced by the fixture of the fretting pads. In such a scenario cracks will typically nucleate from within the highly stressed contact region. Not only different pad geometries may affect the range of the crack tip stress intensity factor, but also the sequence in which the loads are applied. This will be shown by the consideration of different fretting fatigue experiments.

Fully reversing loads

We start by looking at experimental results for a Hetzian contact provided by Nowell, 1988. The constant normal load, P, for the given Hertzian geometry, gives rise to a normal traction characterised by the multiplier L_I, as shown in Section 3.1.1 and where L_I is defined by equation (3.6). Both Q and σ_0 are fully reversing throughout a load

cycle, such that the steady-state slip zone size may be given by (Moore et al., 2018)

$$d = \frac{\Delta K_{II}}{f L_I}, \tag{6.55}$$

and where the variation ΔK_{II} is defined by the variation of tangential loading. From equation (3.13) we obtain

$$\Delta K_{II} = \frac{\Delta Q}{\pi\sqrt{2a}} + \frac{\Delta\sigma_0}{4}\sqrt{\frac{a}{2}}\,. \tag{6.56}$$

The stress intensity factor caused by the contact loading may then be derived from calibrations (6.35). The effect of the tangential loading is given by

$$K_I^c = 2.608\, l\, f\, L_I \left(g_1\left(\frac{d}{l}\right) - 1 \right)\,, \tag{6.57}$$

and at the maximum point in the load cycle the slip zone will have its maximum extent, d, which is also when the function $g_1(d/l)$ takes its maximum value as can be seen from Figure (6.2). At the extreme point of unloading K_I^c will just take the negative of expression (6.57), so that the effect of ΔK_{II} on the variation of K_I^c can be taken as twice of equation (6.57). However, we note that equation (6.57) only shows the effect of the asymptotic shear traction on K_I^c, but that strictly K_I^c cannot take negative values. During half of the load cycle the crack will then be closed with a constant $K_I^c = 0$. The actual variation of the crack tip stress intensity factor is then given by equation (6.57) alone, where we might write ΔK_I^c on the left hand side of the expression.

The bulk tension acting in the specimen needs to be considered separately. It may be accounted for by equation (6.50) where $Y = 1.1215$. As above the crack will be closed during half the load cycle such that we have to introduce a factor of $1/2$ as above. Additionally, close to the contact the bulk tension is shared between the two bodies as discussed in Section 5.3, such that only $\Delta\sigma_0/4$ contributes to ΔK_I^c.

The normal load has a compressive effect on the stress acting parallel with the free

surface. This compression needs to be overcome before the crack starts to open. The range of the crack tip stress intensity factor will then be further reduced due to the normal loading. The resulting range of K_I^c is given by

$$\Delta K_I^c = 2.608\, l\, f\, L_I \left(g_1 \left(\frac{d}{l} \right) - 1 \right) + 1.1215 \frac{\Delta\sigma_0}{4} \sqrt{\pi l} - 1.565\, l\, L_I \,. \qquad (6.58)$$

If the contact geometry and loading is known, we may use equation (6.58) to identify the crack tip stress intensity factor for a varying crack length l, like the blue and red curve in Figure 6.10. If this curve lies everywhere above the threshold, we assume the crack to propagate and to limit the components life. This approach might further be simplified by the assumption that if the curve is below the threshold at $l = b_0$, then the crack will have arrested at some length $l < b_0$, and if it is above the threshold at $l = b_0$ we assume the crack to propagate. It should be noted, that for the asymptotic approach given by equation (6.58), the crack tip stress intensity factor will in every case fall below the threshold, ΔK_0, eventually. This is caused by the fact that, for an increasing crack length, the dominating term becomes the linear and negative term. However, if the transition crack length, b_0, is small compared to any other dimension characterising the contact, we may assume that this point, where the asymptotic approach loses its validity, lies somewhere in the region $l > b_0$.

Setting equation (6.58) equal to (6.52) and choosing $l = b_0$, we can find the range ΔK_{II} sufficient to propagate cracks. From equation (3.6) and (6.56) we find L_I as well as ΔK_{II} not only to depend on the external loads but also on the contact half-width a. This allows us, for given external loads and material parameter, to solve for the contact size, a_0. Regarding the size effect, investigated by Nowell (1988), this is the critical contact size, marking the transition between the short and infinite life regimes. For specific combinations of external loads, given in Table 6.2, we compare the results obtained via the here introduced asymptotic calibration, to the critical contact size found by Nowell (1988) with an experimental approach, as well as those results reported by Araújo and Nowell (1999) following a similar method to the current work, but using a finite description of the contact stress field, i.e. not using an edge

				a_0 [mm]		
Series	p_0 [MPa]	$\Delta Q/2P$	$\Delta\sigma_0/2$ [MPa]	Experiment	Finite	Asymptotes
1	157	0.45	92.7	0.28 - 0.38	0.10	0.46
2	143	0.24	92.7	0.54 - 0.72	-	0.76
3	143	0.45	92.7	0.18 - 0.27	0.18	0.47
4	143	0.45	77.2	0.36 - 0.54	0.27	0.58
5	120	0.45	61.8	0.57 - 0.71	0.42	0.89

Table 6.2: Critical contact size, a_0, found from the asymptotic calibration, compared to experimental results reported by Nowell (1988) and to a finite contact description (Araújo and Nowell, 1999).

asymptote.

Araújo and Nowell, 1999 do not report results for experimental series 2, as the experimental conditions, here, give rise to opposite directions of slip at both ends of the contact, making a finite description much more complicated for them. The asymptotic description of the contact edge, however, allows us to tackle these conditions with the same approach used for equal directions of slip with equal simplicity.

We have to emphasize, again, that the quality of the asymptotic calibration strongly depends on the ratio of crack length to slip zone size (Cwiekala and Hills, 2021c), and we find from equation (6.58) that ultimately the linear term, originating from the normal pressure, will dominate the crack tip stress intensity factor. Consequently, the agreement between the method used here and the reported values is better for experimental conditions giving rise to a large contact size and therefore also larger slip zone sizes than it is for small contact sizes.

Mean value of tangential loading

The simple case of fully reversing loads, discussed for experimental results reported by Nowell (1988), but also found in Szolwinski and Farris (1998), is sufficiently described by equation (6.58). Generally, however, this might not always be the case and we find that Hojjati-Talemi et al. (2014) conducted experiments with a mean value of bulk tension, giving rise to $K_{II,\mathrm{mean}}$, applied before shear force and bulk tension were varied in phase. Also, in experimental series 6 reported by Nowell (1988) we find both, σ_0 and Q, to vary around a mean value $\neq 0$. Here, it appears useful to calculate the maximum

as well as the minimum value for the mode I crack tip stress intensity factor during the load cycle.

The maximum extent of the slip zone as it might appear in the initial (transient) loading is given by

$$d_{\max} = \frac{2K_{II,\max}}{fL_I}, \tag{6.59}$$

and we find this not only to depend on the range of the loading but also on the mean value with $K_{II,\max} = K_{II,\text{mean}} + \Delta K_{II}/2$. Using this relation we find the maximum value for the crack tip stress intensity factor, reached during a load cycle, to

$$K^c_{I,\max} = 2.608\, l\, f\, L_I \left(g_1 \left(\frac{d_{\max}}{l} \right) - 1 \right) + 1.1215 \frac{\sigma_{0,\max}}{2} \sqrt{\pi l} - 1.565\, l\, L_I \,. \tag{6.60}$$

The slip zone extent in the steady state, d, is given by equation (6.55), as before. At the point of minimum loading, the direction of slip is opposite to what we find for the maximum point in the load cycle, but we are still left with locked-in slip displacements in the region $d_\text{s} < r < d_{\max}$, where r is measured from the contact edge (Fleury et al., 2017). These displacements will still affect the stress intensity factor and we find

$$\begin{aligned} K^c_{I,\min} = {} & 2.608\, l\, f\, L_I \left(1 - 2\, g_1 \left(\frac{d}{l} \right) + g_1 \left(\frac{d_{\max}}{l} \right) \right) \\ & + 1.1215 \frac{\sigma_{0,\max} - \Delta\sigma_0}{2} \sqrt{\pi l} - 1.565\, l\, L_I \end{aligned} \tag{6.61}$$

We find $\Delta K^c_I = \max\left(K^c_{I,\max}, 0\right) - \max\left(K^c_{I,\min}, 0\right)$.

6.2.3 Results and Conclusion

As long as we restrict ourselves to incomplete contacts, the methods introduced are applicable to various contact geometries. Only the definition of the asymptotic normal multiplier L_I differs. For a pad geometry of a flat and rounded punch (Fig. 2.4(a)), as considered in experiments by Dini (2004), we find L_I to be given by equation (3.9).

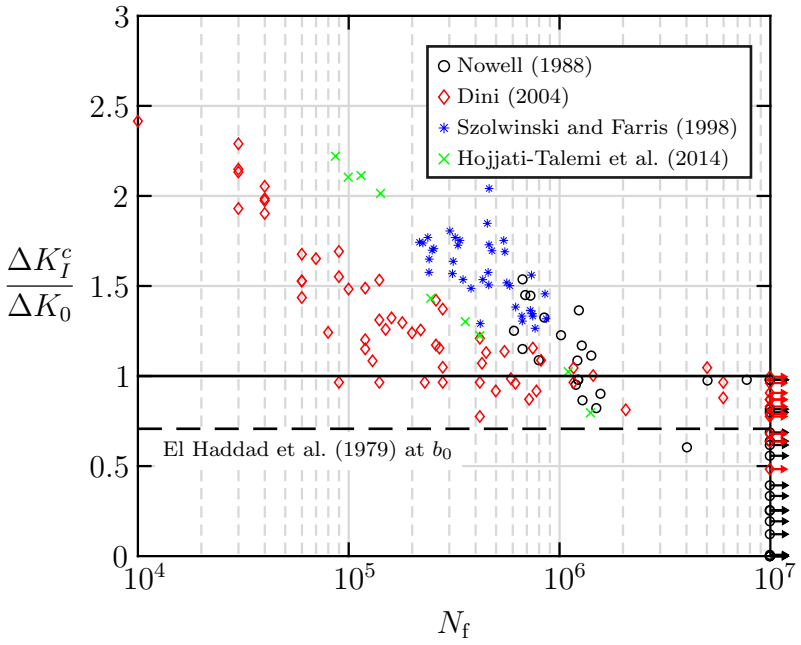


Figure 6.11: Crack tip stress intensity factor, ΔK_I^c, plotted over life cycles, N_f, for different experiments.

For different experimental set-ups, reported by Nowell (1988), Szolwinski and Farris (1998), Hojjati-Talemi et al. (2014) and Dini (2004), we may then calculate the crack tip stress intensity factor at a crack length b_0. The results are plotted in Figure 6.11, over the number of load cycles to failure, N_f, where a number of 10^7 corresponds to a run-out test. The parameters for the loading and geometry of all the considered experimental data is summarised in Appendix B.

It should be noted that for experiments reported by Dini (2004), a mean value of bulk tension is applied before the contact is established. Consequently, it does not contribute to K_{II} and therefore does not affect the size of the slip zone, d. Also, close to the contact region, the mean value of the bulk tension is not shared between the two bodies.

Figure 6.11 shows that for all the 'run-out' tests, at $l = b_0$ the asymptotic approach gives a crack tip stress intensity factor lower than the threshold, i.e. it predicts crack arrest. For the majority of experiments showing failure after a certain number of load cycles this would have been predicted by a crack tip stress intensity factor range higher than ΔK_0. For some tests this is not the case and even though the calculated ΔK_I^c is below the threshold, the tests failed in the experiment. However, all but one of

those tests show a crack tip stress intensity factor range above the more conservative El Haddad et al. (1979) prediction, given by equation (6.54) (note the run-out tests plotted at 10^7 cycles).

6.3 Asymptotic description of fretting wear and fretting fatigue for incomplete contacts

The chapter thus far considered cracks in the neighbourhood of semi-infinite incomplete contacts. Following the same idea, the paper constituting this section considers a change in the surface profile due to long-term wear. Calibrations are identified between the initial contact multipliers and those characterising the state of stress at the edge of the worn, now fully stuck, contact. Additionally, cracks nucleating from inside the wear zone are considered, and the corresponding crack tip stress intensity factors are found.

Asymptotic description of fretting wear and fretting fatigue for incomplete contacts

N. Cwiekala[a,2], D. A. Hills[a]

[a]*Department of Engineering Science, University of Oxford, Parks Road, OX1 3PJ Oxford, United Kingdom*

Abstract

Looking at wear of incomplete contacts in partial slip we start from an asymptotic description of the contact tractions at the contact edges. We introduce distributed dislocations along the slip zone to account for the profile reduction due to wear and find the long term time asymptote where the contact is wholly stuck. The resulting stress field is used to find the crack tip stress intensity factors for short contact edge cracks, which are useful in predicting the crack nucleation threshold.

Keywords:

Short cracks, Fretting wear, Fretting fatigue, Asymptotic analyses, Stress intensity factor

1 Introduction

Fretting occurs when two bodies, pressed into contact, are subject to cyclic tangential loading, leading to local regions of cyclic slip even though the contact is notionally stuck. These cyclic slip displacements are typically caused by vibrations resulting in a large number of load cycles. We find these fretting regions to encourage fatigue crack nucleation, reducing the fatigue life. The study of this phenomenon is referred to as fretting fatigue and is mainly concerned with the change of tractions and therefore the stress field in which cracks nucleate, caused by localised cyclic slip displacements. Additionally, fretting causes a modification of the surface geometry of the contacting bodies due to wear. Most studies of wear look at sliding contacts, where a relative rigid body motion between the two components is present and leads to much higher amplitudes of slip displacement compared to what we find for fretting contacts. Nevertheless, the localised region of cyclic displacements might lead to severe wear even for small amplitudes of slip, and we refer to this phenomenon as fretting wear. The process of wear in both scenarios, macroscopic sliding and local cyclic slip, is similar in terms of surface particles being eroded from the contacting surfaces to produce wear debris. Although this is often done (Ding

[2]Corresponding author

Email address: nils.cwiekala@eng.ox.ac.uk (N. Cwiekala)

et al., 2004), it is *unrealistic* to tackle fretting wear problems by means of traditional wear laws, for example that proposed by Archard (1953), which are calibrated by experiments involving sliding contacts. The environment differs in the sense that for sliding contacts the contact region changes which might favour the escape of debris while the localised slip in a fretting contact leads to debris entrapment.

The surface modification and the corresponding change of contact tractions due to long term wear has been considered by Hills et al. (2009) for a Hertzian contact represented by half-planes and by Dini et al. (2008) for an axi-symmetric Hetzian contact. Here, we intend to look at a semi-infinite representation of the contact edge and find the modification of the contact tractions due to wear. In comparison to the earlier solutions for finite contacts the asymptotic form of the results in this study will allow us to incorporate the solution in a range of different incomplete contact geometries, and hence add universality.

When looking at the near edge contact tractions of an incomplete contact we find the normal traction, $p(r)$, to be square root bounded with

$$L_I = \lim_{r\to 0} \frac{p(r)}{\sqrt{r}}, \tag{6.62}$$

being the asymptotic contact pressure multiplier and r is measured from the contact edge (Fig. 6.12(a)). Generally, L_I depends on the normal loading, P, as well as the geometry and example calibrations can be found from Dini and Hills (2004) and Dini et al. (2004) for a Hertzian and a flat and rounded contact, respectively.

Turning to the effect of tangential loading and assuming the contact to be fully stuck, as shown in Figure 6.12(a), for now, we expect a square root singular response in the shear traction, $q(r)$. This prompts us to define a shear traction stress intensity factor at the contact edge, K^e_{II}, with

$$K^e_{II} = \lim_{r\to 0} q\,(r)\,\sqrt{r}. \tag{6.63}$$

As K^e_{II} characterises the shear traction at the initial edge of the contact, we added the superscript 'e' to distinguish it from multipliers introduced at a later point and related to the state of stress at the wear boundary (Fig. 6.12(d)). The value of K^e_{II} depends on the tangential loading as well as the half-width of the finite contact, a, but is *independent* of the relative profile of the contacting bodies (Hills et al., 2016). We find

$$K^e_{II} = \frac{Q}{\pi\sqrt{2a}} + \frac{\sigma_0}{4}\sqrt{\frac{a}{2}}, \tag{6.64}$$

for the application of a shear force, Q, as well as a differential bulk tension, σ_0.

Allowing for relative displacements between the contacting bodies, with a finite coefficient of friction, f, we find a slip zone close to the contact edge whose extent, d, is given by (Moore et al., 2018)

$$d = \frac{\Delta K^e_{II}}{f L_I}, \tag{6.65}$$

where ΔK^e_{II} is the range of shear load-

ing under conditions of oscillatory shear force and bulk tension. Inside the slip zone the shear traction will be bounded by $fp(r)$ whereas a corrective shear traction acts over the extent of the stick zone. The asymptotic contact tractions for an incomplete contact in partial slip, as shown in Figure 6.12(b), are then given by

$$p(r) = L_I\sqrt{r} \tag{6.66}$$

$$q(r) = fL_I\left(\sqrt{r} - \sqrt{r-d}\right) \tag{6.67}$$

where we adopted the usual convention of the normal traction being positive for compression and both the tractions have to be interpreted in terms of their real parts. We will look at how the contact tractions are modified by wear reducing the contact profile to a point where we find the normal tractions vanishing inside the wear-zone, $0 \leq r < w \leq d$ (Fig. 6.12(c)). We consider wear, and therefore the reduction of the profile, to occur wherever we find relative tangential displacements between the contacting bodies, and to continue until a glancing contact establishes itself in the wear-zone, i.e. all tractions vanish and outside the worn region all slip has ceased. We will consider the wear-zone, $0 \leq r < w$, to establish, starting from the edge of the contact where the slip displacements have their maximum, and nucleate inside the contact. Whenever the contact tractions outside the wear-zone, $w < r$, give rise to partial slip, we expect the wear-zone to continue to expand until just outside the wear-zone the ratio of shear to normal traction is just less then the limiting condition, i.e.

$$\lim_{r\to w^+} \frac{q(r)}{p(r)} = f - \epsilon. \tag{6.68}$$

We find this to be the limiting condition as the wear-zone cannot continue to grow if the contact is in a condition of stick just outside the wear-zone.

2 Formulation

To account for the profile reduction caused by wear as well as the relative tangential displacement between the two bodies we introduce arrays of distributed dislocations along the wear zone, $0 \leq r < w$. The edge of the contacting bodies, for an incomplete contact represented as half-planes, can be thought of as a semi-infinite crack. We find, first, the shear stress caused by an array of distributed glide edge dislocations of density $B_r(\rho)$, positioned along a line drawn from the contact edge

$$\tilde{\sigma}_{r\theta}(r) = \frac{2\mu}{\pi\left(\kappa+1\right)} \int_0^w B_r(\rho) G_{rr\theta}(r,\rho) d\rho, \tag{6.69}$$

where the stress is found along the same line and $G_{rr\theta}(r,\rho)$ is given by Moore et al. (2018) as

$$G_{rr\theta}(r,\rho) = \sqrt{\frac{\rho}{r}}\frac{1}{r-\rho}. \tag{6.70}$$

The normal stress, $\tilde{\sigma}_{\theta\theta}(r)$, caused by a corresponding array of climb edge dislocations, $B_\theta(\rho)$, is described by a similar Kernel function, i.e. $G_{\theta\theta\theta}(r,\rho) = G_{rr\theta}(r,\rho)$, and the problem is uncoupled

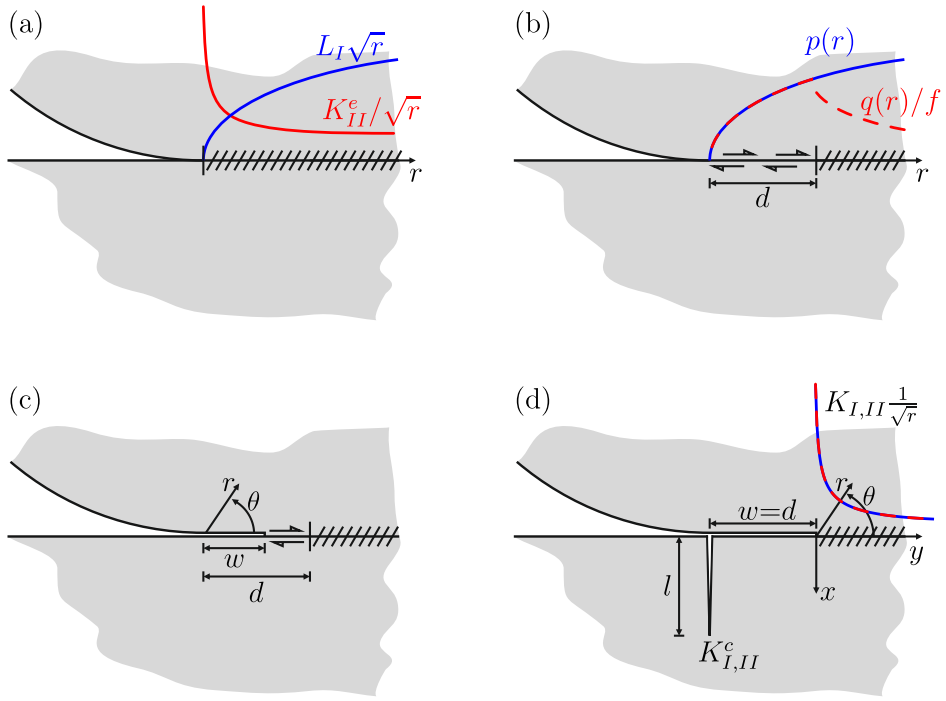


Figure 6.12: Incomplete contact a) in conditions of fully stuck, b) in partial slip c) with wear slit extending into the former slip zone and d) crack nucleating from the final wear zone.

in the sense that $G_{r\theta\theta}(r,\rho) = G_{\theta r\theta}(r,\rho) = 0$.

The normal and shear traction, $N(r)$ and $S(r)$, respectively, are given by two uncoupled algebraic equations

$$N(r) = L_I\sqrt{r} + \frac{2\mu}{\pi\,(\kappa+1)}\frac{1}{\sqrt{r}}\int_0^w \frac{\sqrt{\rho}B_\theta(\rho)}{r-\rho}d\rho, \tag{6.71}$$

$$S(r) = fL_I\left(\sqrt{r}-\sqrt{r-d}\right) + \frac{2\mu}{\pi\,(\kappa+1)}\frac{1}{\sqrt{r}}\int_0^w \frac{\sqrt{\rho}B_r(\rho)}{r-\rho}d\rho, \tag{6.72}$$

as a superposition of the bilateral tractions, $\bar{\sigma}_{\theta\theta} = p(r)$ and $\bar{\sigma}_{r\theta} = q(r)$, in the absence of the wear-slit, and the stress caused by the dislocations, $\tilde{\sigma}_{\theta\theta}(r)$ and $\tilde{\sigma}_{r\theta}(r)$, representing the wear-slit. We identify the unknown dislocation densities, $B_i(\rho)$, by the requirement that the worn contact faces are traction free, i.e. $N(r) = S(r) = 0$ for $0 \le r \le w$. This leads to

$$L_I\sqrt{r} = \frac{2\mu}{\pi\,(\kappa+1)}\frac{1}{\sqrt{r}}\int_0^w \frac{\sqrt{\rho}B_\theta(\rho)}{\rho-r}d\rho, \tag{6.73}$$

$$fL_I\left(\sqrt{r}-\sqrt{r-d}\right) = \frac{2\mu}{\pi\,(\kappa+1)}\frac{1}{\sqrt{r}}\int_0^w \frac{\sqrt{\rho}B_r(\rho)}{\rho-r}d\rho \tag{6.74}$$

for $0 \le r \le w$. The equations differ only by a factor f on the LHS when $w \le d$. We normalise the integral range with

$$s = 2\frac{\rho}{w} - 1 \qquad \text{and} \tag{6.75}$$

$$t = 2\frac{r}{w} - 1, \tag{6.76}$$

to derive

$$\sqrt{\frac{t+1}{2}} = \int_{-1}^{1} \sqrt{\frac{s+1}{t+1}} \frac{\hat{B}_\theta(s)}{s-t} ds, \tag{6.77}$$

$$\left(\sqrt{\frac{t+1}{2}} - \sqrt{\frac{t+1}{2} - \frac{d}{w}} \right) = \int_{-1}^{1} \sqrt{\frac{s+1}{t+1}} \frac{\hat{B}_r(s)}{s-t} ds, \tag{6.78}$$

for $-1 \leq t \leq 1$, and with

$$\hat{B}_\theta(s) = \frac{2\mu}{\pi(\kappa+1)} \frac{B_\theta(s)}{L_I\sqrt{w}}, \tag{6.79}$$

$$\hat{B}_r(s) = \frac{2\mu}{\pi(\kappa+1)} \frac{B_r(s)}{fL_I\sqrt{w}}. \tag{6.80}$$

We can easily see that the two equations (6.77) and (6.78) will have the same solution $\hat{B}_i(s)$ and that the final dislocation density, $B_i(s)$, will differ only by a factor f if $w \leq d$. That is exactly what we would expect as, inside the slip-zone, the shear traction is a scaled version of the normal traction and that the stress Kernels are similar.

We will now consider the implication of this observation for the final extent of the wear-zone. The dislocations introduced along the wear-zone will, of course, not only cause the tractions to vanish along the wear-zone, as required by equations (6.77) and (6.78), but also affect the tractions outside the wear-zone, $r > w$. We just showed that for $w \leq d$ the density of dislocations introduced inside the wear-zone, $B_r(s)$ and $B_\theta(s)$, will differ only by a factor f. Keeping in mind that the Kernel functions $G_{\theta\theta\theta}(r,\rho) = G_{rr\theta}(r,\rho)$, it is evident that the shear stress outside the wear-zone, caused by the glide edge dislocations, $B_r(s)$, will be a scaled version of the stress caused by the climb edge dislocations, $B_\theta(s)$, i.e. $\tilde{\sigma}_{r\theta}(r) = f\tilde{\sigma}_{\theta\theta}(r)$ not only for $r \leq w$ but also for $r > w$ (still only considering cases with $w \leq d$). The total stress is effectively $\sigma_{r\theta}(r) = f\sigma_{\theta\theta}(r)$ for $r \leq d$ and $\sigma_{r\theta}(r) < f\sigma_{\theta\theta}(r)$ for $r > d$, i.e. the extent of the initial slip-zone will not be affected if $w \leq d$. It is clear, that the initial size of the slip-zone, d, will be the final extent of the wear-zone, $w = d$.

To find the tractions present for the worn configuration the two uncoupled singular integral equations of the first kind may be treated in the usual way using the method developed by Erdogan et al. (1973). We expect the solution to be bounded-singular and let

$$B_i(s) = \phi(s)\omega(s), \tag{6.81}$$

with

$$\omega(s) = \sqrt{\frac{1+s}{1-s}}. \tag{6.82}$$

Following the quadrature in Erdogan et al. (1973), the integral will be calculated in a numerical sense where the N integration and collocation points, s_i and t_k respectively, are given by

$$s_i = \cos\left(\pi \frac{2i-1}{2N+1}\right) \quad i = 1, ..., N \tag{6.83}$$

and

$$t_k = \cos\left(\pi \frac{2k}{2N+1}\right) \quad k = 1, ..., N. \tag{6.84}$$

The following system of equations can be inverted to give the solutions $\phi(s)$ at the N integration points s_i (Hills et al., 1996). For example the calculation of the climb edge dislocation density reads

$$\pi \sum_{i=1}^{N} W_i \frac{\sqrt{s_i+1}}{s_i - t_k} \hat{\phi}_\theta(s_i) = \frac{1}{\sqrt{2}} (t_k + 1), \tag{6.85}$$

giving N equations with $k = 1, ..., N$ for the N unknowns $\hat{\phi}_\theta(s_i)$. $\hat{\phi}_\theta(s)$, here, is defined as

$$\hat{\phi}_\theta(s) = \frac{2\mu}{\pi(\kappa+1)} \frac{\phi_\theta(s)}{L_I \sqrt{w}}, \tag{6.86}$$

and following equation (6.85) it is independent of the size of the wear-zone, w. The weights W_i are given by

$$W_i = 2 \frac{1 + s_i}{2N + 1}. \tag{6.87}$$

The dislocation density will correspond to a singularity outside the wear-zone, $r > w$, which is characterised by the contact multiplier K_I, as shown in Figure 6.12(d). From Hills et al. (1996) we find[3]

$$\begin{aligned} K_I &= \sqrt{w} \frac{2\mu}{(\kappa+1)} \phi_\theta(1) \\ \Leftrightarrow \frac{K_I}{L_I w} &= \pi \hat{\phi}_\theta(1), \end{aligned} \tag{6.88}$$

with $\hat{\phi}_\theta(1)$ calculated by Krenk's interpolation (Krenk, 1975). As $\hat{\phi}_\theta(1)$ is independent of the extent of the wear-zone, equation (6.88) represents a universal calibration between the initial normal contact multiplier, L_I, the length of the wear-zone, w, and the resulting multiplier K_I, characterising the singularity at the tip of the wear-zone. We find

$$\frac{K_I}{L_I} = \frac{w}{2}, \tag{6.89}$$

and note that K_I varies with the size of the wear-zone, w, but not with the oscillating shear force. For K_{II} the same relationship, where the LHS is multiplied by $1/f$, holds, for a specific extent of the wear-zone with $w/d \leq 1$, but here, the multiplier, K_{II}, of the singularity at wear-stick boundary does vary with the oscillating shear load. Making use of equation (6.65) we derive

$$\frac{\Delta K_{II}}{\Delta K_{II}^e} = \frac{w}{d}, \tag{6.90}$$

and consequently the multiplier characterising the singularity at the wear-zone boundary will experience the same range as the multiplier characterising the singularity at the initial edge of the unworn contact, i.e. $\Delta K_{II} = \Delta K_{II}^e$ for $w = d$. For the asymptotic assumption $d \ll a$, this corresponds to the results found by Hills et al. (2009) for the finite Hertzian contact.

3 Results

Although we identified the final size of the wear-zone in the previous paragraph, our formulation in terms of distributed dislocations allows us to choose the extent, w. For the here considered assumption of wear proceeding from the edge of the contact, each ratio $w/d \leq 1$, rep-

[3]Note, that in difference to a classical crack tip stress intensity factor, for the contact multiplier we do not connect the tractions and the multiplier by a factor of $1/\sqrt{2\pi}$. Consequently, equation (6.88) is missing a factor of $\sqrt{2\pi}$ compared to what we find in Hills et al. (1996).

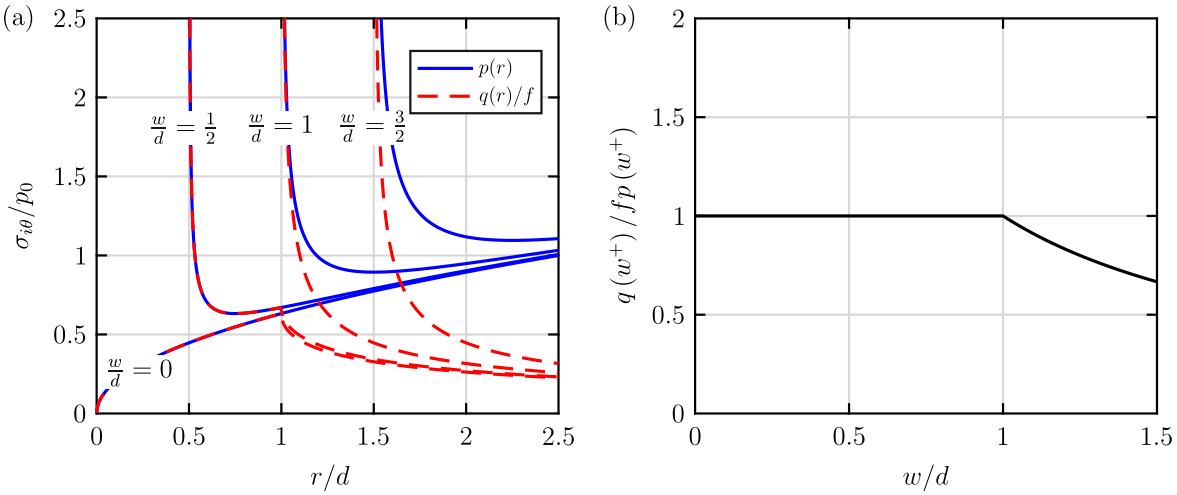


Figure 6.13: (a) Contact tractions for different extents of the wear zone w/d and (b) the ratio of tractions just outside the wear-zone for a continuous variation of w/d.

resents a transient state and we expect wear to continue until $w = d$. We do not expect the wear-zone to extend to $w/d \geq 1$, but our formulation allows us to calculate the corresponding traction also for these cases. Figure 6.13(a) shows the final tractions, $p(r)$ and $q(r)$, for different ratios of the wear-boundary and the initial slip-zone length, w/d. We find the initial tractions of the unworn contact for $w/d = 0$. For $w/d = 0.5$ we see that slip continues outside the wear zone until the end of the initial slip zone, $w \leq r \leq d$. We can immediately see that these states will not represent the final state of the wear-contact as wear will continue until all partial slip has ceased. For the following two ratios of $w/d = 1, 1.5$ we cannot immediately see the ratio of tractions, $q(r)/fp(r)$ just outside the wear-zone, $r \to w^+$, but plotting the traction ratio for a continuous variation of w/d visually confirms the result found in the last paragraph. If we choose $w < d$ the point just outside the wear-zone will be in a state of slip, i.e. $q(r) = fp(r)$ for $r \to w^+$. If we increase the extent of the wear-zone to $w > d$ we find the point outside the wear region to be in a condition of stuck, i.e. $q(r) < fp(r)$ for $r \to w^+$ (Fig. 6.13(b)).

We want to compare the results obtained here, found within an asymptotic formulation, to results for a finite description of the contact. Hills et al. (2009) found the finite solution for a Hertzian contact with a cylinder of radius R pressed into a half-space by a normal load, P, giving rise to a contact half-length, a. Subsequently a fully reversing tangential load, of amplitude Q, is applied. The contact multiplier, L_I, for the specific contact geometry is given to (Dini and Hills, 2004)

$$L_I = \frac{2P}{\pi a}\sqrt{\frac{2}{a}}. \tag{6.91}$$

Figure 6.14 shows a comparison of the resulting wear tractions for the final state of wear, $w = d$, between the asymptotic results and the results found by Hills et al. (2009). For the comparison, x is mea-

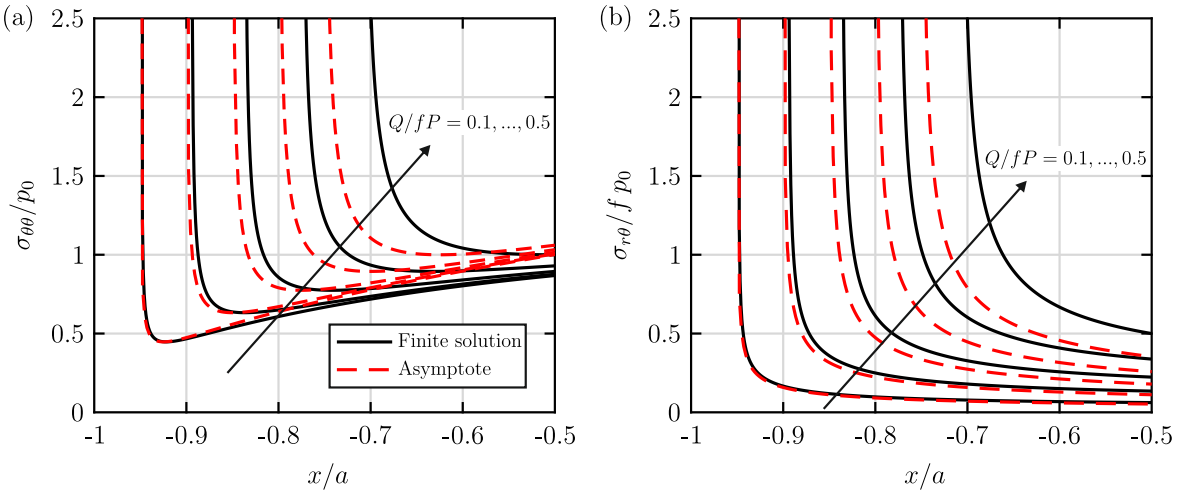


Figure 6.14: Comparison of asymptotic contact (a) normal and (b) shear traction with results for the finite description by Hills et al. (2009) for different ratios of tangential to normal loading $Q/fP = 0.1, ..., 0.5$ (Legend in (a) applies to both subfigures).

sured from the centre of the finite contact, and, consequently $x/a = -1$ denotes the edge of the initial contact. For different tangential loadings, $Q/fP = 0.1, ..., 0.5$, Figure 6.14(a) shows the final normal tractions for the worn contact, where the finite results are shown as solid lines and the results obtained from the asymptotic description are represented by dashed lines. The corresponding results for the shear traction, at the point of maximum shear load, Q, are displayed in Figure 6.14(b) for the trailing edge. We see that the quality of the asymptotic solution strongly depends on the ratio of tangential and normal loading, Q/fP. This follows the asymptotic description of a partial slip contact, which served as a starting point (c.f. equation (6.67)), and requires the slip zone to be small compared to the contact half-width, i.e. $d \ll a$ (Dini and Hills, 2004). The final size of the wear-zone is plotted in Figure 6.15. We compare the extent of the wear-zone, derived for the finite contact in Hills et al. (2009), plotted as

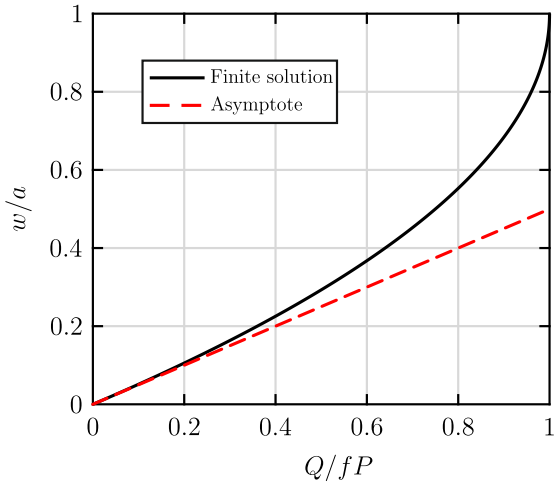


Figure 6.15: Extent of final wear-zone for a Hertzian contact loaded by a tangential load Q/fP, calculated for the finite (solid) and the semi-infinite (dashed) consideration of the contact.

solid lines, to the results from the semi-infinite (asymptotic) model of the contact edge (dashed). For small values of tangential loading, corresponding to small slip zones as a fraction of the contact half-width, we find very good agreement between the asymptote and the finite solution, as required.

Although, this comparison shows results

for a Hertzian contact only, our asymptotic formulation allows us to incorporate the results in various incomplete contact settings as long as we know the asymptotic multiplier, L_I.

4 Fatigue cracks nucleating in the wear-zone

The question arises, how wear, and the resulting tractions, affect the nucleation and propagation of cracks as shown in Figure 6.12(d). We will restrict ourselves to cracks which are short compared to any length characterising the finite contact, so that they only see the asymptotic stress field. For convenience, we consider the point in the load cycle of maximum shear load, with multiplier K_{II} and we want to find the corresponding crack tip stress intensity factors. We can use the same procedure to find the range experienced by the crack tip stress intensity factors, for a range of ΔK_{II}.

We start with finding the stress along the potential crack line, resulting from the final contact tractions. We know that, close to the edge of the wear-zone, both the tractions can be described by the dominating square root singular term. For the final state of wear we find $K_I = fK_{II}$ and $K_{II} = \Delta K_{II}^e/2$ for the normal and shear traction multiplier, respectively. We assume the contact with all its tractions as well as the extent of the wear-zone to be frozen and we can think of the wear-slit as a continuation of the semi-infinite crack in an infinite plane, as the two bodies are stuck together outside the wear-zone, $r > w$. This enables us to use the Williams solution (Williams, 1952) to find the stress field in the (uncracked) lower body, which will now be described with the polar coordinate system having its origin at the wear-stick boundary and not at the initial edge of the contact as before (Fig. 6.12(d)).

We assume cracks to nucleate perpendicular to the surface and together with the crack we introduce a Cartesian coordinate system, whose origin also is at the wear-stick boundary. The x-axis is parallel to the crack and the y-axis aligned with the contact interface, as shown in Figure 6.12(d). For simplicity we start looking at cracks nucleating from the edge of the final contact ($y = 0$ but not the location of the crack shown in Figure 6.12(d)). For a square root singular normal traction the complete bilateral stress field (in the absence of the crack) in polar coordinates as well as the stress along $y = 0$, are obtained by finding the eigenvector corresponding to the eigenvalue $\lambda = 1/2$ from the symmetric part of the Williams solution as

$$\begin{bmatrix} \bar{\sigma}_{rr}(r,\theta) \\ \bar{\sigma}_{\theta\theta}(r,\theta) \\ \bar{\sigma}_{r\theta}(r,\theta) \end{bmatrix} = \frac{-K_I}{4\sqrt{r}} \begin{bmatrix} 5\cos\left(\frac{\theta}{2}\right) - \cos\left(\frac{3\theta}{2}\right) \\ 3\cos\left(\frac{\theta}{2}\right) + \cos\left(\frac{3\theta}{2}\right) \\ \sin\left(\frac{\theta}{2}\right) + \sin\left(\frac{3\theta}{2}\right) \end{bmatrix} = \frac{K_I}{2\sqrt{2}} \frac{1}{\sqrt{r}} \begin{bmatrix} -3 \\ -1 \\ 1 \end{bmatrix}_{\theta=-\frac{\pi}{2}} . \tag{6.92}$$

Analogously we find the stress corresponding to the square-root singular shear traction from the anti-symmetric part of the Williams solution (for the

same eigenvalue $\lambda = 1/2$) to

$$\begin{bmatrix} \bar{\sigma}_{rr}(r,\theta) \\ \bar{\sigma}_{\theta\theta}(r,\theta) \\ \bar{\sigma}_{r\theta}(r,\theta) \end{bmatrix} = \frac{K_{II}}{4\sqrt{r}} \begin{bmatrix} -5\sin\left(\frac{\theta}{2}\right) + 3\sin\left(\frac{3\theta}{2}\right) \\ -3\sin\left(\frac{\theta}{2}\right) - 3\sin\left(\frac{3\theta}{2}\right) \\ \cos\left(\frac{\theta}{2}\right) + 3\cos\left(\frac{3\theta}{2}\right) \end{bmatrix} = \frac{K_{II}}{2\sqrt{2}} \frac{1}{\sqrt{r}} \begin{bmatrix} 1 \\ 3 \\ -1 \end{bmatrix}_{\theta=-\frac{\pi}{2}}. \tag{6.93}$$

The idea is, now, to find a calibration between the crack tip stress intensity factors K_I^c and K_{II}^c and the contact multipliers K_I and K_{II}, characterising the stress field around the edge of the final contact. We follow a similar approach to that used for the calibration between L_I and K_I in §2, only this time we introduce glide and climb edge dislocations along the crack line to ensure the crack faces being traction free with $N(x) = S(x) = 0$ for $0 \leq x \leq l$, where l is the crack length. Corresponding to equations (6.71) and (6.72), the normal and shear traction along the crack line are now given by

$$N(x) = \bar{\sigma}_{yy}(x,0) + \frac{2\mu}{\pi(\kappa+1)} \int_0^l B_y(\xi) G_{yyy}(x,\xi) d\xi, \tag{6.94}$$

and

$$S(x) = \bar{\sigma}_{xy}(x,0) + \frac{2\mu}{\pi(\kappa+1)} \int_0^l B_x(\xi) G_{xxy}(x,\xi) d\xi. \tag{6.95}$$

For the coordinate systems defined as in Figure 6.12(d), we find $\bar{\sigma}_{yy}(x,0) = \bar{\sigma}_{\theta\theta}(r,-\pi/2)$ and $\bar{\sigma}_{xy}(x,0) = \bar{\sigma}_{r\theta}(r,-\pi/2)$. This allows us to use either equation (6.92) or (6.93) for the bilateral stresses, depending on if we want to find the calibration for K_I or K_{II}, respectively. For notational convenience we will describe the following steps for the calibration between K_I and the crack tip stress intensity factors only, but they will be essentially similar for the calibration of K_{II}.

The crack, and therefore the dislocations will be introduced in the lower body, which itself is represented by a half-plane. The corresponding Kernel functions are (Hills et al., 1996)

$$G_{yyy} = G_{xxy} = \frac{1}{x-\xi} - \frac{1}{x+\xi} - \frac{2\xi}{(x+\xi)^2} + \frac{4\xi^2}{(x+\xi)^3}. \tag{6.96}$$

We normalise the integral range, similar to equations (6.75) and (6.76), only, this time using the crack length, l, instead of w. Following the same numerical approach we used in §2, and after dividing equations (6.94) and (6.95) by $K_I/\sqrt{l}$, we are able to find a general solution for the unknowns

$$\hat{\phi}_j(s) = \frac{2\mu}{\pi(\kappa+1)} \frac{\sqrt{l}\phi_j(s)}{K_I}, \tag{6.97}$$

with $j = x, y$ (compare to equation (6.86)). Again, we find the dislocation density at the crack tip by Krenk's interpolation (Krenk, 1975), and the crack tip stress intensity factors to (Hills et al.,

1996)

$$K^c_{I,II} = \sqrt{2\pi}\sqrt{l}\frac{2\mu}{(\kappa+1)}\phi_j(1)$$
$$\Leftrightarrow \frac{K^c_{I,II}}{K_I} = \pi\sqrt{2\pi}\hat{\phi}_j(1), \tag{6.98}$$

where we find K^c_I from ϕ_x and K^c_{II} from ϕ_y. The corresponding calibrations for K_{II}, are then found by choosing equation (6.93) for the bilateral tractions $\bar{\sigma}_{iy}$ in equations (6.94) and (6.95). The corresponding calibration matrix is identified to

$$\begin{Bmatrix} K^c_I \\ K^c_{II} \end{Bmatrix} = \begin{bmatrix} -1.209 & 3.628 \\ 1.209 & -1.209 \end{bmatrix} \begin{Bmatrix} K_I \\ K_{II} \end{Bmatrix}, \tag{6.99}$$

and we point out, again, that this is the result for the crack nucleating from the boundary of the wear-zone.

For the crack nucleating from the edge of the initial contact, as shown in Figure 6.12(d) (or any point within the wear zone), we need to find the stress along a remote line with a distance d. The substitutions $r = \sqrt{x^2+d^2}$ and $\theta = \arctan(x/d) - \pi$, in equation (6.92), together with a rotation of the state of stress by an angle $\varphi = -(\pi/2+\theta)$, to align with the x-y-system, yield expressions for the tractions along the potential crack line caused by a square root singular normal traction, to

$$\bar{\sigma}_{yy}(x,-d) = \frac{K_I}{2\sqrt{2}}\sqrt{\frac{\sqrt{x^2+d^2}-d}{x^2+d^2}} \times \left(1 + \frac{d}{\sqrt{x^2+d^2}} + \frac{2d^2}{x^2+d^2}\right), \tag{6.100}$$

and

$$\bar{\sigma}_{xy}(x,-d) = \frac{K_I}{2\sqrt{2}}\sqrt{\frac{\sqrt{x^2+d^2}+d}{x^2+d^2}} \times \left(1 + \frac{d}{\sqrt{x^2+d^2}} - \frac{2d^2}{x^2+d^2}\right). \tag{6.101}$$

Analogously, we find the tractions along the potential crack line caused by a square root singular shear traction to

$$\bar{\sigma}_{yy}(x,-d) = \frac{1}{2\sqrt{2}}K_{II}\sqrt{\frac{\sqrt{x^2+d^2}+d}{x^2+d^2}} \times \left(3 - \frac{d}{\sqrt{x^2+d^2}} + \frac{2d^2}{x^2+d^2}\right), \tag{6.102}$$

and

$$\bar{\sigma}_{xy}(x,-d) = \frac{1}{2\sqrt{2}}K_{II}\sqrt{\frac{\sqrt{x^2+d^2}-d}{x^2+d^2}} \times \left(1 + \frac{d}{\sqrt{x^2+d^2}} + \frac{2d^2}{x^2+d^2}\right). \tag{6.103}$$

As the bilateral tractions, (6.100) to (6.103), the calibration will now depend on the ratio of crack length and remote distance, d/l, i.e.

$$\begin{Bmatrix} K^c_I \\ K^c_{II} \end{Bmatrix} = \begin{bmatrix} -1.209\, g^1_I(d/l) & 3.628\, g^1_{II}(d/l) \\ 1.209\, g^2_I(d/l) & -1.209\, g^2_{II}(d/l) \end{bmatrix} \begin{Bmatrix} K_I \\ K_{II} \end{Bmatrix}, \tag{6.104}$$

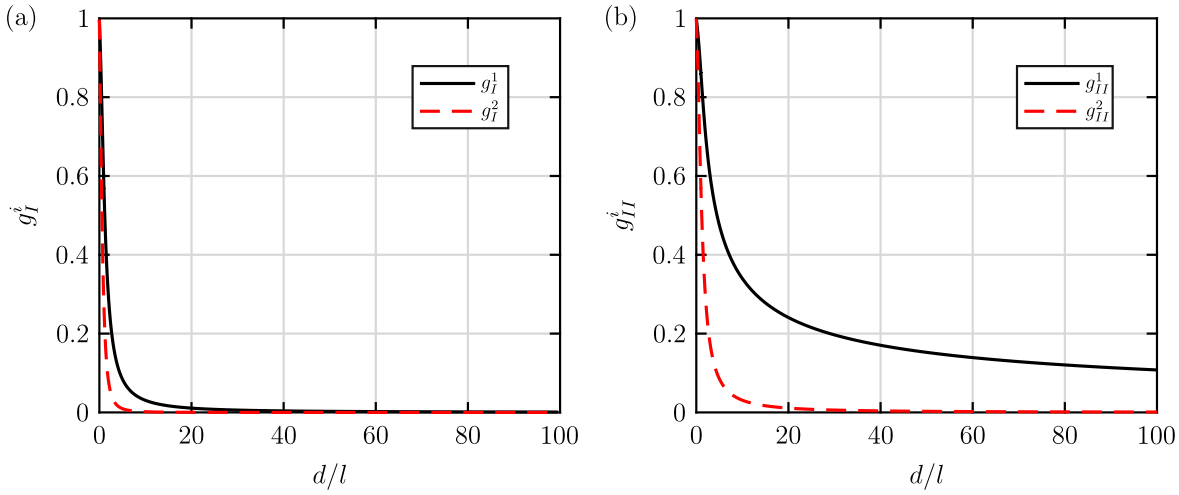


Figure 6.16: Remote calibration between crack tip stress intensity factors $K^c_{I,II}$ and (a) a singular normal traction K_I by means of $g_I^{1,2}$ and (b) a singular shear traction K_{II} by means of $g_{II}^{1,2}$.

where $g_{I,II}^{1,2} = 1$ for $d/l = 0$ (c.f. equation (6.99)). For a varying ratio $0 \leq d/l \leq 100$ the evaluated functions $g_{I,II}^{1,2}$, representing the calibration between crack tip stress intensity factors K_I^c and K_{II}^c and contact multipliers K_I and K_{II}, are shown in Figure 6.16. We find the biggest influence of the contact tractions on the crack tip stress intensity factors, close to the singularity at the edge of the final contact. If the crack length, l, is short compared to the remote distance, d, we find the influence of the contact shear traction on the mode I crack tip stress intensity factor, to dominate. Each point in Figure 6.16, represents the evaluation of the singular integral equations (6.94) and (6.95), where we chose a specific ratio, d/l. Even though we are not able to find closed form expressions for $g_{I,II}^{1,2}$, here, we want to fit rational functions to the results obtained for discrete values of d/l. These rational functions consist of polynomials over polynomials of the form

$$g_{I,II}^{1,2}\left(\frac{d}{l}\right) \approx \frac{\sum_{j=0}^{5} p_j \left(\frac{d}{l}\right)^j}{\sum_{j=0}^{5} q_j \left(\frac{d}{l}\right)^j} \tag{6.105}$$

We used the *Matlab* build in function `fit()` to identify the different coefficients. The highest coefficient, q_i, is generally chosen to 1, and a coefficient p_i or $q_i = 0$, represents the choice of a lower order for the corresponding polynomial, rather than the result of the fit. Furthermore, the constraint $q_i \geq 0$, ensures the avoidance of singularities. The identified coefficients for the four functions $g_{I,II}^{1,2}$ are listed in table 6.3.

The above found calibrations enable us to find the crack tip stress intensity factor for a crack nucleating from the edge

of the initial contact to

$$\frac{K_I^c}{\Delta K_{II}^e} = -\frac{1}{2}\left(1.209\, f\, g_I^1\left(\frac{d}{l}\right) - 3.628\, g_{II}^1\left(\frac{d}{l}\right)\right), \tag{6.106}$$

and

$$\frac{K_{II}^c}{\Delta K_{II}^e} = \frac{1}{2}\left(1.209\, f\, g_I^2\left(\frac{d}{l}\right) - -1.209\, g_{II}^2\left(\frac{d}{l}\right)\right), \tag{6.107}$$

where we used $K_I = fK_{II}$ and $K_{II} = \Delta K_{II}^e/2$ together with equation (6.104) and normalised the resulting relations in terms of the range of the initial contact shear multiplier, ΔK_{II}^e, which is given by equation (6.64). d still denotes the initial slip zone length (6.65), for cracks nucleating from the edge of the initial contact but may be chosen freely to describe cracks nucleating from within the wear-zone. We want to compare the results found from equation (6.106) and (6.107), for cracks nucleating in the asymptotic subsurface stress field, to results for cracks seeing the stress field corresponding to the finite representation of the contact. We find the finite tractions (as for the comparison in §3) from Hills et al. (2009). For brevity we do not want to derive the subsurface stress field for the finite contact, here, but equations for obtaining it from the contact tractions can be found from Vázquez et al. (2012). The crack tip stress intensity factors for the finite solution is the found by replacing the bilateral stress, $\bar{\sigma}_{iy}$, in equations (6.94) and (6.95) by the stress found for the finite description of the subsurface stress field. Figure 6.17 shows, for different ratios of tangential loading, $Q/fP = 0.1, ..., 0.9$, the crack tip stress intensity factor corresponding to the asymptotic considerations, introduced here, to the results we find for a finite description of the contact and the corresponding stress field.

We find good agreement as long as the crack length, l, is short compared to the remote distance, d. For the crack growing from the contact interface, eventually reaching a region where the subsurface stress field is not sufficiently repre-

Table 6.3: Identified coefficients for the fit of rational functions to the results of the remote calibration.

Calibration	p_5	p_4	p_3	p_2	p_1	p_0
g_I^1	0	0.046	7.645	50.94	32.43	45.19
g_I^2	0	0	5.00e-4	-1.26e-3	4.457	19.32
g_{II}^1	6.83e-3	55.77	1.33e4	1.84e5	2.03e4	3.72e5
g_{II}^2	0	0.045	7.645	50.94	32.43	45.19
	q_5	q_4	q_3	q_2	q_1	q_0
g_I^1	1	28.26	48.85	69.06	47.24	45.17
g_I^2	0	1	23.85	21.1	23.49	19.31
g_{II}^1	1	1157	6.53e4	1.85e5	6.05e4	3.72e5
g_{II}^2	1	28.26	48.85	69.06	47.24	45.17

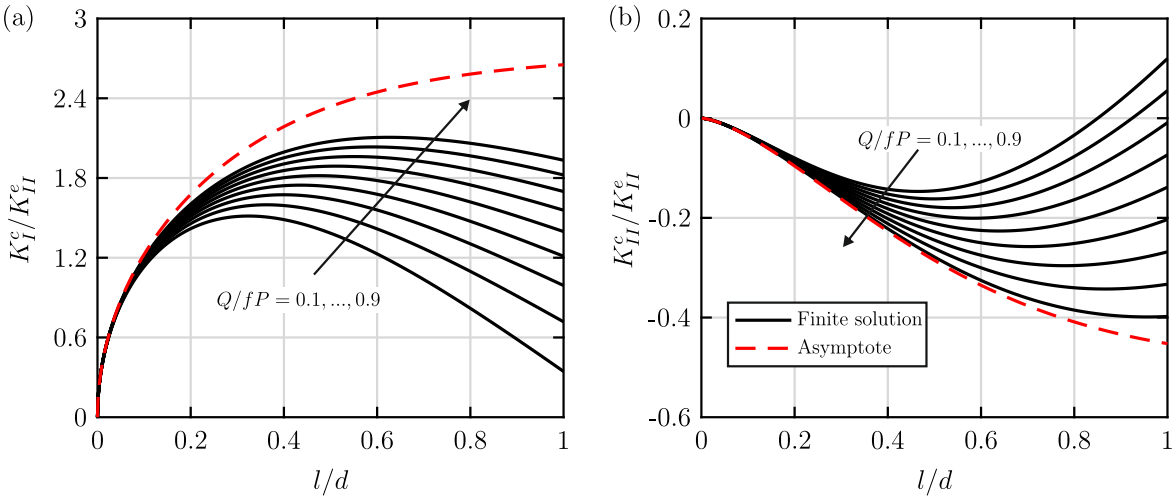


Figure 6.17: Comparison of asymptotic and finite results of crack tip stress intensity factors a) K_I^c and b) K_{II}^c for a crack nucleating from the initial edge of the contact. Different ratios of tangential loading, $Q/fP = 0.1, ..., 0.9$, are considered ($f = 0.75$).

sented by the asymptotic solution, the crack tip stress intensity factor can not be found from the asymptotic considerations any longer. For the chosen normalisation, we find the results corresponding to the asymptotic description, to be independent of the ratio of normal and tangential loading, Q/fP. Furthermore, as for the asymptotic representation of the contact traction, the results shown in Figure 6.17 can be incorporated in any incomplete contact geometry as long as we know the geometry dependent normal multiplier L_I.

5 Conclusion

We have considered a general incomplete contact edge subject to oscillatory tangential loading originating from a shear load, Q, and a differential bulk tension, σ_0. With a semi-infinite consideration of the contact edge, distributed dislocations have been used to account for the profile reduction due to wear. The results derived are not connected to a specific wear law and no attempt was made to describe the growth of the wear-zone in terms of the number of experienced load cycles. The final relations allow us to characterise the singularities in normal and shear traction close to the boundary of the wear-zone, in terms of a calibration between the corresponding contact multipliers, K_I and K_{II}, and those at the initial edge of the unworn contact, L_I and K_{II}^e. A comparison with a finite Hertzian contact shows good agreement as long as the extent of the wear-zone is short compared to the contact half-width.

Based on the asymptotic form of the contact tractions, we found the subsurface stress field corresponding to the final state of the worn contact. Calibrations between crack tip stress intensity factors and the multipliers characterising the contact tractions are given for cracks nucleating from the initial contact interface. The crack might nucleate at the initial edge of the contact, or anywhere

within the wear-zone. The accuracy of the asymptotic crack tip stress intensity factor calibration depends on the crack length and the distance to the edge of the worn contact. Both the calibration for the worn contact tractions as well as for the crack tip stress intensity factors can be incorporated into different incomplete contact problems, as long as the geometry dependent asymptotic multiplier, L_I, is known.

Acknowledgements

N. Cwiekala and D. A. Hills thank Rolls-Royce plc and the EPSRC for the support under the Prosperity Partnership Grant 'Cornerstone: Mechanical Engineering Science to Enable Aero Propulsion Futures', Grant Ref: EP/R004951/1.

Chapter 7

Shakedown of a Continuous Coupled Contact

In Chapter 6, we analysed partial slip contacts with regard to fretting fatigue and fretting wear and how this affects the life of a mechanical structure. Furthermore, the relative slip displacements and the corresponding energy dissipation will affect the system's damping, and in this context, we have already addressed the phenomenon of *shakedown*.

In Section 2.7, a discretised approach to the steady-state behaviour and shakedown of coupled contacts is described from the literature (Ahn et al., 2008; Jang and Barber, 2011a; Barber, 2016). Here, we examine the same phenomenon for a continuous description of the contact.

7.1 Memory-free loading paths for a coupled continuous contact problem with friction

In the first part of this chapter, we analyse a coupled contact capable of an analytic description of the contact tractions. A concise mathematical description reveals the system's main characteristics. Distributed dislocations are used to find the slip-corrected tractions along the contact interface. Conditions for memory-free loading paths are identified, preparing the study of the steady-state response in cyclic loading.

Memory-free loading paths for a coupled continuous contact problem with friction

N. Cwiekala[a,1], J. R. Barber[b], D. A. Hills[a]

[a] *Department of Engineering Science, University of Oxford, Parks Road, OX1 3PJ Oxford, United Kingdom*
[b] *Department of Mechanical Engineering, University of Michigan, Ann Arbor, MI 48109-2125, USA*

Abstract

The plane elastic problem of a circular disk shrink fitted into a hole in an elastically similar plane, with a frictional interface, is studied subject to the application of a radial force and torque both of which vary with time. This is done by the use of edge dislocation distributions to represent slip. The evolution of extent and position of a slip zone as well as the magnitude of slip displacements is studied. Conditions for continuous slip, leading a history or load path independent solution are derived. The results derived prepare for the study of the shakedown behaviour of a continuous coupled contact.

Keywords:
coupled contact, memory-free, partial slip, distributed dislocations, shakedown

1 Introduction

Contacts potentially in partial slip arise in many mechanical assemblies, some very complicated such as a gas turbine. Contacts are often subjected to a constant component of load (such as bolt tightening) or slowly varying load (such as the centrifugal forces developed in the engine) together with a high frequency oscillatory component, normally originating in vibration. Where there is slip in the steady state the conditions are ripe for crack nucleation – so called fretting fatigue – but, on the other hand, the cyclic slip absorbs energy and therefore causes damping, limiting the severity of the effect. If the contact starts off in partial slip but later becomes stuck, owing to the development of locked-in interfacial slip displacements with attendant tractions, it is said to 'shake down', a term borrowed from plasticity theory where it implies the evolution of an initial elastic-plastic phase to an elastic steady state. Contacts which are fully stuck may actually have a slightly higher stress concentration at their edges but do not suffer from surface degradation, and they also, evidently, do not damp energy. One ambition of the gas turbine industry is to produce a 'whole engine model' in which,

[1] Corresponding author
Email address: nils.cwiekala@eng.ox.ac.uk (N. Cwiekala)

at some level of fidelity, all joints or contacts are included, and it would be valuable to know if, in the steady state, they are adhered or suffering cyclic slip.

One possible method of analysis is simply to form a model of the contact and track out the evolution of the interfacial behaviour as a function of time, but this does not seem a very realistic proposition in the case of the engine where there are hundreds of contacts whose responses will, to some extent, interact. So, it would be valuable to be able to predict the steady state response without tracking out the transient, if this is possible. The analogy between frictional slip and plastic slip is quite strong insofar as frictional slip is an orthogonal process *within the slip plane*, but not in an overall sense. The question as to whether Melan's elastic-plastic shakedown theorem (*'if a residual stress state may be found which, together with the applied stress, lies always within the yield (or frictional slip) boundary, shake down to an elastic (or fully stuck) condition* ***will*** *occur'*) applies to frictional contacts was probed analytically from basic principles by Klarbring et al. (2007) as well as Barber et al. (2008). It was concluded that the Melan theorem would apply to frictional contacts only when there is 'no coupling', that is, where a change in interfacial slip displacements produces no change in the normal contact tractions, and vice versa. Uncoupled contacts strictly arise only when the bodies

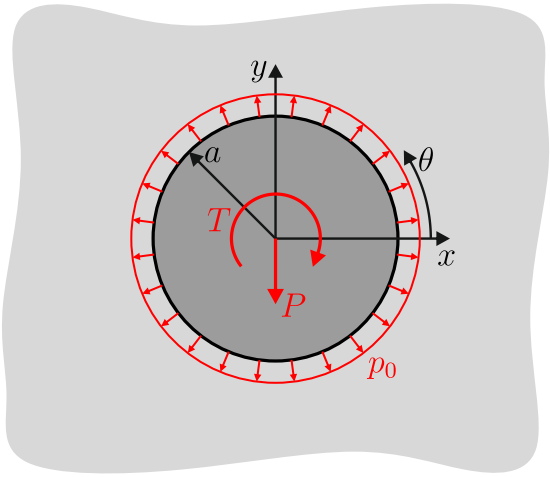


Figure 7.1: Shrink fitted disc in an infinite plane with a hole

pressed together are geometrically the same and made from the same material (i.e. where the contact surface is a plane of symmetry), but this statement is almost true for any incomplete contact which is capable of idealisation within the framework of a half-plane (space), provided Dundurs' elastic mismatch parameter $\beta = 0$. Other contacts can be expected to show at least some degree of coupling.

Incomplete contacts can never achieve a shaken down state because the contact pressure always falls smoothly to zero in a square root bounded manner near the edge, so that it is impossible to inhibit all slip. Equally, complete contacts are either fully stuck at their edges from the outset or have a very complicated local edge behaviour involving a very small region of local separation (Churchman and Hills, 2006) and so neither class represents a good problem to study the shakedown behaviour within the context of a strongly coupled contact capable of analytical attack. Therefore, in this paper we study the problem depicted in Figure

7.1, which does have all the right characteristics.

2 Problem Statement

With an elastic disk of radius a fitted into a circular hole in an infinite plate, the problem shows similarities to that of a circular inclusion studied by Keer et al. (1973) and Kelly et al. (1994) (among others). The essence of the 'inclusion problem' typically is the elastic mismatch, representing a source of coupling. Here, we assume both bodies to be elastically similar, such that the geometry is the sole source of coupling. The hole is slightly smaller than the disk so that an interfacial contact pressure of magnitude p_0 is developed, constant around the circumference, where both surfaces are assumed to be smooth. We start from this axisymmetric state of stress and apply a force, P, in the $\theta = 3\pi/2$ direction as well as a torque of magnitude T, positive in the sense shown, at the origin.

2.1 The bilateral solution

Initially, we assume that the interface remains stuck, so that the *change* in the state of stress due to these loads is the same as that in a monolithic infinite body. The contact tractions,

$$p(\theta) = -\sigma_{rr}(a,\theta)\ ; \quad q(\theta) = -\sigma_{r\theta}(a,\theta)$$

can therefore be found as

$$p(\theta) = p_0 - \frac{\kappa+3}{\kappa+1}\frac{P}{2\pi a}\sin\theta \tag{7.1}$$

$$q(\theta) = -\frac{T}{2\pi a^2} - \frac{\kappa-1}{\kappa+1}\frac{P}{2\pi a}\cos\theta \tag{7.2}$$

(See Barber, 2010, *Elasticity*, p. 119), where κ is Kolosov's constant, defined as

$$\kappa = \begin{cases} 3-4\nu & \text{for plane strain,} \\ \frac{3-\nu}{1+\nu} & \text{for plane stress,} \end{cases}$$

and ν is Poisson's ratio. Slip is avoided provided that, for all θ,

$$|q(\theta)| < f\,p(\theta), \tag{7.3}$$

where f is the coefficient of friction. Using equations (7.1, 7.2), we can express the inequality (7.3) as

$$\left(\frac{\kappa+3}{\kappa+1}\right) f\widetilde{P}\sin\theta \pm \left[\left(\frac{\kappa-1}{\kappa+1}\right)\widetilde{P}\cos\theta + \widetilde{T}\right] < 2\pi f\ , \tag{7.4}$$

where

$$\widetilde{P} = \frac{P}{p_0 a}\ ; \quad \widetilde{T} = \frac{T}{p_0 a^2} \tag{7.5}$$

are the normalized radial load and torque, respectively. The left-hand side of this inequality varies sinusoidally with θ, and elementary calculations show that it will be satisfied for all θ if and only if

$$\chi\left|\widetilde{P}\right| + \left|\widetilde{T}\right| < 2\pi f\ , \tag{7.6}$$

where the dimensionless parameter

$$\chi = \sqrt{\left(\frac{\kappa-1}{\kappa+1}\right)^2 + f^2\left(\frac{\kappa+3}{\kappa+1}\right)^2}\ . \tag{7.7}$$

This condition allows us to identify the region of full-stick in normalised load space, as shown in Figure 7.2. If $\widetilde{P} > 0$,

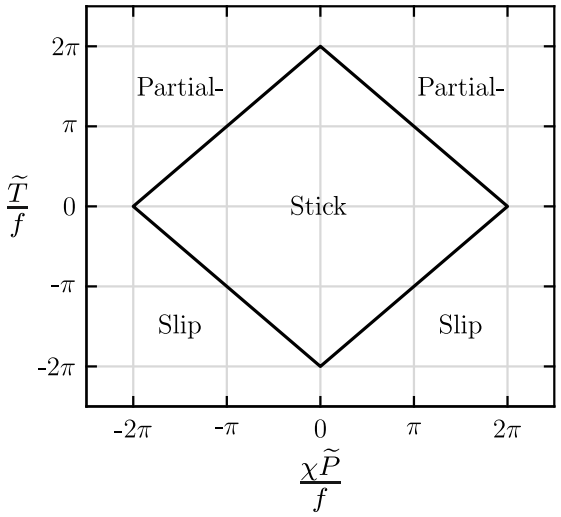


Figure 7.2: Boundaries of the stick region in normalised P-T-space.

and $\widetilde{T} > 0$, the inequality (7.4) can be expressed as

$$\cos(\theta - \alpha) < \lambda \equiv \frac{2\pi f - \widetilde{T}}{\chi \widetilde{P}} \,, \qquad (7.8)$$

where

$$\alpha = \arctan\left(f\frac{\kappa+3}{\kappa-1}\right) \;;\; 0 < \alpha < \frac{\pi}{2} \qquad (7.9)$$

Corresponding results for cases where $\widetilde{P}$ and/or $\widetilde{T}$ are negative can be determined from symmetry arguments. If $\lambda > 1$, the inequality (7.8) is satisfied for all θ, so $\lambda = 1$ defines the boundary of the full stick region in Figure 7.2. If $\widetilde{P}$ and $\widetilde{T}$ are increased so as to cross this boundary, λ will decrease and slip will commence at the point $\theta = \alpha$, which is independent of the actual values of $\widetilde{P}$ and $\widetilde{T}$.

2.2 Memory-free states

If we start from the origin and cross the stick region boundary in Figure 7.2 to an exterior point $\{\widetilde{P}, \widetilde{T}\}$, some slip must occur, which we characterize by the *slip displacement*

$$h(\theta) = u_\theta(a^+, \theta) - u_\theta(a^-, \theta) \,. \qquad (7.10)$$

Generally, the distribution of slip displacement, and therefore the state of stress, will depend on the exact loading path $\boldsymbol{r}(t) = \{\widetilde{P}(t), \widetilde{T}(t)\}$ we take from the origin to the point $\{\widetilde{P}, \widetilde{T}\}$, where t denotes time. However, there exists a subset of 'memory-free' paths $\boldsymbol{r}_C(t)$ for which the final state is not loading-history dependent. A primary purpose of the present paper is to characterize the conditions that must be met for a particular loading path to be memory free, and also to investigate the states reached when these conditions are not met.

In frictional problems, the system memory resides in the non-zero slip displacements h in stick regions that satisfy the inequality (7.3) in the strict sense. Thus, if a state at $\{\widetilde{P}, \widetilde{T}\}$ was reached by a memory-free load path, it must satisfy the linear complementary [LCP] condition

$$h(\theta)\left(|q(\theta)| - fp(\theta)\right) = 0, \qquad (7.11)$$

for all θ. In other words, the interface is partitioned into a stick region, where there is no slip displacement, and a slip region throughout which there is incipient slip with $q(\theta) = \pm fp(\theta)$. States that do not satisfy this condition exhibit regions that slipped during a previous segment of the load path, but which are now strictly below the incipient slip condition. For a given point $\{\widetilde{P}, \widetilde{T}\}$ there exists one and only one memory-free state

$S_C(\widetilde{P},\widetilde{T})$. In other words, the boundary-value problem has a unique solution of which the mathematical formulation is described in the next section.

3 Formulation for partial slip

Partial slip – i.e. slip in part but not all of the interface $0 \leq \theta < 2\pi$ – can be described by superposing distributions of Volterra edge dislocations at the interface on the bilateral solution of Section 2.1. We define the distributions $B_\theta(\phi), B_r(\phi)$ such that in the infinitesimal interval $\theta = [\phi, \phi + \delta\phi]$ we have dislocations with Burgers vector components

$$\begin{aligned} b_\theta &= B_\theta(\phi)\,\delta\phi \qquad \text{and} \\ b_r &= B_r(\phi)\,\delta\phi. \end{aligned} \tag{7.12}$$

Since the materials of the disc and the surrounding space are the same, we use the solution for a dislocation in an infinite plane (see e.g. Weertman, 1996). In particular, it can be shown that a concentrated dislocation $\{b_\theta, b_r\}$ located at (a,ϕ) induces tractions $\{q(\theta), p(\theta)\}$ at (a,θ) given by

$$\begin{Bmatrix} q(\theta) \\ p(\theta) \end{Bmatrix} = \frac{2\mu}{\pi(\kappa+1)\,a} \begin{bmatrix} K_{q\theta} & K_{qr} \\ K_{p\theta} & K_{pr} \end{bmatrix} \begin{Bmatrix} b_\theta(\phi) \\ b_r(\phi) \end{Bmatrix}, \tag{7.13}$$

where μ is the modulus of rigidity and

$$\begin{aligned} K_{q\theta}(\theta,\phi) &= K_{pr}(\theta,\phi) \\ &= \frac{\sin(\theta-\phi)\cos(\theta-\phi)}{2(1-\cos(\theta-\phi))} \\ K_{qr}(\theta,\phi) &= -\frac{1}{2}\cos(\theta-\phi) \\ K_{p\theta}(\theta,\phi) &= \frac{1}{2}(\cos(\theta-\phi)+2). \end{aligned} \tag{7.14}$$

Although the state of stress induced by these dislocations is independent of the path cut, the line of the cut must be chosen so that it follows the line of discontinuity of displacements, i.e. the interface between the two bodies. On the other hand, the path cut has to go to infinity at some point, so it cannot follow the interface exclusively. The problem is similar to that in a crack problem, where the path cut must follow the crack up to the tip after which it can go to infinity by any arbitrary path, because we impose a closure condition.

In this paper, we restrict attention to cases in which the radial force is insufficient to cause separation, so the radial component of displacement is continuous across the interface, the only discontinuity being that in the tangential direction. For this case, the dislocation distributions and the slip displacement are related by the equations (Hills et al., 1996)

$$B_\theta(\phi) = \frac{1}{a}\frac{dh(\phi)}{d\phi}\,; \quad B_r(\phi) = -\frac{h(\phi)}{a} \tag{7.15}$$

and hence

$$B_\theta(\phi) + \frac{dB_r}{d\phi} = 0 \tag{7.16}$$

The contact tractions due to fairly general dislocation distributions can be obtained by convolution on equation (7.13). After superposing the bilateral solution (7.1, 7.2), we obtain

$$p(\theta) = p_0 - \frac{\kappa+3}{\kappa+1}\frac{P}{2\pi a}\sin(\theta) + \frac{2\mu}{\pi(\kappa+1)}\int_{\eta_1}^{\eta_2}[B_\theta(\phi)K_{p\theta}(\theta,\phi) + B_r(\phi)K_{pr}(\theta,\phi)]\,d\phi \tag{7.17}$$

$$q(\theta) = -\frac{T}{2\pi}\frac{1}{a^2} - \frac{\kappa-1}{\kappa+1}\frac{P}{2\pi a}\cos(\theta) + \frac{2\mu}{\pi(\kappa+1)}\int_{\eta_1}^{\eta_2}[B_\theta(\phi)K_{q\theta}(\theta,\phi) + B_r(\phi)K_{qr}(\theta,\phi)]\,d\phi\,, \tag{7.18}$$

where we note that dislocations are present only in the slip zone, defined here as $\eta_1 < \phi < \eta_2$.

3.1 Slip condition

In the slip zone, the contact tractions must satisfy the equality $q(\theta) = \pm f p(\theta)$ and if slip is generated as a result of crossing the boundary in the quadrant in Figure 7.2 corresponding to $P, T > 0$, we must take the negative sign. Equations (7.17, 7.18) with the notation of equations (7.5, 7.7, 7.9) then yield the dimensionless singular integral equation

$$\int_{\eta_1}^{\eta_2}\hat{B}_\theta\,[K_{q\theta}+fK_{p\theta}]+\hat{B}_r\,[K_{qr}+fK_{pr}]\,d\phi = \frac{1}{4}(\cos(\theta-\alpha)-\lambda) \tag{7.19}$$

where

$$\hat{B}_i(\phi) = \frac{\mu}{(\kappa+1)}\frac{B_i(\phi)}{p_0\chi\widetilde{P}}\,, \tag{7.20}$$

$i = r, \theta$, and we have omitted the arguments (ϕ) on $\hat{B}_i$ as well as (θ,ϕ) on $K_{p\theta}$ etc. for brevity.

Throughout this analysis, we have assumed that there is a single slip zone, but if $T = 0$, the problem is symmetrical about the y-axis in Figure 7.1 and first slip will be determined by the development of two symmetrically disposed slip zones on either side of $\theta = \pi/2$.

We also need to satisfy the closure condition

$$\int_{\eta_1}^{\eta_2}\hat{B}_\theta(\phi)d\phi = 0\,, \tag{7.21}$$

which serves to determine the extent of the slip zone.

4 Numerical solution of the integral equation

After normalisation of the integral range (Comninou, 1978)

$$2\phi = (\eta_2-\eta_1)s + (\eta_2+\eta_1) \tag{7.22}$$

and

$$2\theta = (\eta_2-\eta_1)t + (\eta_2+\eta_1)\,, \tag{7.23}$$

the singular integral equation (7.19) can be solved numerically. We employ the Gauss-Chebyshev quadrature introduced by Erdogan and Gupta (1972). Bounded behaviour is enforced at both ends of the slip zone by extracting the factor $\omega(s) = \sqrt{1-s^2}$ from the solution, $B_i(s) = \omega(s)\psi_i(s)$. Following the quadrature for bounded-bounded end-point behaviour, described in Hills et al. (1996), this provides a system of $N+1$ equations to ful-

fil the slip condition at the N integration points s_j. The condition to preserve radial displacement continuity (7.16) provides another equation at each of the N integration points. In discretized form, this reads

$$\omega(s_j)\psi_r(s_j) = \frac{\pi}{2}(\eta_2 - \eta_1)\sum_{m=1}^{j} W_m \psi_\theta(s_m), \tag{7.24}$$

where the weights, W_m, are given in Hills et al. (1996). This leads to a system of $2N+1$ equations for the $2N$ unknowns $\psi_\phi(s_j)$ and $\psi_r(s_j)$ as well as the angles η_1 and η_2.

The presence of the unknown angles η_1 and η_2 makes the system of equations nonlinear. We follow a somewhat similar procedure to that described in Comninou (1977) and Comninou (1978). To each of the $N+1$ equations, expressing the slip condition, we add a dummy variable, ψ_d. The resulting system of equations is linear in the $2N+1$ unknowns $\psi_\phi(s_j)$, $\psi_r(s_j)$ and ψ_d, and can be inverted for a given choice of η_1 and η_2. Employing a minimisation algorithm, we may then find the specific combination of η_1 and η_2, for which $\psi_d = 0$ and equation (7.21) is fulfilled. Notice that, provided the function $\psi_i(s)$ is a polynomial, for a sufficiently high number of integration points, N, the Gauss-Chebyshev quadrature will return *exact* values at the points s_j (Hills et al., 1996). Here, convergence was reached for $N = 80$ integration points.

5 Partial slip results

Figure 7.3(a) shows the contact tractions $p(\theta), q(\theta)$ for the case where $\widetilde{P} = 3$ and

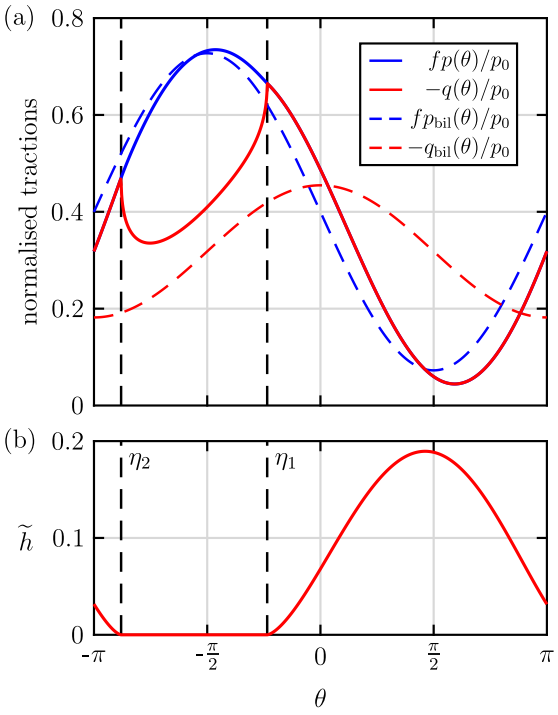


Figure 7.3: (a) Normal and shear traction for $\widetilde{P} = 3$ and $\widetilde{T} = 2$ shown as solid lines, with bilateral solution as dashed lines and (b) normalised tangential slip displacement along the circumference (plane strain with $\nu = 0.3$, $f = 0.4$).

$\widetilde{T} = 2$ in Figure 7.2. The dashed lines show the bilateral tractions of equations (7.1, 7.2) and the solid lines show the tractions as modified by partial slip. Notice that the normal tractions are presented through the combination $fp(\theta)$ since this expression also defines the shear tractions in the slip zone. The corresponding normalized slip displacement

$$\widetilde{h}(\theta) = \frac{\mu h(\theta)}{(\kappa+1)p_0 a} \tag{7.25}$$

is shown in Figure 7.3(b).

Notice that the normal tractions $p(\theta)$ are modified by partial slip, which reflects the normal-tangential coupling in this geometry. One consequence of this is that the boundary in $\{\widetilde{P}, \widetilde{T}\}$ space at

which partial slip gives way to separation is influenced by the coefficient of friction. The shear tractions $q(\theta)$ represent a much larger deviation from the bilateral solution and exhibit the classical square-root bounded asymptotic behaviour at the ends of the stick zone.

6 Boundary of the partial slip region

If the loads $\{\widetilde{P}, \widetilde{T}\}$ move further away from the stick-slip boundary in Figure 7.2, eventually the partial slip state must transition either to full slip, or to a state involving partial slip and separation.

For full slip, we have $q(\theta) = \pm f p(\theta)$ for all θ and the torque can be obtained as

$$T = a^2 \int_0^{2\pi} q(\theta) d\theta = \pm f a^2 \int_0^{2\pi} p(\theta) d\theta \ . \tag{7.26}$$

Subsituting for $p(\theta)$ from (7.17) and evaluating the integrals, we obtain

$$T = \pm 2\pi f p_0 a^2 \quad \text{or} \quad \widetilde{T} = \pm 2\pi f \ , \tag{7.27}$$

since the other terms in (7.17) integrate to zero. For example

$$\int_0^{2\pi} \int_0^{2\pi} B_i(\phi) K_{ji}(\theta, \phi) d\phi d\theta = \int_0^{2\pi} B_i(\phi) \int_0^{2\pi} K_{ji}(\theta, \phi) d\theta d\phi \ . \tag{7.28}$$

The inner integral is zero from (7.14) except for the case $j = p$, $i = \theta$, where the closure condition ensures that the outer integral is zero. Thus the full slip boundary depends only on the applied torque T and is independent of P. This boundary is defined by horizontal solid lines at $\widetilde{T}/f = \pm 2\pi$ in Figure 7.2, and it corresponds to the condition $\lambda = 0$, where λ is defined in equation (7.8).

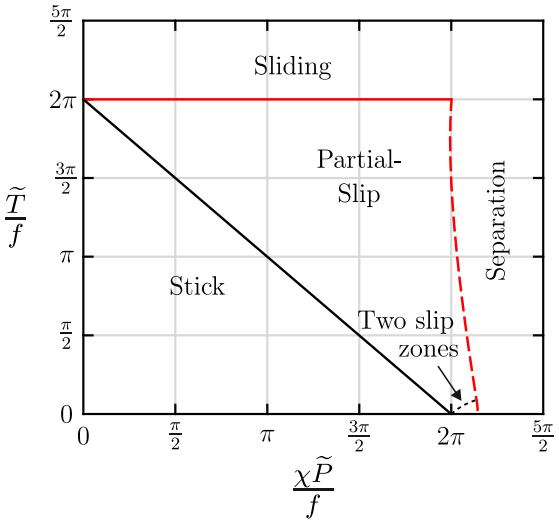


Figure 7.4: Limit state boundaries in normalised P-T-space taking effects of partial slip into consideration (plane strain with $\nu = 0.3$, $f = 0.4$)

By contrast, the shape of the separation boundary depends on the coefficient of friction, the result for $f = 0.4$ and $\nu = 0.3$ being shown in Figure 7.4. This dependence is relatively weak, but we also note that if $\widetilde{T} \ll \widetilde{P}$, memory free loading paths can be found in which a second 'detached' slip zone develops before separation. This range occupies a larger part of the load space at lower values of f.

7 The incremental problem

In this section, we pose the question *"What conditions must be satisfied by a load path $\boldsymbol{r}(t)$ in order that it be memory-free – i.e. ,$\boldsymbol{r} \in \boldsymbol{r}_C$?"*

Suppose we have reached a given point $\{\widetilde{P}, \widetilde{T}\}$ by a memory-free path and we now make an infinitesimal change in the

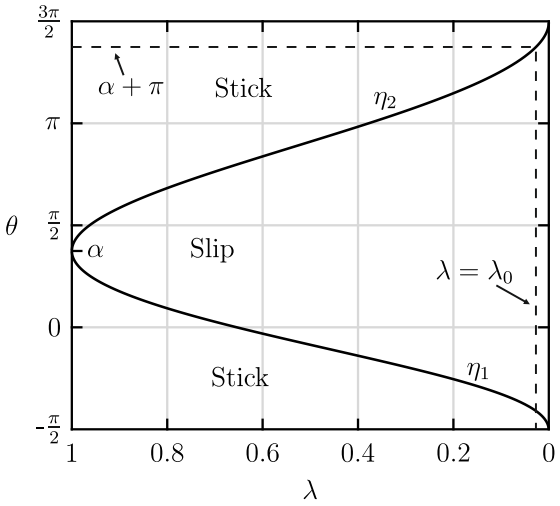


Figure 7.5: Evolution of the slip zone as the loading parameter λ is reduced (plane strain with $\nu = 0.3,\ f = 0.4$)

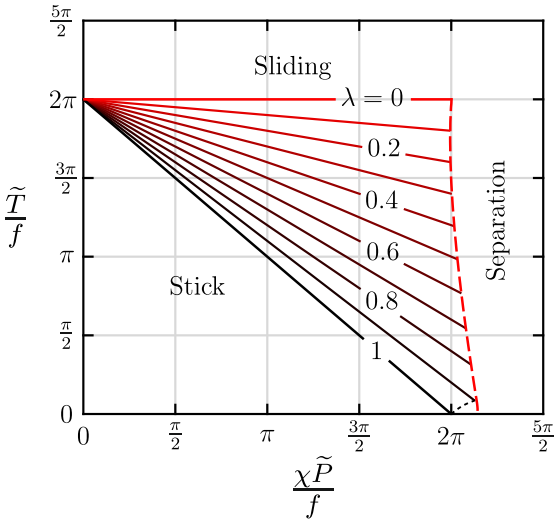


Figure 7.6: Contours of λ and hence of constant slip extent

loads to $\{\widetilde{P}+\delta\widetilde{P}, \widetilde{T}+\delta\widetilde{T}\}$. This new state will also be memory free if and only if the LCP condition (7.11) is satisfied for all θ during the loading increment. In particular, (i) the slip boundaries η_1, η_2 must not recede, and (ii) the slip displacement $\widetilde{h}(\theta)$ must not decrease at any point in the slip zone. If condition (ii) is not satisfied, a stick region will develop from the point of first violation.

We first note that the governing integral equation (7.19) depends on the loads only through the parameter λ defined in equation (7.8). Figure 7.5 shows the evolution of the slip region as we move from the stick boundary $\lambda = 1$ to the full slip boundary $\lambda = 0$. Notice that both boundaries advance as λ is decreased, so a necessary condition for a memory-free path is that $\mathrm{d}\lambda/\mathrm{dt} \leq 0$. Figure 7.6 shows contours of constant slip extent, and hence of constant λ. Equation (7.8) shows that these contours are all straight lines passing through the point $(0, 2\pi)$. Thus, if we are instantaneously at a point on one of the contours, the memory-free condition requires that subsequent motion be directed into the region above and to the right of that contour.

For a given value of λ, the dislocation distributions $B_i(\phi)$ and hence the slip displacements $\widetilde{h}(\theta)$ are proportional to $\widetilde{P}$, from equation (7.20). It follows that if we move along one of the lines of constant λ in Figure 7.6 in the direction of decreasing $\widetilde{P}$, the slip zone extent will remain constant, but the slip displacement will decrease for all θ, violating the LCP condition (7.11). Thus a more stringent condition than $\mathrm{d}\lambda/\mathrm{dt} \leq 0$ must be imposed to ensure that the loading path is memory free in cases where $\widetilde{P}$ is decreasing. This condition can be determined by choosing the loading direction such that all points in the instantaneous slip region continue to slip, except for one point at which the slip velocity is zero. Figure 7.7 shows a set of contours such that to satisfy this condition when $\dot{P} < 0$, these contours must be crossed from below in order that the state remain memory-free.

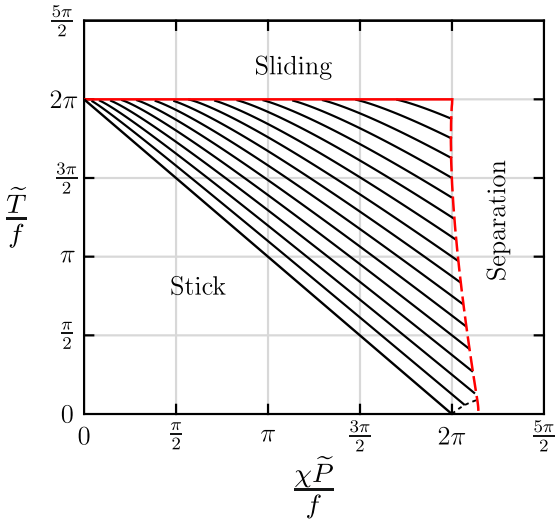


Figure 7.7: Contours which must be crossed from below to ensure a memory-free state when $\dot{P} < 0$ (plane strain with $\nu = 0.3$, $f = 0.4$)

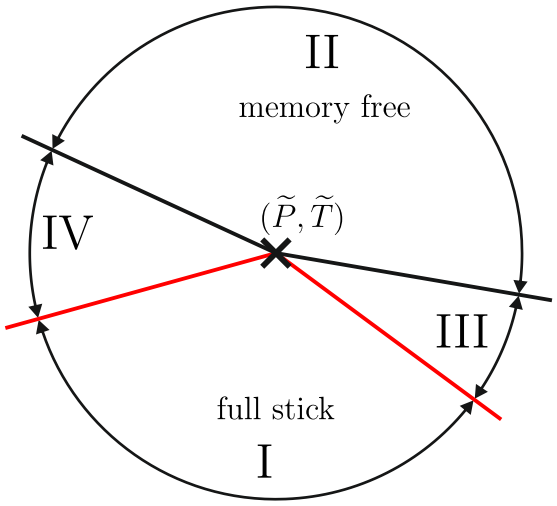


Figure 7.8: Incremental loading pointing into region II in normalised P-T-space will preserve a memory-free state. Region I corresponds to a transition to full stick.

This stationary point is found to be very close to the point of maximum slip displacement which itself moves only very slightly in the range $(\alpha, \pi/2)$ over the entire partial-slip load range.

8 Transition to full stick

If we reach a memory-free state in the partial slip region and then move beyond it, the possible incremental states are characterized by the four regions identified in Figure 7.8. Incremental changes heading into region II will result in a continued memory-free state, the right and left boundaries of this region being defined by the slope of the corresponding contour in Figures 7.6 and 7.7 respectively.

There also exists a range of loading directions, labelled I in Figure 7.8, for which the contact will transition to complete stick, and indeed this state would then persist for a finite load increment in the same direction. If incremental full stick occurs, the changes in traction will be given by the bilateral solution. If $\widetilde{P}$ continues to increase, the boundary between regions I and III in Figure 7.8 must therefore have the same slope as the original stick-slip boundary in Figures 7.4, 7.6 and 7.7, since below this line, the increment in $q(\theta)$ is in the same direction as the instantaneous value and is lower than the increment in $fp(\theta)$ for all θ and *vice versa*.

If $\widetilde{P}$ *decreases*, the maximum value of $[f\delta p(\theta) - \delta q(\theta)]$ occurs at $\theta = \alpha + \pi$. This point will lie inside the original partial slip zone if $\eta_2 > \alpha + \pi$, and hence if $\lambda < \lambda_0$, where λ_0 is defined by the construction in Figure 7.5 and also corresponds to points above the black dashed line in Figure 7.9 for plane strain with $\nu = 0.3$, $f = 0.4$. In this range, the boundary between I and IV in Figure 7.8 is symmetrical to that between I and III — i.e. it has the same slope but opposite sign.

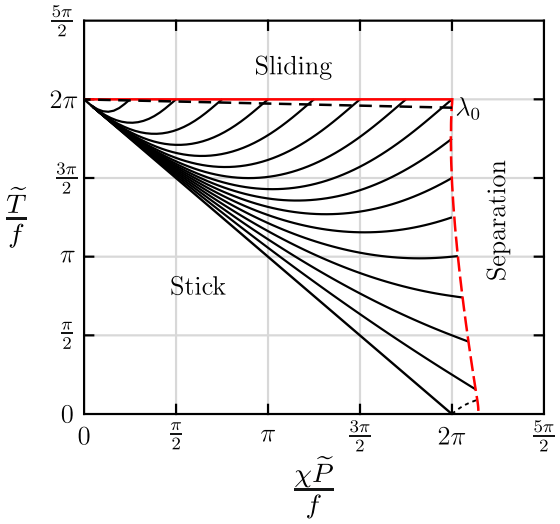


Figure 7.9: Contours defining the slope of the I/IV boundary in Figure 7.8 (plane strain with $\nu = 0.3$, $f = 0.4$)

For $\lambda > \lambda_0$ and $\widetilde{P}$ decreasing, the point most liable to slip will be adjacent to $\theta = \eta_2$, where η_2 is defined in Figure 7.5. It can be shown that additional partial slip will occur if

$$\frac{1}{\chi}\frac{d\widetilde{T}}{d\widetilde{P}} > -\cos(\eta_2 - \alpha)\ . \qquad (7.29)$$

Figure 7.9 shows a set of contours such that the slope of the I/III boundary at any given point is that of the contour through that point. The limiting condition $\lambda = \lambda_0$ is plotted as a black dashed line.

9 Conclusions

We have studied the problem of a disc, shrink-fitted into an infinite plane with a circular hole and then subjected to a radial force and a torque. This problem differs from most of the analytical contact mechanics literature in that there is strong coupling between frictional slip displacements and normal tractions— a factor which is known to influence history-dependence in frictional contact problems. In this paper we have defined the conditions under which the state reached is 'memory-free' — i.e. independent of the precise loading path. We find that this condition is satisfied provided that the slope of the path in $\{\widetilde{P}, \widetilde{T}\}$ space always lies in the region II of Figure 7.8, whose boundaries are defined by the slopes of the contours in Figures 7.6 and 7.7 respectively. We also define the conditions under which a loading increment will result in the entire interface transitioning to stick. The results provide a starting point for a future study of the shakedown behaviour of a continuous coupled contact.

Acknowledgements

N. Cwiekala and D. A. Hills thank Rolls-Royce plc and the EPSRC for the support under the Prosperity Partnership Grant 'Cornerstone: Mechanical Engineering Science to Enable Aero Propulsion Futures', Grant Ref: EP/R004951/1.

7.2 Frictional Shakedown of a Coupled Continuous Contact

As part of the first publication, in this chapter, we have introduced a specific continuous contact possessing all the right characteristics for the study of shakedown behaviour of coupled contacts. Identifying memory-free loading paths prepared the study of the system memory's effect on the steady-state response. As part of this section's publication, we follow different, explicitly not memory-free, loading paths to the entrance of the same load cycle. These load paths create different initial conditions affecting the system's steady-state response. We identify different load factors, characterising the amplitude of cyclic loading, which mark the boundaries between different possible steady-state responses. Furthermore, a phase shift between the cyclically varying loads is considered.

Frictional Shakedown of a Coupled Continuous Contact

N. Cwiekala[a,2], J. R. Barber[b], D. A. Hills[a]

[a] *Department of Engineering Science, University of Oxford, Parks Road, OX1 3PJ Oxford, United Kingdom*
[b] *Department of Mechanical Engineering, University of Michigan, Ann Arbor, MI 48109-2125, USA*

Abstract

The plane elastic problem of a circular disk shrink fitted into a hole in an elastically similar plane, with a frictional interface, is studied. The disc is subject to the application of a radial force and torque, which vary with time. This is done by the use of edge dislocations distributed along the interface to represent slip. It is shown that the steady state response, which might, for example, be cyclic slip or full adhesion for a particular loading regime, depends on the loading history before the steady state loading regime is entered. This is in contradiction of the Melan theorem for shakedown when applied to plasticity.

Keywords:
shakedown, coupled contact, distributed dislocations

1 Introduction

Contacts in mechanical assemblies are often subject to a primary load that remains constant, the centrifugal force in a gas turbine, for example, and, superimposed, a varying load that might stem from vibrations. These loads might cause regions of micro slip to develop along the interface of a notionally stationary contact. The contact is said to be in a state of partial slip and may experience slip displacements fully reversing in each loading cycle, referred to as cyclic slip, or accumulating slip displacements. The latter we refer to as 'ratcheting', a term borrowed from plasticity where it means the accumulation of plastic deformation. It leads to a gradual rigid body displacement over multiple cycles even though there is no instant in time at which the whole contact slips. Examples are a punch pressed into and, by a rocking motion, 'walking' along a half-plane (Mugadu et al., 2004) or the gradual rotation of a bushing in a conrod end (Antoni et al., 2007).

However, during the first few cycles the contact might develop a distribution of slip displacements causing it to reach a state of full stuck in all subsequent load cycles. In such a case the residual stresses caused by relative slip will change the contact tractions such that at no instant during the load cycle it expe-

[2] Corresponding author
Email address: nils.cwiekala@eng.ox.ac.uk (N. Cwiekala)

riences any further slip. We refer to this mechanism as 'frictional shakedown', and again, there is an equivalent in the field of plasticity. Similarities as the ones mentioned above have caused multiple authors (Churchman et al., 2006) to speculate whether principles known from plastic shakedown also apply to friction. In plasticity, for example, the existence of a distribution of residual stresses sufficient to cause a fully elastic response of a deformable body being subject to varying external loads, guarantees the body to eventually shake down, a principle known as 'Melan's theorem' (Melan, 1936). Klarbring et al. (2007) and Barber et al. (2008) have shown that there exists a frictional equivalent to the Melan's theorem for uncoupled contacts, that is where a tangential slip displacement has no effect on the normal tractions along the contact interface, but that it does not apply to coupled contacts. If such a distribution of residual stresses, allowing the contact to shake down, can be found or not primarily depends on the severity of the external loading which here as well as in the literature will be quantified by a scalar load factor, λ, scaling the amplitude of the external loads. For uncoupled contacts there exists a threshold load factor then, below which the contact will shake down and above which it will respond with a steady-state cyclic dissipation.

For coupled contacts, on the other hand, the existence of a distribution of slip displacements causing the contact to remain fully stuck throughout the load cycle is a necessary but not sufficient condition for frictional shakedown. It depends on initial conditions like an initial distribution of slip displacements or the transient loading path before the entry of the steady-state loading if the contact shakes down. However, if this necessary condition is fulfilled or not, will depend on the load factor, and we might identify a threshold, the shakedown limit λ_2, beyond which a sufficient distribution cannot be found. Similarly, we might identify a load factor $\lambda_1 < \lambda_2$ below which we find the 'safe shakedwon range', and the system will unconditionally shake down. In the range $\lambda_1 < \lambda < \lambda_2$ the occurrence of shakedown will then depend on initial conditions or generally the loading history. Ahn et al. (2008) introduced a method to identify the corresponding load factor boundaries for discrete contacts.

Jang and Barber (2011a) further developed the load factor concept using the model of an elastic block in compression, and incorporating an array of arbitrarily oriented cracks which might be 'closed and stuck' or 'closed and slipping' as the block being subject to a cyclic shear load. They showed that for $\lambda > \lambda_2$ the system fails to shake down, but the amount of energy dissipated per load cycle will still depend on initial conditions. However, they identified a point, λ_3, above which the loads are sufficient to cause every point of the contact interface to experience slip at at least one instant during the load cycle. For systems possessing a rigid-body motion degree of freedom this

may lead to ratchetting, and due to a loss of the systems 'memory', which resides in the permanently stuck regions of the contact (Barber, 2011a), the steady-state dissipation asymptotically approaches a unique value, independent of initial conditions. A load factor $\lambda = \lambda_4$ may then refer to the loads sufficient to cause gross slip, i.e. the entire contact interface experiencing slip at a single instant (Barber, 2016).

The complexity of most frictional engineering contact problems does not allow for an analytical attack and hence, so far, the above concepts have almost exclusively been shown for discretised contact formulations like Flicek et al.'s (2015) finite element description of a complete contact.

2 Problem statement

In this paper, we shall examine the behaviour described above for the particular case of a disc, with radius a, shrink fitted into a hole in an infinite plate of the same material, causing an interfacial contact pressure, p_0, constant around the circumference. The disc is subject to a radial load, P, and a torque, T, applied at the origin, in the sense shown in Figure 7.10. These external loads cause contact tractions of the form (Cwiekala et al., 2022b)

$$p(\theta) = p_0 - \frac{\kappa+3}{\kappa+1}\frac{P}{2\pi a}\sin\theta \tag{7.30}$$

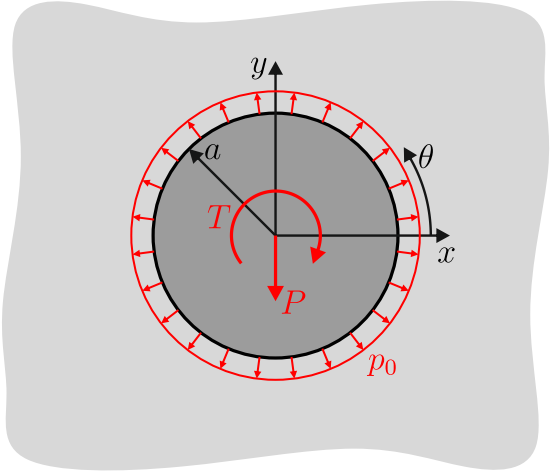


Figure 7.10: Shrink fitted disc in an infinite plane with a hole

$$q(\theta) = -\frac{T}{2\pi a^2} - \frac{\kappa-1}{\kappa+1}\frac{P}{2\pi a}\cos\theta \tag{7.31}$$

where κ is Kolosov's constant, defined as

$$\kappa = \begin{cases} 3-4\nu & \text{for plane strain,} \\ \frac{3-\nu}{1+\nu} & \text{for plane stress,} \end{cases}$$

and ν is Poisson's ratio. The problem of partial slip modifying the contact tractions, was studied in Cwiekala et al. (2022b) for history independent loading conditions, where arrays of distributed edge dislocations, $B_r(\phi)$ and $B_\theta(\phi)$, were arranged along the contact interface to model relative displacements between the disc and the plate.

2.1 Locked-in slip displacements

Here, we are interested in the loading history and how it affects the steady-state behaviour, where one or both loads, P and T, vary in time. The system's memory, that is the residual stress caused by slip in preceding load states, needs to be recorded. A very simple way of doing this

is by keeping track of the locked-in slip displacements represented by edge dislocations.

For the n-th loading step the locked-in slip displacement is represented by the dislocation distributions, $B_\theta^j(\phi)$ and $B_r^j(\phi)$ for $j = 1 \dots n-1$, resulting from all previous steps. The unknown dislocation distributions for the present step, $B_\theta^n(\phi)$ and $B_r^n(\phi)$, are then calculated by solving the slip condition

$$q^n(\theta) = \pm f p^n(\theta) \tag{7.32}$$

inside the current slip region, $\eta_1^n < \theta < \eta_2^n$. In equation (7.32), f is the coefficient of friction and the normal and shear traction, $p^n(\theta)$ and $q^n(\theta)$, are the superposition of the bilateral contact tractions (equations (7.30, 7.31)), with those caused by the dislocations introduced in the different loading steps. The calculation of the dislocation density from equation (7.32) is described in Cwiekala et al. (2022b) and can easily be extended to the current problem by noting that, here, the right hand side of the resulting singular integral equation does not only depend on the external loads but also on the known tractions caused by locked-in slip displacements or the loading history.

2.2 Initial conditions

For certain steady-state loading cycles, if the system shakes down or not, or more generally the cyclic dissipation, is expected to depend on initial conditions, as described in §1. These initial conditions are realised either by specifying specific locked-in slip displacements, or by different transient loading paths, causing such a distribution of slip displacements before the steady-state loading is entered. A special case is a transient loading which does not cause partial slip, such that the contact interface is completely stuck until the entry of the steady-state loading is reached.

The conditions for the contact to be fully stuck were found by Cwiekala et al. (2022b) and the corresponding region in normalised load space is shown in Figure 7.11, where

$$\widetilde{P} = \frac{P}{p_0 a} \; ; \quad \widetilde{T} = \frac{T}{p_0 a^2} \tag{7.33}$$

are the radial load and torque normalised by the radius, a, and (Cwiekala et al., 2022b)

$$\chi = \sqrt{\left(\frac{\kappa-1}{\kappa+1}\right)^2 + f^2 \left(\frac{\kappa+3}{\kappa+1}\right)^2} \, . \tag{7.34}$$

It is easily verified, that for any transient loading path, OA, from the origin to the entry of the steady-state loading, which is completely inside the initial stick-slip boundary, the steady state response will be unique as there will be no locked-in slip displacements at the entry.

To produce a set of different initial conditions, we need to consider different loading paths exceeding the initial stick-slip boundary. Here, this is done by choosing a transient loading trajectory, OIA, via a point I outside the initial stick-slip boundary. For different points I with $\{\widetilde{P}_I, \widetilde{T}_I\}$, this will create different initial

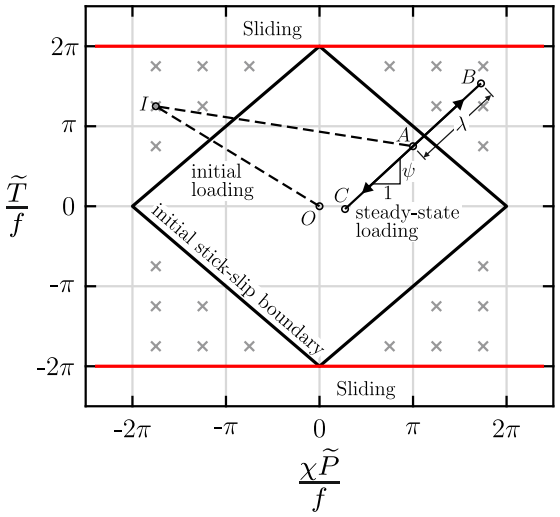


Figure 7.11: Cyclic variation of radial load and torque in normalised load space.

conditions, and we choose combinations of $\pm 3/4\pi$, $\pm 5/4\pi$ and $\pm 7/4\pi$ for $\chi\widetilde{P}_I/f$ and $\widetilde{T}_I/f$, such that the transient loading causes a distribution of locked-in slip displacements while it does not lead sliding or separation. The resulting 24 combinations of radial force and torque are represented by small crosses in Figure 7.11, and will be complemented by the direct entry, OA, of the steady state loading. The choice of points, I, for the transient loading is somewhat arbitrary and by no means comprehensive, but as we will see it suffices to show different ranges of the steady-state response.

2.3 Steady state loading

Generally, during the steady-state loading both, the radial load P and the torque T, may vary with time, t, around a mean value. Such a loading may be described by

$$P(t) = P_0 + P_1 \sin(\omega t) \qquad \text{and}$$
$$T(t) = T_0 + T_1 \sin(\omega t + \varphi)\,, \quad (7.35)$$

where P_0 and T_0 are the mean values of loading, P_1 and T_1 are the amplitudes of the steady-state loading, ω is a frequency and φ is a phase shift. For in-phase loading, $\varphi = 0$, the steady-state load path collapses to a straight line in load space as shown in Figure 7.11. Generally, a phase shift $\varphi \neq 0$ leads an elliptic load path centred around $\{\chi\widetilde{P}_0/f, \widetilde{T}_0/f\}$ whereas the special case of $\varphi = \pi/2$ together with $\chi\widetilde{P}_1 = \widetilde{T}_1$ leads a circular steady-state load path in normalised load space.

Using the normalisations (7.33) and in an effort to adapt to Jang and Barber's load factor formulation, we may write the steady-state loading (7.35) in the form

$$\frac{1}{f}\begin{bmatrix}\chi\widetilde{P}(t)\\ \widetilde{T}(t)\end{bmatrix} = \frac{1}{f}\begin{bmatrix}\chi\widetilde{P}_0\\ \widetilde{T}_0\end{bmatrix} + \frac{\lambda}{\sqrt{1+\psi^2}}\begin{bmatrix}\sin(\omega t)\\ \psi\sin(\omega t+\varphi)\end{bmatrix}. \quad (7.36)$$

Here, λ is a dimensionless load factor defined as

$$\lambda = \frac{1}{f}\sqrt{\left(\chi\widetilde{P}_1\right)^2 + \left(\widetilde{T}_1\right)^2}\,, \quad (7.37)$$

i.e. the distance between point A and B (or A and C) in normalised load space for the special case of $\varphi = 0$, and

$$\psi = \frac{\widetilde{T}_1}{\chi\widetilde{P}_1} \quad (7.38)$$

is the ratio of the load amplitudes, or the slope of the steady-state load path for $\varphi = 0$ as shown in Figure 7.11.

2.4 Steady state response

The steady-state response is characterised in terms of the dissipated energy per load cycle. The rate of energy dissipation due to the rate of slip displacement, $\dot{h}(\theta)$, is given by

$$\dot{W} = -a \int_0^{2\pi} q(\theta)\dot{h}(\theta)d\theta, \qquad (7.39)$$

where $h(\theta) = 0$ in regions which have been permanently stuck and $\dot{h}(\theta) = 0$ outside the current slip zone. The cyclic dissipation per load cycle can then be found to

$$W = \int_{\text{cycle}} \dot{W} dt, \qquad (7.40)$$

and we choose the following normalisation

$$\widetilde{\dot{W}} = \frac{\dot{W}\mu}{(\kappa+1)p_0^2 a^2}. \qquad (7.41)$$

The system experiences the steady-state loading cycle until either i) it shakes down in the sense that there will be no slip displacement at any position or at any instant during one load cycle or ii) the relative change in cyclic dissipation, compared with the previous cycle, is less than 0.01%.

3 In-phase loading

For an in-phase variation of both loads, $\varphi = 0$, we expect the bounding load factors, $\lambda_{1,\dots,4}$, to depend on the mean values of both loads, P_0 and T_0, as well as the slope of the steady-state load path, ψ.

Figure 7.12 shows the normalised steady-state energy dissipation per load cycle for a specific load case with $\chi\widetilde{P}_0/f = \pi$, $\widetilde{T}_0/f = 3\pi/4$ and $\psi = 5/8$. For the example case considered here, we find all the load factor ranges described by Barber (2016). While Figure 7.12(a) shows the entire range of the load factor, up to the point where full sliding occurs, Figure 7.12(b) shows the dissipative range with a finer resolution in λ.

Shakedown cases are represented by a black circle. For $\lambda < \lambda_1$ the system shakes down independent of the initial conditions and so the black circles, for all the different initial conditions described in Section 2.2, are on top of each other. Dissipative load cases are represented by a red dot for cyclic slip and a blue circle for ratchetting. For load factors $\lambda_1 < \lambda < \lambda_3$ we find a range of possible dissipations caused by cyclic slip. In the region $\lambda_1 < \lambda < \lambda_2$ this difference in dissipation might cause the system to shake down or continue to dissipate energy in the steady-state, depending on the initial conditions. It should be noted that the region $\lambda_1 < \lambda < \lambda_2$ is comparatively small. It is, however, unlikely that one of the considered initial conditions favours dissipation the most. The true boundary λ_1 might therefore be at much lower load factors. Flicek et al. (2017) describe the size of the conditional shakedown range, $\lambda_1 < \lambda < \lambda_2$, to increase with the coefficient of friction. A choice of a higher coefficient of friction might therefore increase the distance between λ_1 and λ_2, but as we will show in the following, it proves hard for such a choice

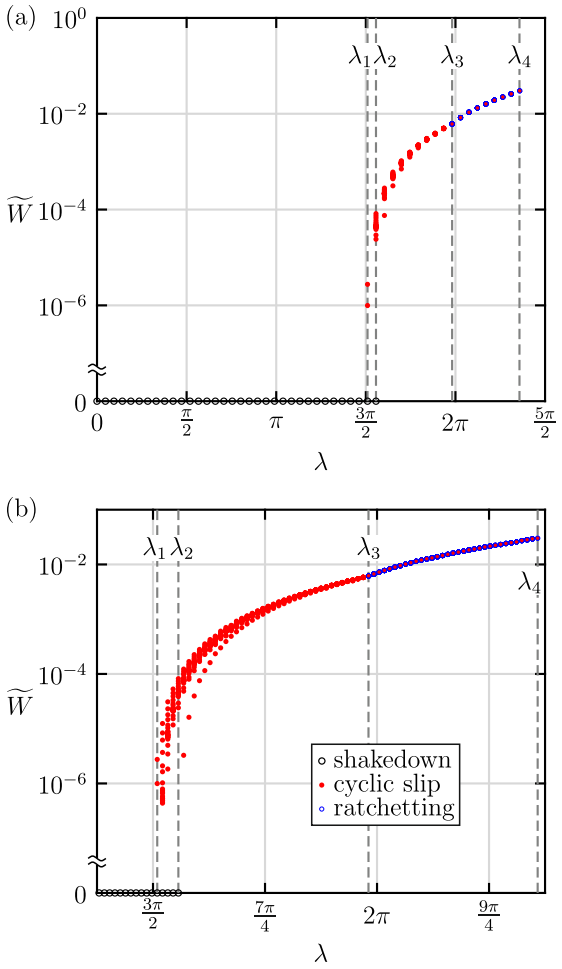


Figure 7.12: Normalised steady-state energy dissipation per load cycle for a varying radial load and torque around the mean values $\chi\widetilde{P}_0/f = \pi$ and $\widetilde{T}_0/f = 3\pi/4$ and a ratio of varying loads $\psi = 5/8$. The figure shows (a) the complete range of the load factor and (b) the dissipative range with a higher resolution (plane strain with $\nu = 0.3$, $f = 0.1$).

to identify load cases showing the entire range of the different responses as it is the case for the results shown in Figure 7.12. Instead, separation might occur before we reach full sliding or different regions might collapse completely.

Generally, for all initial conditions, the dissipation increases with λ. At $\lambda = \lambda_3$ we see a small change in the slope of the dissipation. This is caused by all the load cases with $\lambda < \lambda_3$ dissipating energy purely due to cyclic slip, while load cases with $\lambda > \lambda_3$ show a combination of cyclic slip and ratchetting. Specifically, the amount of cyclic slip continues to increase with λ, but now the disk additionally experiences a rigid body rotation in each load cycle. Some regions along the contact interface slip in one direction only and other regions, those experiencing cyclic slip, slip in one direction first followed by slip of a bigger magnitude in the reverse direction. The difference of forward and backward slip experienced by those regions is equal to the magnitude of slip in those regions slipping in one direction only and increases with λ.

In the following, we will look at the dependence of the different bounding load factors on the mean values of the steady state loading, $\chi\widetilde{P}_0/f$ and $\widetilde{T}_0/f$ as well as the ratio of varying loads ψ. To start with the more straight forward cases where the solution will not depend on initial conditions, we will look at the bounding load factors in reversed order. Beyond the identification of an upper bound of λ_1 for the specific load case shown in Figure 7.12, no attempt will be made to identify its dependence on mean loads and the ratio of load amplitudes.

3.1 Sliding boundary λ_4

As long as we exclude cases of separation, the sliding boundary is independent of the applied radial load (Cwiekala et al., 2022b) and is located at $\widetilde{T}/f = \pm 2\pi$ as shown in Figure 7.11. For our chosen definition of the load factor this corresponds

to

$$\lambda_4 = \pm \frac{\sqrt{1+\psi^2}}{\psi} \left(2\pi - \frac{\widetilde{T}_0}{f} \right) . \quad (7.42)$$

As expected, we find from equation (7.42) that for $\psi \to 0$, i.e. keeping the torque constant and varying the radial load only, full sliding of the disc relative to the plate can never occur.

3.2 Ratchetting boundary λ_3

Ratchetting with a positive rigid body rotation requires the entire contact interface to experience the same amount of forward slip displacements, $h(\theta) = u_\theta(a^+, \theta) - u_\theta(a^-, \theta)$, during one load cycle. Parts of the interface may slip during the entire cycle, but, to avoid full sliding, there must be regions which slip during the loading regime and are stuck during unloading, as well as different regions for which the reverse is true. The condition

$$-\frac{\mathrm{d}q(\theta)}{\mathrm{d}t} > f \frac{\mathrm{d}p(\theta)}{\mathrm{d}t} \quad (7.43)$$

states that at every point, θ, the change in shear and normal traction is such that their ratio approaches the coefficient of friction. Equation (7.43) is therefore a necessary condition for forward slip. For the loading regime (moving from point C to point B in Figure 7.11), equation (7.43) leads

$$\cos(\theta - \alpha) > -\psi , \quad (7.44)$$

while for the unloading regime (moving from point B to point C) we find

$$\cos(\theta - \alpha) < -\psi . \quad (7.45)$$

Inequalities (7.44) and (7.45) can never be fulfilled simultaneously for the same point of the contact interface, θ, but as long as

$$|\psi| \leq 1 , \quad (7.46)$$

there will be a region for which inequality (7.44) is fulfilled and in a different region inequality (7.45) holds. These regions are bounded by two discrete angles, $\gamma_{1,2}$ say, for which the change of normal traction multiplied by the coefficient of friction and shear traction is equal throughout the entire load cycle, i.e. $\Delta q(\gamma_{1,2})/\Delta p(\gamma_{1,2}) = f$ and expression (7.44) (or (7.45)) is equally fulfilled. These angles can be found by equating both sides of inequality (7.43) to lead

$$\gamma_{1,2} = \alpha \mp \arccos(-\psi). \quad (7.47)$$

If inequality (7.46) is not fulfilled, all points around the circumference can experience forward slip only during one of the two loading regimes and there will be no forward slip during the other. The entire contact slipping at the same instant (the *extreme* point of loading or unloading) is then the only possibility for all points to experience forward slip at some point during the steady-state loading cycle. Inequality (7.46), therefore, forms a necessary condition for ratchetting.

Unlike the results shown in Figure 7.12, for specific load cases, depending on the mean values of both loads, P_0 and T_0, as well as the slope of the steady-state load path, ψ, the dissipation in the range $\lambda > \lambda_3$ may result exclusively from accumulative slip (ratchetting), but not in-

clude cyclic slip. Certainly, for these load cases, the dissipation per load cycle $\widetilde{W} = 0$ for $\lambda = \lambda_3$, independent of the initial conditions. Consequently the regions $\lambda_1 < \lambda < \lambda_3$ must be non existent for such cases, i.e. $\lambda_1 = \lambda_2 = \lambda_3$.

For the contact considered here, we found inequality (7.46) to form a necessary condition for ratchetting. If we consider the load case chosen for the results presented in Figure 7.12, but change the mean values of both loads to $\chi\widetilde{P}_0/f = \pi/2$ and $\widetilde{T}_0/f = 6\pi/5$, we find the slip displacements in the steady-state and for $\lambda > \lambda_3$ to exclude cyclic slip as described above. The corresponding pattern of slip regions is shown in Figure 7.13 for a load factor of $\lambda = \sqrt{2}\pi$ and we see that every region of the contact experiences slips at some point during the load cycle but at no instance does the entire contact slip. The angles $\gamma_{1,2}$ separate those regions of the contact which experience periods of stuck during the loading regime and those which stick during unloading while the contact interface just around $\gamma_{1,2}$ continuously slips.

For such cases, not involving cyclic slip, a sufficient condition for ratchetting can be found. It is based on the requirement that for the given loading there exists no distribution of slip displacements modifying the tractions such that $-q(\theta) < f\,p(\theta)$ for every point along the contact interface and at every instant during the load cycle. Correspondingly, there exists a limit case between ratchetting and no ratchetting for which $-q(\theta) \leq f\,p(\theta)$, so

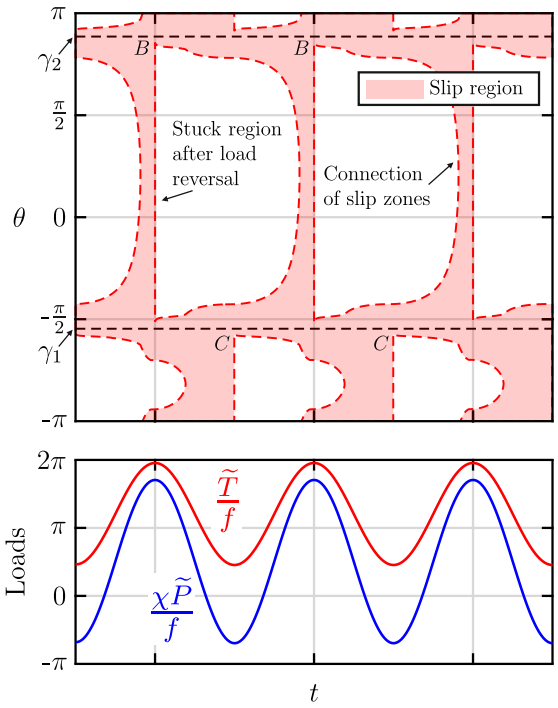


Figure 7.13: Evolution of slip zones along the circumference for $\chi\widetilde{P}_0/f = \pi/2$, $\widetilde{T}_0/f = 6\pi/5$, $\psi = 5/8$ and $\lambda = \sqrt{2}\pi$ (plane strain with $\nu = 0.3$, $f = 0.1$).

that every point reaches the onset of forward slip with $-q(\theta) = f\,p(\theta)$ at exactly one instant during the load cycle, which is either the *extreme* point of loading, B, or unloading, C, and is far away from slipping, i.e. $-q(\theta) < f\,p(\theta)$ at every other instant during the load cycle. Only the discrete angles $\gamma_{1,2}$ are then at the onset of slip throughout the entire load cycle. For the load case considered in Figure 7.13 we may find this limit state by reducing the load factor until the steady state dissipation vanishes. The corresponding normal and shear traction, $p^+(\theta)$ and $q^+(\theta)$ at the maximum loading point, B, as well as those at the end of the unloading regime (point C), $p^-(\theta)$ and $q^-(\theta)$, are shown in Figure 7.14.

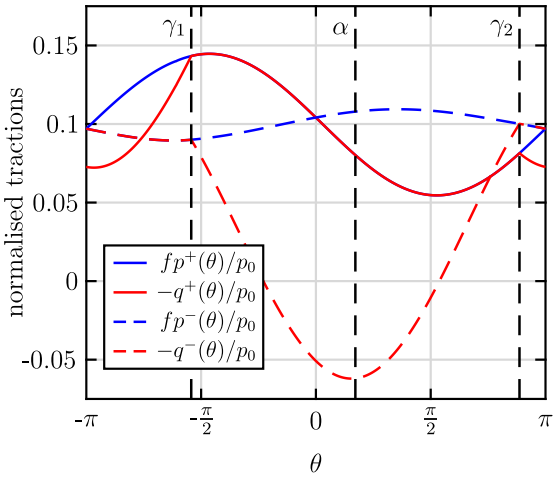


Figure 7.14: Limit case between shakedown and ratchetting for $\chi\widetilde{P}_0/f = \pi/2$, $\widetilde{T}_0/f = 6\pi/5$, $\psi = 5/8$ and $\lambda \approx \pi$ (plane strain with $\nu = 0.3$, $f = 0.1$).

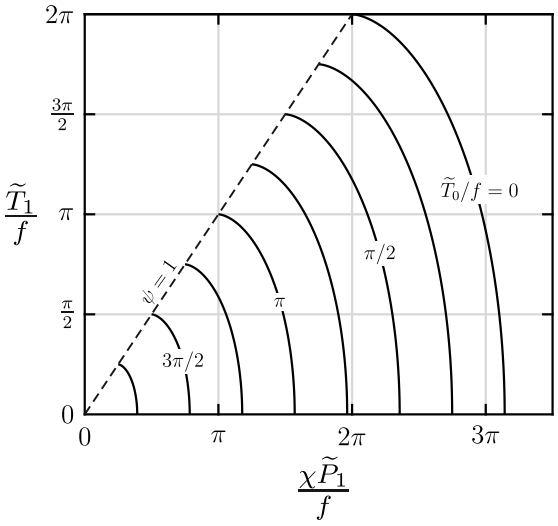


Figure 7.15: Combinations of load amplitudes beyond which ratchetting will occur for $P_0 = 0$ and different values of T_0.

As ratchetting is independent of the choice of initial conditions, we can find the corresponding loads from the bilateral tractions via

$$-\left(\int_{\gamma_1}^{\gamma_2} q^+_{\mathrm{bil}}(\theta)\mathrm{d}\theta + \int_{\gamma_2}^{\gamma_1+2\pi} q^-_{\mathrm{bil}}(\theta)\mathrm{d}\theta\right) = f\left(\int_{\gamma_1}^{\gamma_2} p^+_{\mathrm{bil}}(\theta)\mathrm{d}\theta + \int_{\gamma_2}^{\gamma_1+2\pi} p^-_{\mathrm{bil}}(\theta)\mathrm{d}\theta\right), \tag{7.48}$$

where $p_{\mathrm{bil}}(\theta)$ and $q_{\mathrm{bil}}(\theta)$ are the bilateral normal and shear traction and again the superscripts refer to point B and C in Figure 7.11. Using equations (7.30) and (7.31) for the bilateral tractions and expression (7.47) for the angles $\gamma_{1,2}$, equation (7.48) yields

$$\frac{2\pi f - \widetilde{T}_0}{\chi\widetilde{P}_1} = \frac{2}{\pi}\left(\sqrt{1-\psi^2} + \psi\arcsin(\psi)\right). \tag{7.49}$$

This represents a straight line in normalised load space emanating from the point $\chi\widetilde{P}/f = 0$ and $\widetilde{T}/f = 2\pi$ (the point where the stick and the sliding boundary meet) and whose slope is given by the right hand side of equation (7.49) (Cwiekala et al., 2022b). For each value of $\widetilde{T}_0$ and depending on ψ, this line will show the corresponding value of $\widetilde{P}_1$, necessary to cause ratchetting. In terms of the load factor we can rearrange equation (7.49) to find

$$\lambda_3 = \frac{\pi}{2}\frac{\sqrt{1+\psi^2}\left(2\pi - \widetilde{T}_0/f\right)}{\sqrt{1-\psi^2} + \psi\arcsin(\psi)}. \tag{7.50}$$

Figure 7.15 shows the identified ratchetting boundary. The curved lines show combinations of both load amplitudes representing the ratchetting boundary for different discrete values of $\widetilde{T}_0$. The diagonal dashed line connecting the upper left ends of the curved boundaries represents the slope $\psi = 1$ where for higher values of ψ ratchetting cannot occur.

It should be noted that the boundaries shown in Figure 7.15 simply visualise equation (7.50). However, depending on

the choice of f and ν, it might not be possible to reach these boundaries as the corresponding regions may be excluded by separation. Furthermore, equation (7.50) was obtained under the assumption that the steady-state loading results in exclusively positive slip displacements and therefore does not show cyclic slip. If cyclic slip starts before the ratchetting boundary is reached, again, depends on the coefficient of friction, f as well as ν, but also the mean value of loads, P_0 and T_0. A steady-state loading for which the contact for a certain load factor, $\lambda = \lambda_3$, starts to experience ratchetting and where for $\lambda < \lambda_3$ the system unconditionally shakes down, such that $\lambda_1 = \lambda_2 = \lambda_3$, may still start to experience cyclic slip at load factors $\lambda > \lambda_3$, such that the steady-state includes a mix of cyclic slip and ratchetting. However, for those cases the boundaries shown in Figure 7.15 are correct as the steady-state at $\lambda = \lambda_3$ does only include positive slip displacements as assumed in the derivation of expression (7.50).

3.3 Shakedown limit λ_2

Additionally to the initital conditions corresponding to the different transient loading paths, OIA, described in Section 2.2 and indicated in Figure 7.11, we identify an optimal distribution of initial slip displacements by employing a method described by Björkman and Klarbring (1987) as well as Flicek et al. (2015).

Flicek et al. (2015) use a finite element model to obtain a contact stiffness matrix allowing them to describe the contact tractions caused by the slip displacements specified along the discretised contact interface. The slip displacement is optimised such that the ratio of contact tractions is minimised, leading a 'minimax' optimisation problem.

Here, the formulation of the problem suggests a slightly different procedure, viz, the replacement of stiffness matrix operations by appropriate convolution integrals as suggested by Barber et al. (2008). At a set of points, ϕ_i, distributed along the contact interface, we specify a slip displacement, $h(\phi_i)$. From these slip displacements we find the corresponding dislocation density via

$$B_\theta(\phi) = \frac{1}{a}\frac{dh(\phi)}{d\phi}\ ; \quad B_r(\phi) = -\frac{h(\phi)}{a} \tag{7.51}$$

where we may use finite differences for a numerical approximation of the derivative. Evaluation of the contact tractions caused by these dislocations leads a singular integral equation which can be solved by employing the numerical quadrature introduced by Erdogan and Gupta (1972). For the specific problem under consideration this is described by Cwiekala et al. (2022b) and we choose the interval $[-\pi \quad \pi]$ for the integral range and the corresponding coordinates of the N integration points for our points ϕ_i. While the numerical quadrature provides the contact tractions at $N+1$ observation points, θ_k, distributed along the same interval (Hills et al., 1996), its bounded-bounded end-point behaviour requires the dislocation density to vanish at the integral boundaries (Cwiekala

et al., 2022b). We can specify this without loss of generality as adding a constant slip displacement merely represents a rigid body rotation of the disc relative to the plate and therefore does not affect the contact tractions. In fact a similar constraint has been used by Flicek et al. (2015) in order to improve the convergence of the optimisation.

The resulting optimisation problem, for a given load factor λ, is to optimise the slip displacements, $h(\phi_i)$, at the N integration points in order to minimise the maximum traction ratio at the $N+1$ observation points. The maximum load factor, λ, for which the traction ratio resulting from the steady-state loading together with the residual stress induced by the identified optimal distribution of slip displacements will not exceed the given coefficient of friction, f, constitutes the shakedown limit, λ_2.

Generally, this method identifies the maximum load factor for which shakedown is possible. It does not matter if the limiting slip mechanism is cyclic slip, ratchetting or full sliding. However, all the boundaries identified in the following mark the onset of cyclic slip.

λ_2, identified via the optimal distribution of slip displacements, will generally depend on the mean values of steady-state loading, P_0 and T_0, as well as the ratio of varying loads, ψ. Figure 7.16 shows the cyclic slip boundary in a similar manner to the visualisation of the ratchetting boundary in Figure 7.15. The black curved lines show the bounding load factor, λ_2, in terms of the load amplitudes

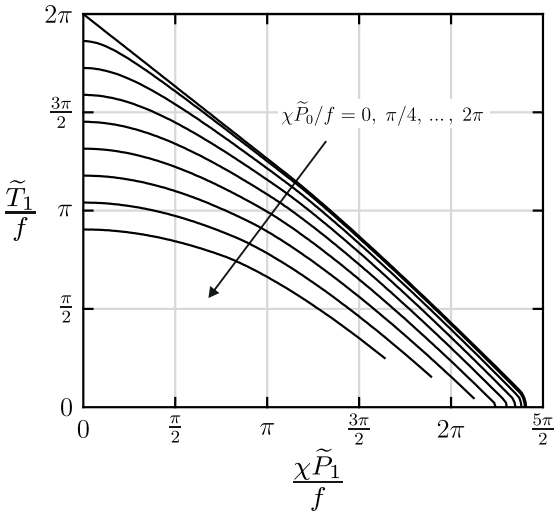


Figure 7.16: Combinations of load amplitudes beyond which shakedown is impossible, and the system will respond with cyclic slip, for $T_0 = 0$ and different values of P_0 (plane strain with $\nu = 0.3$, $f = 0.1$).

P_1 and T_1 for discrete values of P_0. All the boundaries represented in Figure 7.16 were obtained for the choice of $\widetilde{T}_0/f = 0$. However, we find the mean torque only to have a minor effect on the shape of the boundaries. This is comparable to the effect of a mean radial load on the onset of ratchetting.

Unlike the boundaries for ratchetting, presented in Figure 7.15, the start of cyclic slip will depend on the coefficient of friction. Figure 7.17 shows for $\psi = 1$ and different mean loads $\chi\widetilde{P}_0/f$ how the load factor λ_2 varies with the coefficient of friction.

While Figure 7.17 shows results only for $\psi = 1$, we generally find that for $f \to 0$ the shakedown limit approaches the initial stick-slip boundary. For a coefficient of friction $f \approx 0.4$ we find a maximum of the shakedown limit, and we note that this will be the sliding boundary for the

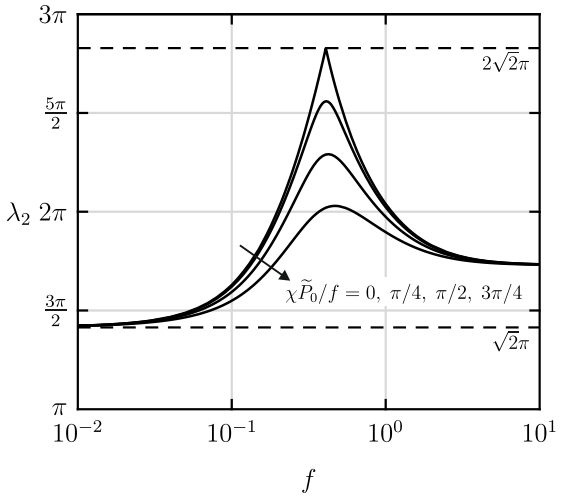


Figure 7.17: Shakedown limit, λ_2, for $\chi\widetilde{P}_0/f = \widetilde{T}_0/f = 0$, $\psi = 1$ and a continuous variation of the coefficients of friction, f (plane strain with $\nu = 0.3$).

special case of $\chi\widetilde{P}_0/f = \widetilde{T}_0/f = 0$. Again, this appears to be independent of ψ, while for $\psi < 1$ reaching this maximum tends to be excluded by separation. For $\widetilde{T}_0/f = 0$ and the shakedown limit to be $\lambda_2 = \lambda_4$ we know that

$$\begin{aligned} q^{+}_{\text{bil}}(\theta) + q_{\text{dis}}(\theta) &= -f(p^{+}_{\text{bil}}(\theta) + p_{\text{dis}}(\theta)) \\ q^{-}_{\text{bil}}(\theta) + q_{\text{dis}}(\theta) &= f(p^{-}_{\text{bil}}(\theta) + p_{\text{dis}}(\theta)) \quad \forall\, \theta\ , \end{aligned} \tag{7.52}$$

i.e. forward and backward sliding for the extreme points of loading and unloading. The subscript 'dis' refers to the residual stresses caused by locked in slip displacements represented by *dis*locations. Using equations (7.30) and (7.31) for the bilateral tractions and the fact that both, $p_{\text{dis}}(\theta)$ and $q_{\text{dis}}(\theta)$, result from the same distribution of slip displacements, $h(\phi)$, i.e. scale with its amplitude, h_0, we can show that fulfilling both equations (7.52) is possible if and only if $\chi\widetilde{P}_0/f = 0$ and

$$f = \sqrt{\frac{\kappa - 1}{\kappa + 3}}. \tag{7.53}$$

For the chosen Poisson's ratio of $\nu = 0.3$ this corresponds to a coefficient of friction of $f = 0.408$ as indicated by the location of the maximum in Figure 7.17.

For a mean value of radial load, $\chi\widetilde{P}_0/f \neq 0$ we find the maximum to be reduced but the shakedown limit still to approach the initial stick-slip boundary for $f \to 0$ and the same finite value for $f \to \infty$ as for the case without a mean radial load. As described above, a mean value of torque, $\widetilde{T}_0/f \neq 0$, only has a negligible effect on the shakedown limit and will therefore simply 'cap' the lines shown in Figure 7.17 at $\lambda_2 = \lambda_4$.

3.4 Discussion

Whereas the sliding boundary, λ_4, is in any case characterised by equation (7.42), the boundaries for cyclic slip and ratchetting, shown in the last two sections, will each only be correct if the other slip mechanism did not occur before. In case the steady-state response of the system starts to show cyclic slip characterised by the boundaries identified in §3.3, we cannot predict the start of ratchetting, λ_3, by equation (7.50). However, equation (7.50) might still serve as an estimation and we certainly know that it will not start for load factors lower than the ones derived from equation (7.50) as the reverse slip never favours the occurrence of ratchetting.

On the other hand, if we do reach the limit for ratchetting (7.50) before we cross the shakedown boundaries identified in §3.3, then ratchetting will indeed start for the load factor identified

in equation (7.50). Cyclic slip may still start to occur at higher load factors, but we know that this means that for every load factor the steady-state response will be unique, i.e. independent of initial conditions.

To a certain degree we may control which of the two slip mechanisms – cyclic slip or ratchetting – the system experiences first. A variation of the mean radial load, $\chi\widetilde{P}_0/f$, will shift the boundaries for ratchetting horizontally while the application of a mean torque, $\widetilde{T}_0/f$, shifts the boundaries for cyclic slip vertically. It is clear then, that the system being subject to high values of mean radial load and small values or no mean torque, $\chi\widetilde{P}_0/f \gg \widetilde{T}_0/f$, will tend to respond with cyclic slip before ratchetting occurs, whereas the reverse case of $\chi\widetilde{P}_0/f \ll \widetilde{T}_0/f$ will favour the occurrence of ratchetting before cyclic slip. For the former case we will find all the different steady-state responses with $\lambda_1 < \lambda_2 < \lambda_3 \leq \lambda_4$, while the latter case will result in $\lambda_1 = \lambda_2 = \lambda_3 \leq \lambda_4$. It should be noted that it is not possible to find a case with $\lambda_1 < \lambda_2 = \lambda_3$ as we would expect the system to show a steady-state dissipation or shakedown in the region $\lambda_1 < \lambda < \lambda_2 = \lambda_3$ depending on initial conditions whereas for $\lambda \to \lambda_3$ the dissipation has to approach the a unique value independent of initial conditions. This contradicts the requirement that the dissipation increases with an increasing load factor.

4 Out-of-phase loading

For a steady-state loading (7.35), a phase shift $\varphi \neq 0$ between periodically applied loads may additionally affect the cyclic dissipation. Jang and Barber (2011b) look at the effect of the relative phase of varying loads on the cyclic energy dissipation. For a simple single-node contact without coupling they show that it may depend on the phase shift if, in the steady state, the contact continuously dissipates energy or becomes fully stuck. They further show that the dissipation reaches a maximum around a phase shift of $\varphi = 6\pi/10$.

Kim et al. (2019) find comparable results in their investigation of a coupled single-node contact. They find the phase dependency of the cyclic dissipation to vary with the degree of coupling. The phase shift for which the maximum dissipation occurs, approaches $\varphi = \pi/2$ when the degree of coupling is increased.

Jang and Barber (2011b) as well as Kim et al. (2019) have effectively shown that the bounding load factors between different steady-state responses depend on the relative phase shift. Despite the consideration of coupling, the single-noded contact did not allow Kim et al. (2019) to consider the effect of initial conditions as for a dissipative steady-state loading the entire contact (the single node) will slip.

Here, we want to consider different initial conditions when looking at the effect of

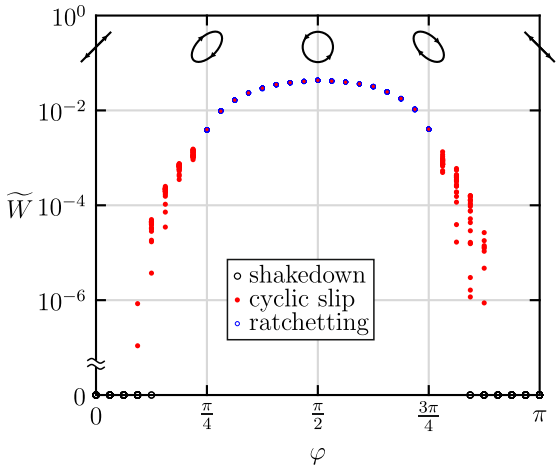


Figure 7.18: Steady-state cyclic dissipation for $\chi\widetilde{P}_0/f = \pi/3$, $\widetilde{T}_0/f = \pi/2$, $\psi = 3/4$, $\lambda = 2\pi$ and a continuous variation of the phase shift, ϕ (plane strain with $\nu = 0.3$, $f = 0.4$).

a relative phase shift between the periodically varying radial load and torque. Similar to the considerations for in-phase loading, we consider the different transient loading paths OIA before the steady-state loading is entered and which are indicated by the small crosses in Figure 7.11. With the additional parameter, φ, compared to the last chapter, we do not aim to exhaustively examine the dependence of the different bounding load factors on the phase shift as well as different mean loads and ratio of load amplitudes. However, Figure 7.18 shows the dependence of the cyclic dissipation on the relative phase shift for a specific load case with $\chi\widetilde{P}_0/f = \pi/3$, $\widetilde{T}_0/f = \pi/2$, $\psi = 3/4$ and $\lambda = 2\pi$. We examine a load case which for the in-phase loading shows unconditional shakedown. The chosen load factor appears to be $\lambda = 2\pi < \lambda_1$. For a small phase shift we find a region in which for certain cases the system responds with a steady-state dissipation and it is dependent on the initial conditions if the system shakes down or not. Consequently, a change in φ affected the bounding load factors such that $\lambda_1 < 2\pi < \lambda_2$. If we further increase φ the system fails to shake down, independent of the initial conditions. However, the amount of dissipated energy per load cycle will depend on the transient loading path. Accordingly, the relative phase shift has caused the system to respond with cyclic slip. If we increase the phase shift even further we find the cyclic dissipation to become unique, i.e. due to the change in φ the bounding load factors changed such that $\lambda_3 < 2\pi < \lambda_4$ and the system responds with ratchetting. It should be noted, though, that the relative phase shift between the external loads makes it possible for every point along the contact interface to experience forward as well as backward slip during one load cycle without the entire contact slipping at once. Something which is not possible for an in-phase variation of the loads. We find the maximum dissipation for $\varphi = \pi/2$. For a phase shift $\pi/2 < \varphi < \pi$ the steady-state response passes through equivalent regions in reversed order until the system unconditionally shakes down for phase shifts close to $\varphi = \pi$. It is easily verified from Figure 7.11 and the fact that the sliding boundaries are not affected by the load history, that the sliding limit, λ_4, is independent of the phase shift.

5 Conclusion

The investigation of a continuous coupled contact problem subject to period-

ically varying loads shows all the different regions of the steady-state response which were previously found for discrete contact formulations. It is shown how the bounding load factors depend on the mean loads as well as the ratio of load amplitudes and how this might cause some of the regions to shrink to zero for specific load cases.

The consideration of a relative phase shift between the externally applied loads together with different initial conditions show how the phase shift not only affects the steady-state cyclic dissipation but also causes a change in the bounding load factors, $\lambda_{1,\ldots,3}$.

Acknowledgements

N. Cwiekala and D. A. Hills thank Rolls-Royce plc and the EPSRC for the support under the Prosperity Partnership Grant 'Cornerstone: Mechanical Engineering Science to Enable Aero Propulsion Futures', Grant Ref: EP/R004951/1.

Chapter 8

Conclusion

This thesis is concerned with the effect of friction on damping (and the nucleation of cracks) for a range of different engineering contacts as classified in Chapter 2. Chapter 5 is concerned with the properties of the state of stress in the widely occurring flat and rounded contact and introduced a graphical approach to determine the elastic limit load. Generally, the combination of different loads, experienced by the contact in Section 5.1, introduce additional parameters on which the elastic limit will depend. However, in all our considerations, we saw that a reduction of surface friction reduces the severity of the subsurface stress field in the sense that the material is less likely to experience plasticity. Natural further steps would include an investigation of the effect of the loading sequence as well as consideration of cyclic loading.

In Chapter 3 we introduced and reviewed analysis of contact edges using asymptotic concepts. The first part of the chapter is concerned with incomplete contacts and the arising contact traction, and in Section 3.2 we turned to the internal stress field. The method reviewed in this section, referred to as the Williams' solution, is particularly powerful in the context of complete contacts, but can be specified to the incomplete contact geometry as shown in Section 5.2. Conventionally, the stress field derived from the Williams' solution is split into symmetric and anti-symmetric parts. The symmetric stress field is then associated with mode I or normal loading while mode II or shear loading is expected to produce an anti-symmetric stress field, but note that these descriptions refer to the bisector of the contact edge total angle as introduced in

Section 3.2. A derivation of the stress field via the Muskhelishvili complex potential, in Section 5.2, has shown that this is indeed true for those solutions for which the stress varies with r^λ, and where r is the distance to the contact edge and λ takes half integer values, i.e. $\lambda + 1/2 \in \mathbb{Z}$. For integer values, $\lambda \in \mathbb{Z}$, we have generally shown that the contact interface is traction free. It might therefore be assumed that these solutions are meaningless for a contact problem. However, they do arise, for example as part of the asymptotic representation of a full sliding stress field where it affects the stress parallel to the surface. For those half-integer terms it has been shown that the anti-symmetric stress field may be associated with normal loading while the symmetric stress field arises in tangential loading.

In the last section of Chapter 5 we presented an effective way to represent a differential bulk tension by the superposition of an equal tension in both the contacting bodies, and a tension and compression of equal magnitude in the two. It has been found that, although leading the same asymptotic form of the shear traction, the mix of shear force and differential bulk tension affects the stress field around the contact edge.

In Chapter 6 we used the subsurface stress field, found in the previous chapter, to derive calibrations between the asymptotic contact multipliers and crack tip stress intensity factors for a short crack, normal to the surface, and nucleating from the contact edge. Figure 8.1 shows the edge of an incomplete contact in an asymptotic or semi-infinite representation and for different configurations of friction and wear. The known solutions for an adhered contact edge (Fig. 8.1(a)) and a state of partial slip were discussed in Chapter 3, as part of the literature review. The contact tractions are characterised by the asymptotic contact multipliers L_I and K_{II}. As part of this thesis we derived in Section 6.1 calibrations between those multipliers and the crack tip stress intensity factors $K^c_{I,II}$ of a crack nucleating from the edge of the fully stuck (Fig. 8.1(d)) or the partial slip (Fig. 8.1(e)) contact edge. In all of these problems it is assumed that the contact profile is preserved, but in Figure 8.1(c) we show an asymptotic representation of a worn-away contact edge. It is assumed that the contact started off in a state of partial slip, as shown in Figure 8.1(b), but that repeated

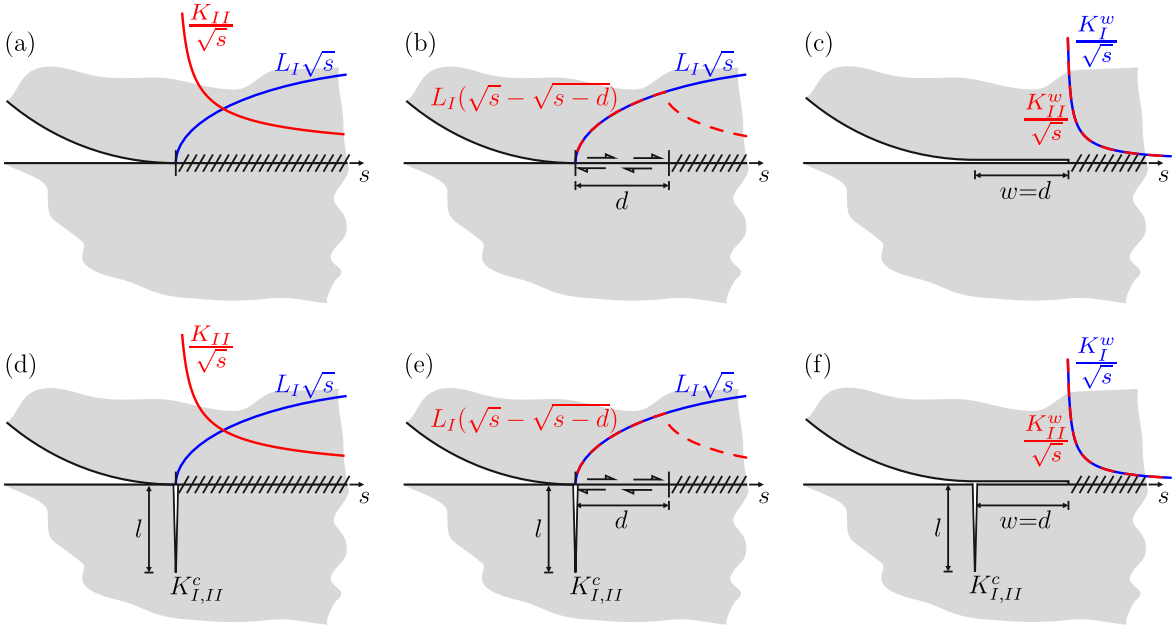


Figure 8.1: Asymptotic representation of an incomplete contact (a) in a state of fully stuck and (b) partial slip, (c) with a worn-away contact edge, and (d-e) show the corresponding contact scenarios with a crack nucleating from the edge.

cyclic slip, within the slip zone d, wore away the surface profile. Within an asymptotic framework we recovered the result that the final extent of the wear zone will correspond to the length of the initial slip zone, i.e. $w = d$, which had previously been shown for a finite description of a Hertzian contact. Calibrations were derived between the initial contact multipliers L_I and K_{II} and those characterising the singularity of the resulting fully stuck contact, $K^w_{I,II}$. As Figure 8.1(e) shows, also a crack in the neighbourhood of a worn contact has been considered.

A comparison to results derived for a finite contact description showed that the two-term representation of the partial slip contact tractions leads very good agreement for cracks up to the length of the slip zone size, i.e. $l = d$. For the single-term representation of the contact normal traction, the effect on the crack tip stress intensity factor can accurately be presented only up to a crack length of 5 % of the smallest characteristic contact length. This might be especially problematic if the contact normal load dominates, or for a flat and rounded contact where the asymptotic representation of the normal traction loses its validity not far from the contact edge. An improvement to the calibrations introduced could be made by considering a more elaborate form

of the asymptotic contact normal traction for flat and rounded contacts, like the one introduced by Sackfield et al. (2003).

The dependence of frictional shakedown on initial conditions has been shown in Chapter 7, for a coupled contact problem. In contrast to the studies previously published in the literature, this has been done for a continuous contact. The partial slip problem was tackled by means of the distributed dislocation technique. Conditions for a memory-free loading path were found. Such a loading regime leads a slip zone of monotonically increasing size, and along which we find monotonically increasing slip displacements. A cyclic loading path will violate these conditions, so that the system's memory resides in regions which previously experienced slip, but now are stuck. It is this memory which causes the shakedown behaviour to be conditional. The existence and extent of different load factor ranges, characterising the steady-state behaviour, has been shown to be dependent on mean components of the cyclically applied loads as well as the combination of load amplitudes. A relative phase shift between the external loads has additionally been considered. Previous results, for discrete contact formulations, showed the dissipation to be dependent on the phase angle. Here, it has been shown that the relative phase between the varying loads does not only affect the dissipation, but also it may cause a contact, which unconditionally shakes down for an in-phase loading, to show cyclic slip or ratchetting as the steady-state response.

It is customary to make remarks on further related problems which may be tackled. Although there is considerable work proceeding in the group at Oxford to quantify conditions for the nucleation of fatigue cracks, that effort is still inconclusive; partly because of the large number of loading scenarios and partly because of the "chestnut" of the transitional problem between nucleation and propagation. For these reasons the 'short crack self arrest' philosophy (discussed here in Section 6.2) still has life in it. A useful next step would be to derive equivalent calibrations for an extended asymptotic representation of the contact edge, not using just a single power order asymptote but a semi-infinite flat and rounded form for the contact profile.

Bibliography

Ahn, Y. J. and Barber, J. R. (2008). "Response of frictional receding contact problems to cyclic loading". In: *International Journal of Mechanical Sciences* 50 (10-11), pp. 1519–1525.

Ahn, Y. J., Bertocchi, E., and Barber, J. R. (2008). "Shakedown of coupled two-dimensional discrete frictional systems". In: *Journal of the Mechanics and Physics of Solids* 56 (12), pp. 3433–3440.

Ahn, Y. J., Klarbring, A., Spagnoli, A., and Terzano, M. (2022). "Shakedown in frictional contact of discrete elastic systems: A review". In: *International Journal of Solids and Structures*, p. 111470.

Amontons, G. (1699). "De la resistance cause'e dans les machines". In: *Mémoires de l'Académie Royale des Sciences*, pp. 206–222.

Andresen, H, Hills, D. A., and Moore, M. R. (2020). "Representation of incomplete contact problems by half-planes". In: *European Journal of Mechanics-A/Solids* 85, p. 104138.

Andresen, H., Hills, D. A., and Vazquez, J. (2019). "Closed-form solutions for tilted three-part piecewise-quadratic half-plane contacts". In: *International Journal of Mechanical Sciences* 150, pp. 127–134.

Antoni, N., Nguyen, Q.-S., Ligier, J.-L., Saffré, P., and Pastor, J. (2007). "On the cumulative microslip phenomenon". In: *European Journal of Mechanics-A/Solids* 26 (4), pp. 626–646.

Araújo, J. A. and Nowell, D (1999). "Analysis of pad size effects in fretting fatigue using short crack arrest methodologies". In: *International Journal of Fatigue* 21 (9), pp. 947–956.

Archard, J. (1953). "Contact and rubbing of flat surfaces". In: *Journal of applied physics* 24 (8), pp. 981–988.

Barber, J. R. (Jan. 2010). *Elasticity*. Vol. 172.

Barber, J. R. (2011a). "Frictional systems subjected to oscillating loads". In: *Annals of Solid and Structural Mechanics* 2 (2-4), pp. 45–55.

Barber, J. R. (2011b). *Intermediate mechanics of materials*. Vol. 618. Springer.

Barber, J. R. (2016). "Nominally static frictional contacts under periodic loading". In: *The Journal of Strain Analysis for Engineering Design* 51 (4), pp. 270–278.

Barber, J. R. (2018). *Contact mechanics*. Vol. 250. Springer.

Barber, J. R., Davies, M, and Hills, D. A. (2011). "Frictional elastic contact with periodic loading". In: *International Journal of Solids and Structures* 48 (13), pp. 2041–2047.

Barber, J. R., Klarbring, A., and Ciavarella, M. (2008). "Shakedown in frictional contact problems for the continuum". In: *Comptes Rendus Mécanique* 336 (1-2), pp. 34–41.

Björkman, G and Klarbring, A (1987). "Shakedown and residual stresses in frictional systems". In: *Contact Mechanics and Wear of Rail/Wheel Systems II: Proceedings of the 2nd international symposium*. University of Waterloo Press, pp. 27–39.

Boussinesq, J. (1885). *Application dès potentiels a l'étude de l'équilibre et du mouvement des solides élastiques*. Gauthier-Villars.

Bueckner, H. F. (1958). "The propagation of cracks and the energy of elastic deformation". In: *Transactions of the American Society of Mechanical Engineers* 80 (6), pp. 1225–1229.

Cattaneo, C. (1938). "Sul Contatto di due Corpi Elasticie: Distribution Locale Degli Sforzi". In: *Reconditi dell Academia Nazionale die Lincei* 27, pp. 474–478.

Chaise, T, Paynter, R. J. H., and Hills, D. A. (2014). "Contact analysis of a semi-infinite strip pressed onto a half plane by a line force". In: *International Journal of Mechanical Sciences* 81, pp. 60–64.

Churchman, C. M. and Hills, D. A. (2006). "General results for complete contacts subject to oscillatory shear". In: *Journal of the Mechanics and Physics of Solids* 54 (6), pp. 1186–1205.

Churchman, C. M., Korsunsky, A. M., and Hills, D. A. (2006). "The application of plasticity principles to friction". In: *The Journal of Strain Analysis for Engineering Design* 41 (4), pp. 323–328.

Ciavarella, M, Hills, D. A., and Monno, G (1998). "The influence of rounded edges on indentation by a flat punch". In: *Proceedings of the Institution of Mechanical Engineers, Part C: Journal of Mechanical Engineering Science* 212 (4), pp. 319–327.

Ciavarella, M and Macina, G (2003). "New results for the fretting-induced stress concentration on Hertzian and flat rounded contacts". In: *International Journal of Mechanical Sciences* 45 (3), pp. 449–467.

Ciavarella, M. (1998). "The generalized Cattaneo partial slip plane contact problem. I - Theory". In: *International Journal of solids and structures* 35 (18), pp. 2349–2362.

Ciavarella, M. and Decuzzi, P. (2001a). "The state of stress induced by the plane frictionless cylindrical contact. I. The case of elastic similarity". In: *International Journal of Solids and Structures* 38 (26-27), pp. 4507–4523.

Ciavarella, M. and Decuzzi, P. (2001b). "The state of stress induced by the plane frictionless cylindrical contact. II. The general case (elastic dissimilarity)". In: *International journal of solids and structures* 38 (26-27), pp. 4525–4533.

Comninou, M. (1976). "Stress singularity at a sharp edge in contact problems with friction". In: *Zeitschrift für angewandte Mathematik und Physik ZAMP* 27 (4), pp. 493–499.

Comninou, M. (1977). "The Interface Crack". In: *Journal of Applied Mechanics* 44 (4), pp. 631–636.

Comninou, M. (1978). "The Interface Crack in a Shear Field". In: *Journal of Applied Mechanics* 45 (2), pp. 287–290.

Coulomb, C. A. (1785). "Théorie des machines simples en ayant égard au frottement de leurs parties et à la roideur du cordage". In: *Mémoire de mathématique et de physique présentes à l'Académie Royal des Sciences*, pp. 161–342.

Cwiekala, N., Barber, J. R., and Hills, D. A. (2022a). "Frictional Shakedown of a Coupled Continuous Contact". In: *International Journal of Solids and Structures*. in preparation.

Cwiekala, N., Barber, J. R., and Hills, D. A. (2022b). "Memory-free loading paths for a coupled continuous contact problem with friction". In: *Mechanics Research Communications* 124, p. 103958.

Cwiekala, N. and Hills, D. A. (2021a). "Asymptotic description of fretting wear and fretting fatigue for incomplete contacts". In: *Engineering Fracture Mechanics* 256, p. 107986.

Cwiekala, N. and Hills, D. A. (2021b). "Half-plane contacts subject to remote tension". In: *The Journal of Strain Analysis for Engineering Design* 56 (8), pp. 539–547.

Cwiekala, N. and Hills, D. A. (2021c). "Stress intensity factor calibration for short cracks at the edge of semi-infinite contacts". In: *Engineering Fracture Mechanics* 247, p. 107692.

Ding, J, Leen, S. B., and McColl, I. R. (2004). "The effect of slip regime on fretting wear-induced stress evolution". In: *International Journal of Fatigue* 26 (5), pp. 521–531.

Dini, D, Churchman, C, Rajasekaran, R, and Hills, D. A. (2004). "A correlation of the process zone properties in complete, incomplete and almost complete fretting contacts". In: *International journal of mechanical sciences* 46 (3), pp. 491–508.

Dini, D, Sackfield, A, and Hills, D. A. (2005). "Comprehensive bounded asymptotic solutions for incomplete contacts in partial slip". In: *Journal of the Mechanics and Physics of Solids* 53 (2), pp. 437–454.

Dini, D, Sackfield, A, and Hills, D. A. (2008). "An axi-symmetric Hertzian Contact subject to cyclic shear and severe wear". In: *Wear* 265 (11-12), pp. 1918–1922.

Dini, D. (2004). "Studies in fretting fatigue with particular application to almost complete contacts". PhD thesis. University of Oxford.

Dini, D. and Hills, D. A. (2004). "Bounded asymptotic solutions for incomplete contacts in partial slip". In: *International journal of solids and structures* 41 (24-25), pp. 7049–7062.

Dundurs, J (1967). "Effect of elastic constants on stress in a composite under plane deformation". In: *Journal of Composite Materials* 1 (3), pp. 310–322.

El Haddad, M. H., Topper, T. H., and Smith, K. N. (1979). "Prediction of non propagating cracks". In: *Engineering fracture mechanics* 11 (3), pp. 573–584.

Erdogan, F and Gupta, G. D (1972). "On the numerical solution of singular integral equations". In: *Quarterly of applied mathematics* 29 (4), pp. 525–534.

Erdogan, F, Gupta, G. D., and Cook, T. S. (1973). "Numerical solution of singular integral equations". In: *Methods of analysis and solutions of crack problems*. Springer, pp. 368–425.

Flamant, A (1892). "Sur la répartition des pressions dans un solide rectangulaire chargé transversalement". In: *CR Acad. Sci. Paris* 114 (1892), pp. 1465–1468.

Fleury, R. M. N., Hills, D. A., Ramesh, R, and Barber, J. R. (2017). "Incomplete contacts in partial slip subject to varying normal and shear loading, and their representation by asymptotes". In: *Journal of the Mechanics and Physics of Solids* 99, pp. 178–191.

Flicek, R. C., Brake, M. R. W., and Hills, D. A. (2017). "Predicting a contact's sensitivity to initial conditions using metrics of frictional coupling". In: *Tribology International* 108, pp. 95–110.

Flicek, R. C., Hills, D. A., Barber, J. R., and Dini, D. (2015). "Determination of the shakedown limit for large, discrete frictional systems". In: *European Journal of Mechanics-A/Solids* 49, pp. 242–250.

Forsyth, P. J. E. (1961). "A two-stage process of fatigue crack growth". In: pp. 76–94.

Hertz, H. (1881). "Über die Berührung fester elastischer Körper". In: *J Reine Angew Math* 5, pp. 12–23.

Hills, D. and Sackfield, A (1984). "Yield and shakedown states in the contact of generally curved bodies". In: *The Journal of Strain Analysis for Engineering Design* 19 (1), pp. 9–14.

Hills, D. A. and Andresen, H. (2021). *Mechanics of Fretting Fatigue*. Springer Netherlands.

Hills, D. A., Davies, M, and Barber, J. R. (2011). "An incremental formulation for half-plane contact problems subject to varying normal load, shear, and tension". In: *The Journal of Strain Analysis for Engineering Design* 46 (6), pp. 436–443.

Hills, D. A., Fleury, R. M. N., and Dini, D (2016). "Partial slip incomplete contacts under constant normal load and subject to periodic loading". In: *International Journal of Mechanical Sciences* 108, pp. 115–121.

Hills, D. A. and Nowell, D. (1994). *Mechanics of Fretting Fatigue*. Solid Mechanics and Its Applications. Springer Netherlands.

Hills, D. A., Nowell, D, and Sackfield, A (1993). *Mechanics of elastic contacts*. Butterworth Heinemann.

Hills, D. A., Sackfield, A, and Paynter, R. J. H. (2009). "Simulation of fretting wear in halfplane geometries: part 1—the solution for long term wear". In: *Journal of tribology* 131 (3).

Hills, D. A. and Urriolagoitia Sosa, G. (1999). "Origins of partial slip in fretting — a review of known and potential solutions". In: *The Journal of Strain Analysis for Engineering Design* 34 (3), pp. 175–181.

Hills, D. A., Kelly, P. A., Dai, D. N., and Korsunsky, A. M. (1996). *Solution of crack problems: the distributed dislocation technique*. Vol. 44. Springer Science & Business Media.

Hojjati-Talemi, R., Wahab, M. A., De Pauw, J., and De Baets, P. (2014). "Prediction of fretting fatigue crack initiation and propagation lifetime for cylindrical contact configuration". In: *Tribology International* 76, pp. 73–91.

Hou, J. P. and Hills, D. A. (2001). "Contact between a pin and a plate with a hole under interference-fit and clearance-fit conditions". In: *Proceedings of the Institution of Mechanical Engineers, Part C: Journal of Mechanical Engineering Science* 215 (6), pp. 629–639.

Jäger, J. (1997). "Ein neues Prinzip der Kontaktmechnik". In: *ZAMM - Journal of Applied Mathematics and Mechanics* 77 (S1), pp. 143–144.

Jang, Y. H. and Barber, J. R. (2011a). "Frictional energy dissipation in materials containing cracks". In: *Journal of the Mechanics and Physics of Solids* 59 (3), pp. 583–594.

Jang, Y. H. and Barber, J. (2011b). "Effect of phase on the frictional dissipation in systems subjected to harmonically varying loads". In: *European Journal of Mechanics-A/Solids* 30 (3), pp. 269–274.

Johnson, K. L. (1963). "Plastic flow and residual stresses in rolling and sliding contact". In: *Proc. Symp. on Fatigue in Rolling Contact, Inst. Mech. Eng., London, 1963.* Vol. 177, pp. 54–65.

Johnson, K. L. (1985). *Contact mechanics*. Cambridge university press.

Keer, L. M., Dundurs, J., and Tsai, K. C. (1972). "Problems involving a receding contact between a layer and a half space". In: *Journal of Applied Mechanics* 39 (4), pp. 1115–1120.

Keer, L. M., Dundurs, J, and Kiattikomol, K (1973). "Separation of a smooth circular inclusion from a matrix". In: *International Journal of Engineering Science* 11 (11), pp. 1221–1233.

Kelly, P., Hills, D. A., and Nowell, D. (1994). "Curved interface cracks between elastically dissimilar media, with application to the analysis of circular inclusions". In: *International journal of mechanical sciences* 36 (3), pp. 173–181.

Kim, S., Ahn, Y. J., and Jang, Y. H. (2019). "Frictional energy dissipation for coupled systems subjected to harmonically varying loads". In: *Tribology International* 134, pp. 205–210.

Kitagawa, H and Takahashi, S (1976). "Applicability of fracture mechanics to very small cracks or the cracks in the early stage". In: *Proceedings of second international conference on mechanical behaviour of materials*, pp. 627–631.

Klarbring, A., Ciavarella, M, and Barber, J. R. (2007). "Shakedown in elastic contact problems with Coulomb friction". In: *International Journal of Solids and Structures* 44 (25-26), pp. 8355–8365.

Krenk, S. (1975). "On the use of the interpolation polynomial for solutions of singular integral equations". In: *Quarterly of Applied Mathematics* 32 (4), pp. 479–484.

Lopes, J. P. and Hills, D. A. (2019). "The axisymmetric frictional receding contact of a layer pressed against a half-space by a point force". In: *International Journal of Solids and Structures* 171, pp. 47–53.

Melan, E. (1936). "Theorie statisch unbestimmter Systeme aus ideal-plastichem Baustoff". In: *Sitzungsber. d. Akad. d. Wiss.* 145, pp. 195–218.

Michell, J. H. (1899). "On the direct determination of stress in an elastic solid, with application to the theory of plates". In: *Proceedings of the London Mathematical Society* 1 (1), pp. 100–124.

Mindlin, R. D. (1949). "Compliance of elastic bodies in contact". In: *J. Appl. Mech., ASME* 16, pp. 259–268.

Moore, M. R., Ramesh, R, Hills, D. A., and Barber, J. R. (2018). "Half-plane partial slip contact problems with a constant normal load subject to a shear force and differential bulk tension". In: *Journal of the Mechanics and Physics of Solids* 118, pp. 245–253.

Mugadu, A, Sackfield, A, and Hills, D. (2004). "Analysis of a rocking and walking punch—Part I: initial transient and steady state". In: *J. Appl. Mech.* 71 (2), pp. 225–233.

Muskhelishvili, N. I. (1964). "Some Fundamental Problems in the Mathematical Theory of Elasticity [in Russian], Izd.-vo Akad". In: *Nauk SSSR, Moscow*.

Nowell, D. (1988). "An analysis of fretting fatigue". PhD thesis. University of Oxford.

Nowell, D and Hills, D. A. (1987). "Mechanics of fretting fatigue tests". In: *International Journal of Mechanical Sciences* 29 (5), pp. 355–365.

Nowell, D, Hills, D. A., and Sackfield, A. (1988). "Contact of dissimilar elastic cylinders under normal and tangential loading". In: *Journal of the Mechanics and Physics of Solids* 36 (1), pp. 59–75.

Persson, A. (1964). "On the Stress Distribution of Cylindrical Elastic Bodies in Contact". PhD thesis. Chalmers Tekniska Högskola, Goteborg.

Sackfield, A, Mugadu, A, Barber, J. R., and Hills, D. A. (2003). "The application of asymptotic solutions to characterising the process zone in almost complete frictionless contacts". In: *Journal of the Mechanics and Physics of Solids* 51 (7), pp. 1333–1346.

Spence, D. A. (1968). "Self similar solutions to adhesive contact problems with incremental loading". In: *Proceedings of the Royal Society of London. Series A. Mathematical and Physical Sciences* 305 (1480), pp. 55–80.

Sundaram, N. and Farris, T. N. (2010a). "Mechanics of advancing pin-loaded contacts with friction". In: *Journal of the Mechanics and Physics of Solids* 58 (11), pp. 1819–1833.

Sundaram, N. and Farris, T. N. (2010b). "The generalized advancing conformal contact problem with friction, pin loads and remote loading–Case of rigid pin". In: *International Journal of Solids and Structures* 47 (6), pp. 801–815.

Szolwinski, M. P. and Farris, T. N. (1998). "Observation, analysis and prediction of fretting fatigue in 2024-T351 aluminum alloy". In: *Wear* 221 (1), pp. 24–36.

Timoshenko, S. P. and Goodier, J. N. (1951). *Theory of elasticity*. McGraw-Hill, New York.

Vázquez, J, Navarro, C, and Domínguez, J (2012). "A new method for obtaining the stress field in plane contacts". In: *International Journal of Solids and Structures* 49 (26), pp. 3659–3665.

Vázquez, J, Navarro, C, and Domínguez, J. (2013). "Explicit equations for sub-surface stress field in plane contacts". In: *International Journal of Mechanical Sciences* 67, pp. 53–58.

Vázquez, J, Sackfield, A, Hills, D. A., and Domínguez, J (2010). "The mechanical behaviour of a symmetrical punch with compound curvature". In: *The Journal of Strain Analysis for Engineering Design* 45 (4), pp. 209–222.

Vázquez, J., Navarro, C., and Domínguez, J. (2014). "Explicit equations for the half-plane sub-surface stress field under a flat rounded contact". In: *The Journal of Strain Analysis for Engineering Design* 49 (8), pp. 562–570.

Weertman, J. (1996). *Dislocation based fracture mechanics*. World Scientific Publishing Company.

Williams, M. L. (1952). "Stress singularities resulting from various boundary conditions in angular corners of plates in extension". In: *Journal of applied mechanics* 19 (4), pp. 526–528.

Appendices

A Subsurface Stress for Flat and Rounded Contacts

This section shows the detailed derivation of explicit expressions for the subsurface stress field of a flat and rounded contact, with the geometry shown in Figure 2.4(a), and subject to different external loadings.

A.1 Normal Loading

The profile of the punch, $g_2(x)$, is given by equation (2.32) and the normal traction, $p(x)$, by equation (2.34). Substitution into equation (2.67) leads the Muskhelishvili complex potential (Vázquez et al., 2014)

$$\phi^n(z) = \begin{cases} \frac{i(z+b)}{2AR} + \frac{2i\sqrt{z^2-a^2}\arccos\left(\frac{b}{a}\right) - (z-b)\ln(G(z,a,b)) + (z+b)\ln(G(z,a,-b))}{2\pi AR} & x \leq 0 \\ \frac{i(z-b)}{2AR} + \frac{-2i\sqrt{z^2-a^2}\arccos\left(\frac{b}{a}\right) - (z-b)\ln(-G(z,a,b)) + (z+b)\ln(-G(z,a,-b))}{2\pi AR} & 0 < x \end{cases}, \tag{A.1}$$

where the complex coordinate $z = x + iy$ and

$$G(z,a,b) = \frac{\sqrt{\frac{z-a}{z+a}} - i\sqrt{\frac{a-b}{a+b}}}{\sqrt{\frac{z-a}{z+a}} + i\sqrt{\frac{a-b}{a+b}}}\,. \tag{A.2}$$

As in Section 2.3, the composite compliance, A, is given by equation (2.19), while a, b and R denote the contact and flat half-width and the edge radius, respectively.
We may separately derive the stress field for the single terms of the potential function, and find the final subsurface stress from superposition. The first term of the potential is given by

$$\phi^{n1}(z) = \frac{i}{2AR} \begin{cases} z+b & x \leq 0 \\ z-b & 0 < x \end{cases} \qquad \text{and} \qquad \frac{\partial}{\partial z}\phi^{n1}(z) = \frac{i}{2AR} \, . \tag{A.3}$$

Substituting equations (A.3) in expressions (2.70) we directly obtain

$$\begin{aligned} \sigma_{xx}^{n1}(x,y) &= -\frac{2y}{AR} \, , \\ \sigma_{yy}^{n1}(x,y) &= 0 \, , \\ \sigma_{xy}^{n1}(x,y) &= 0 \, . \end{aligned} \tag{A.4}$$

For the second term of the potential function we have

$$\phi^{n2}(z) = \frac{i \arccos\left(\frac{b}{a}\right)}{\pi AR} \begin{cases} \sqrt{z^2-a^2} & x \leq 0 \\ -\sqrt{z^2-a^2} & 0 < x \end{cases} \, , \tag{A.5}$$

and the derivative with respect to the complex coordinate, z, is given by

$$\frac{\partial}{\partial z}\phi^{n2}(z) = \frac{i \arccos\left(\frac{b}{a}\right)}{\pi AR} \begin{cases} \frac{z}{\sqrt{z^2-a^2}} & x \leq 0 \\ -\frac{z}{\sqrt{z^2-a^2}} & 0 < x \end{cases} \, . \tag{A.6}$$

Vázquez et al. (2014) show that the occurring square-root terms can be split into real

and imaginary parts, such that we may write

$$\begin{aligned} f_1(z) &= \sqrt{z^2 - a^2} = u_1(x, y, a) + iv_1(x, y, a) \\ f_1(\bar{z}) &= \sqrt{\bar{z}^2 - a^2} = u_1(x, y, a) - iv_1(x, y, a) \\ f_6(z) &= \frac{z}{\sqrt{z^2 - a^2}} = u_6(x, y, a) + iv_6(x, y, a) \\ f_6(\bar{z}) &= \frac{\bar{z}}{\sqrt{\bar{z}^2 - a^2}} = u_6(x, y, a) - iv_6(x, y, a) \end{aligned} , \tag{A.7}$$

where the functions u_i and v_i are defined in Section A.4. Substitution of equations (A.5) and (A.6) into equations (2.70), where we use a split form into real and imaginary part according to equations (A.7), leads

$$\begin{aligned} \sigma_{xx}^{n2}(x, y) &= \frac{1}{\pi AR} \begin{cases} 2\left(v_1 + yu_6\right) \arccos\left(\frac{b}{a}\right) & x \leq 0 \\ -2(v_1 + yu_6) \arccos\left(\frac{b}{a}\right) & 0 < x \end{cases} , \\ \sigma_{yy}^{n2}(x, y) &= \frac{1}{\pi AR} \begin{cases} 2(v_1 - yu_6) \arccos\left(\frac{b}{a}\right) & x \leq 0 \\ -2(v_1 - yu_6) \arccos\left(\frac{b}{a}\right) & 0 < x \end{cases} , \\ \sigma_{xy}^{n2}(x, y) &= \frac{1}{\pi AR} \begin{cases} -2yv_6 \arccos\left(\frac{b}{a}\right) & x \leq 0 \\ 2yv_6 \arccos\left(\frac{b}{a}\right) & 0 < x \end{cases} . \end{aligned} \tag{A.8}$$

The remaining part of the potential function (A.1) is

$$\phi^{n3}(z) = \frac{1}{2\pi AR} \begin{cases} -(z - b) \ln(G(z, b)) + (z + b) \ln(G(z, -b)) & x \leq 0 \\ -(z - b) \ln(-G(z, b)) + (z + b) \ln(-G(z, -b)) & 0 < x \end{cases} , \tag{A.9}$$

and the derivative with respect to z leads

$$\frac{\partial}{\partial z}\phi^{n3}(z) = \frac{1}{2\pi AR} \begin{cases} -\ln(G(z, b)) + \ln(G(z, -b)) & x \leq 0 \\ -\ln(-G(z, b)) + \ln(-G(z, -b)) & 0 < x \end{cases} , \tag{A.10}$$

Again, we may obtain a complex split by noting that (Vázquez et al., 2014)

$$\begin{aligned}
f_2(z) &= \ln(G(z,a,b)) = u_2(x,y,a,b) + iv_2(x,y,a,b) \ , \\
f_2(\bar{z}) &= \ln(G(\bar{z},a,b)) = -u_2(x,y,a,b) + iv_2(x,y,a,b) \ , \\
f_3(z) &= \ln(G(z,a,-b)) = u_3(x,y,a,b) + iv_3(x,y,a,b) \ , \\
f_3(\bar{z}) &= \ln(G(\bar{z},a,-b)) = -u_3(x,y,a,b) + iv_3(x,y,a,b) \ , \\
f_4(z) &= \ln(-G(z,a,b)) = u_2(x,y,a,b) + i(v_2(x,y,a,b) + \pi) \ , \\
f_4(\bar{z}) &= \ln(-G(\bar{z},a,b)) = -u_2(x,y,a,b) + i(v_2(x,y,a,b) + \pi) \ , \\
f_5(z) &= \ln(-G(z,a,-b)) = u_3(x,y,a,b) + i(v_3(x,y,a,b) + \pi) \ , \\
f_5(\bar{z}) &= \ln(-G(\bar{z},a,-b)) = -u_3(x,y,a,b) + i(v_3(x,y,a,b) + \pi) \ .
\end{aligned} \tag{A.11}$$

Splitting equations (A.9) and (A.10) into their real and imaginary parts, according to equations (A.11), and substitution into equations (2.70) leads

$$\begin{aligned}
\sigma_{xx}^{n3}(x,y) &= \frac{(x-b)u_2 - (x+b)u_3 - 2y(v_2 - v_3)}{\pi AR} \ , \\
\sigma_{yy}^{n3}(x,y) &= \frac{(x-b)u_2 - (x+b)u_3}{\pi AR} \ , \\
\sigma_{xy}^{n3}(x,y) &= -\frac{y(u_2 - u_3)}{\pi AR} \ .
\end{aligned} \tag{A.12}$$

A.2 Shear Loading

We obtain the tangential potential function, for full sliding, via $\phi^t(z) = if\phi^n(z)$, where $\phi^n(z)$ is given by equation (A.1). This leads

$$\phi^t(z) = \begin{cases} -f\frac{(z+b)}{2AR} + if\frac{2i\sqrt{z^2-a^2}\arccos\left(\frac{b}{a}\right) - (z-b)\ln(G(z,b)) + (z+b)\ln(G(z,-b))}{2\pi AR} & x \leq 0 \\ -f\frac{(z-b)}{2AR} + if\frac{-2i\sqrt{z^2-a^2}\arccos\left(\frac{b}{a}\right) - (z-b)\ln(-G(z,b)) + (z+b)\ln(-G(z,-b))}{2\pi AR} & 0 < x \end{cases} , \tag{A.13}$$

Again, we will look at each term individually and obtain the final stress field from a superposition. We start with

$$\phi^{t1}(z) = -\frac{f}{2AR}\begin{cases} z+b & x \leq 0 \\ z-b & 0 < x \end{cases} \qquad \text{and} \qquad \frac{\partial}{\partial z}\phi^{t1}(z) = -\frac{f}{2AR}\,, \tag{A.14}$$

as the first term and its derivative. The corresponding stress field can directly be obtained by substituting equations (A.14) into expressions (2.71) to yield

$$\begin{aligned} \sigma_{xx}^{t1}(x,y) &= -2f\frac{1}{AR}\begin{cases} x+b & x \leq 0 \\ x-b & 0 < x \end{cases}\,, \\ \sigma_{yy}^{t1}(x,y) &= 0\,, \\ \sigma_{xy}^{t1}(x,y) &= 2f\frac{y}{AR}\,. \end{aligned} \tag{A.15}$$

For the second term

$$\phi^{t,2}(z) = -f\frac{\arccos\left(\frac{b}{a}\right)}{\pi AR}\begin{cases} \sqrt{z^2-a^2} & x \leq 0 \\ -\sqrt{z^2-a^2} & 0 < x \end{cases}\,, \tag{A.16}$$

we find the derivative with respect to the complex coordinate, z, to

$$\frac{\partial}{\partial z}\phi^{t2}(z) = -f\frac{\arccos\left(\frac{b}{a}\right)}{\pi AR}\begin{cases} \frac{z}{\sqrt{z^2-a^2}} & x \leq 0 \\ -\frac{z}{\sqrt{z^2-a^2}} & 0 < x \end{cases}\,. \tag{A.17}$$

Equations (A.7) are sufficient to separate the real and imaginary parts of expressions (A.16) and (A.17). Subsequently, explicit expressions for the stress field can be obtained

in real algebra from equations (2.71) and are given by

$$\sigma_{xx}^{t2}(x,y) = \frac{2f\arccos\left(\frac{b}{a}\right)}{\pi AR}\begin{cases} -2u_1 + y\,v_6 & x \le 0 \\ 2u_1 - y\,v_6 & 0 < x \end{cases},$$
$$\sigma_{yy}^{t2}(x,y) = \frac{2f\arccos\left(\frac{b}{a}\right)}{\pi AR}\begin{cases} -y\,v_6 & x \le 0 \\ y\,v_6 & 0 < x \end{cases}, \tag{A.18}$$
$$\sigma_{xy}^{t2}(x,y) = \frac{2f\arccos\left(\frac{b}{a}\right)}{\pi AR}\begin{cases} v_1 + y\,u_6 & x \le 0 \\ -v_1 - y\,u_6 & 0 < x \end{cases}.$$

For the last part of the potential function,

$$\phi^{t3}(z) = \frac{if}{2\pi AR}\begin{cases} -(z-b)\ln(G(z,b)) + (z+b)\ln(G(z,-b)) & x \le 0 \\ -(z-b)\ln(-G(z,b)) + (z+b)\ln(-G(z,-b)) & 0 < x \end{cases}, \tag{A.19}$$

the derivative is given by

$$\frac{\partial}{\partial z}\phi^{n3}(z) = \frac{if}{2\pi AR}\begin{cases} -\ln(G(z,b)) + \ln(G(z,-b)) & x \le 0 \\ -\ln(-G(z,b)) + \ln(-G(z,-b)) & 0 < x \end{cases}, \tag{A.20}$$

and equations (A.11) provide the complex split. Substitution into equations (2.71) leads

$$\sigma_{xx}^{t3}(x,y) = \frac{f}{\pi AR}\begin{cases} 2(x-b)v_2 - 2(x+b)v_3 - 3y(u_3-u_2) & x \le 0 \\ 2(x-b)v_2 - 2(x+b)v_3 - 3y(u_3-u_2) - 4\pi b & 0 < x \end{cases}$$
$$\sigma_{yy}^{t3}(x,y) = -\frac{y\,f}{\pi AR}(u_2-u_3) \tag{A.21}$$
$$\sigma_{xy}^{t3}(x,y) = \frac{f}{\pi AR}((x-b)u_2 - (x+b)u_3 - 2y(v_2-v_3)),$$

and the complete stress field, caused by a full sliding shear traction, is given by $\sigma_{ij}^{t} = \sigma_{ij}^{t1} + \sigma_{ij}^{t2} + \sigma_{ij}^{t3}$. For a shear force, $Q < f\,P$, insufficient to cause full sliding, the contact will be in a state of partial slip. The subsurface stress field can be found from a superposition of the full sliding stress field and a negative scaled version of the full sliding stress field. The latter is the stress field caused by the corrective traction, $q^{*}(x)$, and in the corresponding equations we have to replace the contact half-width a by the extent of the the central stick zone, c, as described in Section 5.1.2.

A.3 Differential Bulk Tension

If simultaneously (to the shear load Q) the contacting bodies are subject to a differential bulk tension, σ_0, the stick zone will be shifted along the contact interface. If the bulk tension is such that $e < c - b$, the shift is given implicitly by expression (5.9) (Vázquez et al., 2014). The corrective shear traction, which for the full shear traction needs to be superimposed on the full sliding shear traction, is given by (5.10). We note, that the corrective shear traction itself is a full sliding shear traction, but scaled to the stick zone and due to the shift, e, no longer symmetric around $x = 0$ (nor around $x = e$). The Muskhelishvili complex potential can be obtained from equation (2.68), where for the application of a bulk tension, $\Lambda = \sigma_0/4$ (Vázquez et al., 2012). This leads an additional term in the final potential function of $\phi^{t0}(z) = \sigma_0/8$. If we insert this term into expressions (2.71), it can immediately be seen, that it results in a constant stress parallel to the contact interface of $\sigma_{xx}^{t0}(x, y) = -\sigma_0/2$, while all the other stress components vanish. The stress field caused by the full sliding shear traction is given by equations (5.5), but due to the bulk tension induced asymmetry we cannot use this equation for the stress field caused by the corrective term. For the corrective shear traction for the flat and rounded punch (eq. (5.10)) we find the corresponding potential

function to be given by

$$\phi^t(z) = \frac{f}{2\pi\, A\, R}\left[\pi(z \pm b) \pm \sqrt{(z-e)^2 - c^2}\left(\arccos\left(\frac{b-e}{c}\right) + \arccos\left(\frac{b+e}{c}\right)\right)\right.$$
$$\left. + (z-b)\ln(G(z-e,c,b-e)) - (z+b)\ln(G(z-e,c,-b-e))\right] \tag{A.22}$$

The upper sign in equation (A.22) corresponds to the case $x \leq 0$, and the lower sign to $x > 0$. The function $G(z,c,t)$ is still given by equation (A.2). We note that the first term in the potential function cannot be derived from equation (2.68), but it will cancel out with its counterpart from the full sliding potential (A.13).

We obtain explicit equations for the subsurface stress field in real algebra by considering each of the single parts of the potential (A.22) on its own. For the first term of the potential we find

$$\phi^{t1}(z) = \frac{f}{2AR}\begin{cases} z+b & x \leq 0 \\ z-b & 0 < x \end{cases} \qquad \text{and} \qquad \frac{\partial}{\partial z}\phi^{t1}(z) = \frac{f}{2AR}\,. \tag{A.23}$$

A split into its real and imaginary part can easily be derived by noting that $z = x + i\,y$. By substitution of the separated forms of equations (A.23) in expressions (2.71), we directly obtain

$$\begin{aligned} \sigma_{xx}^{t1}(x,y) &= 2f\frac{1}{AR}\begin{cases} x+b & x \leq 0 \\ x-b & 0 < x \end{cases}, \\ \sigma_{yy}^{t1}(x,y) &= 0\,, \\ \sigma_{xy}^{t1}(x,y) &= -2f\frac{y}{AR}\,. \end{aligned} \tag{A.24}$$

For the second term of the potential function

$$\phi^{t2}(z) = f\frac{\left(\arccos\left(\frac{b-e}{c}\right) + \arccos\left(\frac{b+e}{c}\right)\right)}{2\pi AR}\begin{cases} \sqrt{(z-e)^2 - c^2} & x \leq 0 \\ -\sqrt{(z-e)^2 - c^2} & 0 < x \end{cases} \tag{A.25}$$

the derivative with respect to z leads

$$\frac{\partial}{\partial z}\phi^{t2}(z) = f\frac{\arccos\left(\frac{b-e}{c}\right) + \arccos\left(\frac{b+e}{c}\right)}{2\pi AR}\begin{cases}\frac{z-e}{\sqrt{(z-e)^2-c^2}} & x \leq 0\\ -\frac{z-e}{\sqrt{(z-e)^2-c^2}} & 0 < x\end{cases}. \tag{A.26}$$

Equivalent to the separation defined by Vázquez et al. (2014) and given in equations (A.7), we may use

$$\begin{aligned} f_1(z) &= \sqrt{(z-e)^2-c^2} = u_1(x-e,y,c) + iv_1(x-e,y,c)\\ f_1(\bar{z}) &= \sqrt{(\bar{z}-e)^2-c^2} = u_1(x-e,y,c) - iv_1(x-e,y,c)\\ f_6(z) &= \frac{z-e}{\sqrt{(z-e)^2-c^2}} = u_6(x-e,y,c) + iv_6(x-e,y,c)\,,\\ f_6(\bar{z}) &= \frac{\bar{z}-e}{\sqrt{(\bar{z}-e)^2-c^2}} = u_6(x-e,y,c) - iv_6(x-e,y,c) \end{aligned} \tag{A.27}$$

to separate equations (A.25) and (A.26) into their real and imaginary parts. Substitution into equations (2.71) yields

$$\begin{aligned} \sigma_{xx}^{t2}(x,y) &= f\frac{\arccos\left(\frac{b-e}{c}\right) + \arccos\left(\frac{b+e}{c}\right)}{\pi AR}\begin{cases}2u_1 - yv_6 & x \leq 0\\ -2u_1 + yv_6 & 0 < x\end{cases},\\ \sigma_{yy}^{t2}(x,y) &= f\frac{\arccos\left(\frac{b-e}{c}\right) + \arccos\left(\frac{b+e}{c}\right)}{\pi AR}\begin{cases}yv_6 & x \leq 0\\ -yv_6 & 0 < x\end{cases},\\ \sigma_{xy}^{t2}(x,y) &= f\frac{\arccos\left(\frac{b-e}{c}\right) + \arccos\left(\frac{b+e}{c}\right)}{\pi AR}\begin{cases}-v_1 - yu_6 & x \leq 0\\ +v_1 + yu_6 & 0 < x\end{cases}. \end{aligned} \tag{A.28}$$

where the arguments of the functions u_i and v_i have been dropped for brevity, but are

given in equation (A.27). The remaining part of the potential function is

$$\phi^{t3}(z) = \frac{if}{2\pi AR} \begin{cases} (z-b)\ln(G(z-e,c,b-e)) & \\ -(z+b)\ln(G(z-e,c,-b-e)) & x \leq 0 \\ & \\ (z-b)\ln(-G(z-e,c,b-e)) & \\ -(z+b)\ln(-G(z-e,c,-b-e)) & 0 < x \end{cases} \tag{A.29}$$

and its derivative with respect to z leads

$$\frac{\partial}{\partial z}\phi^{t3}(z) = \frac{if}{2\pi AR} \begin{cases} \ln(G(z-e,c,b-e)) - \ln(G(z-e,c,-b-e)) & \\ + \dfrac{\sqrt{c^2-(b-e)^2} - \sqrt{c^2-(b+e)^2}}{\sqrt{(z-e)^2-c^2}} & x \leq 0 \\ & \\ \ln(-G(z-e,c,b-e)) - \ln(-G(z-e,c,-b-e)) & \\ + \dfrac{\sqrt{c^2-(b-e)^2} - \sqrt{c^2-(b+e)^2}}{\sqrt{(z-e)^2-c^2}} & 0 < x \end{cases} \tag{A.30}$$

For the ln() terms occurring in equations (A.29) and (A.30) we may use separations similar to those expressions given by Vázquez et al. (2014) (eqs. (A.11)), but with

different arguments such that we may write

$$
\begin{aligned}
f_2(z) &= \ln(G(z-e,c,b-e)) = u_2(x-e,y,c,b-e) + iv_2(x-e,y,c,b-e)\ , \\
f_2(\bar{z}) &= \ln(G(\bar{z}-e,c,b-e)) = -u_2(x-e,y,c,b-e) + iv_2(x-e,y,c,b-e)\ , \\
f_3(z) &= \ln(G(z-e,c,-b-e)) = u_3(x-e,y,c,b+e) + iv_3(x-e,y,c,b+e)\ , \\
f_3(\bar{z}) &= \ln(G(\bar{z}-e,c,-b-e)) = -u_3(x-e,y,c,b+e) + iv_3(x-e,y,c,b+e)\ , \\
f_4(z) &= \ln(-G(z-e,c,b-e)) = u_2(x-e,y,c,b-e) + i(v_2(x-e,y,c,b-e)+\pi)\ , \\
f_4(\bar{z}) &= \ln(-G(\bar{z}-e,c,b-e)) = -u_2(x-e,y,c,b-e) + i(v_2(x-e,y,c,b-e)+\pi)\ , \\
f_5(z) &= \ln(-G(z-e,c,-b-e)) = u_3(x-e,y,c,b+e) + i(v_3(x-e,y,c,b+e)+\pi)\ , \\
f_5(\bar{z}) &= \ln(-G(\bar{z}-e,c,-b-e)) = -u_3(x-e,y,c,b+e) + i(v_3(x-e,y,c,b+e)+\pi)\ .
\end{aligned}
\tag{A.31}
$$

For the square-root terms in the derivative of the potential (A.30), we note that

$$
\frac{1}{\sqrt{z^2-a^2}} = \frac{f_1(z)}{z} \tag{A.32}
$$

and are able to obtain a separation into real and imaginary parts given by

$$
\begin{aligned}
f_7(z) &= \frac{1}{\sqrt{(z-e)^2-c^2}} = u_7(x-e,y,c) + iv_7(x-e,y,c)\ , \\
f_7(\bar{z}) &= \frac{1}{\sqrt{(\bar{z}-e)^2-c^2}} = u_7(x-e,y,c) - iv_7(x-e,y,c)\ ,
\end{aligned}
\tag{A.33}
$$

where u_7 and v_7 are given in Section A.4. Substitution of the potential function (A.29) and its derivative (A.30), separated into their real and imaginary parts according to equations (A.31) and (A.33), yields explicit expressions for the subsurface stress field

in real algebra, given by

$$\sigma_{xx}^{t3}(x,y) = \frac{f}{\pi AR}\begin{cases} -2(x-b)v_2 + 2(x+b)v_3 - 3y(u_2-u_3) \\ \quad - yv_7\left(\sqrt{c^2-(b-e)^2} - \sqrt{c^2-(b+e)^2}\right) & x \le 0 \\ -2(x-b)v_2 + 2(x+b)v_3 - 3y(u_2-u_3) + 4\pi b \\ \quad - yv_7\left(\sqrt{c^2-(b-e)^2} - \sqrt{c^2-(b+e)^2}\right) & 0 < x \end{cases}$$

$$\sigma_{yy}^{t3}(x,y) = \frac{y\,f}{\pi AR}\left(u_2 - u_3 + v_7\left(\sqrt{c^2-(b-e)^2} - \sqrt{c^2-(b+e)^2}\right)\right)$$

$$\sigma_{xy}^{t3}(x,y) = \frac{f}{\pi AR}\Big[-(x-b)u_2 + (x+b)u_3 + 2y(v_2-v_3) - yv_7\left(\sqrt{c^2-(b-e)^2} - \sqrt{c^2-(b+e)^2}\right]\Big)\ . \tag{A.34}$$

Again, the arguments of the functions u_i and v_i have been dropped for brevity, but are as specified in equations (A.31) and (A.33). The total stress field caused by the corrective shear traction (5.10) is derived by the superposition $\sigma_{ij}^{t} = \sigma_{ij}^{t1} + \sigma_{ij}^{t2} + \sigma_{ij}^{t3}$, and the result is given by equation (5.11).

A.4 Abbreviations for Complex Split

The abbreviations used for the split of complex functions into their real and imaginary part are given by

$$\begin{aligned}
u_1(x,y,a) &= \sqrt{\frac{\sqrt{c_1}+c_2}{2}}\ , & v_1(x,y,a) &= -\mathrm{sgn}(x)\sqrt{\frac{\sqrt{c_1}+c_2}{2}}\ , \\
u_2(x,y,a,b) &= \frac{\ln(\gamma_1)}{2}\ , & v_2(x,y,a,b) &= \theta_1 - \theta_2\ , \\
u_3(x,y,a,b) &= \frac{\ln(\gamma_2)}{2}\ , & v_3(x,y,a,b) &= \theta_3 - \theta_4\ , \\
u_6(x,y,a) &= \frac{x\left(x^2+y^2-a^2+\sqrt{c_1}\right)}{\sqrt{2c_1(\sqrt{c_1}+c_2)}}\ , & v_6(x,y,a) &= -\frac{y\left(x^2+y^2+a^2-\sqrt{c_1}\right)}{\sqrt{2c_1(\sqrt{c_1}+c_2)}}\ , \\
u_7(x,y,a) &= \sqrt{\frac{\sqrt{c_1}+c_2}{2c_1}}\ , & v_7(x,y,a) &= -\frac{x\,y}{c_1}\sqrt{\frac{2c_1}{\sqrt{c_1}+c_2}}\ .
\end{aligned} \tag{A.35}$$

where we used the expressions

$$
\begin{aligned}
\gamma_1 &= \frac{\sqrt{c_3}+c_5+\sqrt{2c_5}\sqrt{\sqrt{c_3}+c_4}}{\sqrt{c_3}+c_5-\sqrt{2c_5}\sqrt{\sqrt{c_3}+c_4}}\,,\\
\gamma_2 &= \frac{\sqrt{c_3}+1/c_5+\sqrt{2/c_5}\sqrt{\sqrt{c_3}+c_4}}{\sqrt{c_3}+1/c_5-\sqrt{2/c_5}\sqrt{\sqrt{c_3}+c_4}}\,,\\
\theta_1 &= \arctan\left[\sqrt{\frac{\sqrt{c_3}-c_4}{2}},\sqrt{\frac{\sqrt{c_3}+c_4}{2}}+\sqrt{c_5}\right]\,,\\
\theta_2 &= \arctan\left[\sqrt{\frac{\sqrt{c_3}-c_4}{2}},\sqrt{\frac{\sqrt{c_3}+c_4}{2}}-\sqrt{c_5}\right]\,,\\
\theta_3 &= \arctan\left[\sqrt{\frac{\sqrt{c_3}-c_4}{2}},\sqrt{\frac{\sqrt{c_3}+c_4}{2}}+\sqrt{\frac{1}{c_5}}\right]\,,\\
\theta_4 &= \arctan\left[\sqrt{\frac{\sqrt{c_3}-c_4}{2}},\sqrt{\frac{\sqrt{c_3}+c_4}{2}}-\sqrt{\frac{1}{c_5}}\right]\,,
\end{aligned}
\tag{A.36}
$$

as well as

$$
\begin{aligned}
c_1 &= \left((a+x)^2+y^2\right)\left((a-x)^2+y^2\right)\,,\\
c_2 &= x^2-y^2-a^2\,,\\
c_3 &= \frac{(a-x)^2+y^2}{(a+x)^2+y^2}\,,\\
c_4 &= \frac{a^2-x^2-y^2}{(a+x)^2+y^2}\,,\\
c_5 &= \frac{a-b}{a+b}\,.
\end{aligned}
\tag{A.37}
$$

B Experimental Data

In the following we list the experimental data of different fretting fatigue experiments reported in the literature.

B.1 Experimental Results by Nowell

The experiments reported by Nowell (1988) were conducted with a Hertzian pad geometry. Pads and specimen were made from a HE15-TF Al/Cu alloy as reported by Araújo and Nowell (1999) with a fatigue strength of $\sigma_{\mathrm{fl}} = 124$ MPa and a long crack

Test	R [mm]	a [mm]	P/Q [−]	σ_0/p_0 [−]	p_0 [MPa]	P $[\frac{\text{N}}{\text{mm}}]$	Q_m $[\frac{\text{N}}{\text{mm}}]$	ΔQ $[\frac{\text{N}}{\text{mm}}]$	$\sigma_{0,\text{m}}$ [MPa]	$\Delta\sigma_0$ [MPa]	N_f [10^6]
1-25	12.5	0.10	0.45	0.59	157	24.7	0	22.2	0	185.4	10
1-5	25	0.19	0.45	0.59	157	46.9	0	42.2	0	185.4	10
1-26	37.5	0.28	0.45	0.59	157	69.1	0	62.1	0	185.4	10
1-53	50	0.38	0.45	0.59	157	93.7	0	84.3	0	185.4	1.29
1-4	75	0.57	0.45	0.59	157	140.6	0	126.5	0	185.4	0.67
1-7	100	0.76	0.45	0.59	157	187.4	0	168.7	0	185.4	0.85
1-54	125	0.95	0.45	0.59	157	234.3	0	210.9	0	185.4	0.73
1-30	150	1.14	0.45	0.59	157	281.1	0	253.0	0	185.4	0.67
2-24	12.5	0.09	0.24	0.65	143	20.2	0	9.7	0	185.4	10
2-13	25	0.18	0.24	0.65	143	40.4	0	19.4	0	185.4	10
2-28	50	0.36	0.24	0.65	143	80.9	0	38.8	0	185.4	10
2-41	75	0.54	0.24	0.65	143	121.3	0	58.2	0	185.4	10
2-10	100	0.72	0.24	0.65	143	161.7	0	77.6	0	185.4	5.06
2-9	125	0.90	0.24	0.65	143	202.2	0	97.0	0	185.4	1.22
2-8	150	1.08	0.24	0.65	143	242.6	0	116.4	0	185.4	1.28
3-20	12.5	0.09	0.45	0.65	143	20.2	0	18.2	0	185.4	10
3-17	25	0.18	0.45	0.65	143	40.4	0	36.4	0	185.4	10
3-37	37.5	0.27	0.45	0.65	143	60.6	0	54.6	0	185.4	4.04
3-42	50	0.36	0.45	0.65	143	80.9	0	72.8	0	185.4	1.5
3-21	75	0.54	0.45	0.65	143	121.3	0	109.2	0	185.4	0.8
3-22	100	0.72	0.45	0.65	143	161.7	0	145.6	0	185.4	0.61
3-18	125	0.90	0.45	0.65	143	202.2	0	181.9	0	185.4	1.24
3-16	150	1.08	0.45	0.65	143	242.6	0	218.3	0	185.4	0.69
4-36	12.5	0.09	0.45	0.54	143	20.2	0	18.2	0	154.4	10
4-35	25	0.18	0.45	0.54	143	40.4	0	36.4	0	154.4	10
4-31	50	0.36	0.45	0.54	143	80.9	0	72.8	0	154.4	10
4-33	75	0.54	0.45	0.54	143	121.3	0	109.2	0	154.4	1.2
4-32	100	0.72	0.45	0.54	143	161.7	0	145.6	0	154.4	1.42
4-34	125	0.90	0.45	0.54	143	202.2	0	181.9	0	154.4	1.02
5-39	25	0.14	0.45	0.52	120	26.4	0	23.8	0	123.6	10
5-43	37.5	0.21	0.45	0.52	120	39.6	0	35.6	0	123.6	10
5-44	50	0.28	0.45	0.52	120	52.8	0	47.5	0	123.6	10
5-45	75	0.42	0.45	0.52	120	79.2	0	71.3	0	123.6	10
5-47	100	0.57	0.45	0.52	120	107.4	0	96.7	0	123.6	10
5-46	125	0.71	0.45	0.52	120	133.8	0	120.4	0	123.6	1.57
5-49	150	0.85	0.45	0.52	120	160.2	0	144.2	0	123.6	1.23
6-49	150	0.85	0.45	0.52	120	160.2	0	144.2	0	123.6	1.23
6-52	150	0.85	0.45	0.52	120	160.2	5.6	133.0	4.7	123.6	7.77
6-50	150	0.85	0.45	0.52	120	160.2	12.8	118.6	11.0	123.6	10
6-51	150	0.85	0.45	0.52	120	160.2	24.0	96.1	20.6	123.6	10
6-48	150	0.85	0.45	0.52	120	160.2	36.0	72.1	30.9	123.6	10

Table B.1: Summary of test specific parameters and reported number of load cycles, N_f, till failure (except run-outs) for fretting fatigue experiments conducted by Nowell (1988).

(plain) fatigue threshold stress intensity of $\Delta K_0 = 66.4$ N/mm$^{3/2}$. The coefficient of friction for the used material was identified with $f = 0.75$. For all the tests the contact was established by a normal load first and subsequently loaded by a shear force and bulk tension varying in phase. The test specific parameters are given in Table B.1.

Test	R [mm]	a [mm]	P/Q [−]	σ_0/p_0 [−]	p_0 [MPa]	P $\left[\frac{\text{N}}{\text{mm}}\right]$	Q_m $\left[\frac{\text{N}}{\text{mm}}\right]$	ΔQ $\left[\frac{\text{N}}{\text{mm}}\right]$	$\sigma_{0,\text{m}}$ [MPa]	$\Delta\sigma_0$ [MPa]	N_f [10^6]
1-6	4.9	4.13	0.13	0.17	665	1202.5	0	312.6	400.0	228.3	0.06
1-70	4.9	4.13	0.13	0.15	665	1202.5	0	312.6	350.0	199.7	0.08
1-69	4.9	4.13	0.13	0.14	665	1202.5	0	312.6	326.7	186.4	0.12
1-9	4.9	4.13	0.13	0.12	665	1202.5	0	312.6	400.0	159.8	0.12
1-65	4.9	4.13	0.13	0.12	665	1202.5	0	312.6	280.0	159.8	0.23
1-66	4.9	4.13	0.13	0.11	665	1202.5	0	312.6	256.7	146.5	0.72
1-67	4.9	4.13	0.13	0.10	665	1202.5	0	312.6	233.3	133.1	0.42
1-68	4.9	4.13	0.13	0.10	665	1202.5	0	312.6	233.3	133.1	10
1-19	4.9	4.13	0.13	0.09	665	1202.5	0	312.6	210.0	119.8	10
1-20	4.9	4.13	0.13	0.07	665	1202.5	0	312.6	163.3	93.2	10
2-23	13	4.25	0.13	0.24	478	1201.5	0	312.4	400.0	228.3	0.09
2-26	13	4.25	0.13	0.20	478	1201.5	0	312.4	326.7	186.4	0.18
2-24	13	4.25	0.13	0.17	478	1201.5	0	312.4	280.0	159.8	0.45
2-62	13	4.25	0.13	0.15	478	1201.5	0	312.4	256.7	146.5	5.04
2-25	13	4.25	0.13	0.14	478	1201.5	0	312.4	233.3	133.1	10
2-22	13	4.25	0.13	0.11	478	1201.5	0	312.4	186.7	106.5	10
3-27	13	4.35	0.13	0.17	665	1982.3	0	515.4	400.0	228.3	0.06
3-28	13	4.35	0.13	0.14	665	1982.3	0	515.4	326.7	186.4	0.26
3-63	13	4.35	0.13	0.12	665	1982.3	0	515.4	280.0	159.8	0.22
3-64	13	4.35	0.13	0.11	665	1982.3	0	515.4	256.7	146.5	0.26
3-29	13	4.35	0.13	0.10	665	1982.3	0	515.4	233.3	133.1	0.82
3-30	13	4.35	0.13	0.09	665	1982.3	0	515.4	210.0	119.8	1.45
3-71	13	4.35	0.13	0.08	665	1982.3	0	515.4	186.7	106.5	0.5
3-72	13	4.35	0.13	0.08	665	1982.3	0	515.4	186.7	106.5	0.78
3-73	13	4.35	0.13	0.07	665	1982.3	0	515.4	163.3	93.2	10

Table B.2: Summary of test specific parameters and reported number of load cycles, N_f, till failure (except run-outs) for fretting fatigue experiments conducted by Dini (2004) (series 1 to 4).

B.2 Experimental Results by Dini

The experiments reported by Dini (2004) were conducted with a flat and rounded pad geometry with a flat half-width of $b = 4$ mm. Pads and specimen were made from Titanium alloy with a fatigue strength of $\sigma_\text{fl} = 568$ MPa and a long crack (plain) fatigue threshold stress intensity of $\Delta K_0 = 142.3$ N/mm$^{3/2}$. The coefficient of friction for the used material was identified with $f = 0.65$. For all the tests the specimen was loaded with the mean value of bulk tension before the contact was established by a normal load. Subsequently the shear force and bulk tension were varied in phase. The test specific parameters for experimental series 1 – 3 are given in Table B.2 and for series 4 – 8 in Table B.3.

Test	R [mm]	a [mm]	P/Q [−]	σ_0/p_0 [−]	p_0 [MPa]	P $\left[\frac{\text{N}}{\text{mm}}\right]$	Q_m $\left[\frac{\text{N}}{\text{mm}}\right]$	ΔQ $\left[\frac{\text{N}}{\text{mm}}\right]$	$\sigma_{0,\text{m}}$ [MPa]	$\Delta\sigma_0$ [MPa]	N_f [10^6]
4-92	8.2	4.19	0.13	0.33	565	1222.0	0	317.7	653.5	372.9	0.01
4-91	8.2	4.19	0.13	0.26	565	1222.0	0	317.7	513.0	292.8	0.03
4-2	8.2	4.19	0.13	0.20	565	1222.0	0	317.7	400.0	228.3	0.06
4-36	8.2	4.19	0.13	0.20	565	1222.0	0	317.7	400.0	228.3	0.06
4-37	8.2	4.19	0.13	0.16	565	1222.0	0	317.7	326.7	186.4	0.15
4-38	8.2	4.19	0.13	0.14	565	1222.0	0	317.7	280.0	159.8	0.13
4-39	8.2	4.19	0.13	0.13	565	1222.0	0	317.7	256.7	146.5	10
4-40	8.2	4.19	0.13	0.12	565	1222.0	0	317.7	233.3	133.1	10
5-114	8.2	4.19	0.26	0.28	565	1222.0	0	635.4	560.0	319.6	0.03
5-113	8.2	4.19	0.26	0.26	565	1222.0	0	635.4	513.3	292.9	0.03
5-112	8.2	4.19	0.26	0.25	565	1222.0	0	635.4	490.0	279.6	0.04
5-111	8.2	4.19	0.26	0.24	565	1222.0	0	635.4	466.7	266.3	0.04
5-47	8.2	4.19	0.26	0.19	565	1222.0	0	635.4	373.3	213.0	0.07
5-46	8.2	4.19	0.26	0.16	565	1222.0	0	635.4	326.7	186.4	0.12
5-45	8.2	4.19	0.26	0.14	565	1222.0	0	635.4	280.0	159.8	0.16
5-41	8.2	4.19	0.26	0.13	565	1222.0	0	635.4	256.7	146.5	0.2
5-42	8.2	4.19	0.26	0.12	565	1222.0	0	635.4	233.3	133.1	0.75
5-53	8.2	4.19	0.26	0.12	565	1222.0	0	635.4	233.3	133.1	0.27
5-49	8.2	4.19	0.26	0.11	565	1222.0	0	635.4	210.0	119.8	0.43
5-50	8.2	4.19	0.26	0.09	565	1222.0	0	635.4	186.7	106.5	0.59
5-51	8.2	4.19	0.26	0.07	565	1222.0	0	635.4	140.0	79.9	2.07
5-52	8.2	4.19	0.26	0.05	565	1222.0	0	635.4	93.3	53.2	10
6-106	8.2	4.22	0.13	0.24	665	1563.2	0	406.4	560.0	319.6	0.03
6-105	8.2	4.22	0.13	0.22	665	1563.2	0	406.4	513.3	292.9	0.04
6-104	8.2	4.22	0.13	0.21	665	1563.2	0	406.4	490.0	279.6	0.04
6-54	8.2	4.22	0.13	0.16	665	1563.2	0	406.4	373.3	213.0	0.1
6-55	8.2	4.22	0.13	0.14	665	1563.2	0	406.4	326.7	186.4	0.14
6-60	8.2	4.22	0.13	0.12	665	1563.2	0	406.4	280.0	159.8	0.55
6-57	8.2	4.22	0.13	0.11	665	1563.2	0	406.4	256.7	146.5	0.28
6-59	8.2	4.22	0.13	0.10	665	1563.2	0	406.4	233.3	133.1	0.62
6-58	8.2	4.22	0.13	0.09	665	1563.2	0	406.4	210.0	119.8	10
6-61	8.2	4.22	0.13	0.09	665	1563.2	0	406.4	210.0	119.8	10
7-11	4.9	4.13	0.13	0.12	665	1202.5	0	312.6	280.0	159.8	0.09
7-12	4.9	4.13	0.13	0.12	665	1202.5	0	312.6	280.0	159.8	0.14
7-15	4.9	4.13	0.13	0.12	665	1202.5	0	312.6	280.0	159.8	0.28
7-13	4.9	4.13	0.13	0.12	665	1202.5	0	312.6	280.0	159.8	0.42
7-16	4.9	4.13	0.13	0.12	665	1202.5	0	312.6	280.0	159.8	1.17
7-17	4.9	4.13	0.13	0.12	665	1202.5	0	312.6	280.0	159.8	6.01
8-75	8.2	4.19	0.39	0.16	565	1222.0	0	953.2	326.7	186.4	0.09
8-76	8.2	4.19	0.39	0.14	565	1222.0	0	953.2	280.0	159.8	0.14
8-77	8.2	4.19	0.39	0.12	565	1222.0	0	953.2	233.3	133.1	0.28
8-78	8.2	4.19	0.39	0.09	565	1222.0	0	953.2	186.7	106.5	0.42
8-79	8.2	4.19	0.39	0.07	565	1222.0	0	953.2	140.0	79.9	1.17
8-94	8.2	4.19	0.39	0.05	565	1222.0	0	953.2	93.3	53.2	6.01

Table B.3: Summary of test specific parameters and reported number of load cycles, N_f, till failure (except run-outs) for fretting fatigue experiments conducted by Dini (2004) (series 5 to 8).

B.3 Experimental Results by Szolwinski and Farris

The experiments reported by Szolwinski and Farris (1998) were conducted with a Hertzian pad geometry. Pads and specimen were made from a 2024-T351 Aluminium

Test	R [mm]	a [mm]	P/Q [−]	σ_0/p_0 [−]	p_0 [MPa]	P $\left[\frac{\text{N}}{\text{mm}}\right]$	Q_m $\left[\frac{\text{N}}{\text{mm}}\right]$	ΔQ $\left[\frac{\text{N}}{\text{mm}}\right]$	$\sigma_{0,\text{m}}$ [MPa]	$\Delta\sigma_0$ [MPa]	N_f [10^6]
1	127	1.54	0.22	0.45	246.0	595.1	0	261.8	0	220.6	0.31
2	127	1.24	0.28	0.43	197.8	385.3	0	215.8	0	169.4	0.42
3	127	1.31	0.31	0.53	208.4	428.8	0	265.9	0	220.6	0.24
4	127	1.21	0.35	0.50	202.7	385.3	0	269.7	0	201.4	0.24
5	127	1.37	0.31	0.48	230.6	496.2	0	307.7	0	220.6	0.22
6	229	1.76	0.43	0.72	155.7	430.4	0	370.2	0	223.4	0.24
7	229	1.75	0.37	0.73	155.3	426.9	0	315.9	0	225.8	0.25
8	127	1.40	0.23	0.38	223.2	490.8	0	225.8	0	169.6	0.67
9	178	1.66	0.27	0.53	189.2	493.3	0	266.4	0	200	0.35
10	178	1.66	0.27	0.53	189.2	493.3	0	266.4	0	200	0.43
11	127	1.30	0.35	0.43	207.3	423.3	0	296.3	0	176.8	0.56
12	127	1.51	0.31	0.42	240.4	570.2	0	353.5	0	203.8	0.55
13	127	1.51	0.31	0.42	240.4	570.2	0	353.5	0	203.8	0.34
14	178	1.53	0.38	0.49	174.2	418.7	0	318.2	0	171.6	0.58
15	229	1.88	0.32	0.58	166.3	491.1	0	314.3	0	194	0.74
16	178	1.75	0.34	0.57	199.9	549.5	0	373.7	0	226.2	0.46
17	229	1.88	0.32	0.51	166.9	492.9	0	315.4	0	170.8	0.86
18	127	1.28	0.52	0.57	204.0	410.2	0	426.6	0	231.6	0.47
19	178	1.77	0.21	0.42	201.2	559.4	0	234.9	0	170.4	0.67
20	178	1.77	0.21	0.42	201.2	559.4	0	234.9	0	170.4	0.75
21	229	2.00	0.24	0.46	177.3	557.0	0	267.4	0	163.6	0.75
22	229	2.00	0.25	0.46	177.3	557.0	0	278.5	0	163.6	0.73
23	127	1.40	0.35	0.49	223.0	490.4	0	343.3	0	218.4	0.30
24	229	1.73	0.31	0.53	153.4	416.9	0	258.5	0	162	0.87
25	229	1.74	0.26	0.54	153.8	420.4	0	218.6	0	165.8	0.77
26	178	1.79	0.31	0.49	203.6	572.5	0	354.9	0	198.8	0.55
27	229	1.99	0.34	0.62	176.4	551.4	0	375.0	0	219	0.32
28	127	1.49	0.27	0.46	237.8	556.6	0	300.5	0	217.6	0.25
29	229	1.87	0.33	0.67	165.8	487.0	0	321.4	0	221.6	0.48
30	127	1.40	0.36	0.44	224.0	492.6	0	354.7	0	196.4	0.46
31	229	2.01	0.24	0.55	178.3	562.9	0	270.2	0	195.8	0.46
32	178	1.65	0.27	0.45	187.9	487.0	0	263.0	0	169.4	0.62
33	178	1.53	0.36	0.56	174.3	418.9	0	301.6	0	194.8	0.46
34	178	1.69	0.34	0.55	192.1	510.0	0	346.8	0	212.8	0.23
35	178	1.53	0.38	0.63	174.9	420.3	0	319.5	0	221.2	0.33
36	127	1.31	0.33	0.46	209.0	430.1	0	283.8	0	194.2	0.31
37	127	1.50	0.27	0.36	238.6	562.2	0	303.6	0	170.8	0.38

Table B.4: Summary of test specific parameters and reported number of load cycles, N_f, till failure for fretting fatigue experiments conducted by Szolwinski and Farris (1998).

alloy with a fatigue strength of $\sigma_\text{fl} = 124$ MPa and a long crack (plain) fatigue threshold stress intensity of $\Delta K_0 = 66.4\ \text{N/mm}^{3/2}$. The coefficient of friction for the used material was identified with $f = 0.65$. For all the tests the contact was established by a normal load first and subsequently loaded by a shear force and bulk tension varying in phase. The test specific parameters are given in Table B.4.

Test	R [mm]	a [mm]	P/Q [−]	σ_0/p_0 [−]	p_0 [MPa]	P $[\frac{\text{N}}{\text{mm}}]$	Q_m $[\frac{\text{N}}{\text{mm}}]$	ΔQ $[\frac{\text{N}}{\text{mm}}]$	$\sigma_{0,\text{m}}$ [MPa]	$\Delta\sigma_0$ [MPa]	N_f $[10^6]$
1	50	0.46	0.29	0.53	187.0	135.8	0	77.6	55.0	200	1.41
2	50	0.46	0.34	0.62	187.0	135.8	0	93.1	63.3	230	1.11
3	50	0.46	0.41	0.72	187.0	135.8	0	111.9	74.3	270	0.36
4	50	0.46	0.36	0.72	187.0	135.8	0	97.8	74.3	270	0.42
5	50	0.46	0.36	0.86	187.0	135.8	0	96.9	88.0	320	0.25
6	50	0.46	0.61	1.02	187.0	135.8	0	165.1	104.5	380	0.14
7	50	0.46	0.59	1.10	187.0	135.8	0	161.1	112.8	410	0.11
8	50	0.46	0.49	1.18	187.0	135.8	0	133.6	121.0	440	0.10
9	50	0.46	0.59	1.18	187.0	135.8	0	158.9	121.0	440	0.09

Table B.5: Summary of test specific parameters and reported number of load cycles, N_f, till failure for fretting fatigue experiments conducted by Hojjati-Talemi et al. (2014).

B.4 Experimental Results by Hojjati-Talemi et al.

The experiments reported by Hojjati-Talemi et al. (2014) were conducted with a Hertzian pad geometry. As Nowell, 1988, Hojjati-Talemi et al. (2014) uses pads and specimen from a 2024 Aluminium alloy and we therefore assume the same fatigue strength of $\sigma_\text{fl} = 124$ MPa and long crack (plain) fatigue threshold stress intensity of $\Delta K_0 = 66.4$ N/mm$^{3/2}$. The coefficient of friction for the used material was identified with $f = 0.65$. For all the tests the contact was established by a normal load first, followed by the mean value of bulk tension before the shear force and bulk tension were varied in phase. The test specific parameters are given in Table B.5.